UNIVERSITY OF
BIRMINGHAM

EXPERIMENTAL AND COMPUTATIONAL EVALUATION OF ACTIVATED CARBONS FOR CARBON DIOXIDE CAPTURE FROM HIGH PRESSURE GAS MIXTURES

By

SIMON JAMES CALDWELL

A thesis submitted to the University of Birmingham

for the degree of

DOCTOR OF PHILOSOPHY

Reaction and Catalysis Engineering Group

School of Chemical Engineering

College of Engineering and Physical Sciences

University of Birmingham

October 2014

Abstract

This PhD project aimed to study the separation of carbon dioxide from high pressure gas mixtures as it is directly applicable to pre-combustion carbon dioxide capture. Adsorption is a well understood process but the application to capturing carbon dioxide at high pressure, as well as producing a high quality light component stream, has not been widely studied. This project looked at the experimental evaluation of these systems, validation of an adsorption model and simulation of pressure swing adsorption (PSA) cycles.

Two activated carbon materials, an unmodified and a modified material, were studied experimentally. The materials were characterised by SEM images, BET measurement and density measurements. Adsorption isotherms were produced and best fit by the Langmuir-Freundlich and dual-site Langmuir (DSL) isotherms. Breakthrough experiments investigated the separation under dynamic conditions to find the breakthrough capacity of the activated carbons. These experiments showed that adsorption capacities need to be studied on a volumetric basis instead of a mass basis as the size of an adsorbent bed is dictated by the volume of adsorbent required. Several multicomponent isotherm models were studied and compared to the experimental breakthrough capacities. The multicomponent DSL isotherm model was the found to best represent the experimental data.

An axial dispersed plug flow model was validated against the experimental data with a reasonable accuracy. Different correlations were tested and discussed. For the dispersion coefficient, it was found that correlations for non-porous materials were more suitable than those for porous materials due to the high pressure operation.

Cyclic experiments were also validated and were found to be restricted by the surrounding pipework and instruments. A parameter sensitivity analysis was conducted and indicated the particle diameter, bed voidage and particle voidage had the greatest effect on the breakthrough curve.

Pressure swing adsorption systems were simulated. Simple cycles were proven to not produce high quality heavy or light product. Pressure equalisation steps were shown to significantly improve the carbon dioxide purity and the light product capture rate. Counter-current operation was tested and found to not affect the performance indicators. A novel purge recycle step was introduced which improved both the carbon dioxide purity and the light product capture rate. A carbon dioxide purity of 93.8% was achieved by using a rinse step after pressure equalisation steps, but required a compressor and resulted in a significant reduction in carbon dioxide capture rate.

Acknowledgements

It is not possible to complete a PhD on your own and there are many people who greatly helped me along the way.

Firstly I would like to express my deep gratitude to both of my supervisors. Prof. Joe Wood provided many hours of help and guidance through the entire project, especially in reading the many drafts of this thesis. Dr. Bushra Al-Duri was very supportive during the project and was always there when needed.

Thank you to the EPSRC for providing funding. I would like to acknowledge the collaboration partners both in the UK and in China. Prof. Colin Snape, Prof. Jihong Wang, Dr. Hao Liu and Dr. Cheng-gong Sun all helped guide this work. I very much enjoyed working with Dr. Nannan Sun and Yue Wang. My thanks to Dr. Sun and Sarah Bell for conducting the characterisation experiments.

The other staff and students at the University of Birmingham made the entire PhD worthwhile. My colleagues in the lab were always helpful. I will never forget the people in Room 118 and the endless useful and pointless discussions.

I would like to say a special thank you to Sally Clarkson. She had to endure a lot whilst I finished and wrote this thesis but always understood. Through the toughest parts of this PhD she was there and I will never forget that.

Finally I would like to thank my family. Despite never fully understanding the work I was doing they always helped in any way they could. My parents provided me an upbringing and education that allowed me to complete this PhD and for that I will always be grateful.

Table of Contents

List of Figures

List of Tables

List of Abbreviations

AC	Unmodified activated carbon
Ad	Adsorption step
BD	Blowdown step
BET	Brunauer-Emmett-Teller
CCS	Carbon dioxide capture and storage
CMS	Carbon molecular sieves
Depress	Depressurisation step
DR	Dubinin-Radushkevich
DSL	Dual-site Langmuir
ED	Pressure equalisation down
EU	Pressure equalisation up
HPVA	High pressure volumetric analysis
I	Idle step
IAST	Ideal adsorbed solution theory
IGCC	Integrated gasification combined cycle
LDF	Linear driving force
LF	Langmuir-Freundlich
LPSA	Layered pressure swing adsorption
MAC	Modified activated carbon
MCM	Mobile composition of matter molecular sieve
MOF	Metal organic framework
MSL	Multi-site Langmuir

NGCC	Natural gas combined cycle
PAN	Polyacrylnitrole
Press	Pressurisation step
PSA	Pressure swing adsorption
Pur	Purge step
Pur-c	Purge step with clean feed
Pur-r	Purge step with recycle
Rinse	Rinse step
SEM	Scanning electron microscope
SEWGS	sorption enhanced water gas shift
SSD	Normalised sum of the squared of the differences
SSE	Sum of the squared of the errors
STP	Standard temperature and pressure
TSA	Temperature swing adsorption
VPSA	Vacuum pressure swing adsorption
WGS	Water gas shift
Z13X	Zeolite 13X
Z5A	Zeolite 5A

List of Symbols

Alphabetical Symbols

A	Bed cross sectional area	m^2
A_{erg}	Constant for Ergun equations	-
B_i	Langmuir-Freundlich (LF) Constant	Pa^{-n}
$B_{1,i}$	Dual-site Langmuir(DSL) constant site 1	Pa^{-1}
$B_{2,i}$	Dual-site Langmuir(DSL) constant site 2	Pa^{-1}
B_{erg}	Constant for Ergun equations	-
C	Total Concentration	mol m^{-3}
$c_{0,i}$	Component Concentration in feed	mol m^{-3}
$C_{p,a}$	Heat capacity of adsorbent	J kg^{-1} K^{-1}
$C_{p,g}$	Heat capacity of gas	J kg^{-1} K^{-1}
$C_{p,\mathrm{w}}$	Heat capacity of bed wall	J kg^{-1} K^{-1}
C_v	Valve coefficient	-
D_{ax}	Axial dispersion coefficient	m^2 s^{-1}
D_c/r_c^2	Micropore diffusivity over micropore radius squared	s^{-1}
D_k	Knudsen Diffusion	m^2 s^{-1}
D_m	Molecular Diffusion	m^2 s^{-1}
D_{pore}	Pore Diffusion	m^2 s^{-1}
d_b	Bed Diameter	m
d_p	Particle Diameter	m

d_{pore}	Pore Diameter	m
F_i^{out}	Flow of gas in outlet stream	$m^3\ s^{-1}$
h_w	Inside wall heat transfer coefficient	$kW\ m^{-2}\ K^{-1}$
${h_w}^o$	Heat transfer coefficient for stagnant flow	$kW\ m^{-2}\ K^{-1}$
ΔH_i	Component heat of adsorption	$kJ\ mol^{-1}$
k_i	Component mass transfer coefficient	s^{-1}
k_f	External mass transfer coefficient	$m\ s^{-1}$
K_g	Thermal conductivity of the gas	$W\ m^{-1}\ K^{-1}$
K_w	Thermal conductivity of the bed wall	$W\ m^{-1}\ K^{-1}$
$k_{1,i}$	Constant for finding $q_{s,i}$ in LF	$mol\ kg^{-1}$
$k_{2,i}$	Constant for finding $q_{s,i}$ in LF	$J\ mol^{-1}$
$k_{3,i}$	Constant for finding B_i in LF	Pa^{-n}
$k_{4,i}$	Constant for finding B_i in LF	$J\ mol^{-1}$
$k_{1,1,i}$	Constant for finding $q_{1,s,i}$ in DSL	$mol\ kg^{-1}$
$k_{1,2,i}$	Constant for finding $q_{1,s,i}$ in DSL	$J\ mol^{-1}$
$k_{1,3,i}$	Constant for finding $B_{1,i}$ in DSL	Pa^{-n}
$k_{1,4,i}$	Constant for finding $B_{1.i}$ in DSL	$J\ mol^{-1}$
$k_{2,1,i}$	Constant for finding $q_{2,s,i}$ in DSL	$mol\ kg^{-1}$
$k_{2,2,i}$	Constant for finding $q_{2,s,i}$ in DSL	$J\ mol^{-1}$
$k_{2,3,i}$	Constant for finding $B_{2,i}$ in DSL	Pa^{-n}
$k_{2,4,i}$	Constant for finding $B_{2,i}$ in DSL	$J\ mol^{-1}$
M_w	Molecular Weight	$g\ mol^{-1}$
N	Number of data points	-

n_i	Exponent in Langmuir-Freundlich isotherm	-
P	Pressure	Pa
P_{feed}	Pressure of feed stream	Pa
P_{out}	Pressure of stream at bed outlet	Pa
$P_{out\ set}$	Set pressure of stream at bed outlet	Pa
p_i	Component partial pressure	Pa
Q	Volumetric flowrate	$m^3\ s^{-1}$
Q_{feed}	Volumetric flowrate of the feed	$m^3\ s^{-1}$
Q_{out}	Volumetric flowrate of stream at bed outlet	$m^3\ s^{-1}$
$Q_{out\ set}$	Set volumetric flowrate of stream at bed outlet	$m^3\ s^{-1}$
$q_{i,exp}$	Number of moles of component captured in the experiment	$mol\ kg^{-1}$
$q_{i,mod}$	Number of moles of component captured in the model	$mol\ kg^{-1}$
$q_{i,pipe}$	Number of moles of component accumulated in the pipes and surrounding instruments	$mol\ kg^{-1}$
q_i	Component solid phase concentration	$mol\ m^{-3}$
q_i^*	Component solid phase concentration at equilibrium	$mol\ m^{-3}$
$q_{0,i}$	Solid phase concentration at c_0	$mol\ m^{-3}$
$q_{s,i}$	Component solid phase concentration at saturation	$mol\ kg^{-1}$
q_t	Total solid phase concentration	$mol\ m^{-3}$

q_i^{pure}	Solid phase concentration predicted by pure component isotherm	mol m^{-3}
R	Gas Constant	J mol^{-1} K^{-1}
SG	Specific gravity	-
SP	Valve set point	-
T	Temperature	K
T_{amb}	Surroundings temperature	K
T_{feed}	Temperature of feed stream	K
T_{wall}	Temperature of at the bed wall	K
$t_{breakthrough}$	Time for CO_2 to breakthrough	s
t_5	Time for CO_2 to reach 5% of feed concentration	s
t_{50}	Time for CO_2 to reach 50% of feed concentration	s
t_{90}	Time for CO_2 to reach 90% of feed concentration	s
t_{100}	Time for CO_2 to reach 100% of feed concentration	s
v	Velocity	m s^{-1}
x_i	Adsorbed phase component fraction	-
y_i	Component mole fraction	-
$y_{feed,i}$	Component mole fraction in feed	-
$y_{i,exp}$	Component mole fraction from experiment	-
$y_{i.mod}$	Component mole fraction from model	-
z	Axial Position	m

Greek Symbols

α_w	Wall HT coefficient fitting parameter	-
β_{air}	Coefficient for finding external heat transfer coefficient	K^{-1}
δ	Bed wall thickness	m
ε	Voidage	-
$\varepsilon_{AB}/_{\kappa}$	Maximum attractive energy between 2 molecules divided by dilational viscosity	K^{-1}
ε_b	Bed voidage	-
ε_p	Particle voidage	-
ε_t	Total voidage	-
γ_1	Constant for finding dispersion coefficient	-
γ_2	Constant for finding dispersion coefficient	-
λ_{ax}	Thermal axial dispersion coefficient	kW m^{-1} K^{-1}
μ_g	Viscosity	Pa s
ρ_b	Bed density	kg m^{-3}
ρ_g	Gas density	kg m^{-3}
ρ_w	Bed wall density	kg m^{-3}
π_i^0	Spreading pressure	Pa
σ_{AB}	Collision diameter	m
τ	Tortuosity	-

$\Omega_{D,AB}$	Collision integral	-

Dimensionless Groups

Gr	Grashof Number	-
Gr_{air}	Grashof Number for air	-
Pe'	Peclet number for axial dispersion	-
Pr	Prandtl Number	-
Pr_{air}	Prandtl Number for air	-
Re	Reynolds Number	-
Sc	Schmidt Number	-

Chapter 1 – Introduction

1.1 Background

The development of carbon dioxide capture and storage (CCS) technologies to minimise emissions from power plants is essential to meet objectives put in place by many world governments to reduce carbon dioxide levels. It is estimated that the most economical way achieve these goals is to use CCS to reduce 14% of the total emissions (IEA, 2012). Pre combustion carbon dioxide capture is an attractive CCS technology as the gas streams are at elevated pressures and with a high concentration of carbon dioxide. Pressure swing adsorption (PSA) systems are particularly attractive with simple operation and low operating costs (Bell and Towler, 2010). Activated carbons have been shown to be suitable adsorbents for carbon dioxide capture at high pressure where their large microporous nature can be utilised (Drage et al., 2009b).

With this in mind, a collaboration was set up between the University of Birmingham, the University of Nottingham, the University of Warwick, University College London, Tsinghua University and the Chinese Academy of Sciences with funding from the Engineering and Physical Sciences Research Council in project EP/I010955/1. The collaboration aimed to investigate the development of activated carbon materials, the simulation of a PSA unit and the simulation of an integrated gasification combined cycle (IGCC) power plant. The work presented in this study looks at the development of a model for the simulation of PSA cycles.

1.2 Study Aims

The overall aim of this work was to investigate the application of activated carbons for the removal of carbon dioxide from high pressure mixtures both experimentally

and using simulations. The study was readily split into three distinct sections: the experimental investigation of activated carbon under dynamic conditions, the validation of an adsorption model and the application of the adsorption model to a PSA system.

The experimental investigation had two distinct aims. The first was to understand the response of activated carbon materials to a dynamic separation of carbon dioxide from either nitrogen or hydrogen. The literature is predominately based on the study of materials under equilibrium conditions using adsorption isotherms. The isotherm models used to predict the adsorption capacity of the material were compared to the material capacity found from breakthrough experiments to find the applicability of the equilibrium results to conditions more representative of those used in industry. The second aim of the experimental results was to produce data for the validation of an adsorption model.

The computational investigation is split between the validation of an adsorption model and the application of the model to a PSA system. An axial dispersed plug flow model was applied and the validation aimed to evaluate the most suitable equations and correlations for simulating high pressure separations. The validation was then extended further to the cyclic operation of an adsorption bed which is not widely discussed in the literature. Finally, a parameter sensitivity study was conducted to find the properties of the adsorbent material and bed which have the most significant impact on the dynamic separation.

The final aim was to investigate the PSA cycle used in the separation of carbon dioxide from a mixture with nitrogen in order to produce a high quality heavy and light

product, which is not well reported. Previous studies have only presented a final optimum cycle, and so this study aimed to evaluate the effect different cycle steps had on the quality of both gases to understand the steps which gave the most significant improvement. The other objective was to suggest novel step sequences which would aid in the purification of both gases.

1.3 Thesis Outline

There are eight chapters in this thesis. Chapter one outlines the background of the project and the main objectives of the research.

Chapter two is a critical review of the literature relevant to the application of PSA to high pressure systems. The necessity for CCS is briefly discussed and the different technologies for the removal of carbon dioxide applicable to IGCC power plants outlined. The use of activated carbons as an adsorbent is highlighted and in depth discussion of the way these materials are currently characterised for CCS applications is conducted. Finally, the simulation of adsorbent beds and PSA systems in the literature is discussed.

Chapter three details the experimental methods used in this research. First the characterisation techniques are outlined. Following this, the experimental rig used to conduct fixed bed breakthrough experiments is explained.

The theory used in the analysis of experimental results and in the simulation of adsorption systems is provided in Chapter four. The equations that the models are based on are detailed for all of the simulations conducted. The solution techniques used and the simulation structure are also explained.

Chapter five presents the experimental results. It starts by reporting the results of the characterisation of an unmodified and a modified activated carbon to find the respective particle size, BET pore surface area, material voidage and adsorption isotherms. The results of the dynamic experiments follow, including an in depth discussion of the analysis of the breakthrough capacities compared to equilibrium capacities predicted by isotherm models.

The validation and application of an axial dispersed plug flow model to the experimental breakthrough curves is presented in Chapter six. The model which best fits the breakthrough experiments of the unmodified material is first reported before a discussion on the derivation of the most suitable model. The results of further validation against cyclic models and the modified activated carbon are then presented. Finally, a parameter sensitivity study using the validated model is discussed.

Chapter seven presents the application of the validated model to PSA cycles. The application of a simple 4 step PSA cycle is discussed. Following this, the further development of this cycle by the manipulation of the bed sequence and incorporation of different process steps is detailed. The final PSA cycle which gave the best recovery of both the heavy and light component is then presented.

An overview of the conclusions of the experimental and computational evaluation of activated carbons for carbon dioxide capture from high pressure gas mixtures is presented in Chapter eight. Based on the conclusions of the study, suggestions for future work to further advance the field are made.

Chapter 2 – Literature Review

2.1 Introduction

Carbon dioxide capture and storage is now viewed as a technology required for reducing carbon dioxide emissions (Global CCS Institute, 2013). Pre-combustion capture from integrated gasification combined cycle (IGCC) power plants has been suggested as an efficient means of capturing carbon dioxide (Liu et al., 2009). This chapter reviews pre-combustion capture systems and the application of capture technologies. Adsorbent materials used in pressure swing adsorption (PSA) systems are then analysed. Activated carbons are considered as a suitable material for the high pressure separations taking place. The nature in which the adsorption capacity of the activated carbon materials is measured is discussed. Simulation of these processes provides a valuable tool for analysing both adsorbent materials and the PSA unit configuration. The models applied to adsorption systems are discussed before a detailed review of simulations of specific PSA systems is reported. The application of these models for the removal of carbon dioxide from mixtures at high pressure is limited in literature and therefore this literature study also reviews other similar high pressure systems, as well as studies on post-combustion capture of carbon dioxide at low pressure.

2.2 Carbon Dioxide Emissions

2.2.1 Current Energy Trends

Most economies are heavily dependent on fossil fuels, with only 13.3% of total energy derived from nuclear energy, hydroelectricity or renewable source, with oil, coal and natural gas supplying 32.8%, 30.1% and 23.7% respectively (BP, 2014). There is general agreement amongst scientists that rising carbon dioxide levels are

leading to anthropogenic climate change, with the power sector contributing 34% of anthropogenic carbon dioxide emissions (European Commission - Joint Research Centre (JRC)/PBL Netherlands Environmental Assessment Agency, 2011).

China is the largest consumer of coal on the planet but more significantly has seen a rapid rise in consumption, increasing from 868.2 million tonnes of oil equivalent in 2003 to 1925.3 million tonnes of oil equivalent in 2013 (BP, 2014). This sharp rise means that China is now the largest emitter of greenhouse gasses in the world, dominated by its power sector. Of the power sector, 80% is from coal and in 2006 new coal power stations were being built at a rate of 170 GW per year. It is anticipated by 2030 China will be responsible for 26% of global CO_2 emissions with 98% of the power sector emissions coming from coal (Sioshansi, 2009). This emphasises that the power industry is not expected to shift to low carbon technologies in the near future and that coal powered fire stations will continue to be used.

However, there is a need for large reductions in carbon dioxide emissions on a faster timescale. The UK government has put legislation in place dictating carbon dioxide reductions of 80% from 1990 levels by 2050 (Committee on Climate Change, 2010b). Up to this point, yearly emissions targets have been met through increased energy efficiency on a commercial and domestic front (Global CCS Institute, 2013). However, this has largely left the energy market unaddressed, which is reaching a key period as decisions made now will exist for several decades. The UK government has set emissions targets for the power sector of a reduction from approximately 500 $gCO_2\ kWhr^{-1}$ to 50 $gCO_2\ kWhr^{-1}$ by 2030 (Committee on Climate Change, 2010a). In order to achieve this, the Committee on Climate Change (2010a)

states a mix in technology is needed, including coal with carbon capture and sequestration. On a more global scale, a report by the IEA (2012) highlighted the requirement for carbon dioxide capture and storage (CCS) to reach global emission targets by 2050, with the cost of using other mitigation technologies costing a further US$2 trillion.

CCS is clearly required on a global level and attitudes towards it are shifting. A recent study by Liang et al. (2011) looked at the perceptions of opinion leaders in China towards CCS demonstration projects. They found that the policy in China was aimed more towards energy security and energy efficiency than CCS. The study reported that industry leaders viewed climate change as an immediate threat and half of respondents claimed climate change was important to their organisation. At the same time, three quarters believed it would be difficult to achieve substantial cuts in the next two decades. There are still many concerns over the reliability of CCS and the availability of storage sites. However, the opportunity for investment in new technology in China is huge. Potential investment in the power sector in China between 2006 and 2030 is approximately $2.7 trillion. There is also a need to invest in technologies which reduce conventional air pollutants and this is a priority seen in government policy (Sioshansi, 2009). Liang et al. (2011) found that industrial leaders see pre-combustion technology as a suitable capture technique, with 50% favouring this method. The remaining leaders leaned towards post-combustion technology but many said a combination of technologies is required. This means that there is the opportunity for pre-combustion capture to have a significant impact on the carbon dioxide emissions in China.

2.2.2 Carbon Dioxide Capture Strategies

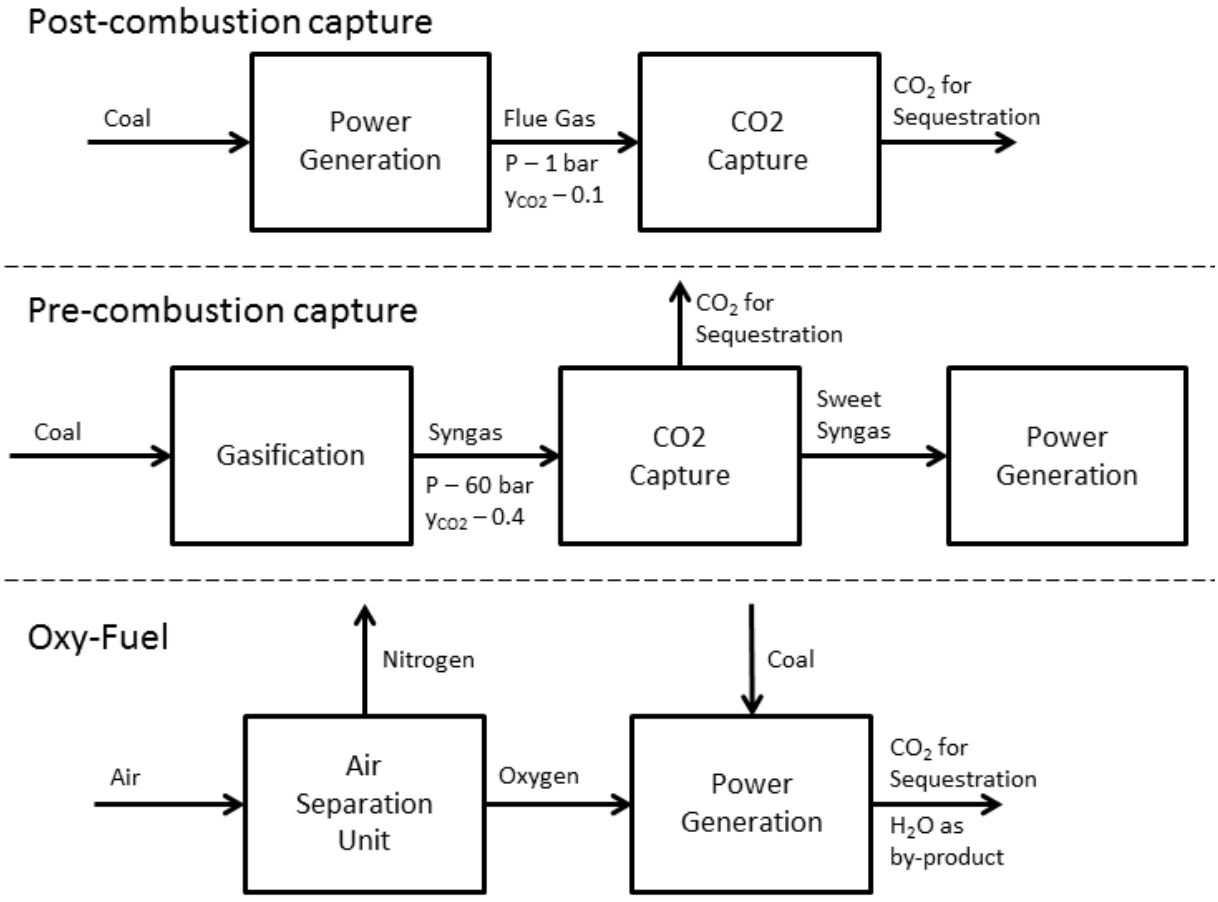

Figure 2.1: The three main capture strategies for CCS for coal fired power plants.

There are three main options for CCS: post-combustion capture, pre-combustion capture and oxy-fuel production, as shown in Figure 2.1. Post-combustion capture removes carbon dioxide from flue gas before being sequestered. Pre-combustion removes carbon dioxide before syngas is combusted, typically in an IGCC power plant. Oxy-fuel involves combusting the fuel using pure oxygen resulting in the only products being carbon dioxide and water, with the water readily removed. Figueroa et al. (2008) completed a review for the U.S. Department of Energy on capture technologies. This work firstly pointed out the expense of capturing carbon dioxide

from power plants, indicating that retrofitting plants with post-combustion capture would reduce power output by a third and new plants with pre-combustion capture would be subject to a power output reduction of 20%, and suggested the need for technology to be further developed. A breakdown of the three types of technologies is provided. It is pointed out that post-combustion capture can be applied to most power stations and is readily retrofitted but has the inherent problem of dilute carbon dioxide (~10% CO2) at atmospheric pressure resulting in low pressure carbon dioxide streams and large capture plants. Pre-combustion capture on the other hand can be achieved from concentrated carbon dioxide streams (~40% CO_2) at high pressure (up to 6 MPa), which increases the driving force for separation and allows a greater scope of technologies to be supplied. The disadvantage of this is that it is not readily retrofitted and requires complex and expensive equipment. Finally Oxy-fuel is examined, which can produce high concentration carbon dioxide and is readily retrofitted but also requires a large oxygen supply, which is costly. Liu et al. (2009) produced a similar review and came to many of the same conclusions. That study also pointed out the capital cost implications of CCS, with a new plant using post-combustion capture and a new plant using pre-combustion capture having 75% and 33% greater capital cost respectively compared to the equivalent plant without. The Global CCS Institute (2013) reported that post-combustion and pre-combustion capture are advancing at the same rate with post-combustion having 13 large scale investment projects and pre-combustion having 11. There are also many large scale pilot facilities, with five pre-combustion capture projects in operation or under construction capable of capturing 8,000 tonnes per annum of carbon dioxide.

2.3 Integrated Gasification Combined Cycle (IGCC) Power Plants

Books by Miller (2011) and by Bell and Towler (2010) discuss the variety of technologies that there are available for production of power from coal. The most widely used technology is pulverised coal power plants using steam turbines. Over recent decades this technology has seen significant advancement, with subcritical power plants now achieving efficiencies of up to 39%. Development of supercritical and potentially ultra-supercritical power plants could lead to the efficiency rising above 42%. Steam turbines generally employ the Rankine cycle for power generation to produce high temperature and pressure steam which is then expanded in a series of turbines to drive electric generators. The efficiency of the system is determined by the difference between the temperature of the heat source and the temperature of the heat sink, i.e. the environment. The combustion of coal is capable of achieving very high temperature steam, however, the materials of construction in the boiler limit this (Miller, 2011).

The other type of cycle possible is the Brayton cycle which is employed in gas turbines. Here compressed air is burnt with the fuel in a combustor and the hot gasses produced are then expanded in a turbine to drive an electric generator. This, however, leads to a large amount of wasted heat as the exhaust discharge temperature is relatively high. The two cycles lend each other to being able to overcome the others disadvantages. The fuel can first be burnt in the gas turbine at high temperature and then the exhaust gasses used to produce steam for use in steam turbines. This is commonly referred to as combined cycle and is often employed with natural gas combined cycles (NGCC). The challenge with coal is that the gas turbine needs to be fed with a gaseous fuel. Coal can be converted to

gaseous fuels by gasification, with the syngas that is produced from this then fed to the combined cycle, which is the process used in an IGCC power plant (Miller, 2011).

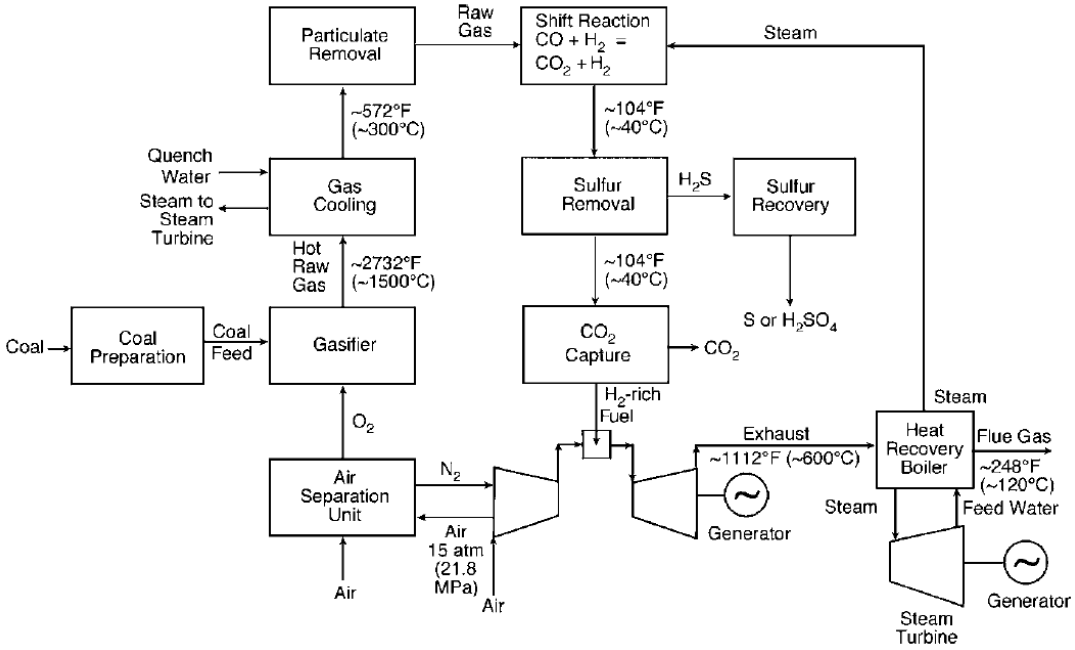

Figure 2.2: Coal fired IGCC power plant block diagram with carbon dioxide capture (Miller, 2011).

The block diagram of a coal fired IGCC power plant with carbon dioxide capture is given in Figure 2.2. A system without carbon dioxide capture would not necessarily include a shift reaction and would not include the carbon dioxide capture block. The gasification step, following coal preparation, partially combusts the coal with oxygen and water vapour for the production of hydrogen and carbon monoxide.

$$2C_{(S)} + O_{2(g)} \rightarrow 2CO_{(g)} \qquad \Delta H°_{rxn} = -221.31\ kJ\ gmole^{-1}$$

$$C_{(S)} + H_2O_{(g)} \rightarrow CO_{(g)} + H_{2(g)} \qquad \Delta H°_{rxn} = +131.46\ kJ\ gmole^{-1}$$

(Bell and Towler, 2010)

There are also many side reactions as well which lead to the formation of carbon dioxide, water and methane. The gas is then cooled either by quenching with water or using syngas coolers. Any particulates are removed to give a clean raw gas (Bell and Towler, 2010).

The next step for an IGCC plant without carbon capture is the removal of sulphur compounds. This is done by acid gas treatment and is achieved by absorption on either a chemical or physical sorbent. Popular processes are Selexol and Rectisol. With the sulphur compounds removed, they are then processed through the Claus process to produce elemental sulphur. Following the sulphur recovery, the cleaned syngas is burnt in the gas turbine with compressed air and then expanded. The exhaust then passes through a heat recovery boiler to generate steam. Some of the steam produced is recycled into the process and the remaining is used to generate power. The flue gas is then vented to atmosphere (Miller, 2011).

IGCC power stations offer significant advantages over the traditional pulverised coal counterparts. The efficiency is in the area of 40-50% with up to 56% achievable with optimization and technology advancements. There is a significant environmental impact with reduced sulphur and NOx emissions, as well as particulates, carbon monoxide, unburned carbon and VOCs. There is also up to 33% less water usage, less CO_2 per unit of electricity produced and reduced ash. However, these advantages come at a 10-20% increase in capital costs as well as the expense of EPC costs of relatively new technology. The availability in early plants has also been shown to be less than desirable. (Bell and Towler, 2010; Miller, 2011).

In order for carbon dioxide capture to take place, two additional steps are required, the water gas shift (WGS) reactor and the capture unit itself, discussed in Section 2.4. After gasification and particle removal the main composition of the syngas is hydrogen and carbon monoxide. The carbon monoxide can be reacted with steam to form carbon dioxide and hydrogen.

$$CO(g) + H_2O(g) \leftrightarrow \quad CO_2(g) + H_2(g) \qquad \Delta H°_{rxn} = -41.21\ kJ\ gmole^{-1}$$

(Bell and Towler, 2010)

For systems aiming to remove carbon dioxide, this ensures the carbon in the system can be captured as carbon dioxide before the gas turbine. Even for systems without carbon capture, the water gas shift reaction leads to a greater concentration of hydrogen and so is often used with gasification when hydrogen is being produced as a product (Bell and Towler, 2010).

2.4 Pre-Combustion Capture Technologies

One of the other key advantages of an IGCC power station is that it is possible to remove carbon dioxide from a stream with a high concentration of carbon dioxide at elevated pressure. This gives an increased driving force for separation making a wide range of capture methods feasible. Compared to a post-combustion system where the carbon dioxide is dilute, the size of the system can also be significantly smaller (Figueroa et al., 2008).

2.4.1 State of the art Technology

Absorption using a liquid solvent is the state of the art technology for both pre- and post-combustion capture systems. The advantage that pre-combustion capture

systems has is in the type of solvent used. Post-combustion carbon dioxide capture is at, or close to, atmospheric pressure and therefore chemical solvents which react with the carbon dioxide are required. However, this requires a large amount of energy to desorb the carbon dioxide. In contrast, pre-combustion systems can use physical solvents which are only weakly bonded to the carbon dioxide with a low heat of absorption, therefore having lower regeneration costs.

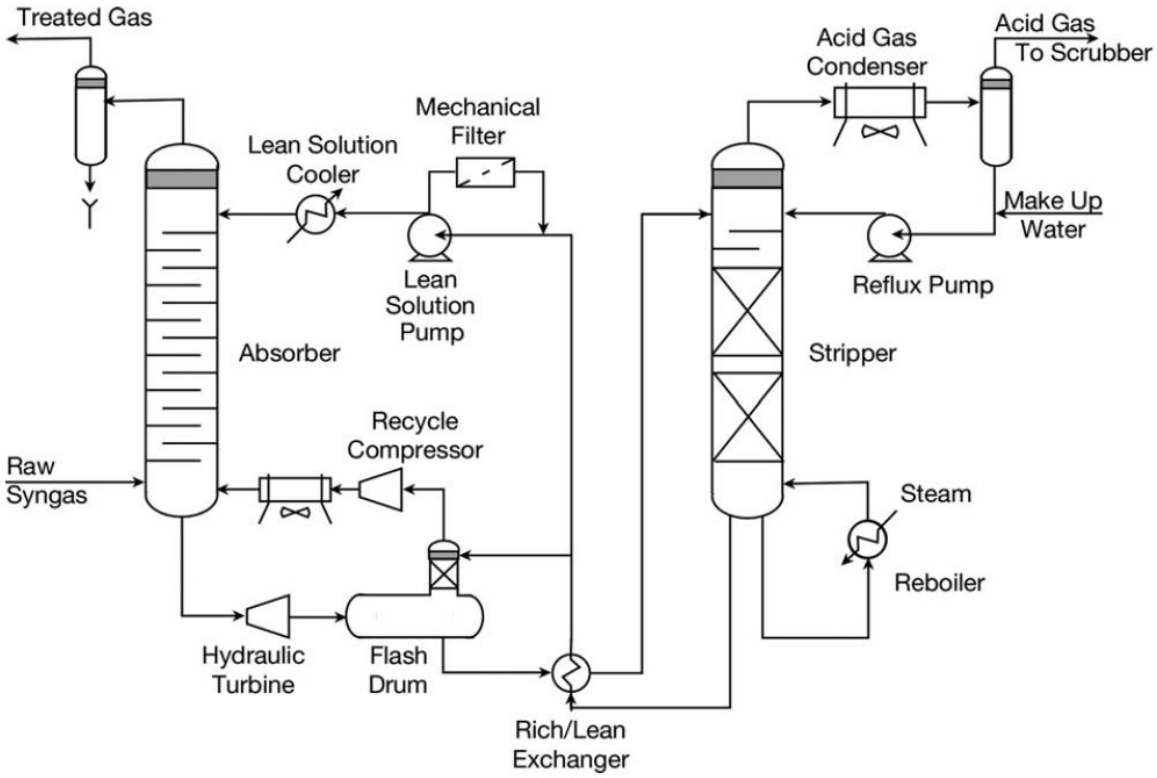

Figure 2.3: Selexol process for the removal of acid gas. (Miller, 2011)

Absorption processes are based around two columns, with the process using Selexol as the absorbent shown in Figure 2.3. In an absorber column, lean solvent flows counter-currently against the sour syngas to produce sweet syngas and a rich solvent loaded with carbon dioxide. A stripper column is then required to remove the

carbon dioxide from the rich solvent by reducing the pressure and/or increasing the temperature of the solvent stream. The two most expensive parts of the process are the stripper column reboiler and the lean solution pump. The Selexol process is considered the most suitable as the dimethyl ethers of polyethylene glycol (DMPEG) can operate at around ambient temperatures. The Rectisol process is only considered where very high purities are required as the methanol absorbent used has an operating temperature below -30°C (Miller, 2011). There are also several chemical solvent processes such as liquid amines which are commercially available (Bell and Towler, 2010). All of the large scale investment projects and large scale test facilities use absorption processes. The Kemper County is an IGCC facility to be completed by the end of 2014 which uses Selexol to remove carbon dioxide. The five largest pilot plant facilities are all either based on Selexol or Amines (Global CCS Institute, 2013). Liquid absorption processes are still energy intensive, even for physical absorption used in pre-combustion capture (Figueroa et al., 2008). There are also issues with the materials of construction of such systems due to corrosion, especially for amine systems. The degradation of the solvent can also result in higher operating costs (Liu et al., 2009). Figueroa et al. (2008) suggested that new technology with higher performance and lower costs is required for the long term implementation of CCS.

2.4.2 Absorption Process Evaluation

There have been significant numbers of publications reporting simulation studies to evaluate the impact capture has on the efficiency of IGCC power plants using absorption processes (Chen and Rubin, 2009; Chiesa et al., 2005; Descamps et al., 2008; Krishnan et al., 2009; Kunze and Spliethoff, 2010; Nord et al., 2009; Ordorica-

Garcia et al., 2006; Romano et al., 2010). The range of net efficiencies predicted is large, with a net efficiency of 50.7% estimated by Romano et al. (2010) and a net efficiency of 30.3% estimated by Krishnan et al. (2009). This is not entirely due to the effectiveness of the capture unit as the efficiency loss caused by the capture unit also varies and not in respect to the overall net efficiency of the power plant. Chen and Rubin (2009) based some of their predictions on advanced technology and estimate efficiency losses as low as 4.3%. Kunze and Spliethoff (2010) on the other hand predicted an efficiency of loss of 10 to 12% and stated that other studies are too optimistic on the impact of capture units. This highlights two aspects of capture process. There is a requirement to increase the efficiency of the capture unit to minimise the efficiency loss. Also, the simulations which evaluate these systems need to be accurate and reliable to give confidence in the predictions of the effect of the capture unit.

2.4.3 Developing Technologies

Figueroa et al. (2008) and Liu et al. (2009) both discussed several other possible separation techniques for separating carbon dioxide in an IGCC power station which are in the developmental stage. Thomas and Benson (2005) discussed in detail several techniques, as well as capture technologies for post-combustion and oxy-fuel systems. Membrane separation is promising as an energy efficient process for capturing carbon dioxide. Shekhawat et al. (2003) published a review for the U.S. Department of Energy. Many types of inorganic membranes, such as alumina, and polymeric membranes are compared, and the study suggested that the future of membranes lies in hybrid organic materials.

There are alternative process technologies which do not require distinct separation units but are instead coupled with other aspects of the IGCC power plants. Sorption enhanced water gas shift (SEWGS) incorporates an adsorbent in the WGS reactor. The adsorbent captures the carbon dioxide as it is produced and the system is operated in multiple beds so the adsorbent can be regenerated. This system has the added benefit of shifting the equilibrium position in the WGS reactor to convert more carbon monoxide (Thomas and Benson, 2005; van Selow et al., 2008). Chemical looping is a technology that is more akin to oxyfuel. The oxygen for combustion is provided by an oxidised metal based compound which is then regenerated in a separate reaction utilising a loop (Thomas and Benson, 2005). For IGCC systems the metal oxide can be used in the gasifier and then further circulated into the WGS reactor to absorb the produced carbon dioxide, providing similar benefits to the SEWGS system but also does not require the expensive air separation unit used in IGCC power plants (Figueroa et al., 2008). Of these technologies, membrane separation is the most advanced. However, Krishnan et al. (2009) produced a simulation to study the effect of membranes on an IGCC power plant compared to a Selexol process and found the efficiency loss was greater for the membranes. All of these technologies are in their infancy and have not been applied at industrial scales. Additional research is needed to transform promising technologies into industrial processes.

Another alternative technology is solid adsorption processes. Unlike other alternative technologies, adsorption systems have been applied to many industrial applications for a considerable time, including hydrogen separation (Yang, 1987). This study will focus on adsorption as a pre-combustion capture method in an IGCC plant. The

biggest hindrance to CCS is economics not technological barriers. The critical challenges lie in finding a technology feasible at an industrial scale, operating at low cost. This will require as simple a system as possible (Liu et al., 2009). Adsorption fits this profile as a highly selective, simple operation, with low regeneration penalty, low corrosiveness of adsorbents compared with absorbent solutions and low overall cost solution (Bell and Towler, 2010).

2.5 Adsorbent Materials

Adsorption processes are based on the ability of a material to preferentially adsorb one gas over one or more other gases. This is done by packing beds with adsorbent materials which have been shown to be selective to one gas in a mixture and then passing the gas mixture over this fixed bed. A material cannot indefinitely adsorb a gas and will become saturated when the adsorption capacity is reached. The regeneration of the bed then allows the adsorbed component to be captured. The desorption process is performed by either changing the pressure of the fixed bed in PSA or the temperature of the fixed bed in temperature swing adsorption (TSA). The adsorption capacity of a material changes with pressure and temperature and so a switch of the pressure or temperature to a level where the adsorbent capacity is lower will cause a release of the adsorbed gas to the point where the material is at equilibrium. PSA processes are discussed in detail in Section 2.8. The main materials for adsorption are activated carbon, zeolites, carbon molecular sieves (CMS) and metal organic frameworks (MOFs) (Ruthven, 1984). The focus of this study is activated carbon as these materials have been shown to be applicable to pre-combustion separation.

2.5.1 Activated Carbons

The adsorption process is seen to be promising for CCS as it has high capacity for carbon dioxide with good selectivity over other components of the gas stream. The adsorbents themselves are known to have good mechanical properties and be stable over repeated cycles (Martin et al., 2010). The efficiency of PSA processes is dictated by the adsorbent material used and by the PSA process employed (Grande, 2012). Adsorption has grown rapidly since the 1980s as a process for gas separation (Bottani and Tascon, 2008). This growth has been mainly associated with the development of adsorbent materials with pore structures that are highly microporous and the ability to design a variety of processes (Sircar et al., 1996).

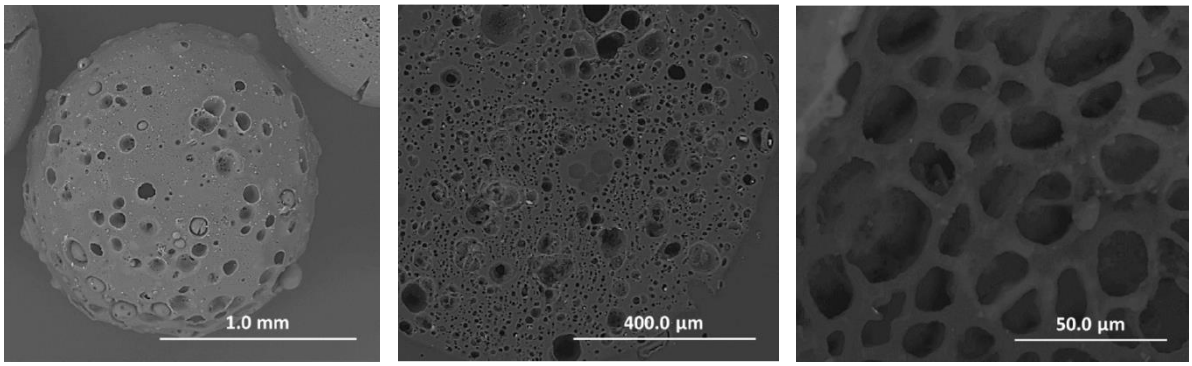

Figure 2.4: SEM for activated carbon beads produced by (Sun et al., 2013) with a magnification of 0.1, 0.4 and 0.05 mm.

Activated Carbons are the mostly widely used adsorbents. They are often defined as carbonaceous materials with an appreciable specific pore surface area (Rouquerol et al., 1999). The exact nature can vary widely but generally microporous activated carbons are disordered structures featuring a twisted network of defective carbon, as shown by the SEM images in Figure 2.4 produced by Sun et al. (2013). The carbon used can be from a range of sources such as coals, peat, woods, nut shells and

synthetic organic polymers (Marsh and Rodriguez-Reinoso, 2006). The carbons are activated by pyrolytic decomposition leading to the formation of graphite lamellae giving rise to free space (Rouquerol et al., 1999). The number of sources coupled with the activation methods allows a large variety of possible adsorbents. This means that materials with a wide range of pore volumes, pore structures, pore size distribution, density, ash content, hardness and surface chemistry can be produced (Sircar et al., 1996).

The analysis of adsorbent materials is based on adsorption capacity, selectivity for carbon dioxide over other gases in the gas stream, adsorption/desorption kinetics, mechanical strength, tolerance to impurities, regeneration of sorbents and sorbent costs (Samanta et al., 2011). Activated carbons are low cost and show many of the properties just described. Physically they have a high pore surface area, are amenable to modification and, unlike several other adsorbents, are easily regenerated (Wang et al., 2011). Sircar et al. (1996) evaluated the application of activated carbons for gas separation for many industrial processes. The variety of different activation methods mean that the application can range considerably. Separation of CO_2/CH_4 mixtures from biogas, removal of carbon dioxide from flue gas and H_2/CO_2 separation from steam-methane reformers are all possible applications of activated carbon adsorbents.

There has been significant work looking at the application of activated carbons to post-combustion carbon dioxide capture. Reviews by Samanta et al. (2011), Wang et al. (2011) and Chen et al. (2013), as well as an evaluation of solid sorbents for retrofit technologies by Sjostrom and Krutka (2010), compared activated carbons to other possible adsorbents such as zeolites, MOFs and amine modified materials.

The low cost nature of activated carbons does not overcome their relatively low adsorption capacity at low pressure. More promising materials have amine groups added to the surface to allow chemical adsorption of the carbon dioxide compared to the physical adsorption which takes place on activated carbon. Siriwardane et al. (2001) investigated activated carbon and zeolite capacities for carbon dioxide, nitrogen and hydrogen up to 20 bar. Their work found that at pressures above about 2 bar the activated carbon capacity for carbon dioxide continued to rise considerably up to 20 bar whereas the zeolites, which had higher capacities at low pressure, did not increase significantly at elevated pressures. This suggests that activated carbon is more suited for separations at high pressures, such as those used in pre-combustion captures

It is thought that at low pressure adsorption is only effective in micropores less than 5 times the molecular size of the adsorbate (Martin-Martinez et al., 1994), meaning that for carbon dioxide (molecular size of 0.2 nm) the pores need to be smaller than 1 nm. However, at higher pressure, carbon dioxide is also adsorbed in the supermicroporosity range of 0.7 to 2 nm, allowing the whole micropore structure to be used (Martin et al., 2011). Studies have been completed by a group at the University of Nottingham to find the most effective activated carbon for pre-combustion capture. Drage et al. (2009b) reported on the characterisation of set of adsorbents based on phenolic resins where the adsorbed amount was proportional to the BET pore surface area. In a separate study Drage et al. (2009a) evaluated several types of activated carbons derived from phenolic resins, polyacrylnitrole (PAN) derived resin and commercially developed activated carbons. They found that an activated PAN derived material had significantly improved adsorption capacity due

to an increased pore surface area. However, evaluation of the material for the adsorption capacity on a volumetric basis found that the PAN material was not the best performing and phenolic resins had higher capacities. The work went on to point out that adsorption capacities on a mass basis are proportional to pore surface area and micropore volume but this is not the case on a volumetric basis. Sun et al. (2013) developed the work on the phenolic resins, testing a novel process for forming the phenolic resin and different activation methods. They found strong correlations between the adsorption capacity on a mass basis and the micropore surface area, the micropore volume and the average pore width. The adsorption capacity was not investigated on a volumetric basis. Separate work by Martin et al. (2010) found the adsorption capacity on mass basis is strongly related to a combination of the micropore volume and the characteristic energy. From the literature studies, phenolic resins based on activated carbons have been shown to be the most suitable for pre-combustion capture.

2.6 Adsorbent Capture Capacity

2.6.1 Equilibrium Isotherms

The development of suitable materials is important in increasing the capture capacity of the system. The capacity of a material for a given gas is found using equilibrium adsorption isotherms. These are produced by measuring the adsorption capacity of the material for a pure gas at a set temperature and pressure for a system which has reached equilibrium. This is then repeated at incremental pressure steps to give a plot of the adsorption capacity against the adsorption pressure at a constant temperature. For systems at high pressure, high pressure volumetric analysis is normally used to measure these isotherms. High pressure measurements for carbon

dioxide adsorption on activated carbons have been focused on natural gas purification until recently. There have been several studies looking at the adsorption isotherm for carbon dioxide, methane, nitrogen and/or hydrogen (Dreisbach et al., 1999; Himeno et al., 2005; Park et al., 1998; Ritter et al., 2011; Rother and Fieback, 2013). More recently there have been studies focusing on pre-combustion capture and producing high pressure isotherms using carbon dioxide, hydrogen and/or nitrogen (García et al., 2013; Lopes et al., 2009; Martín et al., 2012; Schell et al., 2012b; Shen et al., 2010).

The pure component isotherms are useful in showing maximum capacities of materials and for indicating selectivity towards one component over another based on the maximum capacity of each component. However, adsorption systems separate gases from mixtures and therefore the uptake of different gases from a mixture upon the materials is important. Multicomponent isotherms are harder to measure as the composition of the adsorbed gas needs to be found as well as the mass or volume change during the adsorption. Dreisbach et al. (1999) produced isotherms for binary and ternary mixtures for high pressure mixtures involving methane and measured the composition of the adsorbed gas using a gas chromatograph. Rother and Fieback (2013) investigated quarternary gas mixtures of $CH_4/CO_2/N_2/H_2$. Binary mixtures of CO_2/H_2 and CO_2/N_2 were investigated by Schell et al. (2012b) for activated carbon and by Schell et al. (2012a) for MOFs and silicates. In all cases activated carbon was shown to have a high selectivity for carbon dioxide over nitrogen and an even higher selectivity over hydrogen. These works also investigated the suitability of isotherm models for predicting the adsorption capacity which is discussed in Section 2.7.2.

2.6.2 Breakthrough Curves

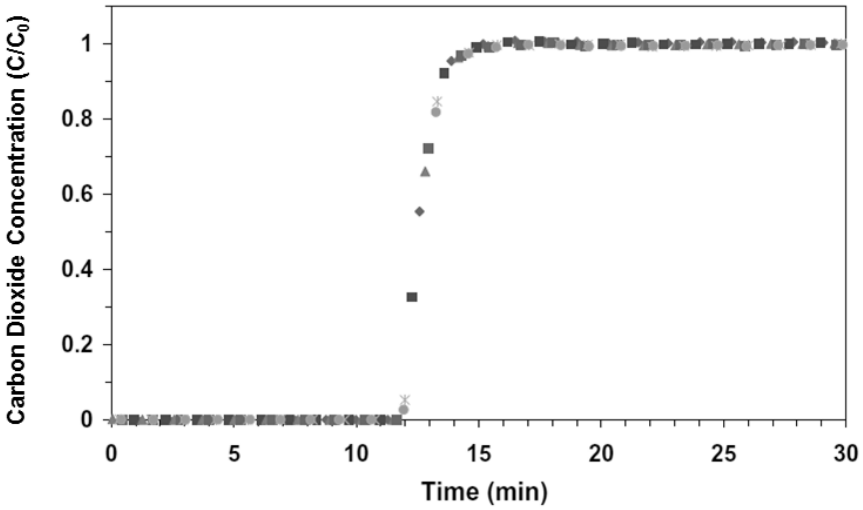

Figure 2.5: Carbon dioxide breakthrough curve for the separation of $CO_2/H_2/N_2$ with 40% CO_2 using activated carbon at 318K and 15 bar produced by Martín et al. (2012)

Isotherms are useful for finding the maximum adsorption capacity and, with the development of multicomponent isotherms, can now indicate the selectivity of materials for carbon dioxide. However, in these systems adsorption takes place until the material reaches equilibrium. PSA processes that are typically used for adsorption processes do not run until the material reaches equilibrium. The first step of a PSA process is the adsorption step at elevated pressure, where the gases being separated are passed over a fixed bed. Breakthrough experiments, such as the results produced by Martín et al. (2012) in Figure 2.5, can be used to replicate the conditions used in the adsorption step but are so far limited when applied to high pressure systems. Breakthrough experiments at low pressures can be used to indicate the kinetics of the system, with diluted breakthrough curves allowing the mass transfer of one material to be found and then, coupled with the adsorption isotherm, used to characterise the adsorbent material (Delgado et al., 2006; Lopes et

al., 2009; Shen et al., 2010). Several studies used high pressure breakthrough experiments to validate adsorption models, discussed in Section 2.7.4, but did not investigate the causes of the shape of the breakthrough curve (Casas et al., 2013a; Casas et al., 2012; Grande et al., 2013; Park et al., 1998).

Martín et al. (2012) investigated fixed bed separations of high pressure mixtures of $CO_2/H_2/N_2$ using activated carbon. Pure component isotherms were also measured. The capacity of the adsorbent for carbon dioxide from the fixed bed experiment was found with a total pressure of 15 bar at 298 K to be 6.5 mol kg^{-1} compared to 8.5 mol kg^{-1} found for the isotherm at a pressure of 15 bar and 298 K. This result was suggested by the authors to indicate the suitability of the material but they did not comment on the difference between the equilibrium and the saturation capacity from the breakthrough experiment. The adsorbent capacity for carbon dioxide was also provided on a volumetric basis which gives a better indication of the size of adsorption column that would be required for a PSA unit. From the same group, García et al. (2013) also investigated fixed bed separation of $CO_2/H_2/N_2$ mixtures at high pressure using activated carbon. Although the saturation capacities were not compared to pure component isotherm predictions, they were instead compared to the predicted multicomponent capacity based on the pure component isotherm. This is more accurate as the adsorption capacity is based on the component partial pressure not the overall pressure. In that work, García et al. (2013) found that the isotherm model was very important in predicting the breakthrough capacity but found for all models the predicted equilibrium capacity was higher than the saturation capacity from the breakthrough experiment. This points out the importance of the

isotherm model used, discussed further in Section 2.7.2, and that isotherm models predict higher capacities than are recorded in adsorbent beds.

There is more scope to study activated carbons under industrial adsorption conditions using breakthrough experiments, as few studies actually consider the adsorption capacity under these conditions. There is also a need to validate equilibrium results against breakthrough results to fully establish if equilibrium isotherms provide enough data to properly compare adsorbent materials. The studies in literature rarely consider the breakthrough capacities on a volumetric basis which is important when considering the size of an adsorption column.

2.7 Adsorption Modelling

2.7.1 Mass and Energy Balance Equations

The modelling of fixed beds for adsorption processes has become very important in process development and design. Fixed bed adsorbers can be modelled with a high degree of accuracy using the dispersion model which allows for a small deviation from plug flow (Levenspiel, 1999). The equations which govern an adsorption bed must include an adsorption isotherm model, a mass and energy balance for the gas phase and a mass and energy balance inside each particle (Yang, 1987). The adsorption isotherm models are equations which predict the adsorption capacity of the material based on the isotherm discussed in Section 2.6.1and are detailed in Section 2.7.2. The mass balance of gas phase is based on the axial dispersed plug flow model, which uses an additional term to the plug flow model to take into account dispersion.

Table 2.1: Adsorption models for high pressure separations. LF – Langmuir--Freundlich, IAST – Ideal adsorbed solution theory, MSL – multi-site Langmuir, LDF – linear driving force, AC – activated carbon, Z5A – zeolite 5A, PSA – pressure swing adsorption, LPSA – layered pressure swing adsorption.

	Application	Isotherm model	Mass Transfer Model	Heat Transfer Equation	Material	Gas Separation	Adsorption Process
Cen et al. (1985)	Hydrogen Purification	LF	LDF	Non-isothermal without wall effects	AC	$H_2/CH_4/H_2S$	PSA
Cen and Yang (1986)	Hydrogen Purification	LF	LDF	Non-isothermal without wall effects	AC	H_2/CO	PSA
Doong and Yang (1986)	Hydrogen Purification	LF and IAST	Pore/Surface Diffusion	Non-isothermal with wall effects	AC	$H_2/CH_4/CO_2$	PSA
Park et al. (1998)	Hydrogen Purification	Langmuir and LF	LDF	Non-isothermal with wall effects	AC	$H_2/CH_4/CO_2/CO$	Breakthrough
Lopes et al. (2009)	Hydrogen Purification	Virial	Bi-LDF	Non-isothermal with wall effects	AC	$H_2/CH_4/CO_2/CO$	Diluted Breakthrough
Lopes et al. (2011)	Hydrogen Purification	Virial	Bi-LDF	Non-isothermal with wall effects	AC	H_2/CO_2, $H_2/CO_2/CO$, $H_2/CH_4/CO_2/CO/N_2$	Breakthrough and PSA
Park et al. (2000)	Hydrogen Purification	Langmuir and IAST	LDF	Non-isothermal with wall effects	Z5A, AC	$H_2/CH_4/CO_2/CO$	LPSA
Ahn et al. (1999)	Hydrogen Purification	LF	LDF	Non-isothermal with wall effects	Z5A, AC	$H_2/CH_4/CO_2/CO/N_2$	LPSA
Ribeiro et al. (2008)	Hydrogen Purification	MSL	Bi-LDF	Non-isothermal for gas, solid and column wall	Zeolite, AC	$H_2/CH_4/CO_2/CO/N_2$	LPSA
Grande et al. (2013)	Methane Production	LF, MSL and Virial	Bi-LDF	Non-isothermal with wall effects	AC	CH_4/CO_2	Breakthrough
Schell et al. (2009)	Pre-combustion capture	Langmuir	LDF	Non-isothermal with wall effects	AC	$CO_2/H_2/CH_4/CO$	PSA
Casas et al. (2012)	Pre-combustion capture	LF	LDF	Non-isothermal with wall effects	AC	CO_2/H_2	Breakthrough
Casas et al. (2013b)	Pre-combustion capture	LF	LDF	Non-isothermal without wall effects	AC	CO_2/N_2	PSA
Xiao et al. (2009)	Pre-combustion capture	DSL	Pore/Surface Diffusion	Non-isothermal with wall effects	Hydrotalcite	$CO_2/H_2/N_2/H_2O$	PSA
Agarwal et al. (2010)	Pre-combustion capture	DSL	LDF	Non-isothermal without wall effects	AC	CO_2/H_2	PSA

$$\frac{\partial C}{\partial t} = -\frac{\partial (Cv)}{\partial z} + D_{ax}\frac{\partial^2 C}{\partial z^2} - \frac{(1-\varepsilon)}{\varepsilon}\frac{\partial q}{\partial t} \qquad 2.1$$

(Ruthven, 1984)

The axial dispersion (D_{ax}) term takes into account all mechanisms which lead to axial spreading (Ruthven, 1984). The energy balance for the gas phase depends on the exact nature of the system being modelled and can be as simple as assuming the system is isothermal (Kikkinides et al., 1993). Typically an energy balance is used and these are either non-isothermal without wall effects, non-isothermal with wall effects or adiabatic, the equations for each are reported in Section 4.6.2, and include an axial thermal conductivity term (Ruthven, 1984).

A mass balance for the pellet itself can be done for individual particles which incorporates pore and/or surface diffusion. However, this adds an unnecessary layer of complexity to the system. Liaw et al. (1979) showed that a rigorous solution is not required as long as the bed is long enough to establish and retain the typical S-shaped breakthrough curve. This means that instead a simple relationship can be provided between the gas phase and adsorbed phase. Although equilibrium relationships, where the solid concentration (q_i) is assumed to be in equilibrium with the gas phase, have been shown to be sufficient in some cases (Delgado et al., 2011; Kikkinides et al., 1993), a linear driving force approximation is widely used, reported in Equation 2.2. This simple approximation is sufficiently accurate as the constant in the system can be extended to incorporate more than one mass transfer resistance to ensure that the rate limiting step is included (Ruthven, 1984). The bi-linear driving force equations have also been used which express the macro and micro mass transfer in two steps, using similar equations to that shown in Equation

2.2 (Lopes et al., 2011). The pellet energy balance is often neglected by assuming the pellets are at thermal equilibrium with the gas phase (Shafeeyan et al., 2014).

$$\frac{\partial q_i}{\partial t} = k_i(q_i^* - q_i) \qquad 2.2$$

There are many studies which model adsorption columns using the axial dispersed plug flow model and Shafeeyan et al. (2014) reviewed these studies. That review details the different assumptions made and the equations that result from them. A summary of a selection of studies which use the axial dispersed plug flow model at high pressure is given in Table 2.2. The models looked at are for hydrogen purification, methane production and pre-combustion capture and mainly use activated carbon. Some of the hydrogen purification studies investigated layered pressure swing adsorption (LPSA) where two adsorbents, typically zeolite and activated carbon, are used in separate layers of the bed to maximise the use of the adsorbent (Park et al., 2000). Early studies on high pressure adsorption focused on hydrogen production and aimed to simplify equations by using the LDF model and not including wall effects whilst still producing accurate models (Cen et al., 1985; Cen and Yang, 1986). Doong and Yang (1986) found that equilibrium models were not sufficiently accurate and instead required the inclusion of surface and pore diffusion effects. Subsequent work has typically used the LDF model (Agarwal et al., 2010; Ahn et al., 1999; Casas et al., 2013b; Casas et al., 2012; Park et al., 2000; Park et al., 1998; Schell et al., 2009). The majority of systems include wall effects in the gas phase energy balance. Ribeiro et al. (2008) included a solid phase energy balance in order to evaluate the assumption that the gas and solid phase were in thermal equilibrium and found the added complexity did not significantly improve the

accuracy the model. Agarwal et al. (2010) and Casas et al. (2013b) do not include the wall effects in the energy balance in order to reduce the computational load.

Studies tend to apply the axial dispersed plug flow model to specific situations and report these results. Nikolic et al. (2008) instead built a generic modelling framework. The report detailed the different inputs depending on the complexity required by the user, e.g. mass transfer described by equilibrium model, LDF, surface diffusion or pore diffusion. That study clearly presented the effect that assumptions, such as the mass transfer or heat transfer model, have on the simulation equations although no attempt was made to suggest which assumptions are the most suitable.

2.7.2 Isotherm Models

Isotherm models are used to describe the capacity of a material for a gas based on measurements such as those described in Section 2.6.1. Books by Ruthven (1984), Yang (1987) and Do (1998) detail the different types of isotherm models used as well as the reasons specific models are preferred for different materials. High pressure systems have been studied for methane purification and more recently carbon dioxide capture for pre-combustion systems.

Table 2.2 summarises several literature works which have compared different isotherm models or studied the carbon dioxide isotherm at high pressure. The Langmuir isotherm, shown in Equation 2.3, is a simple model which has been applied to many situations as it is easy to calculate the fitting parameters and is thermodynamically rigorous (Ruthven, 1984). However, it has been increasingly shown to not accurately represent high pressure systems, often under predicting the adsorption capacity at high pressures (García et al., 2013; Schell et al., 2012b). In

place of this, several other models have shown to match the entire adsorption range, such as the Langmuir-Freundlich (LF), shown in Equation 2.4, model and the dual-site Langmuir (DSL) Model, which is similar in form to Equation 2.3, as well as the multisite Langmuir, Toth, Virial and Dubinin-Radushkevich models.

$$q_i^* = \frac{q_{s,i} B_i P_i}{(1 + B_i P_i)} \qquad 2.3$$

$$q_i^* = \frac{q_{s,i} B_i (P_i)^{n_i}}{(1 + B_i (P_i)^{n_i})} \qquad 2.4$$

Table 2.2: Literature comparison of high pressure adsorption isotherms using pure gases for carbon dioxide adsorption on activated carbon. DSL – Dual Site Langmuir, LF – Langmuir Freundlich, MSL – Multisite Langmuir, IAST – Ideal Adsorbed Solution Theory, DR – Dubinin-Radushkevich

	Gas Components	Isotherm Models	Maximum Pressure (MPa)
Dreisbach et al. (1999)	CO_2, N_2, CH_4	DSL	6
García et al. (2013)	CO_2, N_2, H_2	Langmuir, LF and DSL	3
Grande et al. (2013)	CO_2, CH_4	LF, MSL, Virial	5
Himeno et al. (2005)	CO_2, CH_4	Toth	4
Martin et al. (2010)	CO_2	DR	2
Martín et al. (2012)	CO_2, N_2, H_2	Toth	3
Park et al. (1998)	CO_2, H_2, CH_4, CO	LF and Langmuir	1
Rother and Fieback (2013)	CO_2, N_2, H_2, CH_4	Langmuir, IAST	2
Schell et al. (2012b)	CO_2, N_2, H_2	Langmuir, LF and IAST	8
Shen et al. (2010)	CO_2, N_2	Viral, MSL	4

It is important to be able to predict capacities for individual components from gas mixtures in order to model adsorption beds. Producing multi-component isotherms is difficult, as discussed in Section 2.6.1, and therefore systems use multi-component isotherm models based on pure component data. This was first formulated by extending the Langmuir isotherm to mixtures, as shown in Equation 2.5.

$$q_i^* = \frac{q_{s,i} B_i P y_i}{\left(1 + \sum_{j=1}^{i} B_j P y_j\right)} \qquad 2.5$$

(Yang, 1987)

This was then further extended to the LF equation (also known as the Sips model) as reported in Section 4.2.1. Schell et al. (2012b) applied the extended LF model to high pressure isotherms for CO_2/N_2 mixtures and CO_2/H_2 mixtures and found strong agreement for both gas mixtures. García et al. (2013) compared the extended LF model to saturation capacities from breakthrough experiments for $CO_2/H_2/N_2$ mixtures and found that the extended LF model over predicted the carbon dioxide uptake by up to 45% at high pressures and up to 75% at low pressures. Ritter et al. (2011) extended the DSL model to predict multicomponent adsorption equilibria, as reported in Section 4.2.1, by evaluating the way in which the parameters for each site could interact, as reported in Appendix A. García et al. (2013) applied this instead to predict saturation capacities from breakthrough curves for $CO_2/H_2/N_2$ mixtures to an accuracy of approximately 10%. Dreisbach et al. (1999) had previously applied the dual-site Langmuir isotherm to a multicomponent mixture but not with the simplicity of extending the isotherm as suggested by Ritter et al. (2011).

The other method of predicting multicomponent isotherms from pure component data is to use the Ideal Adsorbed Solution Theory (IAST), outlined in Section 4.2.2 and further detailed in Appendix B. The method was originally developed by Myers and Prausnitz (1965) and is based on the assumption that the adsorbed phase is thermodynamically ideal. Rother and Fieback (2013) applied it to a high degree of accuracy to quaternary isotherms from a $CH_4/CO_2/N_2/H_2$ mixture over zeolites and MOFs using the Langmuir model to predict the pure component data. Schell et al.

(2012b) applied the IAST model to binary isotherms of CO_2/N_2 and CO_2/H_2 mixtures using activated carbon. The pure component data was predicted using the LF model in the IAST model and, when compared to the extended LF model, it was found to give significantly closer fits for CO_2/N_2 mixtures, especially for the nitrogen adsorption, and a similar fit to the extended LF model for CO_2/H_2 mixtures.

Table 2.1 lists the isotherm models used by several adsorption systems for both breakthrough models and simulations of PSA units. The Langmuir model is rarely used for these systems due to the poor representation across the entire pressure range. The most popular model is the extended LF model due to the ease of implementation and the strong fit across the entire pressure range of high pressure isotherms. The extended DSL model has been used in recent years for simulations of pre-combustion capture systems, although there has not been a comparison between the accuracy of the model using the extended DSL and the extended LF isotherm. The IAST model has been applied sparingly to fixed bed modelling due to its implicit nature.

There have been few comparisons of adsorption isotherm capacity predictions to breakthrough capacities. Grande et al. (2013) compared the extended LF, Virial and multisite Langmuir isotherm models to breakthrough capacities for CO_2/CH_4 gas mixtures. They found that all models predicted low pressure carbon dioxide capacities accurately within 5% of the experimental value. At a pressure of 20 bar and a carbon dioxide feed mole fraction of 0.2 the multisite Langmuir and the Virial isotherms over predicted the carbon dioxide adsorption capacity by 9.9% and 9.6% respectively but the LF model under predicted the carbon dioxide capacity by 1.9%. The variation in accuracy was large, with the multisite isotherm over predicting the

carbon dioxide capacity by as much as 25%. The LF isotherm was within 10% for all systems tested.

More studies are needed to properly evaluate the suitability of isotherm models to predict the dynamic response of materials. Evidence of an isotherm model successfully predicting capacities from breakthrough experiments would more clearly indicate the suitability of that isotherm model.

2.7.3 Parameter Correlations

The majority of the parameters for the model, as described in Section 4.6, can be found through independent experiment or are well known properties of the material. However, there are several properties that are based on the interactions between the gas and the adsorbent bed and these need to be found by using correlations. The review by Shafeeyan et al. (2014) and the generic model produced by Nikolic et al. (2008) both listed a large number of these correlations. There are well established relationships for the gas diffusivity, the external film mass transfer coefficient, the Knudsen diffusion, the effective diffusivity the heat dispersion coefficient, and the external heat transfer coefficient which are regularly employed and used in this study, detailed in Section 4.7. The remaining coefficients are the component mass transfer coefficients, the dispersion coefficient and the internal heat transfer coefficient.

The mass transfer coefficient used in the LDF equation is used to represent all of the mass transfer resistances. Glueckauf and Coates (1947) originally suggested the LDF equation and the associated mass transfer coefficient was proportional to the effective diffusivity for a given particle size. However, applications of this in high pressure work is limited to Casas et al. (2013b) who use it as a first approximation for

parameter estimation and find the actual value can vary significantly from that estimated by Glueckauf and Coates (1947). Farooq and Ruthven (1990) suggested a correlation which incorporates the film, macropore and micropore resistances together, reported in Section 4.7.2. This has successfully been implemented by Dantas et al. (2011) and Delgado et al. (2006) for low pressure separation of CO_2/N_2 mixtures, although both perform sensitivity studies and found that order of magnitude variations in the mass transfer coefficient do not significantly alter the breakthrough curve.

The dispersion coefficient is a combination of molecular diffusion and turbulent mixing caused by the particles in a fixed bed. Ruthven (1984) detailed the derivation of a generic formula which combines these effects additively, see Section 4.7.1. The book goes on to describe the different studies that have developed empirical relationships for the proportionality constants of each effect. These correlations tended to have been developed for non-porous materials or non-adsorbing materials. However, Wakao and Funazkri (1978) found that for adsorption systems with fast kinetics and at low Reynolds number the dispersion effect was much greater. An expression, reported in Section 4.7.1, was suggested which limits the minimum value of the dispersion coefficient for a system with a given velocity and particle diameter and is widely used, particularly for low pressure separations (Shafeeyan et al., 2014). For systems with a moderate pressure (up to 11bar) the Wakao and Funazkri (1978) correlation has also been used with success (Ahn et al., 1999; Lopes et al., 2009; Lopes et al., 2011; Ribeiro et al., 2008). However, the general dispersion coefficient was applied with success by Casas et al. (2012), with adsorption pressure up to 25 bar, and Grande et al. (2013), with adsorption pressures up to 50 bar, but they did

not compare their results to simulations using the Wakao and Funazkri (1978) correlation. Farooq and Ruthven (1990) utilised the Hsu and Haynes (1981) correlation in the simulation of low pressure purification of ethylene with success as the conditions for which it was developed matched the experimental conditions that were employed.

The internal heat transfer coefficient tends to be used as a fitting coefficient (Casas et al., 2012; Cavenati et al., 2006; Delgado et al., 2006; Won et al., 2012) or as a fixed number (Agarwal et al., 2010; Grande et al., 2013; Ribeiro et al., 2008). However, several papers employed correlations to predict it. The Leva (1947) correlation has been used for high pressure separations (Lopes et al., 2009; Lopes et al., 2011; Schell et al., 2013). Park et al. (1998) used the Leva (1947) correlation in their initial study for the high pressure purification of hydrogen using LPSA. However, in subsequent work, Park et al. (2000) pointed out that the Leva (1947) correlation underestimates the heat transfer coefficient at low mass flux and instead suggested the use of the Yagi and Kunii (1960) correlation, which had been used previously by Ruthven et al. (1975) and subsequently by Choi et al. (2004).

The variation of parameter correlations used suggests that there is scope to investigate which is the most suitable for a given system. This therefore requires each adsorption system to test different parameter correlations or at least justify the use of a given correlation. A shift away from using parameter estimation will also ensure more rigorous models which can be better applied to scaling-up adsorption systems.

2.7.4 Breakthrough Modelling

Experimentally determined breakthrough curves are discussed in Section 2.6.2. The primary use of these experiments is to provide data for validation of adsorption models. This is widely used and there are many examples for low pressure carbon dioxide separations (Cavenati et al., 2006; Delgado et al., 2006; Gao et al., 2013; Lopes et al., 2009; Lopes et al., 2011; Shen et al., 2010; Won et al., 2012). Some of these models used parameters found from independent investigation but there is also a trend to use parameter estimation, typically with the heat transfer coefficient being the fitting parameter, to match the model to experimental data. Park et al. (1998) investigated layered beds for the separation of hydrogen from mixtures of $H_2/CO_2/CH_4/CO$ using activated carbon and zeolite 5X with pressures up to 26 bar. The adsorption model was compared to experimental breakthrough curves and reasonable agreement was found for all components. In order to match the curve, the mass transfer coefficient was used as a fitting parameter. The heat transfer coefficient was calculated using the Leva (1947) correlation, shown in Section 4.7.3. A comparison of the extended Langmuir isotherm and the extended LF isotherm found the extended Langmuir isotherm gave a better fit to the breakthrough curve despite a poorer fit to the adsorption isotherm.

Grande et al. (2013) simulated breakthrough curves for the separation of CH_4/CO_2 mixtures using activated carbon at pressures up to 50 bar and compared the simulation to experimental results. The thermal and mass transfer parameters were fixed, although the heat transfer coefficient was increased for simulations at higher pressures to account for density variations. Simulations at 5 bar showed strong agreement with experimental results for all isotherm models. At 25 bar, however, the

carbon dioxide breakthrough curve was over predicted. The different isotherm models did not significantly alter the breakthrough time but the extended LF model did produce sharper breakthrough curves. At 50 bar the simulations still over predicted the breakthrough time for carbon dioxide and were less accurate at predicting the methane breakthrough. At these pressures though the isotherm models had different breakthrough times with the breakthrough times in the order: LF isotherm breakthrough time < multisite Langmuir model < Virial model.

Casas et al. (2012) reported excellent agreement between simulations and experimental data for the separation of CO_2/H_2 mixtures using activated carbon at pressures up to 35 bar. The model used the extended LF isotherm. Parameter estimation was used to fit the heat transfer coefficients, with first approximations from the Leva (1947) correlation and heat transfer by natural convection, and the mass transfer coefficients, with first approximations from the Glueckauf and Coates (1947) expression. The parameter estimation shifted each parameter slightly with the hydrogen mass transfer coefficient showing the biggest change from the initial guess from the correlation of 0.33 s^{-1} to the parameter estimated value of 1.0 s^{-1}. Excellent prediction of both the hydrogen and carbon dioxide breakthrough curves was observed for adsorption pressures of 5, 15, 25 and 35 bar at 25°C and 45°C. The temperature of the bed was monitored at five points along the bed and these profiles were also modelled with a reasonable degree of accuracy, although the simulations tended to under predict the peak temperature. The versatility of the model was shown in subsequent work where Casas et al. (2013a) successfully simulated breakthrough curves for the same separation using MOFs.

The modelling of breakthrough systems ensure that a model is validated before it is applied to PSA systems. There is still not full agreement on the most suitable correlations and isotherm models for pre-combustion capture systems. A larger body of work in this area is needed to provide more evidence of the accuracy of the axial dispersed plug flow model and the correlations used.

The validated breakthrough models tend to be used for the development of PSA processes. However, there is another use in investigating the system parameters to make design recommendations to maximise the bed efficiency. Gao et al. (2013) validated an adsorption model for low pressure separation of CO_2/N_2 mixtures using amine-modified MCM-41. In that study, the model was used to investigate the effects several of the system properties had on the breakthrough curve. The bed voidage and bed length altered the breakthrough time but not the shape of the breakthrough curve. A bed voidage decrease from 0.5 to 0.3 caused the breakthrough time to increase by 65% and a bed length increase from 0.05 m to 0.2 m caused the breakthrough time to increase by 131%. Increases in the gas velocity caused a greater degree of spreading whilst maintain a constant adsorption capacity. Changes to the dispersion coefficient and the mass transfer coefficient did not affect the breakthrough capacity but altered the shape of the curve. Higher dispersion coefficients and lower mass transfer coefficients resulted in a higher degree of spreading. This area of parameter sensitivity analysis has not been studied in pre-combustion capture adsorption models but further understanding would aid in the design of future adsorbents.

2.8 Pressure Swing Adsorption

Books by Ruthven (1984) and Yang (1987), as well as a review by Grande (2012), detail the steps used in PSA cycles and the advances made. PSA processes have been used widely in industry with both air separation and hydrogen purification considered mature technologies. Further applications include methane purification, carbon dioxide capture and noble gas purification (Grande, 2012).

2.8.1 Adsorption Steps

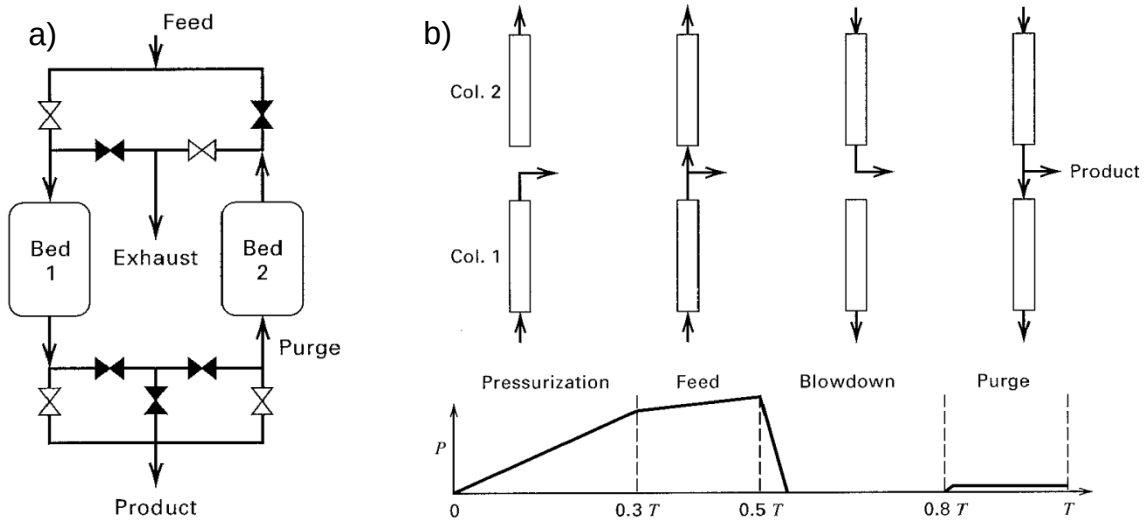

Figure 2.6: Basic 4 step 2 bed PSA cycle showing the a) 2 bed configuration and the b) operation of the bed. (Seader et al., 2010)

The initial adsorption process was the Skarstrom cycle employed for air separation, which utilised two beds operating in parallel. One bed would be depressurising and then adsorbing to produce oxygen and the other would have a blowdown step followed by a purge with oxygen. The two beds then switch operation to complete the cycle. This is summarised by the process shown in Figure 2.6. The pressurisation step is required to increase the pressure to the final adsorption

pressure so that the pressure can be dropped for the regeneration of the bed. The adsorption step is where the more adsorbed component (heavy product) to be removed and the less adsorbed component (light product) pass through the bed. The blowdown step is caused by a depressurisation of the bed leading to the adsorbed phase being driven off when released at lower pressures. Finally a purge step is used to clear the bed of residual heavy product. The traditional process uses a fraction of the light product to do this (Ruthven, 1984; Yang, 1987).

These four steps provide the basis of PSA systems but other steps have been added to improve the separation. Typically the light component is the required product and the purity of this gas is the most important. The purge step plays an important role of not only purging residual gas but, by having the purge flow counter-currently, in shifting any residual gas away from the outlet of the bed (Ruthven, 1984). For some processes, such as hydrogen purification from methane, the heavy product is also desired. The counter-current blowdown step would limit the purity of this product. A co-current depressurisation step was introduced to some processes as way of enhancing the purity of the heavy product by partially depressurising the bed in a co-current direction before the blowdown step. This then increased the concentration of methane in the gas phase. However, there is an issue of the use of the product from the co-current depressurisation step. A solution to this was found by the means of pressure equalisation. For this, a depressurising bed and a pressurising bed are interconnected so that the depressurising bed is used to partially pressurise a low pressure bed until the pressures of the two beds match. Co-current depressurisation and pressure equalisation are still limited in the maximum purity of the heavy product as the concentration of the heavy component will always be limited by the

concentration of the light component in the void space of the bed. An effective way to remove the light component from the void space is to rinse the bed with a pure stream of the heavy component at the adsorption pressure. However, this has the negative effect of requiring a compressor to provide a stream of pure heavy component at elevated pressure (Yang, 1987). The process steps applied to PSA system are limited to the six steps discussed: pressurisation, adsorption, blowdown (either co-currently or counter-currently), pressure equalisation, purge and heavy product rinse. However, the configuration of these steps can become intricate and the optimum solution is mainly found iteratively. Therefore models are required to evaluate the most efficient configuration for making the required products (Grande, 2012).

PSA systems are evaluated by calculating the purity and capture rate of the product gases. The purity of the gas is the total amount of the desired gas captured in the product streams divided by the total amount of gas in those streams for a cycle. The capture rate is defined as the amount of the desired gas captured in the product streams divided by the total amount of desired gas in the feed streams. Formulas for both are discussed in Section 4.12.2. The productivity is the amount of the desired gas captured divided by the amount of adsorbent used and the cycle time, and is also sometimes compared (Grande, 2012; Yang, 1987).

2.8.2 PSA Model Validation

Despite a large number of studies validating the axial dispersed plug flow model for breakthrough curves, as detailed in Section 2.7.4, there has been relatively little published on the validation of PSA cycles for separations involving carbon dioxide. Park et al. (2000) simulated a 9 step process for the production of hydrogen by the

separation of $H_2/CO_2/CH_4/CO$ mixture using a layered bed of activated carbon and zeolite 5A and experimentally studied the same system on a three bed rig. From this work they were able to compare the temperature profiles along the bed with that of the simulation and found reasonable agreement. They were also able to find the hydrogen purity and capture rate from the experiments and compare them to the simulations. Some experiments were modelled with a high degree of accuracy but others were different by as much as 5% for the recovery. Chou and Chen (2004) simulated a VPSA separation of CO_2/N_2 mixtures using zeolite 13X and compared the carbon dioxide capture rates and purities to experimental data. The agreement between the experimental and simulated data was poor, with the most accurate simulation only within 2.5% of the experimental data and the worst being 10% from the experimental data for both the capture rate and purity.

Cavenati et al. (2006) experimentally studied the separation of CO_2/N_2 mixtures using a layered bed of activated carbon and zeolite 13X in a 4 step PSA process. The outlet concentration of the bed was measured periodically using a gas chromatograph. This provided data for the comparison to a simulation of the same 4 step process. The simulation outlet concentrations matched the experimental data well, although the periodic nature of the gas chromatograph measurements meant that large changes of the gas concentration were predicted in between experimental data points. The temperature profile was also compared at three points along the bed and the simulation matched the experimental data within a few degrees at all of the points. A comparison was made between the experimental and simulation capture rate and purity. The capture rate was well simulated but higher levels of purity that were found for certain experimental set-ups were not predicted by the

simulation. A similar comparison was done in the same group by Lopes et al. (2011). The same separation was looked at but this time a 10 step process with three pressure equalisation steps was studied. The same issue of the gas chromatograph measuring too few experimental points, meant it was not possible distinguish the desorption peak that is predicted by the simulation. The points that were found were in good agreement with the simulation. The temperature profile was also simulated at three points in the column and there is agreement within a few degrees. It is important to bear in mind that despite operating three pressure equalisation steps, only one column was used and therefore the pressure equalisation up was approximated using the pressures found during the pressure equalisation down and a pure hydrogen stream.

Schell et al. (2013) has attempted to simulate each step in a PSA cycle in detail. A high pressure separation of CO_2/H_2 mixtures using activated carbon was studied experimentally for a 6 step PSA cycle employing one pressure equalisation step and the concentration profiles of both gases were measured using a mass spectrometer. A simulation was performed of the system behaviour and the desorption steps were compared with the experimental results. Simulations of the beds were not able to replicate the blowdown or purge steps, with the simulation predicting a faster response than observed by the experiment. It was suggested that a model of the surrounding pipework needed to be incorporated but this did not significantly alter the response of the simulation of the composition curve. Instead a stagnant tank was modelled in series with the adsorption bed to try to accommodate the effects of the dead space in the system. This allowed the purge step to be modelled to a higher degree of accuracy compared to the experiment, but the blowdown step was still

predicted to have a faster response than the experimental data. The hydrogen mole fraction during the adsorption step was also not well predicted by the simulation with very little variation in concentration predicted by the simulation despite large variations for the experimental data. The temperature profiles were simulated to a higher degree of accuracy, especially at higher pressures. The carbon dioxide and hydrogen purities and capture rate were simulated within the experimental errors of ± 5.4% for purities and ± 5.8% for capture rates.

There has been a long standing assumption that the accurate simulation of breakthrough curves fully validates models for simulating PSA systems. However, previous work has shown that the validation of each of the steps in a PSA system is difficult. It is therefore important to try to understand the simulation of each of the PSA steps in more detail by comparing simulation results of these steps to experimental data.

2.8.3 PSA Process Modelling

The implementation of PSA processes utilising the process steps described in Section 2.8.1 for post-combustion carbon dioxide capture, methane recovery and hydrogen purification are detailed in Table 2.3, Table 2.4 and Table 2.5 respectively. These systems are detailed as they either focus on the recovery of carbon dioxide or separations at high pressure. It is difficult to compare the individual studies directly as the variation in process conditions can be quite large, resulting in the range of capture rates and purities found for the same processes.

Post-combustion capture differs from the majority of PSA systems as the desired product, carbon dioxide, is the more strongly adsorbed component. The majority of

processes are operated under vacuum pressure swing adsorption (VPSA) as the pressure of flue gas is too low to provide a large enough pressure difference between the adsorption and the purge step. Ko et al. (2005) investigated a 4 step process that purged at atmospheric pressure and a 4 step process that purged under vacuum. The VPSA process was found to give significantly higher capture rates than the PSA process. Liu et al. (2011) showed the development of a VPSA cycle by running simulations of the system with and without rinse and pressure equalisation steps. The rinse step was seen to significantly improve the carbon dioxide purity by almost 20% and the pressure equalisation steps increased the carbon dioxide purity by approximately 8%. Chou and Chen (2004) reported the trade-off that various PSA steps require for the product purity and capture rate. The rinse step can be seen to be highly important for producing high purity carbon dioxide and this can be implemented relatively easily as the adsorption step occurs at atmospheric pressure and therefore carbon dioxide product can be easily recycled (Choi et al., 2003; Chou and Chen, 2004; Liu et al., 2011; Takamura et al., 2001). Post-combustion capture does not require the capture of the light components either and this results in streams such as the product of a rinse stream to simply be collected as waste without concern of the impact on the quality of the light product (Choi et al., 2003). Adaptations have been made to traditional cycles as well. Kikkinides et al. (1993) recycled the product of the rinse stream to the adsorption step which aids recovery whilst allowing high purity carbon dioxide to be produced.

Table 2.3: A selection of PSA processes for carbon dioxide capture from flue gas. Ad –adsorption, BD – blowdown, Press – pressurisation, ED – pressure equalisation down, EU – pressure equalisation up. Unless stated otherwise pressurisation is done by the feed gas, purge by a stream of the light component and rinse by a stream of the heavy component. The arrows represent the flow direction, with ↑ being co-current and being ↓ counter-current flow.

	Gas Mixture	Adsorbent	PSA Steps	Type	CO_2 Purity (%)	CO_2 Capture Rate (%)
Kikkinides et al. (1993)	CO_2/N_2	AC	↑Ad, ↑ Rinse, ↓ BD, ↓ Press - light	VPSA	99.9*	68.4*
Ko et al. (2005)	CO_2/N_2	Z13X	↑Ad, ↓ BD, ↓ Purge, ↑ Press	PSA	71.9	94.4
			↑Ad, ↑ BD, ↓ Purge, ↑ Press	VPSA	90.0	93.8
Liu et al. (2011)	CO_2/N_2	Z13X	↑Ad, ↓ BD, ↓ Purge, ↑ Press	VPSA	50.7	95
			↑Ad, ↑ ED, ↓ BD, ↓ Purge, ↓ EU, ↑ Press	VPSA	58.2	93.6
			↑Ad, ↑ Rinse, ↓ BD, ↓ Purge, ↑ Press	VPSA	69.1	98.9
			↑Ad, ↑ Rinse, ↑ ED, ↓ BD, ↓ Purge, ↓ EU, ↑ Press	VPSA	77.1	91.5
Chou and Chen (2004)	CO_2/N_2	Z13X	↑Press, ↑ Depress, ↓ BD, ↑ Press - light	VPSA	43*	94.5*
			↑Ad, ↑ Depress, ↓ BD, ↑ Press - light, ↑ Press	VPSA	38*	89*
			↑Ad, ↓ BD, ↓ Purge, ↑ Press - light	VPSA	57*	75*
			↑Ad, ↑ Rinse, ↑ Depress, ↓ BD, ↑ Press - light, ↑ Press	VPSA	58*	65*
Delgado et al. (2011)	CO_2/N_2	AC	↑Ad, ↑ ED, ↑ ED with Compressor, ↑ ED2, ↓ BD, Idle, ↓ EU1, Idle, ↓ EU2, ↓ EU3 with Compressor, ↑ Press	VPSA	99.6	92.8
Choi et al. (2003)	CO_2/N_2	Z13X	↑Ad, ↑ ED, ↑ Press - heavy, ↑ Rinse, ↓ BD, ↓ EU, ↑ Press	VPSA	95	72.5
Takamura et al. (2001)	$CO_2/N_2/O_2$	Layered Zeolites	↑Ad, ↑ Rinse, ↑ ED, ↓ Blow, ↓ Purge, ↓ EU, ↓ Press	VPSA	91.6	58.8

*study offers a range of values, chosen value indicates optimal separation.

Table 2.4: A selection of PSA processes for methane purification. Ad – adsorption, BD – blowdown, Press – pressurisation, ED – pressure equalisation down, EU – pressure equalisation up. Unless stated otherwise pressurisation is done by the feed gas and purge by a stream of the light component. The arrows represent the flow direction, with ↑ being co-current and being ↓ counter-current flow.

	Gas Mixture	Adsorbent	PSA Steps	Type	CH_4 Purity (%)	CH_4 Capture Rate (%)
Cavenati et al. (2006)	$CH_4/CO_2/N_2$	Layered Z13X and CMS 3K	↑Ad, ↓ BD, ↓ Purge, ↓ Press - light	VPSA	87.2	70.5
Santos et al. (2011)	CH_4/CO_2	Z13X	↑Ad, ↑ ED, ↓ BD, ↓ Purge, ↓ EU, ↑ Press	VPSA	99.2	85
Delgado and Rodrigues (2008)	CH_4/CO_2	Silicates	↑Ad, ↓ ED, ↓ BD, ↓ Purge, ↑ EU, ↑ Press	PSA	100	33.7

*study offers a range of values, chosen value indicates optimal separation.

Table 2.5: A selection of PSA processes for hydrogen purification. Ad – adsorption, BD – blowdown, Press – pressurisation, ED – pressure equalisation down, EU – pressure equalisation up, Depress – co-current depressurisation. Unless stated otherwise pressurisation is done by the feed gas, purge by a stream of the light component and rinse by a stream of the heavy component. The arrows represent the flow direction, with ↑ being co-current and being ↓ counter-current flow.

	Gas Mixture	Adsorbent	PSA Steps	Type	H_2 Purity (%)	H_2 Capture Rate (%)
Cen et al. (1985)	$H_2/CH_4/H_2S$	AC	↑ Ad, ↑ Depress, ↓ BD, ↑ Press	VPSA	99.2	94.9
Cen and Yang (1986)	H_2/CO	AC	↑ Ad, ↑ Depress, ↓ BD, ↓ Purge, ↑ Press	PSA	94.5	96.2
Doong and Yang (1987a)	H_2/CH_4	AC	↑ Ad, ↑ Depress, ↓ BD, ↓ Purge, ↑ Press	PSA	87.2	96.8
Yang and Doong (1985)	H_2/CH_4	AC	↑ Ad, ↑ Depress, ↓ BD, ↓ Purge, ↑ Press	PSA	94.5*	94.4*
Doong and Yang (1987b)	H_2/CH_4	Z5A	↑ Ad, ↑ ED1, ↑ Depress, ↑ ED2, ↓ BD, ↓ Purge, ↓ EU1, ↓ EU2, ↓ Press - light	PSA	99.9	79.6
Ahn et al. (1999)	$H_2/CO_2/N_2/CO/CH_4$	Layered AC and Z5A	↑ Ad, ↑ ED, ↓ BD, ↓ Purge, ↓ EU, ↑ Press	PSA	97.8*	78.0*
			↑ Ad, ↑ ED, ↓ BD, ↓ Purge, ↓ EU, ↓ Press - light , ↑ Press	PSA	99.9*	66.2*
Yang and Lee (1998)	$H_2/CO_2/N_2/CO/CH_4$	Layered AC and Z5A	↑ Ad, ↑ ED, ↓ BD, ↓ Purge, ↓ EU, ↓ Press - light , ↑ Press	PSA	-	-
Ribeiro et al. (2008)	$H_2/CO_2/N_2/CO/CH_4$	Layered AC and Zeolite	↑ Ad, ↑ ED1, ↑ ED2, ↓ BD, ↓ Purge, ↓ EU1, ↓ EU2, ↓ Press	PSA	99.9*	91.8*
Warmuzinski and Tanczyk (1997)	$H_2/N_2/CO/CH_4$	Layered AC and Z5A	↑ Ad, ↑ ED1, ↑ ED2, ↓ BD, ↓ Purge, ↓ EU1, ↓ EU2, ↓ Press	PSA	99.8	84.6
Park et al. (2000)	$H_2/CO_2/$ CO/CH_4	Layered AC and Z5A	↑ Ad, ↑ ED1, ↑ Depress, ↑ ED2, ↓ BD, ↓ Rinse - Depress product, ↓ EU1, ↓ EU2, ↓ Press - light	PSA	99.9*	84.2*
Lopes et al. (2011)	$H_2/CO_2/CO/CH_4/N_2$	AC	↑ Ad, ↑ ED, ↓ BD, ↓ Purge, ↓ EU, ↓ Press - light	VPSA	99.9*	71.0*

*study offers a range of values, chosen value indicates optimal separation.

Table 2.6: A selection of PSA processes for pre-combustion carbon dioxide capture. Ad – adsorption, BD – blowdown, Press – pressurisation, ED – pressure equalisation down, EU – pressure equalisation up. Unless stated otherwise pressurisation is done by the feed gas and purge by feed gas. The arrows represent the flow direction, with ↑ being co-current and being ↓ counter-current flow.

	Gas Mixture	Adsorbent	PSA Steps	Type	H_2 Purity (%)	H_2 Capture Rate (%)	CO_2 Purity (%)	CO_2 Capture Rate (%)
Xiao et al. (2009)	$CO_2/H_2O/N_2$	Hydrotalcite	↑ Ad, ↑ ED1, ↑ ED2 - compressor, ↓ BD, ↓ BD, ↓ EU1, ↓ EU2 - compressor, ↑ Press	VPSA	97.4	-	93.9	91.3
Schell et al. (2013)	CO_2/H_2	AC	↑ Ad, ↓ ED, ↓ BD, ↓ Purge, ↑ EU, ↑ Press	PSA	88.5*	93.0*	92.6*	88.0*
Casas et al. (2013b)	CO_2/H_2	AC	↑ Ad, ↑ ED1, ↑ ED2, ↑ BD, ↓ Purge, ↑ EU1, ↑ EU2, ↑ Press	PSA	-	-	93.0*	90.0*
Agarwal et al. (2010)	CO_2/H_2	AC	see Figure 2.7	VPSA	93.0	91.6	90.0	92.0

*study offers a range of values, chosen value indicates optimal separation.

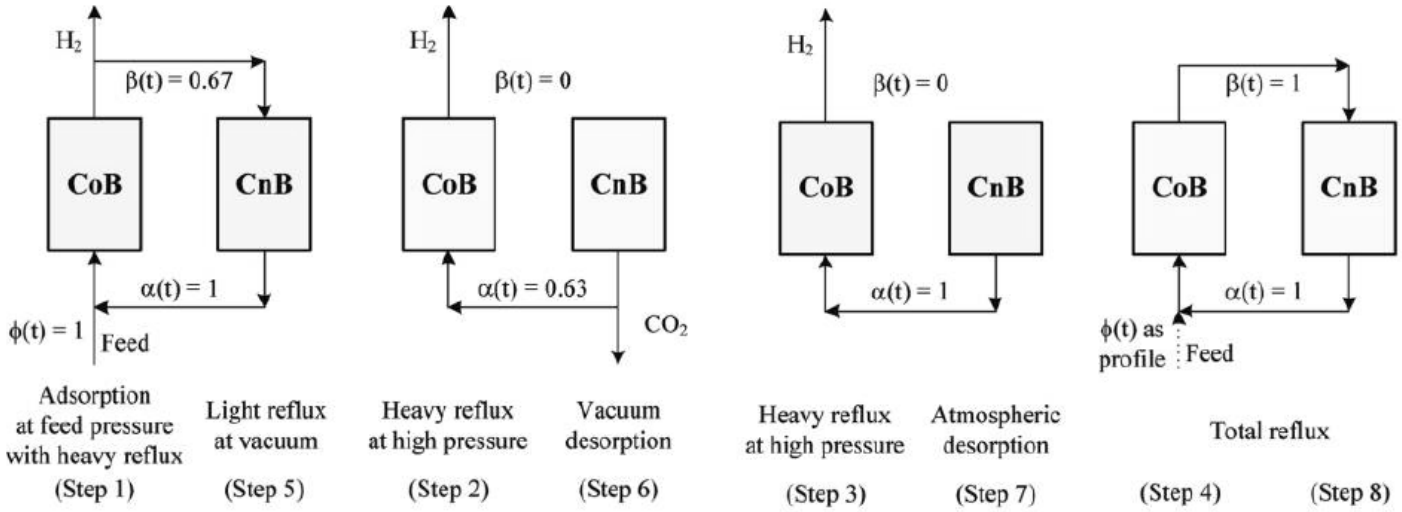

Figure 2.7: 8 step 2 bed system used by Agarwal et al. (2010) for a pre-combustion capture system. CoB stands for co-current bed and CnB for counter-current bed. After 4 steps the beds switch to complete the cycle. α represents the fraction of the counter-current bed, β the fraction of the co-current bed and ϕ the fraction of the feed.

Methane purification is relevant to pre-combustion capture as the systems are at similar pressure and carbon dioxide is being separated from another gas. Table 2.4 presents three studies which have investigated this process. Cavenati et al. (2006) used the four basic steps with the purge under vacuum to purify the carbon dioxide. An optimisation was performed to find the most suitable ratio of zeolite to carbon molecular sieve and this was able to produce a methane purity of 87% and a recovery of 70%. Santos et al. (2011) used pressure equalisation steps with the VPSA system and were able to achieve a considerably higher methane capture rate of 99.2% and methane purity of 85%. Delgado and Rodrigues (2008) used a similar 6 step cycle but did not operate the purge step under vacuum. This resulted in impressive purities, however, the methane capture rate was very low at 33%.

Hydrogen purification is directly relevant to pre-combustion capture as the separation is done at high pressure with hydrogen as the light product. This is a well established field with a selection of studies presented in Table 2.5. The initial investigations of this were for the separation of hydrogen and methane, where it was quickly discovered that a co-current depressurisation step was required to produce higher purity methane (Cen and Yang, 1986; Doong and Yang, 1987a; Yang and Doong, 1985). Doong and Yang (1987b) implemented pressure equalisation steps either side of the co-current depressurisation step and were able to produce high purity hydrogen, although this was at the detriment to the hydrogen capture rate. Subsequent work focussed on the production of high purity hydrogen from mixtures with multiple components although this was often at the detriment to the hydrogen capture rate. Following on from the work by Doong and Yang (1987b), subsequent work utilised pressure equalisation steps. Process innovations were made by

pressurising the bed with the light component, known as a backfill step (Ahn et al., 1999; Lopes et al., 2011; Yang and Lee, 1998). Ahn et al. (1999) compared systems with and without this and found the backfill step increased the hydrogen purity by 2%. Layered beds have been shown to improve the capture rate for hydrogen considerably (Ahn et al., 1999; Park et al., 2000; Warmuzinski and Tanczyk, 1997; Yang and Lee, 1998). Lopes et al. (2011) only used activated carbon as an adsorbent and one pressure equalisation step, resulting in a significant drop in capture rate compared to other studies despite the use of a VPSA cycle.

Pre-combustion capture using a PSA process has not been widely simulated, with the main studies detailed in Table 2.6. Xiao et al. (2009) studied a high temperature separation of $CO_2/H_2O/N_2$ mixtures at 27 bar using hydrotalcite and a two stage process for the same separation using zeolite 13X. A two stage process was required for the zeolite 13X as the water was removed in the first stream. The simulations were done using a numerical simulator (MINSA) developed by the group. The process studied included a two step pressure equalisation process. After the two beds equalising reached the same pressure a compressor was used to continue to pressurise one bed from the depressurising bed. VPSA was also used to maximise the working capacity of the beds. The hydrotalcite process was able to achieve a high carbon dioxide capture rate of 94.8% and a carbon dioxide purity of 97.2%. The zeolite 13X process had a similar purity but a drop in capture rate of 3.7% as well was requiring double the energy input. The recovery of the nitrogen was not studied.

Agarwal et al. (2010) presented the optimal solution of a PSA superstructure for the separation of CO_2/H_2 mixtures using activated carbon. The PSA superstructure

involves two beds and is capable of suggesting multiple operation steps by controlling each bed pressure, the total flowrate in and the fractions of each stream which is used for reflux of the other bed. The optimisation led to the process displayed in Figure 2.7. The hydrogen purity was 93.3% and the capture rate 91.64%. The carbon dioxide purity was 90% and the capture rate 92%, which were both assigned and then all other parameters were allowed to vary to minimise the power consumption of the system. The unibed approach, where it is assumed that only two beds are interconnected, can then be extended to a full model by using multiples of the pair so as to give a continuous output. The down side of this approach is that a vacuum system was incorporated as the reflux of the desorbing bed would be at low pressure. For the optimisation of the system to minimise the power consumption, a power consumption of 46.82 kWh tonne^{-1} CO_2 captured was calculated.

A parametric study was performed by Casas et al. (2013b). The capture of carbon dioxide form CO_2/H_2 mixtures using activated carbon was studied. Compared to the studies by Xiao et al. (2009) and Agarwal et al. (2010), the PSA process used was limited to the four basic steps shown in Figure 2.6 and multiple pressure equalisation steps. A 5 bed system was used with three pressure equalisation steps. The timing of the steps was sequenced to give a continuous adsorption step and therefore a continuous flow of light product. Contrary to most other systems, only the purge step was operated in a counter-current direction. Pareto analysis was used to compare the different process variables and an optimum point of a purity of 93.1% and a capture rate of 90.3% was suggested. It was found that there was a limit to the carbon dioxide purity of 95% caused by the selectivity dictated by the isotherm. The

use of counter-current desorption was compared and found to give lower capture rates and purities. The number of pressure equalisation steps was investigated and increasing the number of steps increased the maximum purity achievable but did not affect the maximum capture rate. However, this caused a reduction in the productivity of the beds. A continuation of the work by Casas et al. (2013b) was studied by Schell et al. (2013), where the model produced by Casas et al. (2013b) was compared to experimental data in order to validate it, as discussed in Section 2.8.2. A 6 step system was studied based on the four steps described in Figure 2.6 and one pressure equalisation step. The system was not optimised for either the purity or capture rate of the hydrogen or carbon dioxide but several simulations were run, which gave a range of results. The result of the best performing runs is presented in Table 2.6.

Despite a large body of work on the simulation of PSA to systems involving carbon dioxide, there have only been a few studies for simulating the removal of carbon dioxide from high pressure mixtures. These studies have shown the promise of the system but the importance of each process configuration is rarely analysed. The variation in process configurations shows the difficulty in separating a mixture into two distinct products. An evaluation of the effect of each PSA step would help to indicate the most difficult areas of separation. Any further advances in process configurations would help make PSA systems a viable process for pre-combustion carbon capture.

2.9 Summary

There is a strong agreement that CCS is required to achieve carbon dioxide emission targets. Pre-combustion capture provides an efficient means of capture of carbon

dioxide from new build power plants as the high pressures of the carbon dioxide containing streams aid in the separation. The state-of-the-art technology is liquid absorption but there are many other capture technologies that are in development. Adsorption using PSA units is an attractive alternative as it has been well used on an industrial scale for other similar sectors.

Activated carbon has been shown to be the most suitable adsorbent for pre-combustion capture using adsorbents. Studies have found that phenolic resins derived activated carbons are promising for these systems. The typical method for evaluating the suitability of these materials is by producing equilibrium adsorption isotherms. However, the use of adsorbents in PSA systems under dynamic conditions has not been well studied. In particular, adsorption capacities on a volumetric scale have rarely been mentioned despite dictating the size of an adsorbent bed. The equilibrium isotherms have not been compared to breakthrough capacities in great detail and therefore the suitability of this measurement for analysis of adsorbents is not well understood. Following from this, the isotherm models used for simulating these systems are rarely evaluated in comparison to breakthrough capacities, which would give more confidence in applying them to simulations.

Simulations of adsorption systems are useful in evaluating the design of PSA units. Breakthrough experiments are often used to validate the adsorption model. There is further scope to use the breakthrough models to identify the adsorbent parameters which most greatly affect the adsorption system, but this has rarely been done. The validation of the models against a full PSA cycle has proved problematic in literature

and more needs to be done to analyse the effectiveness of these models to simulate a whole PSA cycle.

PSA cycles have been well studied for similar separations to mixtures with carbon dioxide at high pressure but there are only a few systems which specifically look at pre-combustion systems and the production of two products. The studies that have been done have shown the promise of this technology. However, the full evaluation of each of the process steps has not been done. Further development of the PSA steps is required to analyse other possible configurations to improve the efficiency of the separation to make it a more viable alternative to liquid absorption systems.

Chapter 3 – Experimental Methods

3.1 Introduction

One of the aims of this study was to investigate the dynamic response of activated carbons for the separation of gases at high pressure. This chapter outlines the preparation of the activated carbon materials studied and the characterisation techniques used, followed by the experimental methods used in the dynamic breakthrough tests.

3.2 Material Preparation

An unmodified and a modified activated carbon prepared from phenolic resins are used in this study. Both materials were prepared by the University of Nottingham, with the preparation techniques of the base activated carbon described by Sun et al. (2013). Activated carbon beads were prepared using a hydrothermal process from phenolic resins. The beads were then activated using mild oxidation at 300°C for 2 hours in air, to produce an unmodified activated carbon. The modified activated carbons were prepared from the unmodified base by oxidation with nitric acid. The beads were mixed with nitric acid, with a ratio of 10g of activated to 250 ml of nitric acid, and held at room temperature for 1 hour. The oxidised beads were washed and dried before being aminated in a tube furnace under ammonia at 800°C. Activated carbon beads are shown in Figure 3.1.

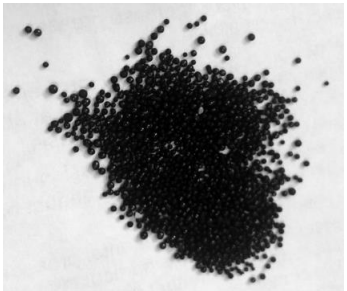

Figure 3.1: Unmodified activated carbon beads prepared by the University of Nottingham.

3.3 Characterisation Techniques

It is necessary to fully characterise the materials as their properties are required for accurately simulating pressure swing adsorption (PSA) systems. The characterisation was performed by external parties at the University of Nottingham and the University of Birmingham.

3.3.1 SEM Images

Scanning electron microscopy was used to investigate the surface of the activated carbons. Samples were examined using a Quanta 600 SEM, with images of the unmodified and modified activated carbons taken at 3kV. ImageJ software was used to measure the particle diameter from the SEM images.

3.3.2 BET Analysis

BET analysis was carried out using a Micrometrics ASAP 2420 to study the textural properties of the activated carbons. Following the method described by Sun et al. (2013), nitrogen physisorption was used with nitrogen at -196°C following degassing of the sample at 120°C for 5 hours. The results were used to find the pore surface area, pore volume and pore diameter for the unmodified and modified activated carbon. The calculations used for the unmodified activated carbon are given in Appendix C.

3.3.3 Density Measurements

3.3.3.1 Particle Density

The particle density was found using a standard pycnometer. Water was used as the known fluid and it was assumed that no water enters the pores of the material. An empty glass pycnometer was weighed. A small sample of material was placed in the

pycnometer and the system reweighed. The pycnometer was then filled with a known mass of water and the mass of displaced water found. From the density of the water, the volume of water displaced was found and equated to the volume of the adsorbent. The particle density was then found by dividing the mass of the sample by the volume of the sample. This was repeated three times for each material.

3.3.3.2 Material Density

The material density was found using a Micrometrics AccuPyc II 1340 Gas Displacement Density Analyser. Unlike a standard liquid pycnometer, a gas displacement pycnometer ensures that the pores of the adsorbent are filled and therefore the actual material density can be found. The sample phase volume was found based on the system pressures observed having filled the sample chamber and subsequently discharged to an adjacent empty chamber. The sample chamber used was 1 cm^3 and helium was used as the displacement gas. The runs were automatically repeated until successive measurements converged.

3.4 Adsorption Isotherms

High pressure isotherms were measured on both the unmodified and modified activated carbons by the University of Nottingham using the method described by Sun et al. (2013). The isotherms were produced by a Particulate Systems High Pressure Volumetric Analyser (HPVA-100) using a static volumetric method. The test procedure involved placing approximately 0.5g of sample into a 2 mL stainless steel tube. Physisorbed moisture and carbon dioxide were removed by evacuating the system overnight at 120°C. The sealed sample cell was then transferred to the HPVA and analysis was performed at a set temperature and a pressure up to 40 bar. For the unmodified material, isotherms were found for pure carbon dioxide and pure

nitrogen streams at 30°C and 45°C. For the modified material, isotherms were recorded for the same gases at 25°C, 30°C, 45°C and 50°C.

3.5 Fixed Bed Experimental Rig

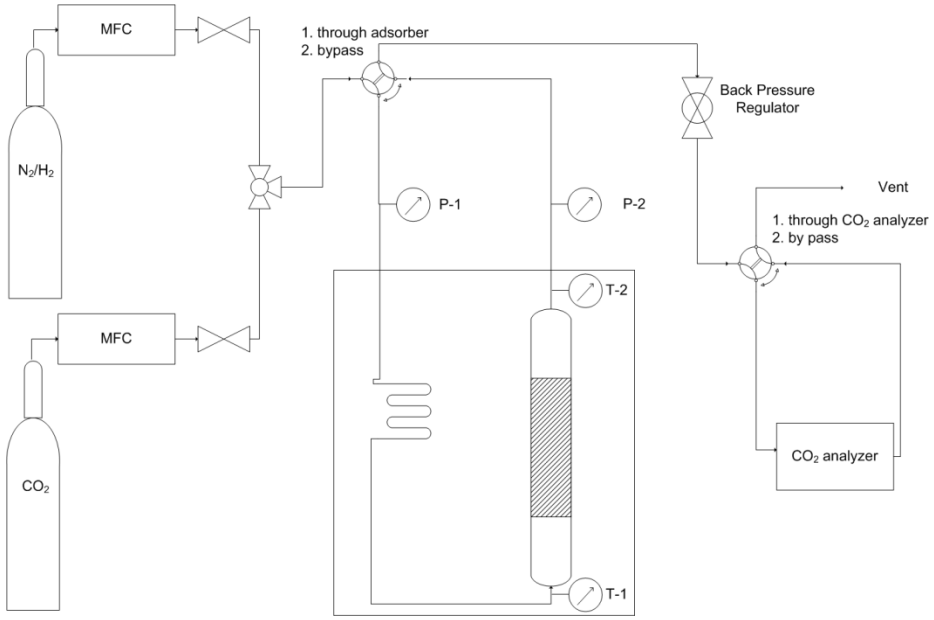

Figure 3.2: Experimental rig set-up for dynamic breakthrough experiments.

The experimental set-up for testing the dynamic response of activated carbon for CO_2/N_2 separations and CO_2/H_2 separations at high pressures is shown in Figure 3.2. The system was fed by pure carbon dioxide and either pure nitrogen or pure hydrogen, the flow of which was controlled by mass flow controllers. A fixed bed packed with activated carbon was situated inside an oven in order to control the temperature of the adsorption bed. A back pressure regulator was used to control the pressure of the system. A CO_2 analyser was used to monitor the concentration of carbon dioxide in the outlet streams. The systems in the rig were connected using 1/8” stainless steel pipe. Two-way valves were used to be able to bypass the bed

and the CO_2 analyser. The temperature and pressure were monitored upstream and downstream using temperature probes and pressure transducers.

The bed was fed by pure carbon dioxide, nitrogen and hydrogen. Both gases were supplied by BOC Industrial Gases. The nitrogen gas had a purity of 99.9995% and a bottle pressure of 20 MPa. Research grade carbon dioxide was used with a liquid withdrawal at a purity of 99.999% and a bottle pressure of 5 MPa. The hydrogen used was zero grade with a purity of 99.995% and a bottle pressure of 20 MPa.

3.5.1 Adsorption Bed

The bed is depicted in Figure 3.3. It was made from stainless steel pipe with an internal diameter of 0.025 m, with a wall thickness of 0.0015 m, and a length of 0.069 m. Swagelok pipe fittings were used to connect the bed to the adjoining 1/8” pipes using two reducers. The entire bed was filled with the activated carbon adsorbent described in Section 3.2 and there was no structure to the packing. The bed density was calculated by dividing weight of adsorbent added by the volume of the bed. For both the unmodified and modified activated carbon the same volume of adsorbent was used.

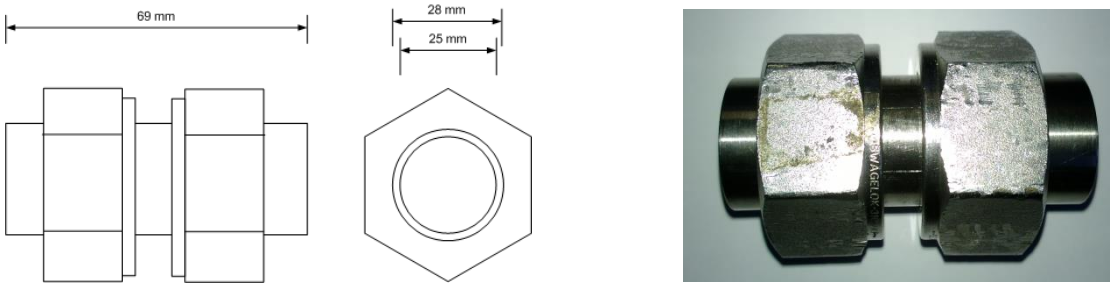

Figure 3.3: Fixed bed

3.5.2 CO_2 Analyser

The CO_2 analyser used was a Servomex 5200 Multi Purpose portable benchtop gas analyser, depicted in Figure 3.4, ranging from 0-100% carbon dioxide. It is rated with a maximum pressure of 68.9 kPag. The intrinsic error within the system is ± 2% of the full scale range. The manufacturer rated response time with a desiccant drying tube fitted to the inlet is 75 seconds. High and low calibrations were performed weekly as recommended by the manufacturer using the method described in the user manual. A simple data logger was used to record the reading every second.

Figure 3.4: CO_2 Analyser

3.5.3 Oven

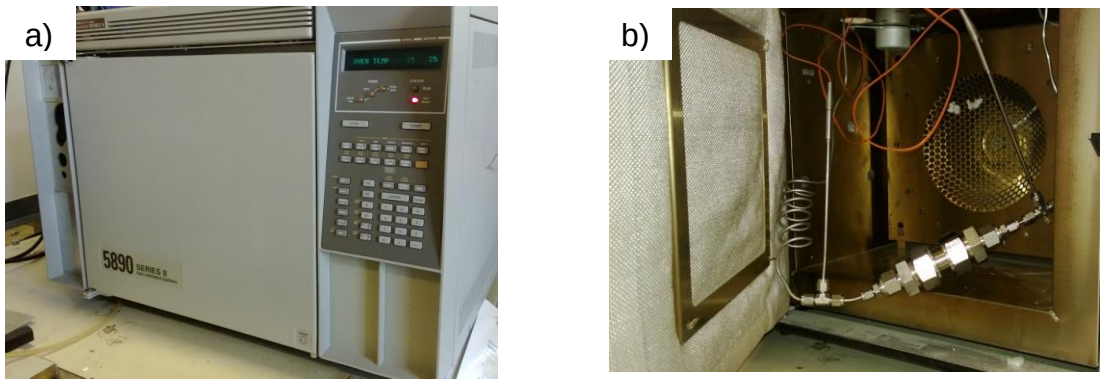

Figure 3.5: a) oven for maintaining bed temperature and b) bed placement within oven

A HP 5890 series II gas chromatograph oven, Figure 3.5a, was used to control the temperature of the bed. The oven has a temperature range of 7°C - 450°C. Temperature programs were used to heat the oven at a set rate, maintain oven temperature and cool the oven. The bed was placed in the oven as shown in Figure 3.5b. Sufficient pipe was used upstream of the bed to ensure the gases were at the same temperature as the oven before passing through the bed and the temperature checked by a temperature probe upstream of the bed.

3.5.4 Backpressure Regulator

A Swagelok backpressure regulator was used to control the pressure of the system. It was made from stainless steel using a PEEK seal and has a valve coefficient of 0.2. It is rated to a pressure of 0-3.44 MPa.

3.5.5 Mass Flow Controllers

The flow of the gases into the system was controlled by two Brooks 5850 thermal mass flow controllers. Both controllers are rated up to 10 MPa. The calibration for the nitrogen flow controller was for a maximum flowrate of 400 Nml min^{-1} and for the carbon dioxide controller was 100 Nml min^{-1}, with standard conditions at 0°C and atmospheric pressure. A correction factor was required for carbon dioxide flowrates, given in Appendix D. Hydrogen flowrate was controlled using the nitrogen flow controller with a correction factor of 1.008 supplied by the flow controller manufacturer. An IGI Systems dIGIbox combined USB-RS485 communication and power supply was used to interface the mass controllers with the operating computer and the IGI control software was used.

3.5.6 Temperature and Pressure Measurement

The temperatures of the gas upstream and downstream of the bed were measured using two K-type thermocouples. The thermocouples have stainless steel sheaths, a sheath diameter of 1/8” and a grounded sensing junction. The thermocouples were fixed into the system using a Swagelok stainless steel union tube with 1/8” diameter connections, as shown in Figure 3.6.

Figure 3.6: Temperature Probe

The pressures upstream and downstream of the bed were measured by two Swagelok S-type pressure transducers. The transducers have a pressure range of 0 to 4.14 MPa and had an accuracy of ≤ 0.5%.

3.6 System Experiments

Experiments were run to find the dynamic response of the system without the bed. This was done for the CO_2 analyser on its own and for the entire system with the bed removed and the inlet and outlet connected directly.

3.6.1 CO_2 Analyser Response

The experimental set-up used to analyse the dynamic response of the CO_2 analyser is shown in Figure 3.2. The two way valve before the adsorption bed was set to position 2 so as to bypass the bed system. Initially a flow of pure nitrogen at

200 Nml min^{-1} was passed through the system with the two way valve upstream of the CO_2 analyser in position 1 so as to purge any residual carbon dioxide in the CO_2 analyser. When the reading on the CO_2 analyser was stable at zero, the two way valve was switched to position 2 so as to bypass the CO_2 analyser. A 0.4 mole fraction of carbon dioxide was then introduced so as to keep the overall flowrate at 200 Nml min^{-1}. The system ran for 5 minutes to ensure all pipe work up to the two-way valve had a carbon dioxide mole fraction of 0.4. The two-way valve was then switched to position 1 to allow the gas to flow through the CO_2 analyser, with this time recorded as time zero, and run for 5 minutes. This was repeated twice and the entire experiment was repeated for carbon dioxide mole fractions of 0.1, 0.2, 0.3 and 0.5.

3.6.2 Surround System Response

The system without the fixed bed was investigated by removing the bed and joining the pipe connections together as shown in Figure 3.7. All other connections in the system were the same so that the response of the system to a step change in carbon dioxide in the feed could be found.

Pure nitrogen was fed to the system at atmospheric pressure at a rate of 200 Nml min^{-1} for 10 minutes to purge any residual carbon dioxide. The bed was pressurised to 2.5 MPa using the backpressure regulator and held at this pressure for 5 minutes. A 0.4 mole fraction of carbon dioxide was introduced whilst maintaining an overall flowrate of 200 Nml min^{-1}, with this recorded as time zero. The system was then run for 10 minutes. After the system has been depressurised, the experiment was repeated twice. Experimental runs were also conducted for carbon

dioxide feeds fractions of 0.1, 0.2, 0.3 and 0.5. All experiments were repeated for a CO_2/H_2 system, with the hydrogen used in the same way as nitrogen.

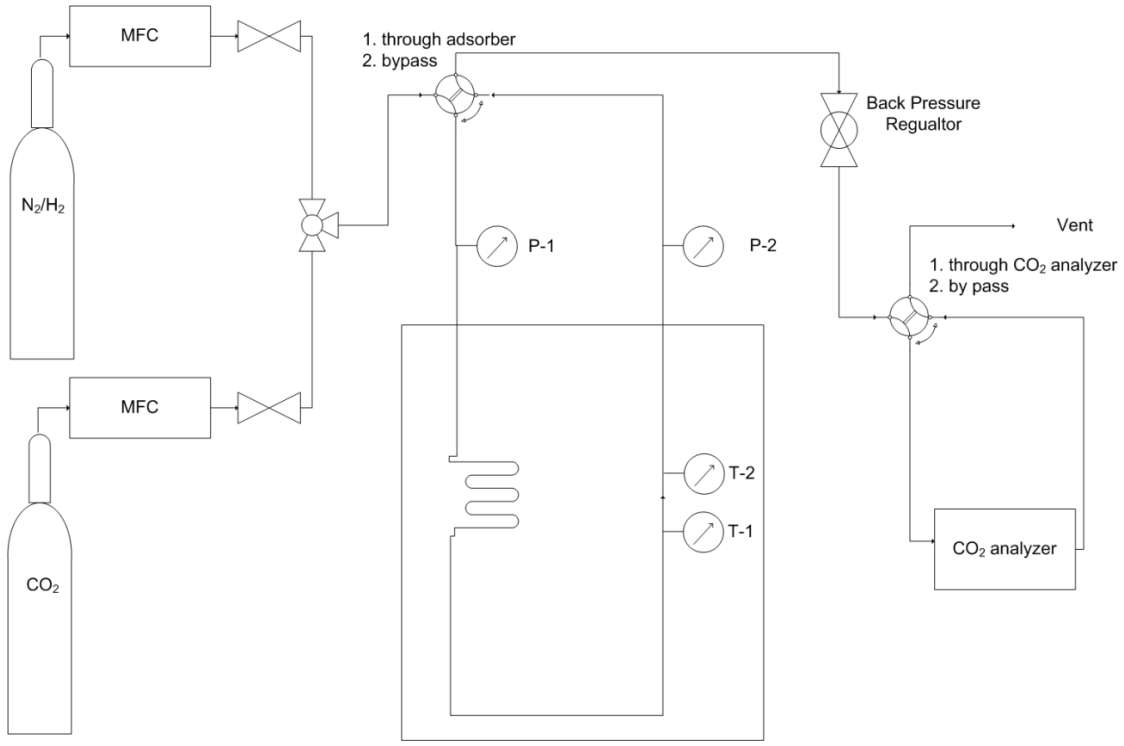

Figure 3.7: Experimental breakthrough rig set-up for a system without a fixed bed

3.7 Experimental Procedure

Breakthrough experiments for beds packed with both the unmodified and modified activated carbon were carried out using the experimental set-up shown in Figure 3.2. The empty beds were weighed. The bed was packed completely with the adsorbent by pouring the material into the bed and tapping the bed to ensure even distribution and then reweighed. The adsorbent itself was repacked for each different experimental sequence.

3.7.1 Bed Regeneration

The bed was first fully regenerated in order to ensure there was no residual carbon dioxide adsorbed on the active carbon. The system was run under a stream of pure nitrogen at 200 Nml min^{-1} for CO_2/N_2 systems at atmospheric pressure. The oven was heated at a rate of 10°C/min from 25°C to 125°C and then held at 125°C for 1800 seconds. After this the bed was allowed to cool to 25°C whilst maintaining a pure nitrogen stream before any adsorption experiments were conducted. For CO_2/H_2 systems, pure hydrogen was used in place of pure nitrogen.

3.7.2 Breakthrough Experiments

Following the regeneration sequence and the bed having cooled completely, breakthrough experiments were conducted. Under a pure nitrogen flow at 200 Nml min^{-1}, the bed was pressurized to 2.5 MPa and allowed to equilibrate for 300 seconds. The flow of nitrogen was reduced and the flow of carbon dioxide was increased to give a carbon dioxide feed fraction of 0.4, whilst maintaining an overall flow of 200 Nml min^{-1}. The system was allowed to run for 3600 seconds to ensure the bed reached full saturation to give the complete breakthrough curve. The bed was then regenerated by desorbing the system. The system was switched back to a pure nitrogen flow of 200 Nml min^{-1} and the pressure was reduced to atmospheric pressure. This was then run for at least 2700 seconds to ensure all residual carbon dioxide had been purged from the bed. The breakthrough experiment was repeated two more times. Full regeneration was not found to be required between each cycle. The experiment was then repeated three times for carbon dioxide mole fractions of 0.1, 0.2, 0.3 and 0.5, including the regeneration step before the first cycle. For carbon dioxide feed fraction of 0.1 and 0.2 the breakthrough experiment was run for

5400 seconds and 4500 seconds respectively. The modified activated carbon was tested for separations of CO_2/N_2 mixtures using the same procedure and repeated for CO_2/H_2 mixtures, where the hydrogen was used in place of the nitrogen.

3.7.3 Three Step Cyclic Experiments

Cyclic experiments were performed to evaluate the response of the bed to the regeneration steps used in PSA cycles. A three step process was investigated which involved a pressurisation step, an adsorption step and a regeneration step. The first cycle was proceeded by the bed regeneration described in Section 3.7.1. The pressurisation step and adsorption step followed the same procedure described in Section 3.7.2, with the bed pressurised fully and allowed to equilibrate for 300 seconds and the adsorption step lasting 3600 seconds for carbon dioxide feed mole fraction of 0.4. Following the end of the adsorption step, the regeneration was then carried out in a controlled way, with all outputs recorded. The feed to the bed was switched back to a flow of pure nitrogen at 200 Nml min^{-1} and the bed was depressurised to atmospheric pressure linearly over a 60 second period by opening the backpressure regulator. The system then continued to run under the pure nitrogen flow for 2640 seconds. The experiment was repeated for two more cycles. As with the breakthrough experiments, the 3 step cycles were conducted for carbon dioxide mole fractions of 0.1, 0.2, 0.3 and 0.4. The experiments were then repeated using the modified activated carbon for separations of CO_2/N_2 mixtures and CO_2/H_2 mixtures.

3.7.4 Four Step Cyclic Experiments

A four step cycle was also tested that more closely represented an industrial PSA process. This process has a pressurisation step, an adsorption step, a blowdown

step and a purge step. The bed was run to breakthrough instead of complete saturation. Before each run the bed was regenerated using the procedure described in Section 3.7.1. The bed was pressurised and the adsorption step started as described in Section 3.7.2. The adsorption ran for 1510 seconds to match a carbon dioxide mole fraction of 0.02 (5% of the carbon dioxide feed fraction) as found by the breakthrough experiments. The total flow to the bed was then switched to 0 Nml min^{-1} and the bed depressurised down to atmospheric pressure linearly over 60 seconds. The bed was held in this state for a further 540 seconds. This proceeded the bed being purged using a pure nitrogen flow at 200 Nml min^{-1} for 2100 seconds. The cycle was run two more times. The experiment was repeated for a bed packed with the modified activated carbon. For the modified activated carbon the breakthrough time was 1210 seconds.

3.8 Risk Assessment

A risk assessment was carried out for the fixed bed rig shown in Figure 3.2 and is provided in Appendix E. This details the minor risks involved in the operation of the experimental rig and the practices used to mitigate these.

Chapter 4 – Theory

4.1 Introduction

The simulation of adsorption systems is a complex process utilising many interconnected equations. This chapter details the equations that have been used in this study. The theory presented allows the prediction of adsorption capacities for breakthrough experiments, the simulation of the experimental set-up including cyclic models and the simulation of pressure swing adsorption (PSA) processes.

4.2 Adsorption Isotherms

Isotherm models allow the capacity (q_i^*) of a material for a given gas to be found based on the pressure of that system. In this work they were used to characterise materials, predict the adsorption capacity for given systems and in simulations to predict breakthrough curves and pressure swing adsorption cycles.

4.2.1 Isotherm Models

Table 4.1: Pure component isotherm models

Langmuir Isotherm	$q_i^* = \frac{q_{s,i} B_i P_i}{(1 + B_i P_i)}$	4.1
Langmuir-Freundlich Isotherm	$q_i^* = \frac{q_{s,i} B_i (P_i)^{n_i}}{(1 + B_i (P_i)^{n_i})}$	4.2
Dual-Site Langmuir Isotherm	$q_i^* = \frac{q_{1,s,i} B_{1,i} P_i}{(1 + B_{1,i} P_i)} + \frac{q_{2,s,i} B_{2,i} P_i}{(1 + B_{2,i} P_i)}$	4.3
Temperature Independent Parameters – LF	$q_{s,i} = k_{1,i} \times e^{k_{2,i}/RT}$	4.4
	$B_i = k_{3,i} \times e^{k_{4,i}/RT}$	4.5
Temperature Independent Parameters – DSL	$q_{1,s,i} = k_{1,1,i} \times e^{k_{1,2,i}/RT}$	4.6
	$q_{2,s,i} = k_{2,1,i} \times e^{k_{2,2,i}/RT}$	4.7
	$B_{1,i} = k_{1,3,i} \times e^{k_{1,4,i}/RT}$	4.8
	$B_{2,i} = k_{2,3,i} \times e^{k_{2,4,i}/RT}$	4.9
Sum of the Squared Relative Errors	$SSE(\%) = \left(\frac{\sum \left[\left(q_{i,exp}^* - q_{i,mod}^* \right) / q_{i,exp}^* \right]^2}{N - 1} \right)^{0.5} \times 100$	4.10

Pure component isotherms were obtained in this study by the use of high pressure volumetric analysis (HPVA) as described in Section 3.4. These isotherms were found using pure gases and therefore pure component isotherm models were applied to fit this data. Three isotherm models were considered here and are shown in Table 4.1. The Langmuir model (Langmuir, 1918) is the simplest model and is presented in Equation 4.1. It is a theoretically rigorous model which is thermodynamically consistent (Ruthven, 1984). This model has often been modified by applying a power law function to the pressure term to give the Langmuir-Freundlich isotherm (Sips, 1948) in Equation 4.2. This does not have the same thermodynamic consistency as the Langmuir isotherm but has been shown to be applicable to a range of separations. The final isotherm model implemented is the Dual Site Langmuir Model (DSL) (Langmuir, 1918) given in Equation 4.3. This makes the assumption that there are two monolayer sites compared to the one assumed in the Langmuir model and still retains the thermodynamic consistency of the Langmuir model (Myers and Prausnitz, 1965). The comparison of these three models to the experimental isotherm data is reported in Section 5.2.4. The parameters are found iteratively by minimising the sum of the squared relative errors (SSE) between the experimental data and the model data, given by Equation 4.10, as used by García et al. (2013).

In order to accurately use the isotherm models they must be converted into a temperature independent form. This was performed for the LF model using Equations 4.4 and 4.5 and for the DSL model using Equations 4.6 to 4.8. The isotherm constant (B_i) has a standard Arrhenius type temperature dependence and this work also included an Arrhenius type temperature dependence of the saturation

capacity ($q_{s,i}$) (Do, 1998). This removes the thermodynamic consistency of the isotherm but has been applied previously for both the LF and DSL isotherm models (García et al., 2013; Schell et al., 2012b). The suitability of this assumption is discussed with the results for applying the temperature independence to the isotherm models in Section 5.2.4.

Multicomponent systems for gas mixtures require special isotherm models as multicomponent isotherms are difficult to produce experimentally. There are several models which allow the capacity for each component of a gas mixture to be found based on their pure component isotherm. Table 4.2 presents the multicomponent isotherm models studied in this work. Equation 4.11 is the extended Langmuir-Freundlich model and Equation 4.12 is the extended Dual Site Langmuir isotherm. Both are based on the original extension of the Langmuir model which can be found theoretically (Ruthven, 1984). Neither is thermodynamically rigorous as this requires the saturation capacity for all gases to be the same, but this has not previously been applied to the separations studied here. As for the pure component isotherms, the temperature independent parameters are represented by Equations 4.4 to 4.9 as previously. The binary pairs for the DSL isotherm, explained in Appendix A, were evaluated based on which configuration gave the greatest adsorption capacity. The suitability of these models is discussed in Section 5.4.2 and 5.5.1.1.

Table 4.2: Multicomponent isotherm models

Multicomponent Langmuir-Freundlich Isotherm	$$q_i^* = \frac{q_{s,i} B_i (P y_i)^{n_i}}{\left(1 + \sum_{j=1}^{i} B_j \left(P y_j\right)^{n_j}\right)}$$	4.11
Multicomponent Dual Site Langmuir Isotherm	$$q_i^* = \frac{q_{1,s,i} B_{1,i} P y_i}{\left(1 + \sum_{j=1}^{i} B_{1,j} P y_j\right)} + \frac{q_{2,s,i} B_{2,i} P y_i}{\left(1 + \sum_{j=1}^{i} B_{2,j} P y_j\right)}$$	4.12

4.2.2 Ideal Adsorbed Solution Theory

Instead of using extended pure component equations as detailed in Section 4.2.1, it is possible to apply the ideal adsorbed solution theory (IAST) as developed by Myers and Prausnitz (1965), which also uses the pure component data to predict the multicomponent capacity. It is based on the assumption that the adsorbed phase is thermodynamically ideal and therefore the spreading pressures (π_i^0) for each component are equal (Rouquerol et al., 1999). The equations required for calculating the adsorption capacities by the IAST using the LF and DSL isotherms are reported in Table 4.3. Equation 4.13 relates the spreading pressure to the equilibrium pressure which can then be equated for each component. This has been applied to the LF and DSL models in Equation 4.16 and Equation 4.17 respectively, the full derivation is given in Appendix H. These equations were solved implicitly to find x_i which was then used in Equation 4.14 and 4.15 to give the adsorbent capacity for each component.

Table 4.3: Equations for applying the IAST to the LF and DSL models

IAST Base Equations	$\frac{\pi_i^0 A}{RT} = \int_0^{p_i^o} \frac{q_i^{pure}}{p_i} dp_i$	4.13
	$\frac{1}{q_t} = \sum \frac{x_i}{q_i^{pure}}$	4.14
	$q_i = x_i q_t$	4.15
IAST – LF model	$q_{s1} ln\left(1 + B_1 \left(\frac{p_1}{x_1}\right)^{n_1}\right) = q_{s2} ln\left(1 + B_2 \left(\frac{p_2}{1 - x_1}\right)^{n_2}\right)$	4.16
IAST – DSL model	$q_{1,s1} ln\left(1 + \frac{B_{1,1} p_1}{x_1}\right) + q_{2,s1} ln\left(1 + \frac{B_{2,1} p_1}{x_1}\right) = q_{1,s2} ln\left(1 + \frac{B_{1,2} p_2}{1 - x_1}\right) + q_{2,s2} ln\left(1 + \frac{B_{2,2} p_2}{1 - x_1}\right)$	4.17

4.3 Heat of Adsorption

Table 4.4: Clausius-Clapeyron relationship for calculating the heat of adsorption

Clausius-Clapeyron Relationship	$\left(\frac{\partial\left(ln(p)\right)}{\partial T}\right)_q = \frac{\Delta H_s}{RT^2}$	4.18
	$\ln(p) = constant - \frac{\Delta H_s}{RT}$	4.19

The isoteric heat of adsorption (ΔH_s) is the enthalpy change that takes place due to adsorption. Table 4.4 reports the Clausius-Clapeyron correlation in Equation 4.18, which connects the isoteric heat of adsorption with the adsorption pressure and temperature. This is derived based on the chemical potential of the gas and adsorbed phased being equal and by applying the Gibbs-Helmholtz equation (Ruthven, 1984). The adsorption pressure for a given saturation amounts at various temperatures can found by using the isotherm equations in Section 4.2.1. Based on the integration of Equation 4.18 to Equation 4.19, plots of $\ln(p)$ against $^1/_T$ were used to calculate the isoteric heat of adsorption for the unmodified and modified activated carbons

4.4 Breakthrough Capacity

In this work the adsorbent capacity for carbon dioxide was calculated based on the amount adsorbed in the bed up until the breakthrough point. The total amount of carbon dioxide accumulated in the system was found by multiplying the breakthrough time by the flow rate of carbon dioxide into the system. In order to find the amount of carbon dioxide adsorbed onto the activated carbon, the amount accumulated in the residual piping and the amount of carbon dioxide in the system voids were subtracted

from the total amount of carbon dioxide fed to the system, Equation 4.20. The amount of carbon dioxide accumulated in the pipe system was calculated by Equation 4.21.

Table 4.5: Calculation for finding the amount of carbon dioxide adsorbed up to the breakthrough point.

Carbon dioxide breakthrough capacity	$q_{CO2,exp} = Q_{CO2,feed} t_{breakthrough} - q_{CO2,pipes} - \frac{\varepsilon_t V_{bed} P y_{CO2,feed}}{RT}$	4.20
System Capacity	$q_{CO2,pipes} = \int Q_{feed}(y_{CO2,feed} - y_{CO2})\, dt$	4.21

4.5 gProms Implementation

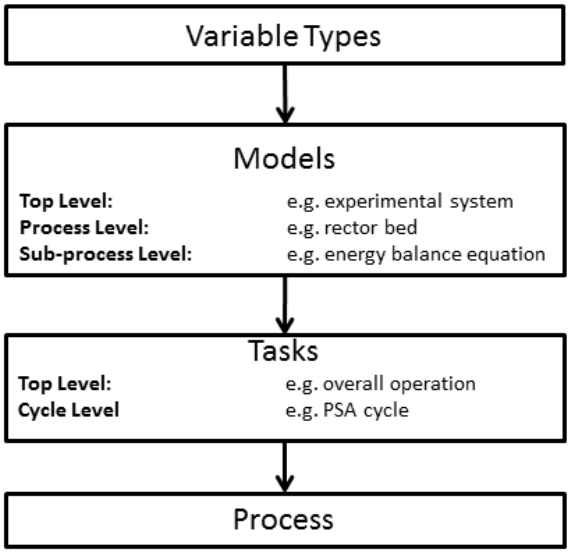

Figure 4.1: gProms hierarchy structure.

The simulation work in this study was conducted using gProms simulation software produced by Process System Enterprise Limited. This is an equation based software package for high fidelity predictive modelling capable of solving complex partial differential equations under dynamic conditions. The general gProms hierarchy is

shown in Figure 4.1. The first input is the 'VARIABLE TYPE' where the types of variables were defined, e.g. pressure, temperature etc. The generalised models were set-up in the 'MODEL' section. Here the parameters and variables, set by the 'VARIABLE TYPE', were defined, as well as the equations that need to be solved. A hierarchy structure was set up where a top level model calls upon a lower tier model, e.g. a system model combining different process equipment models. The 'TASKS' element allowed the way in which the model will be run to be defined, e.g. run for a set period, and was also given a hierarchy structure to allow a regularly used 'TASK' to be repeated e.g. to set a given PSA cycle. Finally the 'MODEL' and 'TASK' were called by the 'PROCESS'. This defined the parameter values and sets the initial conditions of the model, meaning through the use of different 'PROCESS' operations models can be readily run under different conditions. Examples of the MODEL and TASK gPROMS code used are provided in Appendix F.

4.6 Axial Dispersed Plug Flow Model

The axial dispersed plug flow model was used to model the adsorption bed, as shown in Figure 4.2, and is derived from a mass balance which incorporates axial dispersion. The model also requires a mass transfer equation to connect the gas phase and the adsorbed phase and an isotherm model to describe the adsorbed phase. The isotherm models used were the multicomponent isotherm models reported in Section 4.2. Further complexity was added by including an energy balance and pressure drop equation.

For the model used here, several assumptions were made:

1. The ideal gas law holds for the bulk phase.

2. There are no gradients of concentration, pressure or velocity in the radial direction.

3. Transport and physical properties are assumed to be constant and based on the inlet conditions.

4. Thermal equilibrium between the particles and the bulk phase is achieved.

5. Mass transfer is dictated by the Linear Driving Force (LDF) equation, with pore and surface diffusion accounted for in the mass transfer coefficient.

6. The responses of upstream and downstream piping, as well as the CO_2 analyser, are accounted for by an empirical model, described in Section 4.9.

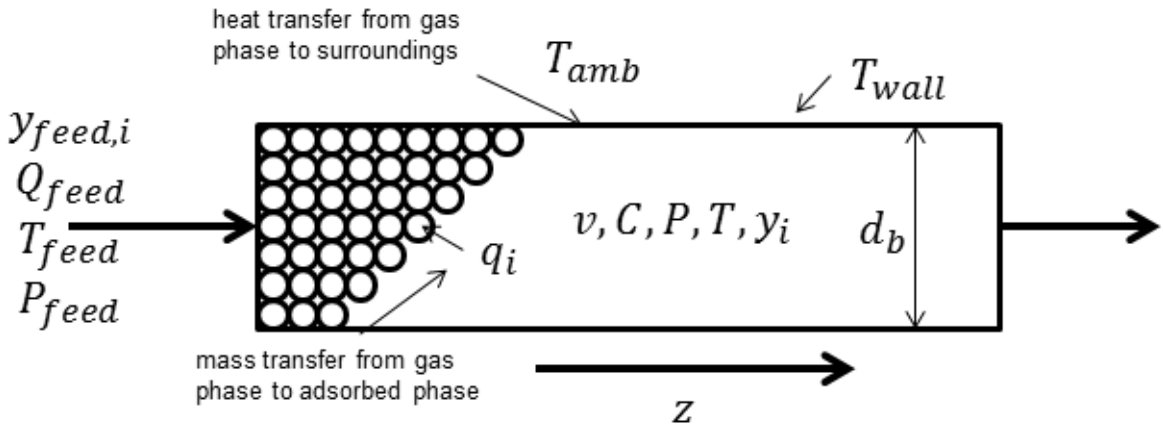

$y_{feed,i}$ – component mole fraction in feed (-)
Q_{feed} – volumetric flowrate of feed (m^3s^{-1})
T_{feed} – temperature of feed stream (K)
P_{feed} – temperature of feed stream (Pa)
T_{amb} – surroundings temperature (K)
T_{wall} – temperature of bed wall (K)
d_b – bed diameter (m)
z – axial position (m)

q_i –component solid phase concentration (mol m^{-3})
y_i – component mole fraction (-)
v – velocity (m s^{-1})
C – total gas phase concentration (mol m^{-3})
T – bed temperature (K)
T – bed pressure (Pa)

Figure 4.2: A fixed system to be simulated by the axial dispersed plug flow model.

The use of the ideal gas law is justified by Casas et al. (2012) for a high pressure system based on the compressibility of the gas mixture being above 0.9. The Peng-Robinson equation of state was used to find the compressibility of the feed stream and this assumption was found to be valid for all possible gas mixtures, these results are detailed in Appendix G. Shafeeyan et al. (2014) reported that assuming there are no radial gradients is well defined in literature. The assumptions which place the particles in thermal equilibrium with the bulk phase has been taken as there is insufficient data to validate the temperature differences. Pore diffusion and surface diffusion models are not used as they have been shown in literature to have little effect as long as the typical S-shape of the breakthrough curve is observed (Liaw et al., 1979).

4.6.1 Mass Balance

The component and overall mass balance used are presented in Table 4.6 and were derived from a differential mass balance over an element of a fixed bed (Ruthven, 1984). Both equations have four parts: an accumulation term, a convective term, a dispersive term and an adsorption term presented in that order. The component mass balance in Equation 4.23 combines the overall mass balance and a mass balance of component *i* as detailed by Ko et al. (2005) and shown in Appendix H. The voidages have been assigned respectively to total voidage (ε_t) and bed voidage (ε_b) following Casas et al. (2012). Supplementary equations were needed to specify the concentration and voidages. The total concentration was calculated using the ideal gas law in Equation 4.24 and the component concentration was related to the

total concentration by the mole fraction in Equation 4.25. The total voidage was calculated from the specified bed voidage and particle voidage (ε_p) by Equation 4.26.

Table 4.6: Mass balance equations for the axial dispersed plug flow model and supplementary equations

Overall	$\varepsilon_t \frac{\partial C}{\partial t} = -\varepsilon_b \frac{\partial (Cv)}{\partial z} + \varepsilon_b D_{ax} \frac{\partial^2 C}{\partial z^2} - \rho_b \sum_{i=1}^{n} \frac{\partial q_i}{\partial t}$	4.22
Component	$\varepsilon_t \frac{\partial y_i}{\partial t} = -\varepsilon_b v \frac{\partial y_i}{\partial z} + \varepsilon_b D_{ax} \left(\frac{\partial^2 y_i}{\partial z^2} + \frac{2}{C} \frac{\partial y_i}{\partial z} \frac{\partial C}{\partial z} \right) - \frac{\rho_b}{C} \left(\frac{\partial q_i}{\partial t} - y_i \sum_{i=1}^{n} \frac{\partial q_i}{\partial t} \right)$	4.23
Ideal Gas Law	$C = \frac{P}{RT}$	4.24
Component Concentration	$c_i = C\, y_i$	4.25
Total Voidage	$\varepsilon_t = \varepsilon_b + \varepsilon_p - \varepsilon_b \varepsilon_p$	4.26

4.6.2 Energy Balance

An energy balance is required if the system is non-isothermal. There are three main types of energy balance: non-isothermal without wall effects, adiabatic and non-isothermal with wall effects. For a non-isothermal system without wall effects the additional assumptions that thermal equilibrium between the bed wall and the surroundings is attained and that the surrounding temperature is constant are required.

The energy balances which dictate these three operating modes are given in Table 4.7 by Equations 4.27 to 4.29. These all include an accumulation term, a convective flux, a dispersive flux and an energy generation term. The difference between them is in the last term where the energy dissipation out of the system is described. For the system without wall effects this is described by heat transfer to the surroundings, for

the adiabatic system this term is not included and for the system with wall effects this is described with heat transfer to the bed wall. The system with wall effects also requires a separate energy balance for the bed wall given by Equation 4.30.

Table 4.7: Energy balance equations for a system without wall effects, an adiabatic system and a system with wall effects

System without Wall Effects	$$\left(\varepsilon_t \rho_g C_{p,g} + \rho_b C_{p,a}\right)\frac{\partial T}{\partial t} = -\rho_g C_{p,g}\varepsilon_b \frac{\partial (vT)}{\partial z} + \lambda_{ax}\frac{\partial^2 T}{\partial z^2} + \rho_b \sum_{i=1}^{n} \Delta H_i \frac{\partial q_i}{\partial t} + \frac{4h_w}{d_b}(T - T_{amb})$$	4.27
Adiabatic	$$\left(\varepsilon_t \rho_g C_{p,g} + \rho_b C_{p,a}\right)\frac{\partial T}{\partial t} = -\rho_g C_{p,g}\varepsilon_b \frac{\partial (vT)}{\partial z} + \lambda_{ax}\frac{\partial^2 T}{\partial z^2} + \rho_b \sum_{i=1}^{n} \Delta H_i \frac{\partial q_i}{\partial t}$$	4.28
System including Wall Effects	$$\left(\varepsilon_t \rho_g C_{p,g} + \rho_b C_{p,a}\right)\frac{\partial T}{\partial t} = -\rho_g C_{p,g}\varepsilon_b \frac{\partial (vT)}{\partial z} + \lambda_{ax}\frac{\partial^2 T}{\partial z^2} + \rho_b \sum_{i=1}^{n} \Delta H_i \frac{\partial q_i}{\partial t} + \frac{4k_w}{d_b}(T - T_{wall})$$	4.29
	$$\rho_w C_{p,w}\pi\left(\left(\frac{d_b}{2} + l\right)^2 - \left(\frac{d_b}{2}\right)^2\right)\frac{\partial T_{wall}}{\partial t} = 2\pi\frac{d_b}{2}k_w(T - T_{wall}) - 2\pi\left(\frac{d_b}{2} + l\right)h_o(T_{wall} - T_{amb})$$	4.30

4.6.3 Mass Transfer Equation

The mass transfer equation relates the gas concentration to the overall uptake rate (Yang, 1987). The simplest relationship is to assume instant equilibrium between the two phases, however, this does not represent any mass transfer effects. The more widely used equation is the LDF equation, presented in Equation 4.31, which relates

the two phases by a single mass transfer resistance. This has been shown to be sufficient for simple adsorption processes (Liaw et al., 1979).

Table 4.8: Linear driving force equation

LDF	$\frac{\partial q_i}{\partial t} = k_i(q_i^* - q_i)$	4.31

4.6.4 Pressure Drop

The pressure drop across the bed is given by the modified Ergun equation presented in Equations 4.32 to 4.34. The ratio of particle diameter (d_p) to bed diameter (d_b) is 25 and the wall effects must be taken into account when this ratio is less than 50 (Mehta and Hawley, 1969), requiring the modified Ergun equation to be used instead of the standard Ergun equation.

Table 4.9: Pressure drop across the bed described the modified Ergun equation

Modified Ergun Equation	$-\frac{\partial P}{\partial z} = 150\mu_g v \frac{(1-\varepsilon_b)^2}{{d_p}^2 {\varepsilon_b}^3} + 1.75\rho_g v\lvert v\rvert \frac{(1-\varepsilon_b)}{d_p {\varepsilon_b}^3}$	4.32
	$A_{erg} = 150\left(1 + \frac{2d_p}{3d_b(1-\varepsilon_b)}\right)^2$	4.33
	$B_{erg} = 1.75\left(1 + \frac{2d_p}{3d_b(1-\varepsilon_b)}\right)$	4.34

4.7 Correlations

The equations presented in Section 4.6 describe the interactions in the system but parameter values are needed to characterise the system within the model. The majority of properties are gas or adsorbent properties that were found by independent experiment or from literature values. There are, however, some properties which are dependent on the interaction between the gas and the adsorbent and it is difficult to find values independently. These parameters include

the dispersion coefficient (D_{ax}), the mass transfer coefficient (k_i), the heat transfer coefficient (h_w) and the heat dispersion coefficient (λ_{ax}). Correlations based on the gas, system and adsorbent properties were used instead. The dimensionless groups that were used in these correlations are given in Table 4.10.

Table 4.10: Dimensionless groups used within the parameter correlations

Dimensionless Groups	$Re = \frac{\rho_g u_0 d_p}{\mu_g}$; $Sc = \frac{\mu_{g,0}}{\rho_{g,0} D_{m,0}}$; $Pe' = \frac{u_0 d_p}{\varepsilon_b D_{ax}}$; $Pr = \frac{C_{p,g}\mu_g}{K_g}$	4.35

4.7.1 Dispersion

Table 4.11: Correlations used to find the dispersion coefficient

General Correlation	$\frac{1}{Pe'} = \frac{\gamma_1 \varepsilon_t}{Re_0 Sc} + \gamma_2$	4.36
Hsu and Haynes (1981) Correlation	$\frac{1}{Pe'} = \frac{0.328}{Re_0 Sc} + \frac{3.33}{1 + \frac{0.59}{Re_0 Sc}}$	4.37
Wakao and Funazkri (1978) Correlation	$\frac{1}{Pe'} = \frac{20}{Re_0 Sc} + 0.5$	4.38

There are several correlations for predicting the dispersion coefficient and the ones used in this study are presented in Table 4.11. Axial dispersion is a combination of molecular diffusivity (D_m) and turbulent mixing caused by the flow around adsorbent particles. The simplest relationship is by combining these two affects additively, as seen in Equation 4.36, resulting in the general correlation. The constants γ_1 and γ_2 have typical values of 0.7 and 0.5, although their value has been the study of much work (Ruthven, 1984). The correlation by Hsu and Haynes (1981), which was evaluated for similar conditions as those used in this study, developed the more complex relationship presented in Equation 4.37. Both of these correlations were

developed for non-porous particles, but Wakao and Funazkri (1978) found that for porous particles under adsorbing conditions the dispersion was much greater than predicted by previous correlations, especially at low Reynolds numbers. They instead suggested the correlation presented by Equation 4.38 which predicts much higher dispersion at low Reynolds numbers. All three of these correlations are evaluated in Section 6.3.2.2.

4.7.2 Mass Transfer Coefficient

Table 4.12: Correlations for calculating the mass transfer coefficient

Mass Transfer Coefficient	$\frac{1}{k_i} = \frac{d_p q_{0,i}}{6 k_f c_{0,i}} + \frac{d_{pore}^2 q_{0,i}}{60 \varepsilon_p D_{pore} c_{0,i}} + \frac{r_c^2}{15 D_c}$	4.39
Surface Mass Transfer	$k_f = \frac{D_m}{d_p}\left(2.0 + 1.1 Re^{0.6} Sc^{1/3}\right)$	4.40
	$D_{pore} = \frac{\varepsilon_p D_k D_m}{\tau (D_k + D_m)}$	4.41
	$D_k = 9700 \frac{d_{pore}}{2}\left(\frac{T}{M_w}\right)^{1/2}$	4.42
Pore Diffusivity	$D_m = 0.0018583 \sqrt{T^3 \left(\frac{1}{M_{w,A}} + \frac{1}{M_{w,B}}\right)} \frac{1}{P \sigma_{AB}^2 \Omega_{D,AB}}$	4.43
	$\sigma_{AB} = \frac{1}{2}(\sigma_A + \sigma_A)$	4.44
	$\varepsilon_{AB} = \sqrt{\varepsilon_A \varepsilon_B}$	4.45
	$T_{dim} = \frac{\kappa T}{\varepsilon_{AB}}$	4.46

The use of the LDF model as the only description of the mass transfer requires the mass transfer coefficient to incorporate all three mass transfer resistances, namely external mass transfer (k_f), pore diffusion (D_{pore}) and micropore diffusion (D_c). All of the equations used in this study to calculate the mass transfer coefficient are reported in Table 4.12. The correlation used by Farooq and Ruthven (1990) for the

mass transfer coefficient incorporates the three mass transfer resistances and is presented in Equation 4.39. The external mass transfer coefficient was found using the correlation, Equation 4.40, suggested by Wakao and Funazkri (1978). The diffusivity was found from the Chapman-Enskog equation, Equation 4.43, as given by Bird et al. (2001) and the Knudsen diffusion (D_k) was calculated using Equation 4.42 (Nikolic et al., 2008). The pore diffusion was then calculated by combining the effect of the Knudsen diffusion and diffusivity by Equation 4.41 (Nikolic et al., 2008). There are no suitable correlations for finding the micropore diffusivity used in the third term of Equation 4.39 and so in this study the values reported by Shen et al. (2010) are used.

4.7.3 Heat Balance Coefficients

Table 4.13 reports the correlations needed for the heat transfer coefficient, the heat dispersion coefficient for all energy balances considered and a further correlation for the external heat transfer coefficient, which is needed for a system that considers the wall effects. The heat transfer coefficient is predicted using either the Yagi and Kunii (1960) correlation, Equation 4.47, or the Leva (1947) correlation, Equation 4.48, with the merits of each equation discussed in Section 6.3.2.4. The heat dispersion coefficient is predicted using the Wakao et al. (1979) correlation, Equation 4.49. The external heat transfer from the bed wall to the surrounding air (h_o) is assumed to be natural convection and is described by the Nusselt equation, Equation 4.50, which is based on the Grashoff number, Equation 4.51, and the Prandtl number for a horizontal cylinder with $a = 0.53$ and $m = 0.25$ (Perry et al., 1997).

Table 4.13: Correlations used for parameters in the energy balance

Yagi and Kunii (1960) Correlation	$h_w = h_w^o + \alpha_w(C_{p,g}\rho_g u)$	4.47
Leva (1947) Correlation	$h_w = \frac{0.813Re^{0.9}K_g}{d_b} e^{\left(\frac{-6d_p}{d_b}\right)}$	4.48
Heat Dispersion Coefficient	$\lambda_{ax} = K_g(7 + 0.5PrRe)$	4.49
	$h_o = \frac{K_{air}}{(d_b + 2\delta)} a(Gr_{air}Pr_{air})^m$	4.50
External Heat Transfer Coefficient	$Gr = \frac{g\beta(T_{wall} - T_{air})(d_b + 2\delta)^3}{\left(\frac{\mu}{\rho}\right)^2}$	4.51
	$\beta_{air} = \frac{1}{T_{air}}$	4.52

4.8 Boundary and Initial Conditions

The boundary conditions are presented in Table 4.14. They are based on the well known Danckwert's Boundary conditions (Danckwerts, 1953) and the conditions of the inlet stream. These represent the reactor as a closed system and allow for the flow just inside the reactor to take into account convection and diffusion.

Table 4.14: Model Boundary Conditions

Boundary Conditions	$-D_{ax}\left.\frac{\partial y_i}{\partial t}\right\|_{z=0} = v\|_{z=0}(y_{feed} - y_i\|_{z=0})$ $P\|_{z=0} = P_{feed}; \quad T\|_{z=0} = T_{feed}; \quad v\|_{z=0} = \frac{Q_{feed}}{A\varepsilon_t}$ $\left.\frac{\partial T}{\partial z}\right\|_{z=L} = 0; \quad \left.\frac{\partial P}{\partial z}\right\|_{z=L} = 0; \quad \left.\frac{\partial y_i}{\partial z}\right\|_{z=L} = 0; \quad \left.\frac{\partial v}{\partial z}\right\|_{z=L} = 0$	4.53

The initial conditions which describe the state of the bed at time zero are given in Table 4.15. They assume that initially the flow through the bed is the same as the feed flow and that the only gas in the bed is nitrogen. They also state that the

adsorbed state is not changing and as the bed is saturated with nitrogen, neither is the adsorbed state.

Table 4.15: Model Initial Conditions

Initial Conditions	$\frac{\partial q_i}{\partial t} = 0$ $y_{CO_2} = 0; \quad y_{N_2} = 1$ $v = \frac{Q_{feed}}{A\varepsilon_t}$	4.54

4.9 Empirical System Model

The model described in Section 4.6 describes an adsorption bed but it does not simulate the response of the surrounding system. The piping system that connects the adsorption bed in the experimental set-up, described in Figure 3.7, is complex with many valves and pipe bends and is difficult to simulate with simple theoretical models. The response of the piping system is found through independent experiments described in Section 3.6.2. A model based on the axial dispersed plug flow model of a simplified bed is used to replicate the produced experimental breakthrough curves. The model assumes that the bed velocity, pressure and temperature are all fixed and that no adsorption takes place. This reduces Equations 4.22, 4.23, 4.27 and 4.31 to Equations 4.55 to 4.58 presented in Table 4.16.

Table 4.16: Reduced axial dispersed plug flow model for simulating system surrounding the adsorption bed

Empirical Model	$\frac{\partial y_i}{\partial t} = -v\frac{\partial y_i}{\partial z} + D_{ax}\frac{\partial^2 y_i}{\partial z^2}$	4.55
	$\frac{\partial v}{\partial z} = 0$	4.56
	$T = T_{feed}$	4.57
	$P = P_{feed}$	4.58

In order to fit the breakthrough curves for a system without an adsorption bed, a model was established with the configuration shown in Figure 4.3. The fitting of the simulation output to the experimental breakthrough curves was achieved by using the Parameter Estimation tool within gProms. Within the system the bed area and dispersion coefficient were used as fitting parameters for each of the bed models. The parameters found were empirical with accurate replication of experimental breakthrough curves the main concern. This was done by first fitting beds 1 and 2 to the output of the response of the CO_2 analyser described in Section 3.6.1. The parameters in these beds were then fixed and the beds were connected in a model to beds 3 and 4. The process was repeated using parameters within beds 3 and 4 in the Parameter Estimation tool to match the output of the system without a bed described in Section 3.6.2.

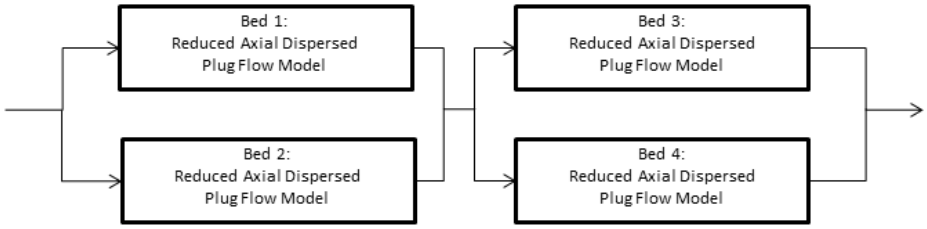

Figure 4.3: Configuration of empirical models for simulating the response of the system surrounding the adsorption bed

4.10 Solver Implementation

The solution method used is important in ensuring the stability and the accuracy of the model. The solution methods in gProms use method of lines numerical solvers. The main reactor bed used a second order backward finite difference method with 30 elements. The backward finite difference method is used to oppose the direction of flow and the second order nature ensures the accuracy of the system (LeVaque,

2007). It is generally preferred as it is easy to implement and unconditionally stable (Yang, 1987). The length of the bed means that 30 elements gives sufficient data points to accurately model the system.

4.11 Validation Models

4.11.1 Model Configuration

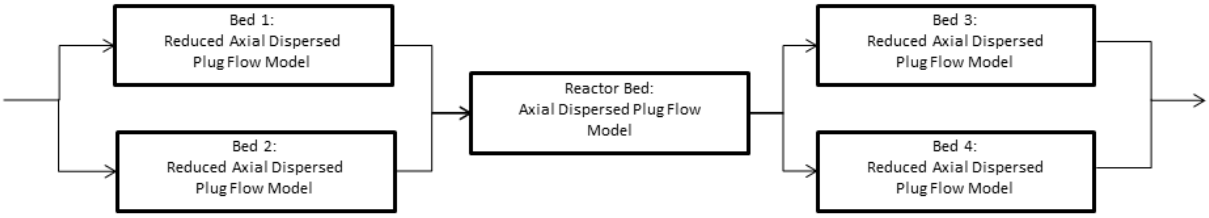

Figure 4.4: Configuration of reactor bed within the model for simulating the entire experimental system

In order to validate the model that is described in Section 4.6, the model output was compared to experimental data. The experimental set-up and procedure is described in Section 3.7.2. As discussed in Section 4.9, the surrounding system requires an empirical model that simulates the response of the piping system around the reactor which is simulated by 4 beds arranged as shown in Figure 4.3 using the reduced axial dispersed plug flow model. The system with the adsorption bed is simulated by including a model for a bed using the axial dispersed plug flow model in the configuration shown in Figure 4.4. All of the validation simulations used this bed configuration.

4.11.2 Breakthrough Models

Simulations were run for carbon dioxide feed mole fractions of 0.1, 0.2, 0.3, 0.4 and 0.5 for both the unmodified and modified activated carbon. The parameter values are provided in Table 5.12 or by the correlations listed in Section 4.7, the use of

which are discussed in Section 6.3.2. The operation of the models is controlled to match the experimental procedure described in Section 3.7.2. For the breakthrough models there are no changes in the input conditions and therefore the simulation is based on the initial conditions and the boundary conditions outlined in Section 4.8 and the model is run for the same length of time as the experiment, i.e. 5400 seconds.

4.11.3 Cyclic Models

The 3 step and 4 step models required for simulating the experiments described in Section 3.7.3 and 3.7.4 respectively are more complex as the feed conditions of the system change depending on the step.

Table 4.17: Relationship for changing the flowrate in pressure swing adsorption cycles.

Feed Flowrate	$\frac{\partial Q}{\partial t} = constant$	4.59

It is necessary to build the change of conditions for each step into the simulation. Three of the feed conditions can change when the system switches to the next step: the mole fraction of each gas, the flowrate and the pressure. The mole fraction was changed by introducing a discontinuity into the system by reassigning the values in the simulation. The flowrate and pressure on the other hand could not be changed by reassigning the value as the solver was not able to incorporate the discontinuity. The flowrate changes in the 4 step model were achieved by a linear relationship as described by Equation 4.59 in Table 4.17. The constant used in that equation was the difference between the final flowrate and the initial flowrate divided by the time for the flowrate change to take place.

The bed pressure is more difficult to control. This is often done using a pressure profile (Cen and Yang, 1986; Yang and Doong, 1985). It was not possible to implement a linear relationship similar to the one used for the flowrate as used by Ko et al. (2005) because this led to a rapidly increasing exit velocity with a large spike for a depressurisation time of 60 seconds, which is unrealistic and can cause errors in the simulation. Instead a control system was used to maintain a constant flowrate at the bed exit. This has previously been achieved using a control valve equation, such as Equation 4.68, in order to connect models (Choi and Wen-Chung, 1994; Nikolic et al., 2008). However the produced system where the exit flowrate is set as a boundary condition becomes too stiff and was not able to solve.

Table 4.18: Equations used on the control of the bed pressure

Valve Equation	$Q = C_v . SP . \sqrt{\frac{\Delta P^2}{SG_g}}$	4.60
Bed Pressure	$\frac{\partial P}{\partial t} = -depress\ rate$	4.61
	$Error = P_{out\ set} - P_{out}$	4.62
	$depress\ rate = depress\ rate \times (Error \times Proportion\ Constant + 1)$	4.63

This work instead set the rate of change of pressure to a variable, Equation 4.61, which was then controlled in a while loop. The while loop, shown in Figure 4.5, maintains the exit flowrate whilst the bed is depressurising by comparing the exit flowrate to the desired flowrate and then reducing the depressurisation rate if the exit flowrate is too high. The depressurisation rate was not manipulated if the flowrate is too low, but instead maintained for that iteration as a constant depressurisation rate produces a rising flowrate profile. The equations used for this are given in Table

4.18, with the depressurisation rate manipulated in Equation 4.63 based on the difference between the set pressure and actual pressure given in Equation 4.62.

Simulations were run to match the experiments described in Section 3.7.3. For both cases the pressurisation step was not simulated as the experimental outputs during this step remain constant and therefore comparison of the simulation with them would be meaningless. Instead, the systems were assumed to start with the adsorption step with the same conditions as for the breakthrough model. For the 3 step model, carbon dioxide feed mole fractions of 0.1, 0.2, 0.3, 0.4 and 0.5 were simulated for both the unmodified and modified activated carbon. The operation of the beds in a 3 step system is shown in Figure 4.6a, with the regeneration step split into two beds so as to clearly show the 60 second depressurisation that occurs at the start of this step. The cycle time varied depending on the carbon dioxide feed mole fraction. The adsorption step for carbon dioxide feed fraction of 0.1 is 5400 seconds, for 0.2 is 4500 seconds and for 0.3 – 0.5 are 3600 seconds to match the experimental runs. For all cases the regeneration step was 2700 seconds, with a 60 second depressurisation followed by a 2640 second purge.

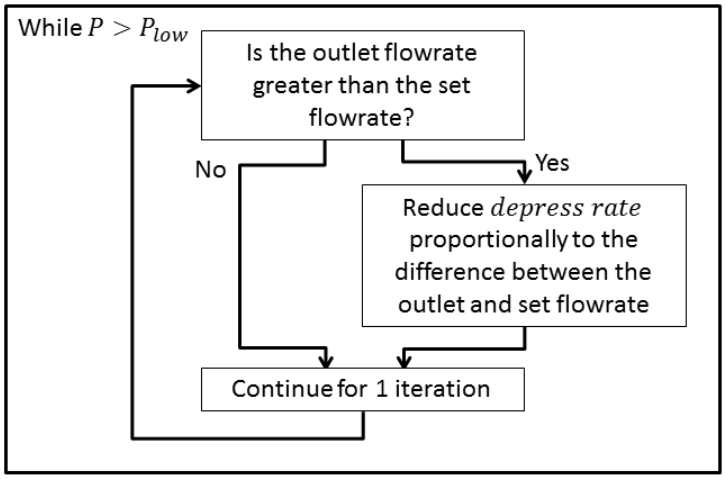

Figure 4.5: While loop for controlling the bed exit flowrate during depressurisation

Simulations were run for the 4 step system using a carbon dioxide feed fraction of 0.4 for both the unmodified and modified activated carbon. The operation of the 4 step process is shown in Figure 4.6b. In order to match the experiments described in Section 3.7.4, the adsorption step was run for 1510 seconds for the unmodified activated carbon and 1260 seconds for the modified activated carbon, the blowdown step was run for 600 seconds, with the depressurisation occurring in the first 60 seconds, and the purge step for 2100 seconds.

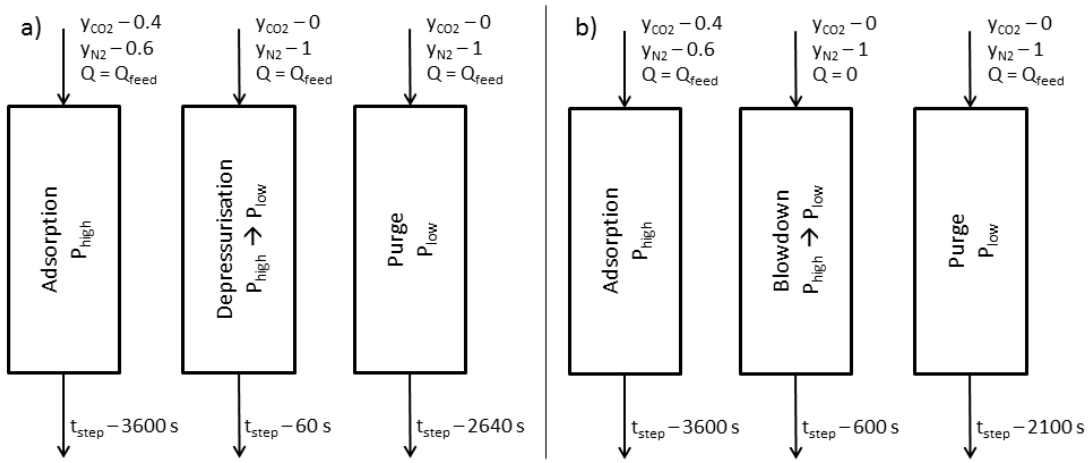

Figure 4.6: Operation steps for the a) 3 step cycle and b) 4 step cycle

4.11.4 Performance Indicator

The experimental and simulation breakthrough curves were compared numerically by using the normalised sum of the squared differences (SSD) between the experimental mole fraction at a set time and the simulation output for that time. The normalised version was used so that systems with a different number of data points could be compared. The sum of the squared of the differences has been used previously by Won et al. (2012) for the same comparison. It should be noted that the graphs should also be compared qualitatively as a lower SSD can be found for a system that is a poorer fit to the shape of a breakthrough curve (Won et al., 2012).

Table 4.19: Equation for the normalised sum of the squared differences

Normalised sum of the squared differences	$SSD = \left(\frac{\sum \left(y_{i,exp} - y_{i,mod} \right)^2}{N - 1} \right)^{0.5}$	4.64

4.12 Pressure Swing Adsorption Models

The validated model was used to simulate several PSA systems, which are detailed in their individual sections in Chapter 7. They were all based on the axial dispersed plug flow model, surrounding equations and assumptions detailed in Section 4.6 as well as the boundary and initial conditions outlined in Sections 4.8. The empirical system model was not included as only the adsorption bed is simulated, not the surrounding system from the experimental set-up.

4.12.1 Model Set-up and Solvers Used

PSA models involve connecting multiple beds together. This was achieved by building models which combine multiple beds based on the same underlying adsorption model. The feed conditions to each bed were the only aspects manipulated based on the PSA step each bed was operating under. For steps where beds are connected to each other, e.g. pressure equalisation, the feed conditions of the downstream bed were set to the outlet conditions of the upstream bed. The switching between steps was achieved in the same way as for the validation models. Changes to feed mole fraction were implemented by introducing a discontinuity and reassigning the value. Changes in flowrate were achieved using the linear relationship given by Equation 4.59. For beds that are interconnected, the flowrate of each bed was manipulated to be the same and then the connection was implemented so as to avoid large discontinuities. Depressurisation was controlled by

maintaining a constant exit flowrate using the control loop described by Figure 4.5 and the equations from Table 4.18.

Table 4.20: Equations for controlling bed pressurisation

Bed Pressure	$\frac{\partial P}{\partial t} = repress\ rate$	4.65
	$Error = Q_{out} - Q_{out\ set}$	4.66
	$repress\ rate = repress\ rate \times (Error \times Proportion\ Constant + 1)$	4.67

The pressurisation steps were controlled in the same manner as the depressurisation steps. Changing the boundary conditions to set the exit flowrate to 0 $m^3\ s^{-1}$ makes the system stiff and difficult to solve. Instead a similar control loop to that described in Figure 4.5 was used but instead the $repress\ rate$ was controlled and was increased if the outlet flowrate was above the set value and was reduced if the outlet flowrate was below the set value. Computationally, zero is difficult to implement and therefore the outlet flowrate is set to two orders of magnitude below the overall feed flowrate. The equations used in the control are provided in Table 4.20.

The number of beds simulated was dependent on the system. For system where there are no interconnections between the beds, only one bed is modelled. All other beds are then assumed to have the same outputs but starting from a different step. Systems where beds are connected require all of the beds in the system to be simulated. The exception to this is for a 6 step system using one equalisation step as the cycles match in such a way that 3 bed pairs are formed which do not interact with other bed pairs. Therefore only one bed pair was simulated.

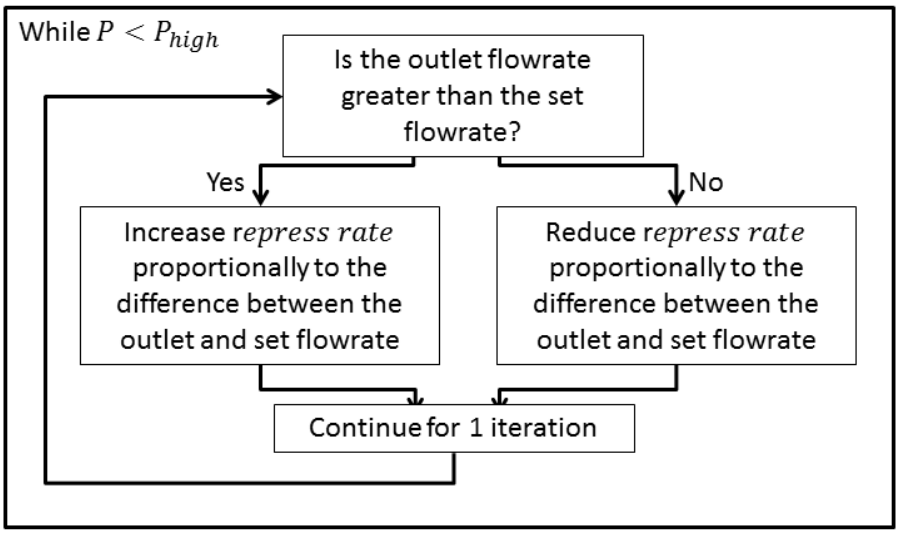

Figure 4.7: While loop for controlling the bed exit flowrate during pressurisation

The solvers used for co-current flow are described in Section 4.10. Some models operated with co-current and counter-current flow, with counter-current operation requiring the ends that the boundary conditions apply to be switched. The forward finite difference method was used for these steps instead of the backward finite difference method to match the change in direction of flow.

4.12.2 Performance Indicators

Table 4.21: Carbon dioxide and nitrogen capture rates and purities

Purities and Capture Rates	$$CO_2\ Purity = \frac{\int_{purge} F_{CO2}^{out} dt + \int_{blow} F_{CO2}^{out} dt}{\int_{purge} (F_{CO2}^{out} + F_{N2}^{out}) dt + \int_{blow} (F_{CO2}^{out} + F_{N2}^{out}) dt}$$	4.68
	$$CO_2\ Capture\ Rate = \frac{\int_{purge} F_{CO2}^{out} dt + \int_{blow} F_{CO2}^{out} dt}{\int_{purge} F_{CO2}^{in} dt + \int_{ads} F_{CO2}^{in} dt + \int_{press} F_{CO2}^{in} dt}$$	4.69
	$$N_2\ Purity = \frac{\int_{ads} F_{N2}^{out} dt}{\int_{ads} (F_{CO2}^{out} + F_{N2}^{out}) dt}$$	4.70
	$$N_2\ Capture\ Rate = \frac{\int_{ads} F_{N2}^{out} dt}{\int_{purge} F_{N2}^{in} dt + \int_{ads} F_{N2}^{in} dt + \int_{press} F_{N2}^{in} dt}$$	4.71

It is necessary to use performance indicators to describe the effectiveness of the separation achieved by the PSA processes evaluated. The gas purities and capture rates were used to establish the viability of a process (Grande, 2012) and the equations to calculate these values are presented in Table 4.21. The gas purity is the volume averaged concentration of the product streams as the nature of PSA means that the outlet concentrations of the gases will not be constant (Yang, 1987) and reflects the quality of the gas produced. It was calculated by Equation 4.68 for carbon dioxide and by Equation 4.70 for nitrogen. In both cases it is the amount of the desired gas collected in the steps which that gas is produced as product divided by the amount of gas produced in those steps. The capture rate is the commonly used term to refer to the percentage of the gas input into the system that is captured, also referred to as recovery in literature. It is the amount of the desired gas collected in the steps which that gas is produced as product divided by the amount of the desired gas that is input into the system. This reflects the efficiency of the process. The carbon dioxide capture rate was calculated using Equation 4.69 and the nitrogen capture rate by Equation 4.71.

The theory presented in this chapter outlines the equations used to describe adsorption processes. The implementation of these equations has been described to show the models built to simulate these processes. The results chapters discuss the suitability of their implementation.

Chapter 5 – Evaluation of Activated Carbon Materials and their Dynamic Capacities

5.1 Introduction

It is necessary to investigate adsorbent materials experimentally in order to obtain the necessary data to design and improve pressure swing adsorption (PSA) processes. These materials need to be investigated under conditions similar to those used on an industrial scale. Adsorbent materials are typically studied under equilibrium conditions using pure gases only. However, since a PSA unit typically applied for industrial separations would not reach full saturation, adsorbent capacity for carbon dioxide under dynamic conditions from gas mixtures needs to be studied. This gives a more realistic estimate of the potential uptake of carbon dioxide and facilitates scale up of the process. The work on this in the literature has been relatively limited for high pressure separations, with few authors attempting to connect the dynamic capacity to the performance of the material. García et al. (2011) and Grande et al. (2013) in separate studies look at the dynamic capacity without evaluating the equilibrium capacity. Several works have studied the dynamic response of the system without actually evaluating the adsorbent capacity (Casas et al., 2012; Lopes et al., 2009; Lopes et al., 2011; Shen et al., 2010). Many studies have looked at the pure component capacity but only a few have evaluated the multicomponent capacities of activated carbons at high pressure (Dreisbach et al., 1999; García et al., 2013; Schell et al., 2012b). Therefore further work is required to evaluate the effectiveness of equilibrium experiments and to suggest the most suitable material for a dynamic separation.

In this work, studies are reported for two adsorbent materials that have been previously investigated in literature (Sun et al., 2013). The two materials are the base unmodified activated carbon and a modified activated carbon which showed the

highest carbon dioxide adsorption capacity under equilibrium conditions by the University of Nottingham. Full characterisation results of the two materials are presented and discussed in this chapter. Investigations are reported of a fixed bed experiment to find the breakthrough response under a range of carbon dioxide feed conditions. The breakthrough capacities are compared to a range of multicomponent models to find which is the most suitable. Finally, PSA cycles are investigated to better understand the dynamic response of the two materials.

5.2 Characterisation of Materials

The characterisation of the adsorbent materials allows the underlying causes that affect their performance to be understood. These parameters are also essential for accurate modelling of adsorbent systems reported in Chapter 5. Measurements of the particle size, BET pore surface area and density indicate the capability of the adsorbents (Gregg and Sing, 1991). Pure component isotherms allow the equilibrium capacity of a material for a specific gas as a function of pressure at constant temperature to be found. This indicates the affinity of different adsorbent materials for certain gases and allows multicomponent capacities to be predicted.

5.2.1 Particle Size

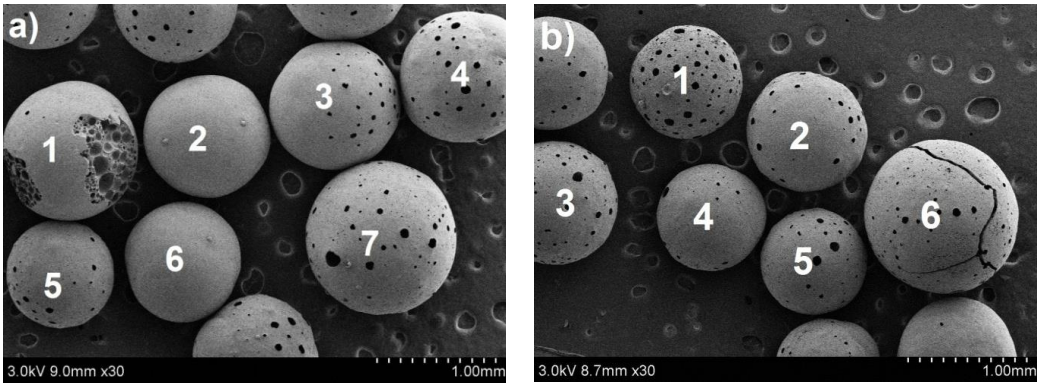

Figure 5.1: SEM images of a) unmodified activated carbon and b) modified activated carbon

Spherical activated carbon beads were selected for characterisation as a material suitable for industrial scale PSA (Sun et al., 2013). Figure 5.1 shows SEM images for both the unmodified and modified activated carbon materials, with the preparation technique described in Section 3.2. The surface of the materials show the pores of the activated carbon and bead 1 in Figure 5.1a shows the heterogeneous pore nature that exists under the surface of the bead. Image processing software ImageJ was used to find the diameter of the particles by comparing them to the scale. The results of the pellet size measurements are given in Table 5.1 for the labelled particles shown in Figure 5.1. The average diameter for the unmodified materials is 1.08 mm with a standard deviation of 0.12 mm and the modified material is 1.01 mm with a standard deviation of 0.15 mm. The small variation in pellet size will ensure consistent and repeatable behaviour.

Table 5.1: Particle sizes for unmodified and modified activated carbon based on Figure 5.1

Activated Carbon		Modified Activated Carbon	
	d_p (mm)		d_p (mm)
1	1.16	1	0.95
2	1.03	2	0.99
3	1.08	3	1.03
4	1.12	4	0.90
5	0.91	5	0.88
6	0.99	6	1.29
7	1.28		
Average	1.08	Average	1.01

5.2.2 BET Surface Measurements

Table 5.2: BET surface measurement results for the unmodified and modified activated carbon material.

	SA_{BET} ($m^2\ g^{-1}$)	V_{total} ($cm^3\ g^{-1}$)	D_{avg} (nm)	SA_{micro}[a] ($m^2\ g^{-1}$)	V_{micro}[a] ($cm^3\ g^{-1}$)
AC	900	0.49	2.19	856	0.36
MAC	1106	0.49	1.76	1052	0.41

[a] Calculated by t-plot method

BET surface measurements allow the structural properties of the unmodified and modified activated carbon to be compared, with analysis of the results reported in Appendix C. Table 5.2 shows that the modified material has a significantly greater pore surface area than the unmodified material as well as a slight increase in the wide microporous volume. Materials with higher pore surface areas have shown to have greater adsorption capacities as the physical adsorption that takes place on activated carbon at high pressures is highly dependent on pore surface area (Drage et al., 2009a; Siriwardane et al., 2001; Sun et al., 2013). Martin et al. (2010) reported that the carbon dioxide uptake at high pressures was directly related to the micropore volume. Both of these indicate that the modified material should have a higher uptake of carbon dioxide. The total pore volume for the materials is very similar and the modified material has a slight reduction in the average pore diameter. The reduction in pore size could increase the mass transfer resistance, discussed in Section 5.4.1, but only if the pore diffusion is the limiting mass transfer case (Farooq and Ruthven, 1990).

5.2.3 Density and Particle Voidage

Drage et al. (2009a) showed that on a mass basis the adsorption capacity for carbon dioxide can be correlated to the pore surface area of the adsorbent but, this is less well defined on a volumetric basis. It is important to study the adsorption capacity on a volumetric basis as the size of the PSA column will be based on the volumetric capacity. The material density, the particle density and the bed density are considered as each indicates different aspects of the fixed bed adsorption process. The bed density for a given mass of adsorbent dictates the size of the bed and should be maximised to reduce the volume of adsorbent required for a separation.

The particle density and material density are inversely related to the particle porosity, but a higher voidage suggests that more pores have been opened for adsorption (Lopes et al., 2009). These two aspects have opposite effects as a more porous material will lead to a lower bed density and therefore a balance must be struck between the porosity of a material and the total bed volume required to hold that material.

Table 5.3: Density and voidage measurements for AC and MAC

		Activated Carbon	Modified Activated Carbon
Material Density	(kg m^{-3})	2040	2068
Particle Density	(kg m^{-3})	500	320
Bed Density	(kg m^{-3})	262	191
Particle Voidage	(-)	0.75	0.85
Bed Voidage	(-)	0.48	0.40
Total Voidage	(-)	0.87	0.91

The material density was found by using a gas displacement pycnometer, as described in Section 3.3.3.2, the particle density was found using a liquid displacement pycnometer, as described in Section 3.3.3.1, and the bed density was calculated by dividing the mass of adsorbent by the volume of the bed. The bed and particle voidages can be calculated from the respective densities. Table 5.3 reports the densities and voidage of the two materials studied here. The difference in particle density, whilst maintaining a similar material density, suggest the beads are more porous for the modified activated carbon, while the material itself remains unchanged. This explains the pore surface area results shown in Table 5.2, where the modified material has a much greater pore surface area than the unmodified

material. However, the larger voidage leads to a significantly lower overall bed density. The modified activated carbon is 37% less dense than the unmodified activated carbon. The capacity of an adsorption bed per unit volume for a given gas is found by multiplying the material capacity on a mass basis by the bed density. This means that for a bed of a fixed volume, the modified material will need a 37% larger capacity in order to for the bed to have the same capacity per unit volume.

5.2.4 Adsorption Isotherms

Pure component isotherm data shows the capacity for a given gas at a set of pressures, while steadily increasing the pressure. The isotherms here were measured using a High Pressure Volumetric Analyser (HPVA), with the experimental procedure given in Section 3.4. It is possible to fit models to this data, which can be used to predict the capacity for the tested gases and applied to multicomponent models. Both the pure component and multicomponent models are described in Section 4.2.

5.2.4.1 Activated Carbon

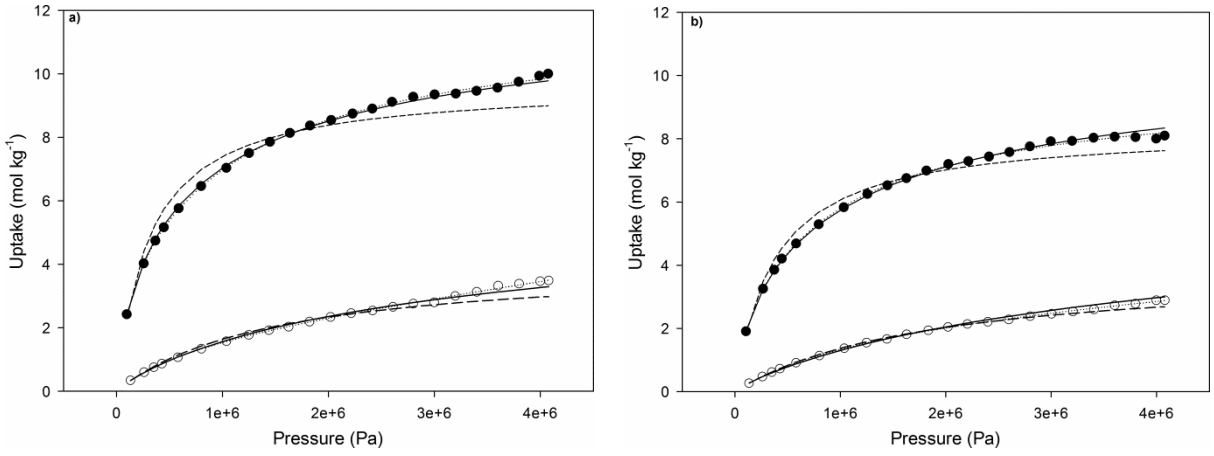

Figure 5.2: Experimental Isotherms for unmodified Activated Carbon for CO_2 (black circles) and N_2 (white circles) at 30°C (a) and 45°C (b) and their corresponding isotherm models: Langmuir (dashed), Langmuir-Freundlich (solid) and Dual-site Langmuir (dotted)

Figure 5.2 shows the high pressure isotherm results for nitrogen and carbon dioxide uptakes for the unmodified activated carbon. The desorption results are not shown as there is only a small amount of hysteresis, in agreement with Sun et al. (2013). For each experimental point, equilibrium was reached at that pressure before the capacity at the next pressure step was measured. For both of sets of data, the Langmuir, Langmuir-Freundlich (LF) and Dual-Site Langmuir (DSL) isotherm models were fitted, with their equations given in Section 4.2. Simpler isotherms such as the linear isotherms expressed by the Henry constant are not considered as the entire range needs to be matched in this work and multicomponent extensions of isotherms require the same pure component model to be used for each gas (Ruthven, 1984). From Figure 5.2 it is clear that there is little difference between the three models for the nitrogen isotherm. This is because the shape of the isotherm is close to linear which can be fitted reasonably well with these isotherm models (García et al., 2013; Park et al., 1998; Schell et al., 2012b). The carbon dioxide isotherm, on the other hand, is much better fitted by the LF and DSL models than the Langmuir model. The Langmuir model, which literature suggests is suitable at low pressures (García et al., 2013; Schell et al., 2012b), shows an over prediction at low pressures and an under prediction at high pressures. The LF model gives much improved agreement across the whole range of pressures, especially the higher pressures used in pre-combustion capture. This is due to the heterogeneous nature of the activated carbon surface and the high number of interactions with carbon dioxide (Schell et al., 2012b). The DSL model also shows much stronger agreement in the high pressure range than the Langmuir isotherm. García et al. (2013) showed similar agreement between the DSL model and a carbon dioxide isotherm on activated carbon, which is

again said to give better agreement to the high pressure region. More complex isotherms such as the Virial isotherm used by Shen et al. (2010) were not used due to the good fit of the LF and DSL isotherms.

Table 5.4: Langmuir-Freundlich isotherm values for unmodified activated carbon for N_2 and CO_2, the isotherm model equations are given in Table 4.1.

Parameter		N_2	CO_2
$B_{i,30°C}$	Pa^{-n}	2.10×10^{-6}	6.13×10^{-5}
$B_{i,45°C}$	Pa^{-n}	1.51×10^{-6}	5.04×10^{-5}
$q_{s,i,30°C}$	mol kg^{-1}	3.89	12.6
$q_{s,i,45°C}$	mol kg^{-1}	4.18	11.3
n_i	-	0.87	0.72
$k_{1,i}$	mol kg^{-1}	18.5	1.18
$k_{2,i}$	J mol^{-1}	3.93×10^{3}	-5.97×10^{3}
$k_{3,i}$	Pa^{-n}	1.86×10^{-9}	9.61×10^{-7}
$k_{4,i}$	J mol^{-1}	-1.77×10^{4}	-1.05×10^{4}

The fitted Langmuir-Freundlich parameters are shown in Table 5.4 for both temperatures of adsorption. By fitting the isotherms at 30°C and 45°C, the temperature dependence of the Langmuir parameter and the saturation capacity can be found. García et al. (2013) kept the saturation capacity fixed for all temperatures, as is commonly assumed for Langmuir models, as this maintains the thermodynamic consistency. However, the LF model is itself not thermodynamically consistent and therefore it is not necessary to keep saturation capacity constant as it is already an empirical model (Do, 1998). It was decided to give the saturation capacity a temperature dependence as it gives a better fit across all of the data, with a sum of the squared errors (SSE) of 6.35% for a constant saturation capacity and 1.82% for a temperature dependent saturation capacity. The Langmuir parameter and the saturation capacity were fitted to an Arrhenius type relationship, as is commonly

done (Ahn et al., 1999; Do, 1998; García et al., 2013; Park et al., 1998; Schell et al., 2012b), with the resultant parameters shown in Table 5.4. In previous work the exponent has also been given a temperature dependence (Park et al., 1998; Schell et al., 2012b). However, including a temperature dependence does not significantly improve the fit and so, in the model, the exponent is kept constant.

There is reasonable agreement to literature values for both gases, with García et al. (2013), Park et al. (1998) and Schell et al. (2012b) all applying the LF isotherm to adsorption on activated carbons. The saturation capacity in literature for carbon dioxide at 30°C ranged from 10.1-11.5 mol kg^{-1} and for nitrogen at 30°C ranges from 5.6-6.6 mol kg^{-1}. The Langmuir constant for carbon dioxide and nitrogen at 30°C ranged from 1.0×10^{-6} - 1.0×10^{-5} Pa^{-1} and 3.5×10^{-8} - 4.9×10^{-7} Pa^{-1} respectively. The range for the exponent is large, for carbon dioxide at 30°C being 0.74 – 0.95 and for nitrogen at 30°C being 0.86 – 0.92. The differences between the literature and this work can be attributed to variation in the activated carbons studied.

The parameters for the DSL model are given in Table 5. The temperature independence of these parameters was found by comparing the isotherms at different temperatures and fitted to an Arrhenius type relationship. Despite the DSL model itself being thermodynamically rigorous, allowing the saturation capacity to vary with temperature improves the sum of the squared errors (SSE) from 3.25% down to 1.35%. As the LF model is not thermodynamically consistent and is the main point of comparison, it is not necessary to maintain the rigour of the DSL model. This has been suggested for the DSL isotherm by Agarwal et al. (2010) and for the Langmuir isotherm in several studies (Chou and Chen, 2004; Chue et al., 1995; Nikolic et al., 2008; Park et al., 2000; Schell et al., 2012b). García et al. (2013),

Ritter et al. (2011) and Agarwal et al. (2010) applied the DSL isotherm to carbon dioxide adsorption on activated carbons and found saturation capacities and Langmuir constants of the same order of magnitude as the results in Table 5.5.

Table 5.5: Dual-Site Langmuir isotherm values for the unmodified activated carbon for N_2 and CO_2, the isotherm model equations are given in Table 4.1.

Parameter		N_2		CO_2	
		30°C	45°C	30°C	45°C
$B_{1,i}$	Pa^{-1}	1.32×10^{-6}	7.31×10^{-7}	1.14×10^{-5}	1.07×10^{-5}
$B_{2,i}$	Pa^{-1}	3.08×10^{-9}	4.16×10^{-9}	8.32×10^{-7}	1.01×10^{-6}
$q_{1,s,i}$	mol kg^{-1}	1.86	2.63	3.44	2.27
$q_{2,s,i}$	mol kg^{-1}	156	54.4	8.41	7.43
$k_{1,1,i}$	mol kg^{-1}	3000		5.27×10^{-4}	
$k_{1,2,i}$	J mol^{-1}	-18600		22100	
$k_{1,3,i}$	Pa^{-1}	4.96×10^{-12}		3.25×10^{-6}	
$k_{1,4,i}$	J mol^{-1}	31463		3150	
$k_{2,1,i}$	mol kg^{-1}	3.15×10^{-8}		0.61	
$k_{2,2,i}$	J mol^{-1}	31463		6610	
$k_{2,3,i}$	Pa^{-1}	1.86×10^{-6}		4.71×10^{-5}	
$k_{2,4,i}$	J mol^{-1}	-16100		-10200	

The values for nitrogen in this study, on the other hand, are quite different to literature values with the saturation capacity on one site being considerably higher than the other. García et al. (2013) apply the DSL model to a nitrogen isotherm on activated carbon and calculate values for the saturation capacity on each site to be the same order of magnitude. Ritter et al. (2011) list values for a large number of materials for different gases, although not nitrogen, and do not find any material gives a saturation capacity greater than 5.11 mol kg^{-1}. These large saturation values compared to those found in literature suggest that they do not have a theoretical basis and that the application of the DSL model to this material for nitrogen is highly

empirical. This is used as the aim of this work is to produce the best fit and the accurate prediction of the capacity is required for the simulation studies in Chapter 6.

5.2.4.2 Modified Activated Carbon

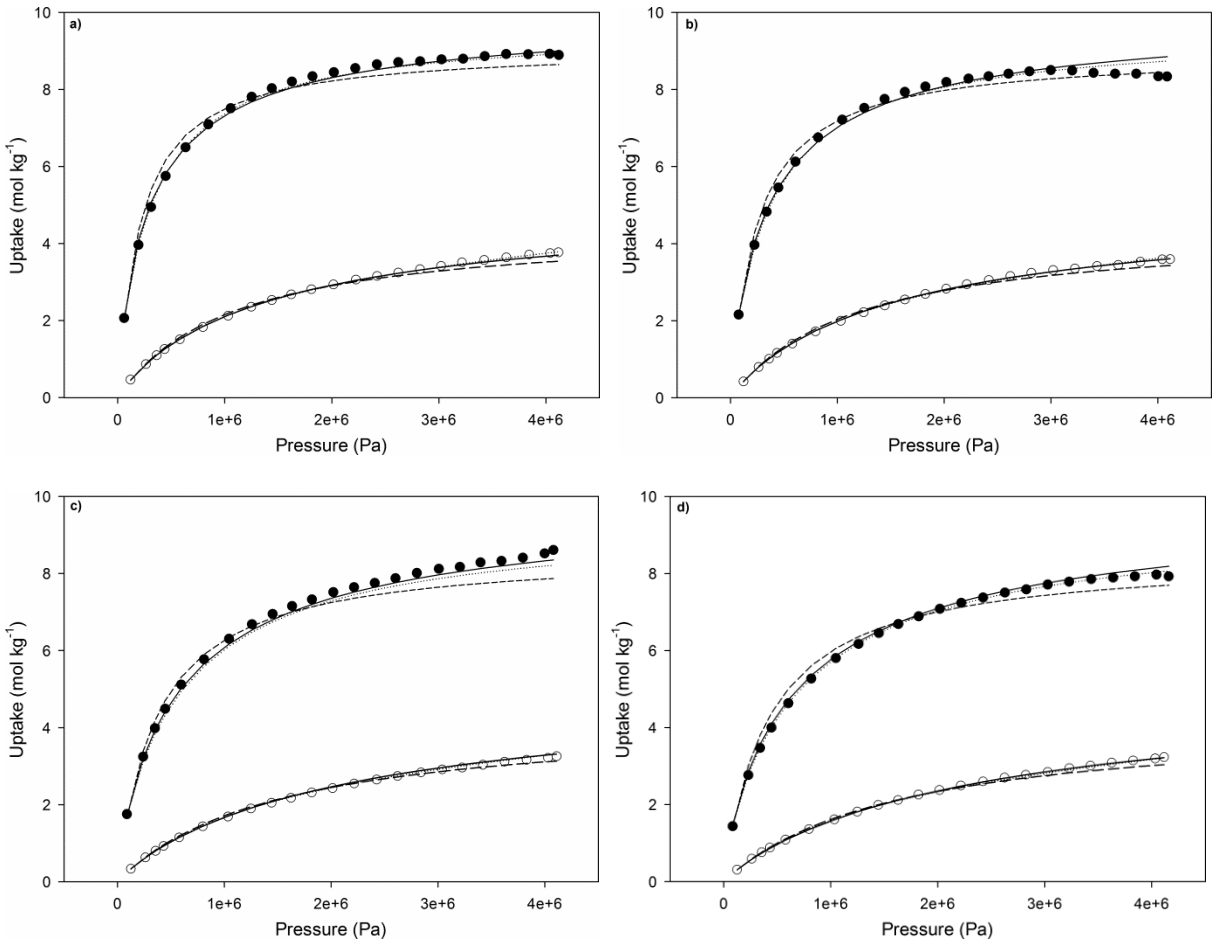

Figure 5.3: Experimental Isotherms for modified Activated Carbon for CO_2 (black circles) and N_2 (white circles) at 25°C (a), 30°C (b) 45°C (c) and 50°C (b) and their corresponding isotherm models: Langmuir (dashed), Langmuir-Freundlich (solid) and Dual-site Langmuir (dotted line).

The isotherm results for the modified activated carbon are shown in Figure 5.3, where isotherms were measured at temperatures of 25°C, 30°C, 45°C and 50°C, and compared to the Langmuir, LF and DSL models. The isotherm models shown are based on the predicted values for saturation capacities and Langmuir parameters given by temperature independent parameters in Table 5.6, Table 5.7 and Table 5.8

respectively. Similar trends are seen for the modified material as the unmodified material. The nitrogen isotherm is well matched by all three models used. The carbon dioxide isotherm is much better described by the LF and DSL models, with the Langmuir model showing the same over prediction at low pressures and under prediction at high pressures.

It is possible to compare the isotherms at 30°C and 45°C of the unmodified and modified activated carbons. At 30°C the unmodified material, Figure 5.2a, actually shows higher maximum adsorption capacity than the modified material, Figure 5.3b, with the highest values being 10.0 mol kg^{-1} and 8.5 mol kg^{-1} respectively. The maximum values at 45°C show the reverse trend with the unmodified material, Figure 5.2b, having a maximum of 8.1 mol kg^{-1} and the modified material, Figure 5.3c, a maximum of 8.6 mol kg^{-1}. Based on the pore surface area results the modified material would be expected to have a greater capacity for carbon dioxide, as seen with the measurements at 45°C. The modified material has maximum capacities under the conditions studied of 8.92 mol kg^{-1} at 25°C, 8.56 mol kg^{-1} at 30°C, 8.61 mol kg^{-1} at 45°C and 7.97 mol kg^{-1} at 50°C, suggesting that there is a much more limited temperature dependence compared to the unmodified material and that the saturation capacity is close to being achieved at 4 MPa for all temperatures. The unmodified material on the other hand sees greater difference between the maximum value at 30°C and at 45°C, suggesting that temperature has a greater effect on the capacity and that the saturation capacity has not been reached at 4 MPa at higher temperatures. This could indicate that the modified material does not have a significant increase at pressure higher than those studied here and future work is required to study this.

Table 5.6: Langmuir-Freundlich isotherm values for modified activated carbon for N_2 and CO_2

Parameter		N_2	CO_2
$B_{i,25°C}$	Pa^{-n}	1.96×10^{-6}	2.56×10^{-5}
$B_{i,30°C}$	Pa^{-n}	1.73×10^{-6}	2.26×10^{-5}
$B_{i,45°C}$	Pa^{-n}	1.35×10^{-6}	1.51×10^{-5}
$B_{i,50°C}$	Pa^{-n}	1.18×10^{-6}	1.27×10^{-5}
$q_{s,i,25°C}$	mol kg^{-1}	5.14	10.1
$q_{s,i,30°C}$	mol kg^{-1}	5.20	9.92
$q_{s,i,45°C}$	mol kg^{-1}	5.07	10.1
$q_{s,i,50°C}$	mol kg^{-1}	5.37	9.94
n_i	-	0.93	0.84
$k_{1,i}$	mol kg^{-1}	6.73	10.06
$k_{2,i}$	J mol^{-1}	670	13.5
$k_{3,i}$	Pa^{-n}	3.89×10^{-9}	3.22×10^{-9}
$k_{4,i}$	J mol^{-1}	-15400	-22300

The LF isotherm parameters are given in Table 5.6. The saturation capacities found are almost constant at the various temperatures which is in agreement with García et al. (2013) using a constant value at all temperatures. In order to be consistent with the unmodified material, a temperature dependence is maintained despite the effect being minimal for the modified activated carbon. Table 5.7 gives the parameters for the DSL model for nitrogen upon the modified activated carbon, with similar trends to the unmodified material observed. The nitrogen parameters include a predicted saturation capacity that is significantly larger than values typically found in literature, discussed in Section 5.2.4.1, but, as with the unmodified material, these values give the best fit to the isotherm data. The carbon dioxide parameters are given in Table 5.8, where the saturation capacities are more consistent with the literature values discussed in Section 5.2.4.1. Each half the DSL isotherm refers to a particular adsorption site. The saturation capacity for site 2 is considerably higher than that of

site 1, as has been previously seen for activated carbons (García et al., 2013), suggesting that the majority of adsorption is taking place on this site.

Table 5.7: Dual-site Langmuir isotherm values for modified activated carbon for N_2

Parameter		N_2			
		25°C	25°C	45°C	50°C
$B_{1,i}$	Pa^{-1}	1.06×10^{-6}	9.80×10^{-7}	7.85×10^{-7}	7.32×10^{-7}
$B_{2,i}$	Pa^{-1}	1.04×10^{-9}	1.35×10^{-9}	2.76×10^{-9}	3.45×10^{-9}
$q_{1,s,i}$	mol kg^{-1}	3.74	3.66	3.42	3.35
$q_{2,s,i}$	mol kg^{-1}	172	132	62.2	49.2
$k_{1,1,i}$	mol kg^{-1}	0.90			
$k_{1,2,i}$	J mol^{-1}	3523			
$k_{1,3,i}$	Pa^{-1}	8.91×10^{-9}			
$k_{1,4,i}$	J mol^{-1}	11838			
$k_{2,1,i}$	mol kg^{-1}	1.59×10^{-5}			
$k_{2,2,i}$	J mol^{-1}	40100			
$k_{2,3,i}$	Pa^{-1}	5.51×10^{-3}			
$k_{2,4,i}$	J mol^{-1}	-38358			

Table 5.8: Dual-site Langmuir isotherm values for modified activated carbon for CO_2

Parameter		CO_2			
		25°C	30°C	45°C	50°C
$B_{1,i}$	Pa^{-1}	1.17×10^{-4}	7.16×10^{-5}	1.80×10^{-5}	1.17×10^{-5}
$B_{2,i}$	Pa^{-1}	3.00×10^{-6}	2.48×10^{-6}	1.47×10^{-6}	1.24×10^{-6}
$q_{1,s,i}$	mol kg^{-1}	0.81	0.91	1.24	1.37
$q_{2,s,i}$	mol kg^{-1}	8.77	8.61	8.16	8.02
$k_{1,1,i}$	mol kg^{-1}	737			
$k_{1,2,i}$	J mol^{-1}	-16900			
$k_{1,3,i}$	Pa^{-1}	1.43×10^{-17}			
$k_{1,4,i}$	J mol^{-1}	73700			
$k_{2,1,i}$	mol kg^{-1}	2.78			
$k_{2,2,i}$	J mol^{-1}	2850			
$k_{2,3,i}$	Pa^{-1}	3.46×10^{-11}			
$k_{2,4,i}$	J mol^{-1}	28200			

5.2.5 Heat of Adsorption

The heat of adsorption can be found using the Clausius-Clapeyron relationship, as described in Section 4.3. The values are based on the predicted capacity from the pure component data at each temperature using the LF model. As the Clausius-Clapeyron relationship is only applicable to regions where there is an ideal bulk gas phase and a negligible adsorbed phase volume (Pan et al., 1998), the range of capacities from which the heat of adsorption can be calculated is up to 4 mol kg^{-1} for carbon dioxide and 2 mol kg^{-1} for nitrogen where the heat of adsorption remains linear for each gas (Gao et al., 2004; Grande et al., 2013; Schell et al., 2012b). The heats of adsorption at different adsorbed amounts for carbon dioxide are shown in Figure 5.4a and for nitrogen in Figure 5.4b. The gradient of the plots is influenced by the changing saturation capacity with temperature for the unmodified material, with a decrease in saturation capacity at higher temperatures resulting in an increase in heat capacity with higher adsorbed amounts and vice versa (Do, 1998). The average values for the carbon dioxide heat of adsorption are 24.7 kJ mol^{-1} and 26.6 kJ mol^{-1} for the unmodified and modified activated carbons respectively and for nitrogen are 14.9 kJ mol^{-1} and 15.7 kJ mol^{-1}. These values are in agreement with literature for activated carbons which range from 21-30 kJ mol^{-1} for carbon dioxide and 10-17.5 kJ mol^{-1} for nitrogen (Agarwal et al., 2010; Chue et al., 1995; Dantas et al., 2011; Grande et al., 2013; Himeno et al., 2005; Lopes et al., 2011; Salem et al., 1998; Schell et al., 2012b; Shen et al., 2010).

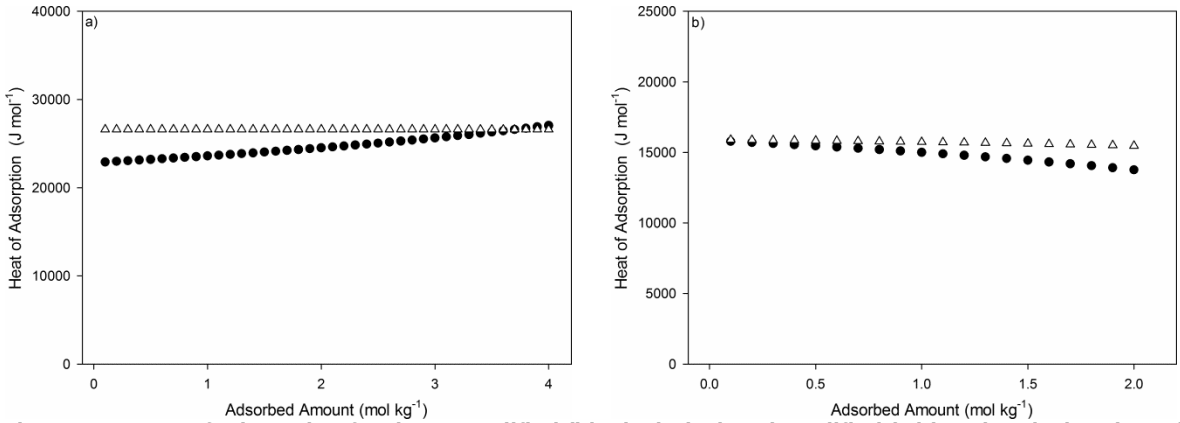

Figure 5.4: Heat of adsorption for the unmodified (black circles) and modified (white triangles) activated carbons for a) CO_2 and b) N_2

5.3 Breakthrough Rig Calibration

Breakthrough experiments characterise the dynamic response of a given system to a mixture of carbon dioxide and a less adsorbed gas (i.e. nitrogen or hydrogen), a full experimental description is given in Section 3.6. The CO_2 analyser at the end of the bed records the fraction of carbon dioxide in the outlet stream. Breakthrough curves are produced by plotting the output of the CO_2 analyser against time. The curves are recorded from when a flow of carbon dioxide is introduced and mixed with a less adsorbed component.

It is first necessary to find the dynamic response of the system that surrounds the fixed bed before it is possible to evaluate the separation that takes place. In order to gain a full understanding of the system, the response of the CO_2 analyser was found followed by the response of the system without the bed, i.e. the bed removed and the surrounding pipes connected directly. The system itself will have a certain residence time and breakthrough which can be recorded by the CO_2 analyser. It is necessary to find the capacity for carbon dioxide in the system in order to accurately find the dynamic capacity of the material in the fixed bed without the effects of the

surrounding system. The breakthrough curves without the bed installed are used to correct the adsorption results as it is difficult to accurately measure the volume of the surrounding system due to the pipe fittings and valves.

5.3.1 CO_2 Analyser Response

A full description of the method used to find the response of the CO_2 analyser is given in Section 3.6.1. The experiments were conducted at atmospheric pressure, 298K and a total flowrate of 200 Nml min^{-1}. Runs were performed using CO_2/N_2 mixtures with carbon dioxide molar feed fractions of 0.1, 0.2, 0.3, 0.4 and 0.5 in order to evaluate the full range of responses for the analyser. The experiments found the response of the CO_2 analyser for when a gas mixture is introduced to the CO_2 analyser feed pipe and the CO_2 analyser, as shown in Figure 3.2.

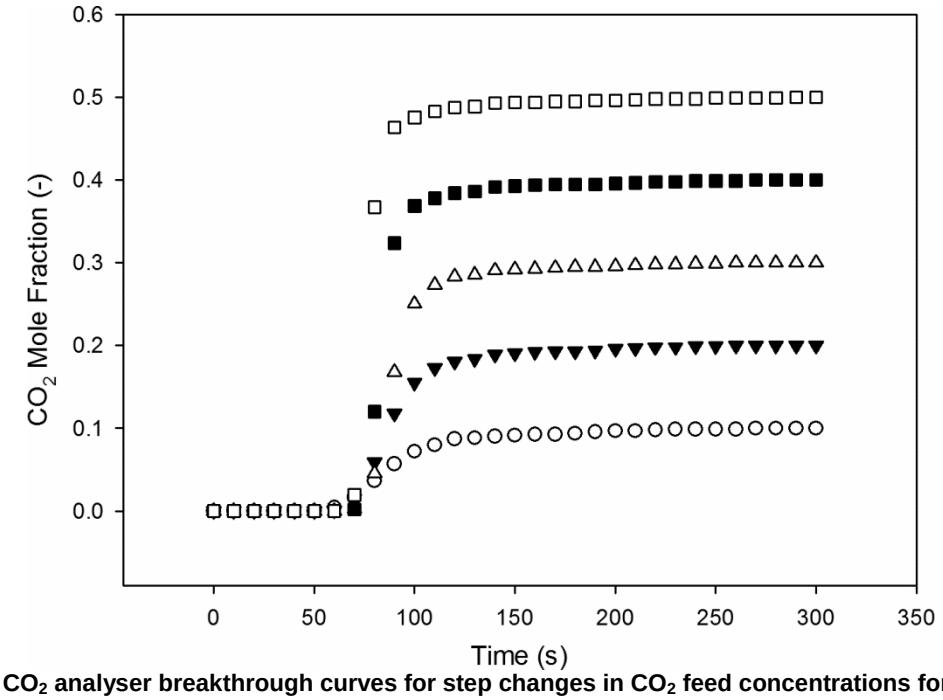

Figure 5.5: CO_2 analyser breakthrough curves for step changes in CO_2 feed concentrations for CO_2/N_2 mixtures at CO_2 feed fractions of 0.1 (white circles), 0.2 (black triangles), 0.3 (white triangles), 0.4 (black sqaures) and 0.5 (white squares).

Figure 5.5 shows the breakthrough curves for the response of the CO_2 analyser to a step change in carbon dioxide for all feed fractions tested. The time for the response of any step change is consistent across the range of carbon dioxide concentrations tested. The response times at different fractions of the inlet CO_2 fraction for the breakthrough are given in Table 5.9. The initial breakthrough is relatively consistent, as are the times for complete breakthrough. The manufacturer gives a t_{90} response of 75 seconds, which is lower than all responses found here. There is good agreement across the range of mole fractions for the initial breakthrough time, t_5, and the time to reach complete saturation, t_{100}, suggesting that the analyser responds in the same way at all concentrations. The time taken from breakthrough to reach complete saturation is considerably longer than the initial breakthrough time, with the majority of this being in the last 0.01 mole fraction of the absolute reading as seen in the final column in Table 5.9. Therefore, it is important that this delay for the final aspects of the carbon dioxide concentration is attributed to the response of the measurement device.

Table 5.9: Response times for the CO_2 analyser at various feed concentrations given at percentages of the feed concentration

CO_2 Feed Fraction	Response Time			
	t_5 (s)	t_{90} (s)	t_{100} (s)	$t_{0.01,mf}$ (s)
0.1	62	139	264	139
0.2	68	119	259	150
0.3	76	107	259	134
0.4	75	97	267	140
0.5	71	87	280	136

5.3.2 System Characterisation

Breakthrough curves were produced for an experimental set up with the fixed bed removed and the inlet and outlet pipes connected directly, as shown in Figure 3.7. A

full description of the experimental procedure is given in Section 3.7.2. The experiment was performed for both CO_2/N_2 mixtures and CO_2/H_2 mixtures to find the carbon dioxide captured by the system for both gas mixtures. All experiments were conducted at 2.5 MPa, 298K and a total flowrate of 200 Nml min^{-1}.

5.3.2.1 CO_2/N_2 System Response

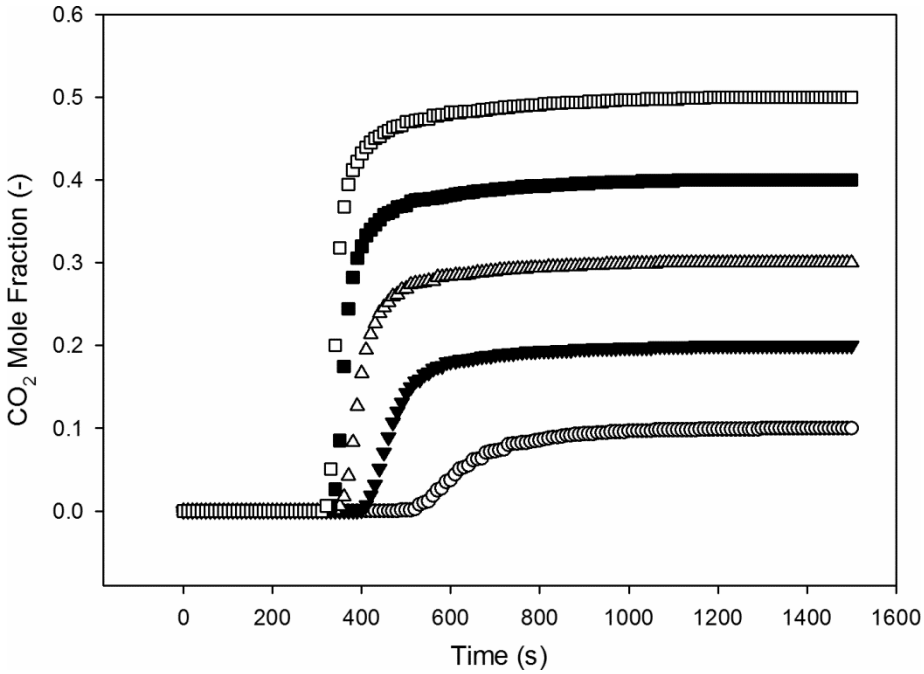

Figure 5.6: Breakthrough curves for a system without a bed when step changes in CO_2 feed concentrations for CO_2/N_2 mixtures are introduced at CO_2 feed fractions of 0.1 (white circles), 0.2 (black triangles), 0.3 (white triangles), 0.4 (black sqaures) and 0.5 (white squares).

The breakthrough curves for the system without the packed bed and the pipe connections linked directly are shown in Figure 5.6 and the corresponding response times are shown in Table 5.10 for a CO_2/N_2 mixture. The system does not respond as a perfect plug flow system with the same breakthrough time for all feed fractions of carbon dioxide. This is caused by dispersion in a section of pipe between the mass flow controller regulating the flow of carbon dioxide and the junction where the

nitrogen and carbon dioxide mix. The residence time for the carbon dioxide in this pipe varies for each run as the overall flowrate is kept constant, meaning the carbon dioxide flowrate is varied to achieve this. The system shows a similar trend to the CO_2 analyser result, with considerably longer times between the $t_{50} \rightarrow t_{100}$ than for the $t_5 \rightarrow t_{50}$. This will be partly due to the response of the analyser, discussed in Section 5.3.1, but will also be due to some dispersion in the general system leading to a spreading of the breakthrough curve. The amount of carbon dioxide that remains in the system for each feed fraction is also given in Table 5.10. It can be seen that there is a constant increase of 5.1×10^{-3} mol for each increase of 0.1 in feed mole fraction. The carbon dioxide in the pipe between the CO_2 control valve and the mixing junction is given by the intercept of a straight line plot, shown in Appendix I, between the amount of carbon dioxide accumulated and the CO_2 feed fraction, with a value of 4.7×10^{-3} mol. The total value for carbon dioxide accumulated in the system, as given in Table 5.10, can be subtracted from the total capacity found for the fixed bed adsorption systems to give the amount of carbon dioxide captured by the fixed bed.

Table 5.10: Response times for the system without a bed at various feed concentrations of a CO_2/N_2 given at percentages of the feed concentration

CO_2 Feed Fraction	Response Time			CO_2 Captured (mol)
	t_5 (s)	t_{50} (s)	t_{100} (s)	
0.1	530	619	1300	1.00×10^{-2}
0.2	414	467	1148	1.52×10^{-2}
0.3	358	396	1066	1.99×10^{-2}
0.4	338	364	1108	2.51×10^{-2}
0.5	327	344	1173	3.09×10^{-2}

5.3.2.2 CO_2/H_2 System Response

The breakthrough results for a CO_2/H_2 mixture passed through a system without a bed are shown in Figure 5.7. The breakthrough times and accumulated carbon dioxide in the surrounding pipes and valves are given in Table 5.11, showing very similar results to those given by CO_2/N_2 mixtures. Based on the capacity results, the system without a bed shows an increase in accumulated carbon dioxide of 4.4×10^{-3} mol for each carbon dioxide feed fraction increase of 0.1. The amount of carbon dioxide accumulated in the pipe leading to the mixing junction was 5.6×10^{-3} mol, based on the plot of the CO_2 feed fraction versus the accumulated carbon dioxide as done for the CO_2/N_2 mixture. These values for the accumulated carbon dioxide in the surrounding pipes and fittings for the fixed bed measurements using CO_2/H_2 mixtures can be subtracted from the readings with the bed installed, so that the carbon dioxide capacity for the breakthrough experiments with the bed included will be more accurate.

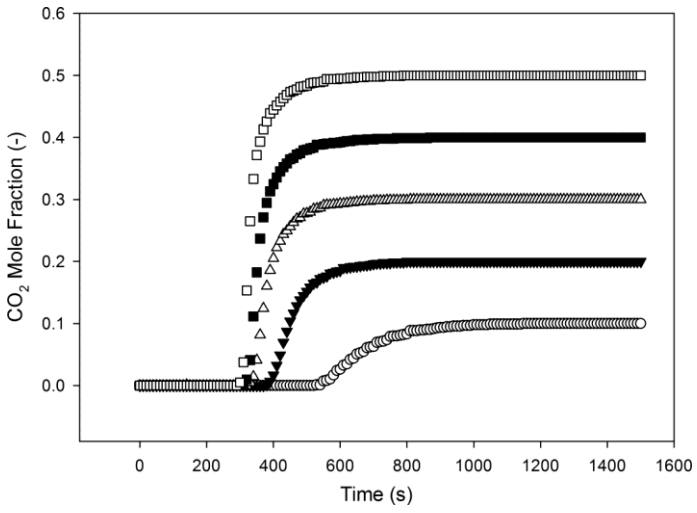

Figure 5.7: Breakthrough curves for a system without a bed when step changes in CO_2 feed concentrations for CO_2/H_2 mixtures are introduced at CO_2 feed fractions of 0.1 (white circles), 0.2 (black triangles), 0.3 (white triangles), 0.4 (black sqaures) and 0.5 (white squares).

Table 5.11: Response times for the system without a bed at various feed concentrations of a CO_2/H_2 mixture given at percentages of the feed concentration

CO_2 Feed Fraction	Response Time				CO_2 Captured (mol)
	t_5 (s)	t_{50} (s)	t_{90} (s)	t_{100} (s)	
0.1	549	648	855	1150	1.02×10^{-2}
0.2	393	448	562	797	1.43×10^{-2}
0.3	341	377	480	803	1.84×10^{-2}
0.4	325	353	447	867	2.35×10^{-2}
0.5	308	328	407	785	2.78×10^{-2}

5.4 Activated Carbon Breakthrough Experiments

Breakthrough curves for separation of CO_2/N_2 mixtures using unmodified activated carbon were conducted as described in Section 3.7.2. The experimental conditions are given in Table 5.12.

Table 5.12: Experimental conditions for separations using the unmodified activated carbon

Bed Length	m	0.069
Bed Diameter	m	0.025
Adsorption Pressure	MPa	2.5
Temperature	K	298
Feed Flowrate	Nml min^{-1}	200
Adsorbent Mass	g	8.88

5.4.1 Experimental Breakthrough Curves

Figure 5.8 shows the response of the CO_2 analyser to a step change in carbon dioxide in the feed stream for the whole experimental set-up to give the carbon dioxide breakthrough curves at varying carbon dioxide feed mole fractions for the unmodified activated carbon. As the response of the system without a bed is not a simple time delay, as shown in Section 5.3.2, it is not possible to remove the effect on the breakthrough curve. This is instead evaluated in the adsorption capacity see Section 5.4.2. The results are shown at 100 s intervals so as to distinguish the

individual points. The breakthrough time is found by taking the time at which the outlet CO_2 fraction reaches 5% of the inlet CO_2 fraction. As the feed mole fraction increases, a proportional drop in breakthrough time would be expected if the capacity was constant. However, the breakthrough times do not decrease proportionally with the increase in carbon dioxide concentration, showing higher adsorption capacities at higher CO_2 feed fractions. This is consistent with the isotherm data where at higher pressures of carbon dioxide a larger amount of carbon dioxide is adsorbed.

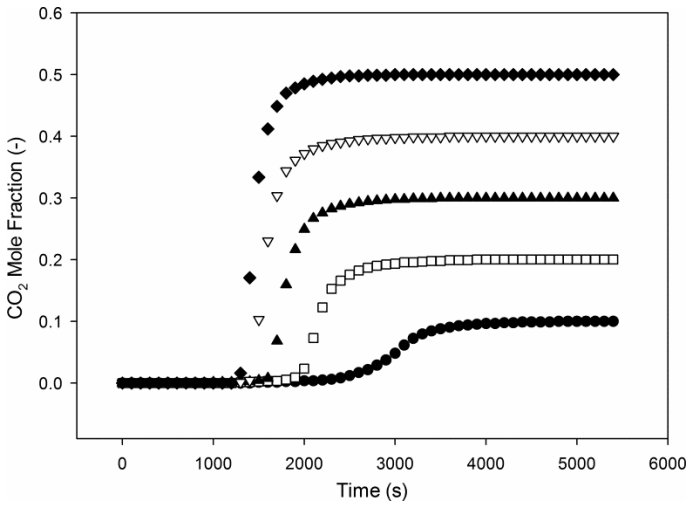

Figure 5.8: Breakthrough curves for the separation of a CO_2/N_2 mixture using unmodified activated carbon at CO_2 feed fractions of 0.1 (black circles), 0.2 (white squares), 0.3 (black triangles), 0.4 (white triangles) and 0.5 (black diamonds)

The shape of the breakthrough curve gives strong indications of the dispersion characteristics and mass transfer limitations of the system. Systems with large dispersion or mass transfer resistances have long shallow breakthrough curves (Ruthven, 1984). Garg and Ruthven (1975) suggest the effect both the mass transfer coefficient and the dispersion coefficient is additive but there is no way to attribute the cause of the steepness of the breakthrough curve to one effect or the other. The steepness of the curves in Figure 5.8 indicates that this effect is relatively small in the

work reported here, i.e. neither coefficient is significantly affecting the breakthrough curve. The breakthrough for a CO_2 feed fraction of 0.1 displays the greatest amount of spreading. This is to be expected as the residence time is the longest. The error on this reading will also be the highest and the mole fraction recorded by the CO_2 analyser has an absolute error of ± 0.01, leading to a 10% error on the 0.1 run. It is suggested by Garcia et al. (2011) that higher pressures lead to greater spreading due to higher degrees of dispersion, but it is not clear if this is attributed to higher absolute pressures or carbon dioxide partial pressures. This work shows that higher partial pressures with a fixed absolute pressure give less mass transfer and dispersion limitations.

Table 5.13: The overall mass transfer coefficient as well as the contribution of each mass transfer resistance for a system with a CO_2 feed fraction of 0.4

		CO_2	N_2
Overall Mass Transfer Coefficient	s^{-1}	0.099	0.815
Film Mass Transfer	s^{-1}	0.67	8.60
Pore Mass Transfer	s^{-1}	0.43	5.47
Micropore Mass Transfer	s^{-1}	0.16	1.08

It is possible to quantify the dispersion and mass transfer effects by using correlations that are given in Section 4.7. The Hsu and Haynes (1981) correlation is shown in Section 6.3.2.2 to be the most suitable for the experiments here and this predicts a dispersion coefficient of 1.5×10^{-6} m^2 s^{-1}. The mass transfer correlation suggested by Farooq and Ruthven (1990) combines all three mass transfer modes without the need for individual equations for each mass transfer mode and is used in the simulation of the breakthrough curves in Section 6.3.2. It is possible to calculate the degree to which each mass transfer resistance affects the overall mass transfer

resistance by calculating the individual parts of Equation 4.39, the results are presented in Table 5.13. These results show that all three resistances impact the overall mass transfer but the micropore resistance is the most significant. This disagrees with Farooq and Ruthven (1990), who find the micropore resistance negligible, although this was found for zeolite 5A. Shen et al. (2010) show that micropore resistance for activated carbon using carbon dioxide and nitrogen controls the diffusion mechanism, which agrees with the micropore mass transfer resistance being the most significant. The total mass transfer coefficient agrees with the experimental results found by Casas et al. (2012), who found a carbon dioxide and hydrogen mass transfer coefficient of 0.15 s^{-1} and 1.0 s^{-1} respectively. The values for the dispersion and mass transfer coefficients confirm that the system is not significantly affected by either effect leading to the steep breakthrough curves shown in Figure 5.8.

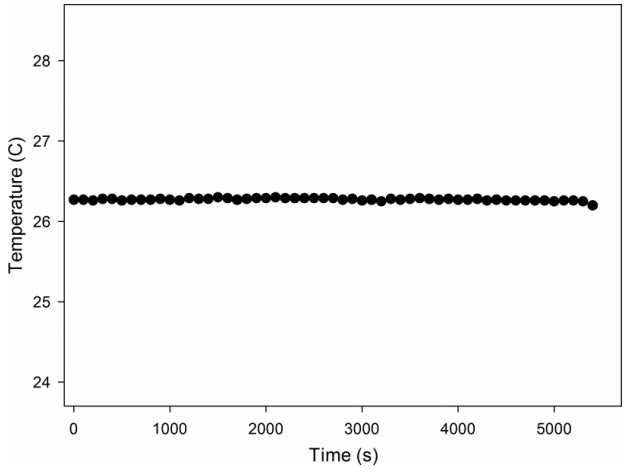

Figure 5.9: Temperature profile for the separation using a CO_2 feed fraction of 0.1

Figure 5.9 shows the experimentally measured temperature at the bed exit for the adsorption at a CO_2 feed fraction of 0.1, with similar temperature profiles (not shown)

for all other CO_2 feed fractions. It should be noted that due to the Swagelok fittings required the thermocouple was located slightly downstream of the bed and any possible rise in temperature in the bed might not have been detected due to the cooling of gas as it flowed out of the bed. It is clear from Figure 9 that there is no significant detectable temperature change at the bed exit which differs from literature, with Casas et al. (2012) reporting increases of up to 40°C. The breakthrough curve itself suggests that there is an internal temperature change. A temperature increase in the bed would not reduce the overall capacity as the adsorbent capacity would increase as the bed cools, instead a broadening of the breakthrough curve would be observed (Ruthven et al., 1975). The curves in Figure 5.8 are asymmetric, with the second part of each of the curves much broader than the initial, similar to the results seen by Lopes et al. (2009) and by Casas et al. (2012). The temperature front often moves at a different velocity to the mass transfer front leading to an asymmetric breakthrough curve, suggesting there is a temperature change taking place and the broader top half of the curve indicates a lagging temperature profile (Ruthven et al., 1975). The steepness of the breakthrough curves and absence of temperature change at the bed exit suggests that any temperature changes are being dissipated very quickly. The distance between the temperature probe and the bed exit would give further chance for the gas to cool. The work by Ruthven et al. (1975) show theoretically that the steepness of the breakthrough curve is associated with the heat transfer rates out of the bed, with high heat transfer values leading to steep breakthrough curves as observed in Figure 5.8. A high heat transfer coefficient would be consistent with there being no significant temperature change detected at the bed exit. These two factors suggest that there is most likely an internal

temperature change in the bed but that the heat is rapidly dissipated before the gas reaches the temperature probe.

5.4.2 Breakthrough CO_2 Capacity

The dynamic capacity of the bed is considered based on the breakthrough capacity rather than the total saturation capacity. A PSA system would not be run until complete saturation of the bed and therefore a breakthrough capacity is a more realistic prediction of the working capacity of a process unit. This is found by assuming that all carbon dioxide input to the system up until the breakthrough time is captured by the system. The system capacities found for the experimental setup without a bed, given in Table 5.10, were subtracted to give the capacity of the bed only. The carbon dioxide that occupies the void space in the bed is also deducted to give the amount of carbon dioxide that is in the adsorbed phase. The average capacity over three cycles is given for each feed fraction in Table 5.14. The capacity found by the experimental set up would be expected to be higher than that of a PSA unit as the bed is fully cleaned between each run. The results show that the increase in breakthrough capacity is larger between lower feed fractions than the highest feed fractions. This is in agreement with the isotherm data, shown in Figure 5.2, where an increase in pressure at lower values has a greater increase in capacity than it does at higher pressures. Table 5.14 also gives the predicted values for the carbon dioxide capacity for pure component data at the equivalent partial pressure. The isotherm gives a value for equilibrium conditions and it is also for pure component data, i.e. assuming that the nitrogen in the mixture does not interact or compete with carbon dioxide. Both of these factors explain the large disparity between the values. The greater difference between the breakthrough capacity and the predicted isotherm

value for a feed fraction of 0.1 further emphasises the larger degree of spreading in the breakthrough curve at the lower feed fractions, and the further the system from equilibrium. The almost constant difference for all other values suggests the mass transfer front is well established for all those runs.

It is important to find an isotherm model which can accurately represent the experimental data. The large difference between the isotherm models and the breakthrough data suggest that the presence of nitrogen has a significant impact on the carbon dioxide capacity and models capable of replicating this are required. It is easier to produce pure component isotherm data rather than multicomponent data. As discussed in Section 4.2, there are several models that use pure component data to predict multicomponent adsorption capacities. Due to the strong agreement for the pure component isotherms shown in Section 5.2.4.1, the multicomponent Langmuir-Freundlich (LF) model and multicomponent dual site Langmuir (DSL) model were used to predict the carbon dioxide capacity. For each of these models, the Ideal Adsorbed Solution Theory (IAST) was also applied to their corresponding pure component results, with the theory behind this discussed in Section 4.2.2.

Table 5.14: The breakthrough capacities of CO_2/N_2 mixtures separated using unmodified activated carbon for each experimental run and the predicted capacity for pure components based on the LF and DSL models

CO_2 Feed Fraction (-)	Breakthrough Capacity (mol kg^{-1})	LF Model (mol kg^{-1})	DSL Model (mol kg^{-1})
0.1	2.12 ± 0.14	4.38	4.43
0.2	4.05 ± 0.15	5.93	5.94
0.3	5.01 ± 0.08	6.88	6.86
0.4	5.54 ± 0.17	7.55	7.51
0.5	6.09 ± 0.06	8.06	8.02

Table 5.15 compares the predicted capacity for both carbon dioxide and nitrogen by the multicomponent LF, the IAST LF, the multicomponent DSL and the IAST DSL. It can be seen that the various models differ in their prediction of the carbon dioxide capacity. The IAST LF predicts a higher capacity for carbon dioxide than the multicomponent LF and a lower capacity for nitrogen. The IAST model also predicts a much higher selectivity for carbon dioxide, especially at higher carbon dioxide partial pressures. Both models show considerably higher capacities than the breakthrough capacities. The comparisons in literature have been to experimental multicomponent isotherms, where the IAST model has been shown to have similar prediction capabilities as multicomponent models (Dreisbach et al., 1999; Rother and Fieback, 2013; Schell et al., 2012b).

Table 5.15: Predicted multicomponent adsorption capacities based on the multicomponent LF and DSL models and the corresponding IAST models for CO_2/N_2 mixtures separated using unmodified activated carbon

CO_2 Feed Fraction (-)	CO_2 Breakthrough Capacity (mol kg^{-1})	IAST – LF Model (mol kg^{-1})		LF Model (mol kg^{-1})		IAST – DSL Model (mol kg^{-1})		DSL Model (mol kg^{-1})	
		CO_2	N_2	CO_2	N_2	CO_2	N_2	CO_2	N_2
0.1	2.12 ± 0.14	2.80	0.94	2.88	2.04	2.55	1.11	2.95	1.97
0.2	4.05 ± 0.15	4.49	0.60	4.27	1.66	3.88	0.79	4.75	1.43
0.3	5.01 ± 0.08	5.70	0.40	5.30	1.37	4.82	0.60	5.99	1.06
0.4	5.54 ± 0.17	6.60	0.27	6.12	1.13	5.58	0.46	6.91	0.79
0.5	6.09 ± 0.06	7.30	0.18	6.82	0.91	6.21	0.35	7.62	0.59

The DSL models show the opposite trend with the IAST-DSL model predicting lower carbon dioxide and nitrogen capacities than the multicomponent DSL model. The difference may lie in the way that the multicomponent system predicts the capacity. As there are two sites, the way the two component isotherms interact can vary and results here are all assumed to be for a positive-positive system, as discussed in

Appendix A, but the IAST model is unable to take this into account. Reversing the interaction of the DSL sites results in a dramatically lower prediction in capacity and therefore that model has been discounted. The IAST model under predicts the breakthrough capacity, with the values for feed fraction of 0.3 and 0.4 actually being lower than the breakthrough capacity. This is because the IAST model is unable to take the interaction of the sites into account. The application of the DSL is limited in literature and the application to the IAST model even more so. It has previously been applied to the IAST model for activated carbons by Dreisbach et al. (1999), however, a Freundlich type exponent was included as well. The IAST does not always provide a better fit to multicomponent data (Schell et al., 2012b) and in this case the data in Table 5.15 indicates that the IAST model under predicts the breakthrough capacity, with the multicomponent DSL a better fit.

For both models, the solution method which predicts the higher capacity is more likely to be accurate. There is still an appreciable degree of spreading shown in Figure 5.8 which would suggest that the breakthrough capacity should still be significantly lower than an equilibrium capacity. On this basis, the IAST LF and the multicomponent DSL models are more suitable.

5.5 Modified Activated Carbon Breakthrough Experiments

The experimental set up for the modified material is the same as the unmodified material and is described in detail in Section 3.7.2. The key experimental conditions are given in Table 5.16.

Table 5.16: Experimental conditions for separations using the modified activated carbon

Bed Length	m	0.065
Bed Diameter	m	0.025
Adsorption Pressure	MPa	2.5
Temperature	K	298
Feed Flowrate	Nml min^{-1}	200
Adsorbent Mass	g	6.11

5.5.1 CO_2/N_2 Separations

5.5.1.1 Breakthrough Curves and Capacities

The breakthrough curves for the modified activated carbon are shown in Figure 5.10 alongside the breakthrough curves for the unmodified material. As for the unmodified activated carbon in Section 5.4.1, the steepness of the curves show there is still very limited mass transfer and dispersion effects. From the correlations discussed in Section 5.4.1, the dispersion coefficient here was found to be 1.86 x 10^{-6} m^2 s^{-1} and the mass transfer coefficients to be 0.07 s^{-1} and 0.99 s^{-1} for the carbon dioxide and nitrogen respectively. These values suggest that dispersion and mass transfer limitations have only a slightly larger effect than for the unmodified material. The breakthrough times are slightly shorter for the modified material. This is mainly due to there being significantly less adsorbent, on a mass basis, in the bed. The difference in density means that the fixed bed for the modified material is almost 33% lighter. The capacity would actually be expected to be less than found here considering the large difference in bed density with only a slight increase in capacity shown by the isotherms.

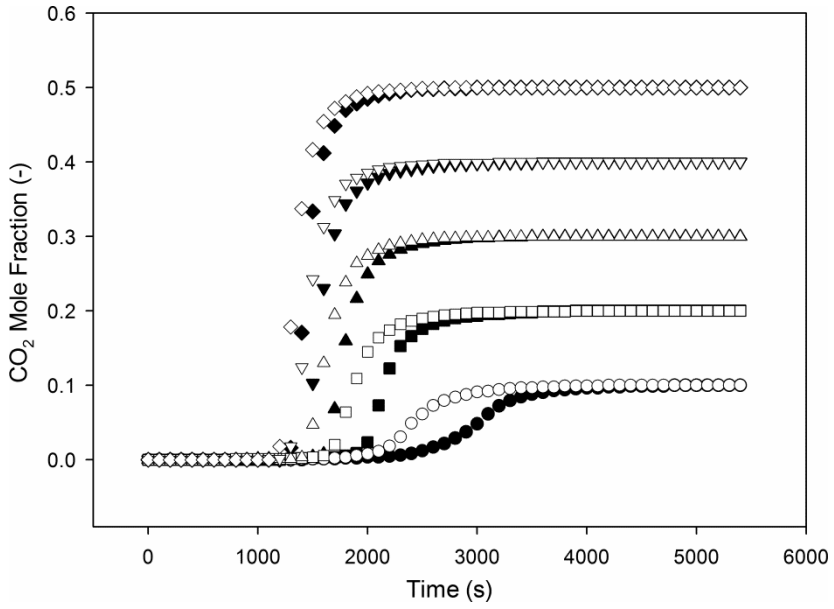

Figure 5.10: Breakthrough curves for the separation of a CO_2/N_2 mixture using unmodified activated (black) compared with the modified activated carbon material (white).

The breakthrough capacity for each run is given in Table 5.17 as well as a comparison to the pure component capacity as predicted by the LF and DSL models. At lower feed fractions the difference between the breakthrough capacity and the equilibrium capacity from the isotherm is considerable but this reduces as the carbon dioxide feed fraction increases. As the material has not reached saturation at breakthrough, the small differences between the isotherm prediction and the breakthrough capacity at higher feed fractions can be mainly attributed to the material not being at equilibrium. This suggests that the higher concentration of carbon dioxide and better selectivity mean the majority of the adsorption sites are occupied by carbon dioxide and the interaction by the nitrogen is limited allowing the carbon dioxide capacity to approach that of a pure component.

Table 5.17: The breakthrough capacities of CO_2/N_2 mixtures separated using modified activated carbon for each experimental run and the predicted capacity for pure components based on the LF and DSL models.

CO_2 Feed Fraction (-)	Breakthrough Capacity (mol kg^{-1})	LF (mol kg^{-1})	DSL (mol kg^{-1})
0.1	2.61 ± 0.13	4.61	4.53
0.2	4.67 ± 0.04	6.05	6.07
0.3	5.88 ± 0.14	6.83	6.88
0.4	6.84 ± 0.16	7.32	7.39
0.5	7.48 ± 0.09	7.68	7.74

Table 5.18: Predicted multicomponent adsorption capacities based on the multicomponent LF and DSL models and the corresponding IAST models for CO_2/N_2 mixtures separated using modified activated carbon

CO_2 Feed Fraction (-)	CO_2 Breakthrough Capacity (mol kg^{-1})	IAST – LF Model (mol kg^{-1})		LF Model (mol kg^{-1})		IAST – DSL Model (mol kg^{-1})		DSL Model (mol kg^{-1})	
		CO_2	N_2	CO_2	N_2	CO_2	N_2	CO_2	N_2
0.1	2.61 ± 0.13	2.74	1.24	2.58	2.27	2.74	1.21	4.48	0.50
0.2	4.67 ± 0.04	4.46	0.77	3.98	1.76	4.38	0.80	6.02	0.27
0.3	5.88 ± 0.14	5.62	0.49	4.98	1.39	5.45	0.57	6.85	0.17
0.4	6.84 ± 0.16	6.43	0.32	5.77	1.09	6.19	0.41	7.37	0.12
0.5	7.48 ± 0.09	7.01	0.21	6.40	0.85	6.73	0.30	7.72	0.08

A similar comparison is made in Table 5.18 between the multicomponent models for predicting the capacity of the material for each gas and the experimental breakthrough capacities. The same trend is seen as for the unmodified material, with the multicomponent LF and the IAST DSL predicting lower carbon dioxide capacities than their counterparts. In these cases the two IAST models also predict similar carbon dioxide capacities for all feed fractions. However, the IAST models and the multicomponent LF model under predict the breakthrough capacity at higher feed fractions. The multicomponent DSL model is the only one that predicts a greater equilibrium capacity than the breakthrough capacity for all feed fractions. This is because the predicted nitrogen interaction is the least and therefore the predicted

carbon dioxide capacities are very similar to the pure component equilibrium prediction. As the breakthrough capacity results suggest very limited interaction with the nitrogen, this model most suitably represents the system.

5.5.1.2 Capacity Comparison to Unmodified Activated Carbon

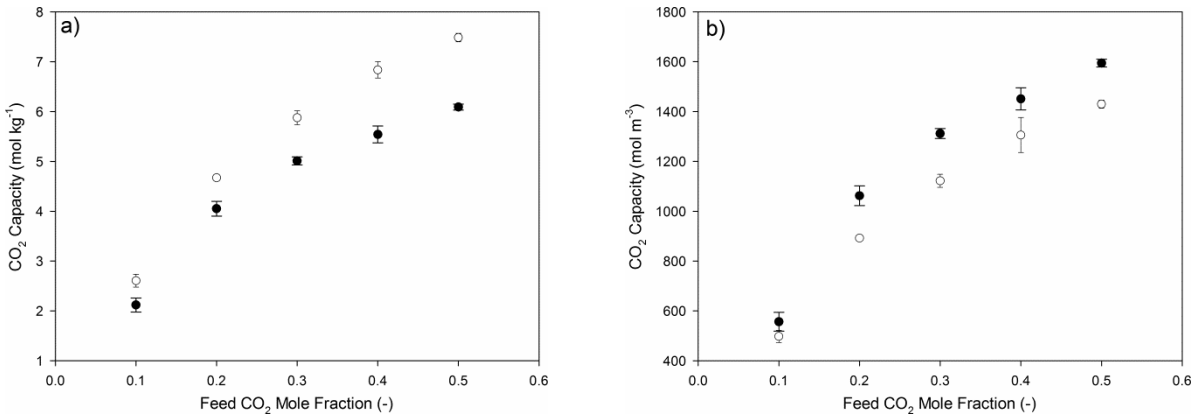

Figure 5.11: Comparison of unmodified (black circles) and modified (white circles) activated carbon breakthrough capacities for the separation of CO_2/N_2 mixtures on a a) mass and b) volumetric basis

A comparison can be performed between the breakthrough capacities for each material. In Section 5.2.4, the isotherms show that the unmodified material has slightly greater equilibrium capacities than the modified material. Figure 5.11a compares the breakthrough capacities of the material on the same mass basis. The modified material outperforms the unmodified activated carbon for all feed fractions, with the greatest difference at higher feed fractions. It is apparent that the selectivity for carbon dioxide over nitrogen is greater for the modified material as the breakthrough capacities are much closer to the pure component equilibrium value. This effect is more apparent at higher carbon dioxide partial pressures, which might explain the greater difference in breakthrough capacity between the two values at higher feed fractions.

Although the carbon dioxide capacity on a mass basis is often quoted for materials, it is actually the capacity on a volumetric basis that is more important for a PSA process. Section 5.2.3 shows that the unmodified material has a higher bulk density than the modified material, meaning a higher mass of material fits in the same bed volume. The number of moles of carbon dioxide captured per meter cubed of bed can be found by multiplying the mass capacity by the bulk density of the bed. The results of this upon the carbon dioxide capacity per unit volume are shown in Figure 5.11b, with the unmodified material greatly outperforming the modified material. This is to be expected as the bulk density is considerably larger for the unmodified material with only a slight decrease in equilibrium capacity found by the isotherm. This emphasises the importance of finding the carbon dioxide capacity on a volumetric basis. Drage et al. (2009a) indicate this in their evaluation of materials for pre-combustion capture. However, literature values for dynamic capacities are rarely quoted and often on a mass basis for comparison to equilibrium values found from isotherms (García et al., 2011). The work by Martin et al. (2012) briefly comments on this but the materials being compared show a very limited difference in density and therefore in their volumetric capacity. Capacities being quoted on a mass basis instead of a volumetric basis when found from isotherms also calls into question observations that capacity increases for materials with greater pore surface area (Drage et al., 2009a; Sun et al., 2013). This is true on a mass basis but often this greater pore surface area results in a lower density as there needs to be greater pore structures to give the higher pore surface area. An increase in pore surface area is often the focus of modification to activated carbons, however, may not have an effect on the volumetric capacity and therefore the capacity of a fixed bed PSA unit.

5.5.2 CO_2/H_2 Separations

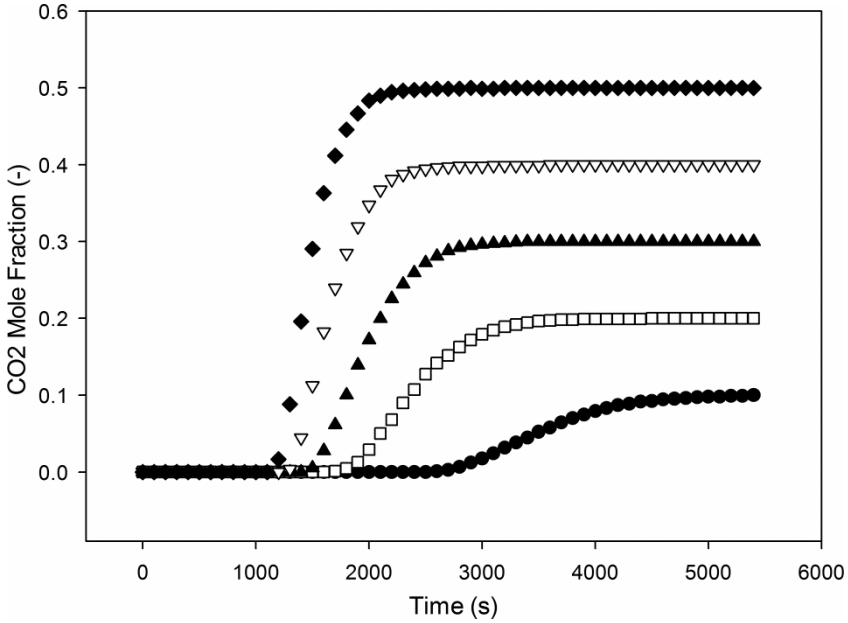

Figure 5.12: Breakthrough curves for the separation of a CO_2/H_2 mixture using modified activated carbon at CO_2 feed fractions of 0.1 (black circles), 0.2 (white squares), 0.3 (black triangles), 0.4 (white triangles) and 0.5 (black diamonds)

For the development of PSA processes for the separation of carbon dioxide at high pressures, it is important to consider a CO_2/H_2 mixture to ensure the results of a simulation using CO_2/N_2 would give reasonable indications for applications towards CO_2/H_2 mixtures. Therefore, the fixed bed experiments were repeated for the modified activated carbon using a CO_2/H_2 gas mixture. The breakthrough curves, given in Figure 5.12, show that there is a much greater degree of spreading than for the CO_2/N_2 mixture separations. It is possible to predict the mass transfer and dispersion coefficients by correlations as done in Section 5.4.1. For the CO_2/N_2 system, the rate limiting step for mass transfer was into the micropores. These are highly system specific and require complex experiments to find which was outside the scope of this work. However, as a different micropore diffusion would only affect

the hydrogen mass transfer coefficient, there is no reason for the carbon dioxide mass transfer coefficient to be affected by the use of hydrogen instead of nitrogen and therefore is likely to be constant for the system. The surface and macropore mass transfer resistances are calculated using isotherm data. As a first approximation, it can be assumed that no hydrogen is adsorbed and this gave a carbon dioxide mass transfer coefficient of 0.156 s^{-1} and a hydrogen mass transfer coefficient of 1.08 s^{-1}. These are slightly larger than the mass transfer coefficients for the CO_2/N_2 system and would therefore not lead to the larger degree of spreading.

The other coefficient that strongly affects the shape of the breakthrough curve is the dispersion coefficient, calculated from the Peclet number. The main properties that affect this are the density, viscosity and the diffusivity of the gas mixture. However, the Peclet number is a product of the Reynolds and Schmidt number which cause the viscosity and density effects to cancel out, making it only reliant on the mixture diffusivity. For a CO_2/H_2 mixture the calculated diffusivity increases (Bird et al., 2001). This gives a decrease in the Reynolds and Schmidt number product for the CO_2/H_2 mixture compared to the CO_2/N_2 mixture, as shown in Appendix J. For the Hsu and Haynes (1981) correlation the dispersion coefficient can be calculated to give a value of 1.62 x 10^{-6} m^2 s^{-1} for CO_2/H_2 mixtures compared to 1.86 x 10^{-6} m^2 s^{-1} for CO_2/N_2 mixtures over the modified activated carbon. This does not explain the greater degree of spreading for the CO_2/H_2 breakthrough curves shown in Figure 5.12. It is most likely that a different dispersion coefficient correlation, where the dispersion coefficient is predicted to be larger for CO_2/H_2 mixtures, see Appendix J, is required for these mixtures.

Table 5.19: The breakthrough capacities of CO_2/H_2 mixtures separated using modified activated carbon for each experimental run and the predicted capacity for pure components based on the LF and DSL models

CO_2 Feed Fraction (-)	Breakthrough Capacity (mol kg^{-1})	LF Model (mol kg^{-1})	DSL Model (mol kg^{-1})
0.1	4.32 ± 0.08	4.61	4.53
0.2	5.72 ± 0.01	6.05	6.07
0.3	6.62 ± 0.02	6.83	6.88
0.4	7.34 ± 0.01	7.32	7.39
0.5	7.67 ± 0.04	7.68	7.74

The breakthrough capacities for the CO_2/H_2 separations are given in Table 5.19. The closeness of the breakthrough capacity to the pure component equilibrium capacity suggests that the hydrogen has a limited effect on the capacity for carbon dioxide. The selectivity is greatest at higher feed fractions where the breakthrough capacity is almost at parity with the equilibrium capacity. In literature, it has been shown that the hydrogen capacity on activated carbon is considerably lower than nitrogen (García et al., 2013; Lopes et al., 2009; Martín et al., 2012; Schell et al., 2012b; Siriwardane et al., 2001). This low capacity suggests hydrogen in the gas mixture has very little impact on the capacity for carbon dioxide. It is not possible to calculate the multicomponent predictions by the isotherm models as equipment limitations meant the hydrogen isotherm was not found.

By comparing these to values given for CO_2/N_2 separations in Table 5.17, it is clear that the carbon dioxide capacity for CO_2/H_2 mixtures is greater than for CO_2/N_2 mixtures. However, at the higher feed fractions the difference is minimal. This suggests that for both separations, the weakly adsorbed component has less of an effect as the carbon dioxide partial pressure increases. The selectivity for carbon dioxide over hydrogen is high for all runs but is also high for CO_2/N_2 mixtures when

carbon dioxide feed fractions increases. This limited difference in capacity for CO_2/N_2 mixtures and CO_2/H_2 mixtures at higher feed fractions is promising for validation of a computer model using a CO_2/N_2 mixture as pre-combustion application of a PSA system would also have high fractions of carbon dioxide present.

5.6 Cyclic Experiments

The experimental set up has been used to investigate aspects of a PSA cycle. Both 3 step and 4 step cycles, as described in detail in Section 3.7, were investigated to study the selectivity of the materials for carbon dioxide over the less adsorbed gas, nitrogen.

5.6.1 Three step cycle

The 3 step cycle consists of an adsorption step, a joint depressurisation and purge step, and a pressurisation step. The outlet carbon dioxide feed fraction for the first 2 steps for a separation for a CO_2/N_2 mixture with 40% carbon dioxide using unmodified activated carbon is given in Figure 5.13 and is typical of 3 step cycles for both materials at all feed fractions. As the bed is run to complete saturation, the adsorption step gives the same results as Figure 5.8. The depressurisation and purge step initially displays a large spike in the fraction of carbon dioxide. This is because the adsorbent material releases the adsorbed gases when the pressure of the system is decreased. As there is more carbon dioxide adsorbed than nitrogen, the fraction of carbon dioxide increases. After depressurising the bed, the fraction of carbon dioxide rapidly decreases as the released carbon dioxide is driven away by the supply of pure nitrogen.

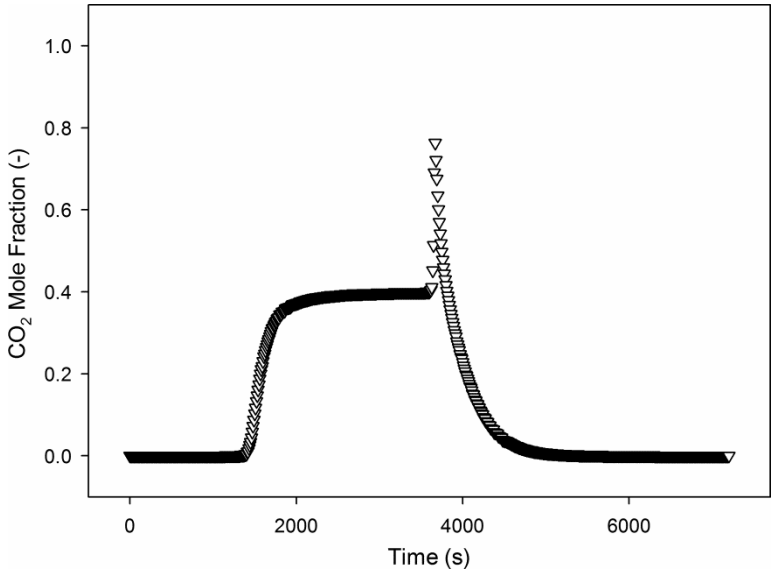

Figure 5.13: CO_2 exit fraction for the separation of a CO_2/N_2 mixture using unmodified activated carbon at a CO_2 feed fraction of 0.4 followed by a depressurisation and purge under a pure nitrogen flow

The peak of the depressurisation curve gives an indication of the amount of carbon dioxide in the adsorbed phase. It does not give the actual selectivity due to the nitrogen purge gas mixing with the released carbon dioxide but does give a qualitative guide. The peak values for various mole fractions for both the unmodified material and modified material are given in Table 5.20. The error on the peak values is generally within the experimental error for the analyser of ± 0.01. Greater error is possible as the analyser required calibration which was set to the carbon dioxide mole feed fraction as this was controlled. For all three experimental sets there is a considerable increase between feed fractions of 0.1 and 0.2. The CO_2/N_2 mixtures then display a further step up when the feed fraction is increased to 0.3. All remaining feed fractions then give relatively consistent peak values. This emphasises that the nitrogen plays a significant role in the separation at lower carbon dioxide partial pressures but this is greatly reduced at the highest carbon dioxide

feed fractions. This mimics the comparison of the breakthrough capacities with the carbon dioxide pure component isotherm predictions given in Sections 5.4.2, 5.5.1 and 5.5.2, where the difference is much less at higher feed fractions of carbon dioxide. The CO_2/H_2 separation using the modified material reaches higher selectivity at lower feed fractions due to the low amount of hydrogen adsorbed by activated carbons as described in Section 5.5.2, meaning it reaches a consistent level of exit fraction, with the hydrogen having limited interaction effects, at lower partial pressures of carbon dioxide.

Table 5.20: Average peak desorption exit fractions for the unmodified and modified materials using CO_2/N_2 and CO_2/H_2 mixtures

CO_2 Feed Fraction (-)	Peak Desorption Exit CO_2 Fraction (-)		
	AC – CO_2/N_2	MAC – CO_2/N_2	MAC – CO_2/H_2
0.1	0.57 ± 0.009	0.51 ± 0.015	0.65 ± 0.012
0.2	0.69 ± 0.003	0.63 ± 0.006	0.71 ± 0.018
0.3	0.75 ± 0.009	0.70 ± 0.003	0.70 ± 0.007
0.4	0.77 ± 0.006	0.71 ± 0.029	0.73 ± 0.004
0.5	0.78 ± 0.006	0.74 ± 0.008	0.75 ± 0.016

5.6.2 Four step cycle

As discussed in Section 2.8, a typical PSA cycle is four steps, requiring an adsorption step, a blowdown step, a purge step and a pressurisation step. The system was run with the unmodified and modified activated carbon in the bed for the separation of CO_2/N_2 mixtures. The adsorption step used a CO_2 feed fraction of 0.4 and lasted for 1510 s for the unmodified material and 1260 s for the modified material based on the breakthrough time found in Sections 5.4.1 and 5.5.1.1 respectively. The CO_2 mole fraction at the exit of the bed for these first three steps for a bed packed with the unmodified activated carbon is given in Figure 5.14. The cycle shown is typical for the modified activated carbon as well. The adsorption step shows that after 1510 s

there is a small amount of carbon dioxide in the outlet stream. During the blowdown step, the rapid pressure change causes the carbon dioxide fraction to rise rapidly. The remaining part of the blowdown step allows the system to equilibrate so that the outlet fraction recorded by the analyser is the same as that in the bed. The purge step is then similar to that of the 3 step cycle, with the carbon dioxide exit fraction decreasing rapidly as the nitrogen flow flushes it out of the system.

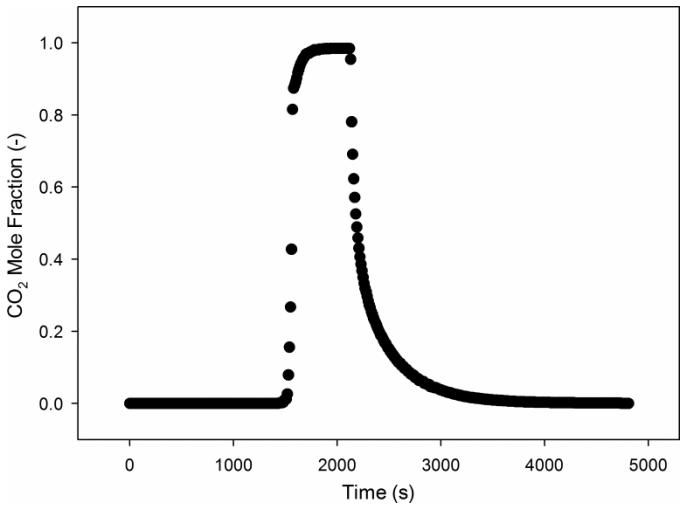

Figure 5.14: CO_2 exit fraction for the separation of a CO_2/N_2 mixture using unmodified activated carbon at a CO_2 feed fraction of 0.4 for 1510 s followed by a depressurisation with no flow for 600 s and then purge under a pure nitrogen flow for 2100 s. Results shown every 10 seconds.

The highest mole fraction reached during the blowdown step gives a quantitative indication of the selectivity for carbon dioxide. The 4 step runs for both the unmodified and modified activated carbons for separations of CO_2/N_2 mixtures gave average maximum values of 0.983 ± 0.006 and 0.985 ± 0.011 mole fraction respectively. The selectivity can be estimated by assuming the maximum concentration was the same as the adsorbed concentration before blowdown, predicting a selectivity of 59.9 mol_{CO2} /mol_{N2} for the unmodified activated carbon and 65.9 mol_{CO2} /mol_{N2} for the modified activated carbon.

The selectivity predicted here can be compared with multicomponent models, as they indicate the selectivity for carbon dioxide over the lighter component, to further suggest which multicomponent is most suitable. The high selectivity predicted by the blowdown step indicates that the multicomponent isotherm model should give low values of nitrogen adsorbed. From the values given in Table 5.15 and Table 5.18, the selectivity can be calculated by dividing the carbon dioxide capacity by the nitrogen capacity. The selectivities for both the unmodified and modified material for carbon dioxide over nitrogen from the capacities predicted by the various multicomponent isotherm models are reported in Table 5.21. For the unmodified material the IAST models predict higher selectivities than the extended models. The trend is the same for LF model for the modified material but the extended DSL model predicts a much higher selectivity than all other isotherm models. This is the value closest to the selectivity predicted by the cyclic experiments and further suggests the extended DSL is the most suitable multicomponent isotherm model for these systems.

Table 5.21: Selectivities predicted from different multicomponent isotherm models for CO_2/N_2 separations.

		IAST – LF	Extended LF	IAST – DSL	Extended DSL
AC	(mol_{CO2} /mol_{N2})	24.4	5.42	12.1	8.75
MAC	(mol_{CO2} /mol_{N2})	20.1	5.29	15.1	61.4

5.7 Conclusion

The work presented here gives a complete investigation of two activated carbon materials for the application of high pressure PSA processes. The materials were fully characterised. The isotherms showed that the modified activated carbon had a

slightly higher capacity for carbon dioxide. For both materials pure component isotherms were fitted and it was found that the LF and DSL models gave the best fit for carbon dioxide and nitrogen. The bulk density of the modified activated carbon beads was significantly less than the unmodified material indicating that for a given bed volume, a high carbon dioxide capacity was required to give the same efficiency as a separation using the unmodified material.

Breakthrough experiments were performed for the separation of CO_2/N_2 mixtures using both materials and for the separation of CO_2/H_2 mixtures using the modified activated carbon. For all breakthrough curves the mass transfer and dispersion limitations were found to be minimal, although more significant for the CO_2/H_2 mixtures. In comparing the capacity of both materials for the separation of CO_2/N_2 mixtures, the modified material was found to have higher carbon dioxide capacities on a mass basis. However, when these capacities were compared on a volumetric basis, which is more important for PSA applications as it affects the size of the adsorbent bed, the unmodified material had a superior capacity for carbon dioxide. This result shows that pore surface area does not necessarily have a strong effect on the volumetric capacity, especially if the materials which show higher capacities for carbon dioxide on a mass basis have sacrificed bulk density to achieve a higher pore surface area.

Four multicomponent isotherm models were compared with the breakthrough capacities found for the separations of CO_2/N_2 on both materials, the multicomponent LF, the IAST model applied to the LF model, the multicomponent DSL and the IAST model applied to the DSL model. It was found the multicomponent DSL model was more suitable as the others under predicted the carbon dioxide capacity for the

modified material and the multicomponent LF and the IAST-DSL under predicted the capacity for the unmodified material.

Cyclic experiments were conducted. The main result was to indicate the high selectivity that both materials exhibit for carbon dioxide over nitrogen, especially at higher carbon dioxide feed fractions. The 3 step experiments did this qualitatively and a 4 step experiment gave some quantitative evidence. The 4 step experiment suggested, for a feed fraction of 0.4, that the selectivity for carbon dioxide over nitrogen was approximately 59.9. This high selectivity gives further evidence that the multicomponent DSL model is most suitable for the separations tested here.

Chapter 6 – Validation of an axial dispersed plug flow model

6.1 Introduction

Models capable of simulating adsorption processes are key in aiding the design of adsorbent processes and materials (Shafeeyan et al., 2014). In order to use these models with confidence it is necessary to validate them against data from experiments under similar conditions to the industrial process, e.g. pressure, feed gas composition and temperature.

An axial dispersed plug flow model and the correlations required for this application to pressure swing adsorption (PSA) systems are detailed in Section 4.6. The mass and energy balances are commonly applied for simulating fixed bed separations of gas mixtures by adsorption (Ruthven, 1984). However, there are only a few models that have been validated against breakthrough data for separations at high pressure, as applicable in pre-combustion capture plants employing pressure swing adsorption separations (Casas et al., 2013a; Casas et al., 2012; Grande et al., 2013; Park et al., 1998). Only the model by Grande et al. (2013) is based on theoretical data rather than using parameter estimation to match the simulation to the experimental breakthrough curve. There are more models that do not use parameter estimation for low pressure separations (Gao et al., 2013; Lopes et al., 2009; Lopes et al., 2011), but the majority of low pressure separation models use parameter estimation. Parameter estimation involves the fitting of parameters to the experimental data using least squares regression or similar algorithms. However, the values found are highly dependent on the starting value used in the estimation and, in the case of a large number of parameters to be estimated, multiple solutions of the model. Overall, this leads to a low confidence in the predicted values of the parameters and the estimated parameters may not be physically meaningful. Instead, the use of

independent parameters and correlations based on independent parameters provides confidence in extrapolating the model outside of the validation range for testing different operational conditions and for scaling the model.

In this chapter the development of a model which has later been applied for simulating PSA systems is presented. First, simulations of the surrounding system (pipes, connectors, valves and CO_2 analyser) validated against experimental data are reported. Parameter estimation is only used here to provide a highly accurate fit so that this model can be used in series with the fixed bed model to account for the surrounding system effects. Following this, the set of correlations and parameters for the fixed bed that most closely match the breakthrough curves for the unmodified activated carbon are presented. These are based on a literature survey that was carried out to find suitable correlations for the necessary model parameters. A discussion of the quality of fit of the tested correlations follows the presentation of the best fit simulations. The model is then compared against pressure swing adsorption (PSA) experiments to test the accuracy for predicting the regenerative steps. The simulated results for the modified activated carbon are also analysed to investigate the flexibility of the model. Finally a parameter sensitivity analysis is presented in order to indicate which parameters most strongly affect the process and thus should be the focus in the design of PSA systems.

6.2 System Modelling

When modelling an experimental system and comparing the results to validate the model, it is necessary to ensure the model accurately represents the measuring devices. In this case it was necessary to include models of the pipework and fittings that surround the adsorption bed and to allow for lag in the response of the analyser

to the input gas. The work by Schell et al. (2013) showed that this is especially important for cyclic systems. The response of the surrounding system to a CO_2/N_2 mixture is discussed in Section 5.3.2. A simplified model of the surrounding system was set-up, detailed in Section 4.9. This was an empirical model, used to replicate the CO_2 analyser response for the system without the bed and the feed and outlet pipes connected directly. Four parameters were estimated using the parameter estimation tool within gProms, which varied these four fitting parameters to match the simulation with the experimental results. The fitted parameters are based on the dispersion and cross sectional area of a series of fixed beds in order to replicate the breakthrough curve found experimentally, with the predicted parameters presented in Appendix K, but there is no scientific significance to the parameters used.

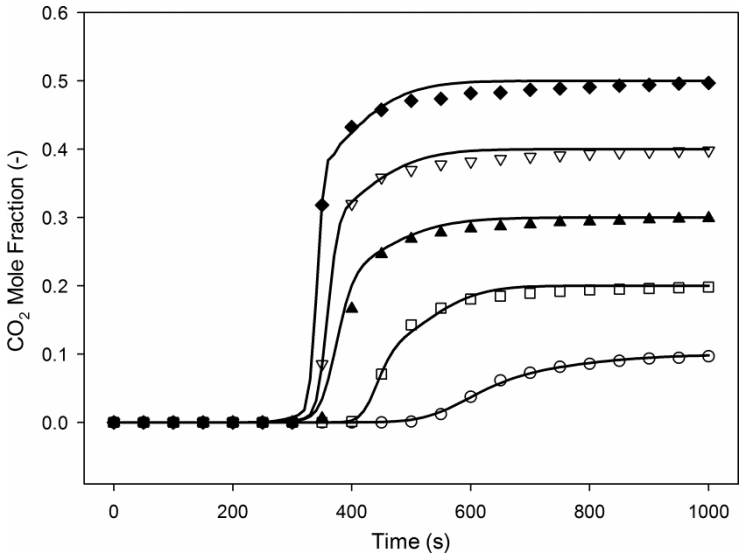

Figure 6.1: Experimental results for a system without a bed plotted with models for each CO_2 feed fraction

The output of the model and a comparison to the experimental data is given in Figure 6.1. For all systems the normalised sum of the squares of the differences (SSD) was used to analyse the fit of each of the models, as described in Section 4.11.4.

Excellent agreement is seen between the simulation and experimental data with the largest SSD of 1.59 x 10^{-3} for a carbon dioxide feed mole fraction of 0.5. All simulations of the system that use the fixed bed include this empirical model in series with the bed model, with the conditions of the empirical model matching those of the fixed bed. This gives confidence that the results for simulations with the bed are accurately representing the response of the bed and not the surrounding system.

6.3 Unmodified Activated Carbon Breakthrough Modelling

The focus of the validation work was to accurately simulate the experimental results for the unmodified activated carbon presented in Section 5.4.1. Details of the model are given in Section 4.6, with the options for different correlations of the model specified. This section first presents the final validated model and then goes on to discuss the choice of correlations used.

6.3.1 Best Fit Model Output

There are several aspects of the model that can be simulated using different expressions or correlations based on literature and the elements which gave the best fit are reported here and further discussed in Section 6.3.2. The Dual-Site Langmuir isotherm model is used to find the adsorbed equilibrium amount (Section 6.3.2.1), and the temperature independent isotherm parameters are given in Table 5.5. The dispersion coefficient (Section 6.3.2.2) is found using the Hsu and Haynes (1981) correlation. The energy balance (Section 6.3.2.3) used does not include the wall effects of the system and uses the Yagi and Kunii (1960) correlation to find the heat transfer coefficient (Section 6.3.2.4).

Table 6.1: Parameters used for the best fit simulation

Feed Pressure	MPa	2.5	Set
Feed Temperature	K	298	Set
Feed Flowrate	Nml min^{-1}	200	Set
Ambient Temperature	K	298	Measurement
Bed Length	m	0.069	Measurement
Bed Diameter	m	0.025	Measurement
Bed Density	kg m^3	262	Measurement
Particle Diameter	m	1 x 10^{-3}	Measurement
Pore Diameter	m	2.19 x 10^{-9}	Measurement
Bed Voidage	-	0.48	Measurement
Particle Voidage	-	0.75	Measurement
Particle Tortuosity	-	1.41	Ruthven (1984)
CO_2 Micropore Diffusivity	s^{-1}	1.06 x 10^{-2}	Shen et al. (2010)
N_2 Micropore Diffusivity	s^{-1}	7.19 x 10^{-2}	Shen et al. (2010)
Heat Capacity of Adsorbent	kJ kg^{-1} K^{-1}	1	Casas et al. (2012)
Heat Transfer Coefficient of stagnant gas	kJ s^{-1} m^{-2} K^{-1}	22 x 10^{-2}	See Section 6.3.2.4
Heat Transfer Fitting Parameter	-	0.041	See Section 6.3.2.4
CO_2 Heat of Adsorption	kJ mol^{-1}	24.7	Measurement
N_2 Heat of Adsorption	kJ mol^{-1}	14.9	Measurement

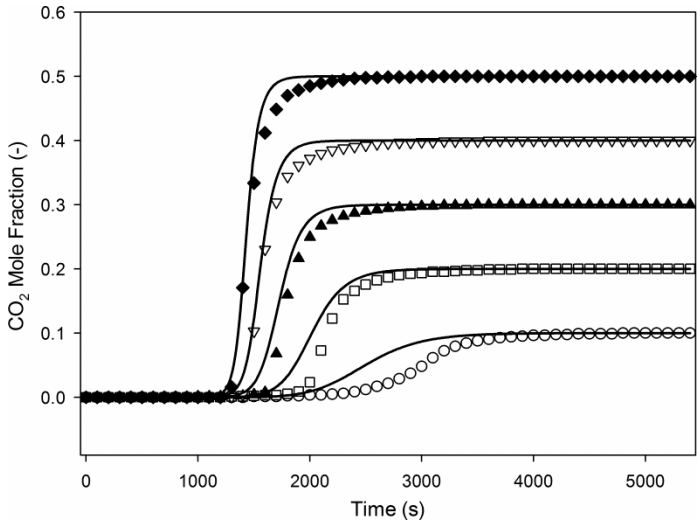

Figure 6.2: Simulation break through curves plotted against the corresponding experimental data with CO_2 feed fraction of 0.1 (white circles), 0.2 (white squares), 0.3 (black triangles), 0.4 (white triangles) and 0.5 (black diamonds).

The remaining parameters used for the best fit of the experimental data are given in Table 6.1. Unless otherwise stated these are from independent measurements of

the system. The gas properties are from Multiflash Version 4.1.24. The mass transfer coefficient is found using the correlation suggested by Farooq and Ruthven (1990) as it incorporates the surface, macropore and micropore mass transfer limitations together. Details of the predicted value for the mass transfer coefficient are reported in Appendix J.

Table 6.2: SSD values and the difference in breakthrough time for the comparison of the best fit simulation to the experimental breakthrough data for AC.

CO_2 Feed Fraction	SSD	Breakthrough Time Difference
0.1	0.0168	14.9%
0.2	0.0163	15.0%
0.3	0.0151	9.3%
0.4	0.0115	4.9%
0.5	0.0126	2.3%
Total	0.0723	-

The simulation breakthrough curves with the closest fit to the corresponding experimental data for the unmodified activated carbon are plotted against time together with the corresponding experimental data in Figure 6.2. Table 6.2 shows the calculated SSD between the simulation and experimental data for each carbon dioxide mole fraction. The agreement between the simulation data and the experimental data is better at higher CO_2 feed fractions, shown by lower SSDs. In all cases the simulation predicts breakthrough sooner than it occurs for the experimental data. This indicates that the simulation is under predicting the capacity for carbon dioxide. The main part of the model which accounts for the capacity of carbon dioxide is the multicomponent isotherm. At the lower values of CO_2 feed fractions, the capacity is significantly under predicted and this is most likely due to the model overestimating the reduction in carbon dioxide capacity caused by the presence of

nitrogen, which is more significant for low feed fractions. The multicomponent DSL model predicted high selectivity for carbon dioxide over nitrogen at higher CO_2 feed fractions which explains the strong agreement between the simulation and experimental data at these feed fractions as the nitrogen interactions are less.

The difference between the breakthrough times as a percentage of the experimental breakthrough time are shown in Table 6.2. For the simulation of carbon dioxide feed fractions of 0.4 and 0.5, the breakthrough times match within 5% of the experimental breakthrough time. However, the asymmetrical nature of the breakthrough curve is not fully replicated. The experimental data has an increased spreading in the second half of the curve associated with a bed cooling allowing more carbon dioxide to be captured at the end of breakthrough. This suggests that the simulation is underestimating the temperature change that occurs in the bed, however, as discussed in Section 6.3.2.4, simulations that predict a higher temperature rise lead to a reduction in predicted breakthrough time. For a PSA system that is not run to saturation, the breakthrough time is more important than the shape of the breakthrough curve. This informs when the cycle step needs to change and therefore dictates the cycle time, a key parameter in PSA modelling. PSA systems are often simplified to not include spreading terms such as the dispersion coefficient as the shape of the breakthrough curve is not considered important (Agarwal et al., 2010; Casas et al., 2013b). Therefore, the best fit model presented here is used for simulating PSA systems as it most closely simulates the breakthrough times.

The degree of success in literature for high pressure models varies depending on the use of parameter estimation. Casas et al. (2012) and Casas et al. (2013a) obtained excellent agreement but use the heat and mass transfer coefficients as fitting

parameters. Park et al. (1998) use the mass transfer coefficient to fit the simulation to the experimental results but obtained similar under prediction of the carbon dioxide capacity shown in Figure 6.2. The breakthrough time for their simulation matches within 7% of the experimental breakthrough time. Grande et al. (2013) investigated the high pressure simulation of CH_4/CO_2 mixtures, without parameter estimation. For pressures greater than 5 Mpa, their work resulted in an over prediction in carbon dioxide capacity by the simulation, with breakthrough times differing by as much as 20% of the experimental breakthrough time. Based on comparisons to other similar models, the degree of agreement obtained here, especially in predicting breakthrough times, is comparable to literature.

6.3.2 Model Development

Section 6.3.1presents the model that most closely matches the experimental results and is mainly based on parameters found independently to the fixed bed experiment. There are some parameters based on correlations, where the literature is not in agreement over which is most suitable. In these cases the different correlations were tested and compared with the experimental data. The SSD was used to indicate which correlation gave the best match. These results must be treated with caution as the system with the lowest SSD may not be representing all of the effects seen in the system (Won and Lee, 2011). The results presented in the following Sections use the parameters given in Table 6.1 for the best fit model unless otherwise stated. The figures are for a CO_2 feed fraction of 0.4 only, with the other feed fractions showing the same trends.

6.3.2.1 Isotherm Comparison

Three different isotherm models were compared in Section 5.2.4 based on their fit to the experimental isotherms, where the Langmuir-Freundlich (LF) and Dual-Site Langmuir (DSL) isotherm models gave the best fit to the pure component data. Different multicomponent isotherm models were then compared in Section 5.4.2 based on their ability to predict the material capacity for carbon dioxide and these included the multicomponent LF, the ideal adsorbed solution theory (IAST) using the LF model, the multicomponent DSL and the IAST using the DSL model. It was found that the multicomponent DSL was the most suitable followed the IAST-LF. It is possible to use either of the multicomponent models in the breakthrough simulation. Due to the implicit nature of the IAST models, it is generally not used. Doong and Yang (1986) found the IAST model gave similar results to the extended LF model but increased the computational time by 70%. Therefore to limit the complexity of the model, it is not studied here.

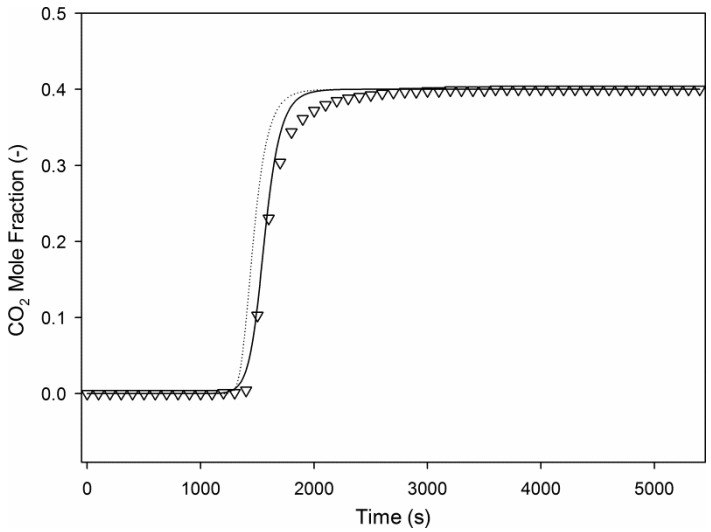

Figure 6.3: Comparison the multicomponent DSL (solid line) and the multicomponent LF (dotted line) isotherm models against the experimental data at a CO_2 feed fraction of 0.4

Figure 6.3 compares the DSL and LF multicomponent models with the experimental breakthrough data using the isotherm parameters given in Table 5.4. The DSL model gives a better match than the LF model, with the SSDs for each being 0.011 and 0.032 respectively for a carbon dioxide feed fraction of 0.4 and SSDs of 0.072 and 0.146 for all carbon dioxide feed fractions combined. The LF model under predicts the capacity of the activated carbon for carbon dioxide and this leads to breakthrough occurring 100 seconds before the experimental time compared to 70 seconds for the DSL model than for the experimental data. The higher capacity predicted by the DSL model is observed in the simulation, leading to a longer breakthrough time than the simulation using the LF model. Both models under predict the asymmetrical nature of the curve and therefore complete saturation is predicted earlier in the simulations. The LF model has been shown previously to produce a steep breakthrough curve (Grande et al., 2013). The work by Casas et al. (2012) reports simulations for high pressure separation of CO_2/H_2 mixtures using active carbon and finds that the LF model accurately predicts their experimental data, although this must be taken with caution as parameter estimation was used. Park et al. (1998) found the opposite, suggesting the Langmuir isotherm was more suitable than the LF isotherm. There is no work in literature that uses the DSL model at high pressure to compare experimental and simulation breakthrough curves. Agarwal et al. (2010) use the DSL model for simulating PSA cycles for a pre-combustion system but without an experimental validation. Garcia et al. (2013) showed experimentally it is more suitable for predicting breakthrough capacities for multicomponent systems. Gao et al. (2013) used the DSL model for a CO_2/N_2 separation using modified

activated carbons at atmospheric pressure and find strong agreement but do not compare this to the LF model.

6.3.2.2 Dispersion Coefficient Correlation Comparison

The dispersion coefficient predicts the degree of axial mixing that occurs within a system by combining all of the contributing mechanisms (Ruthven, 1984). This is highly dependent on the system and therefore relies on correlations, which are shown in Section 4.7, to predict the value of the coefficient.

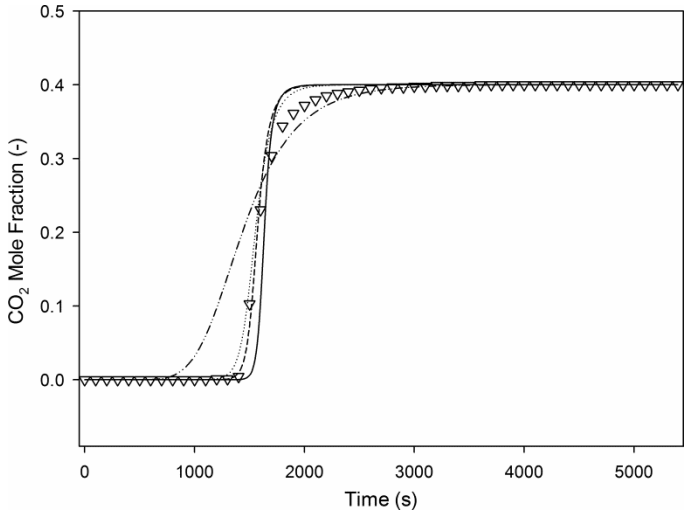

Figure 6.4: Comparison of simulation outputs with no dispersion (solid line) and dispersion coefficients predicted by the general (dashed line), Hsu and Haynes (dotted line) and Wakao (dot dash line) correlations with experimental data

A comparison of the correlations used is given in Figure 6.4 and the SSDs for these runs and for all of the CO_2 feed fraction runs combined are given in Table 6.3. Wakao et al. (1978) showed that correlations for non-porous particles cannot necessarily be applied to porous materials and instead suggested a different correlation. This was said to be an especially important factor at low Reynolds numbers, such as those in this work. It has been used for many low pressure

separations with good success (Cavenati et al., 2006; Delgado et al., 2006; Lopes et al., 2009; Lopes et al., 2011; Won and Lee, 2011) However, for this system, the Wakao et al. (1978) correlation greatly over predicts the degree of spreading that takes place, with breakthrough occurring 500 seconds before the experimental results.

A model of the system without any dispersion minimises the spreading of the mass transfer front and therefore increases the breakthrough time, giving an improved fit. However, the effect of dispersion on the system is seen in the shape of the curve and a system without dispersion is not able to accurately model the breakthrough curve and led to an over prediction of the breakthrough time.

Table 6.3: Comparison of SSE values between the model for a given dispersion coefficient correlation and the experimental results for a CO_2 feed fraction of 0.4 and for all CO_2 feed fractions combined

Correlation	SSD for 0.4	Total SSD
No Dispersion Coefficient	0.024	0.091
Wakao (1978)	0.040	0.172
Hsu and Haynes (1981)	0.011	0.072
General	0.013	0.074

The Hsu and Haynes (1981) correlation, as used by Farooq and Ruthven (1990), and the general correlation, as described by Ruthven (1984), are able to reflect the small dispersion effects seen. Both correlations are very similar, with minimal difference for the total SSD. The use of a correlation other than the Wakao et al. (1978) correlation fits with other high pressure work (Casas et al., 2012; Grande et al., 2013) where the general equation for dispersion described by Ruthven (1984) has been used. This suggests that, despite the low Reynolds numbers used in this work, the high pressure negates the added dispersion from porous particles making correlations for non-porous materials more suitable. The Hsu and Haynes (1981) correlation is

applicable to 0.72 mm diameter particles and for 0.08 < ReSc < 1, which fits with the system here which has a particle diameter of 1 mm and a ReSc of 0.101. The conditions for which the general correlation can be applied are not given. Since the experimental conditions match those used for the Hsu and Haynes (1981) correlation, it is preferred.

6.3.2.3 Energy Balance Comparison

Adsorption processes are exothermic and therefore a suitable energy balance is required to predict the temperature changes occurring in the adsorption bed. The experimental results did not show a significant temperature change at the bed exit, with variations no greater than 1 degree. However, as discussed in Section 5.4.1, this is most likely due to the distance between the bed exit and the temperature probe allowing the gas to cool. The asymmetric nature of the breakthrough curve suggests a temperature change occurred as it is indicative of a capacity increase as the bed cools.

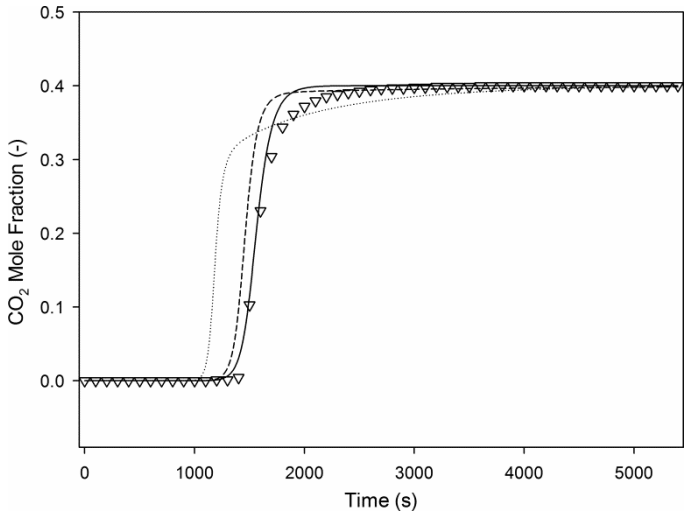

Figure 6.5: Breakthrough simulations for energy balances based on a non-isothermal system without wall effects (solid line), non-isothermal system with wall effects (dashed line) and an adiabatic system (dotted line) plotted against the experimental results for a CO_2 feed fraction of 0.4.

There are three main types of energy balance used in PSA systems, non-isothermal without wall effects, non-isothermal with wall effects and adiabatic systems (Nikolic et al., 2008), with each of these detailed in Section 4.6.2. When these are implemented in the simulations, they have a significant effect on the breakthrough curve, as illustrated in Figure 6.5. The simulation using the adiabatic model gives a poor fit in terms of breakthrough time and shape of the breakthrough curve. The energy balance that includes wall effects gives a better fit for the shape of the curve but the breakthrough is earlier than the experimental results without producing a change in the shape of the curve. The non-isothermal model without wall effects gives the best fit for the breakthrough, although the shape of the curve is still not fully matched, as discussed in Section 6.3.2.4.

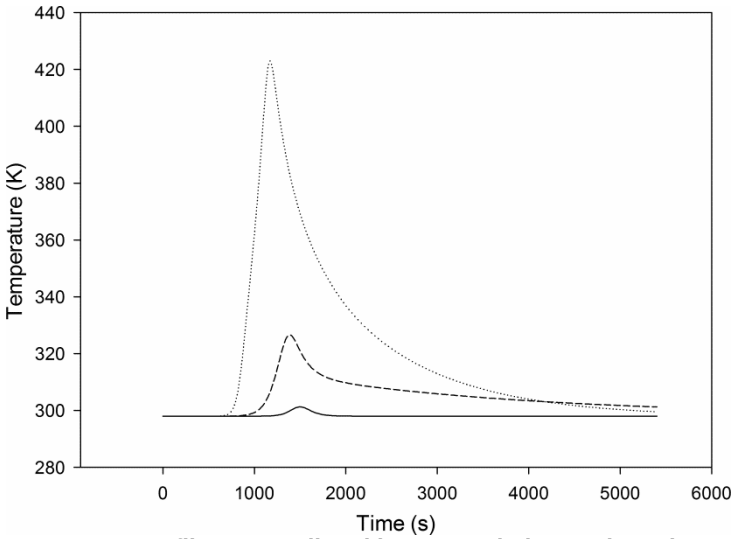

Figure 6.6: Bed exit temperature profiles as predicted by energy balances based on a non-isothermal system without wall effects (solid line), non-isothermal system with wall effects (dashed line) and an adiabatic system (dotted line)

The differences in the shape of the breakthrough curve for the different energy balances in Figure 6.5 is best explained by the temperature profiles of the stream at the bed exit, shown in Figure 6.6. The adiabatic system has a sharp temperature

rise followed by a decaying curve that returns close to ambient temperature. The magnitude of the steep temperature rise leads to a loss in the capacity which explains the short breakthrough time. The decaying nature of the temperature profile then gives rise to a breakthrough curve which tends to the inlet concentration (Ruthven, 1984). The non-isothermal system with wall effects shows a smaller, but not insignificant, peak and then a temperature decrease at a very low rate. This leads to the breakthrough curve being steeper but then not quite reaching the final concentration of carbon dioxide. The non-isothermal system without wall effects leads to a slight temperature increase which cools rapidly so that the temperature profile is symmetrical. This small temperature has the least effect on the breakthrough time and the symmetrical temperature profile leads to a more symmetrical breakthrough curve, meaning the asymmetric nature of the breakthrough curve is not produced in the simulation.

Simulations that did not include wall effects have traditionally been used in literature for PSA models (Farooq and Ruthven, 1990), where the temperature of the column wall is assumed to be the same as the ambient temperature allowing the heat effects to be lumped together. However, with increasing computational power, more recent models, for both high pressure and low pressure systems, have included these effects (Casas et al., 2012; Grande et al., 2013; Lopes et al., 2011). Without an internal temperature profile or a temperature profile of the wall it is not possible to validate the temperature profiles of the model. Therefore, the validation of the model must rely on the breakthrough data which suggests that a model without wall effects is the most accurate.

6.3.2.4 Heat Transfer Coefficient Correlation Comparison

As discussed in Section 6.3.2.3, even with the inclusion of the energy balance the asymmetrical shape of the breakthrough curve is not fully matched. The shape of the simulation breakthrough curve is affected by the heat transfer rate from the gas phase to the surroundings. The two main correlations considered for fixed beds are the Leva (1947) correlation and the Yagi and Kunii (1960) correlation, detailed in Section 4.7.3. Both correlations predict very similar values for the heat transfer coefficient, with the Leva (1947) correlations and Yagi and Kunii (1960) predicting values of 3.8×10^{-3} $kJs^{-1}m^{-2}K^{-1}$ and 2.2×10^{-3} $kJs^{-1}m^{-2}K^{-1}$ respectively. This leads to no visible difference between two simulations with the same conditions. Several literature models have used the Leva (1947) correlation to good success (Casas et al., 2013a; Casas et al., 2012; Park et al., 1998) However, having reported the use of the Leva (1947) correlation initially (Park et al., 1998), in subsequent work, Park et al. (2000) suggested that the Leva (1947) correlation under predicts the heat transfer rate at low mass fluxes, such as those used in that work and used here. For this reason the Yagi and Kunii (1960).

The Yagi and Kunii (1960) correlation is based on the heat transfer coefficient when the gas phase is stagnant,h_w^0, and a fitting parameter, α_w. Yagi and Kunii (1960) showed that the heat transfer coefficient becomes constant for systems with Re<30 and that the term with α_w approaches zero. This means that the heat transfer coefficient is the same as h_w^0. Ofuchi and Kunii (1965) produced a graph which predicts the heat transfer coefficient of the stagnant gas based on the ratio of solid to fluid thermal conductivity but for the solid medium inside the bed rather than into the

bed wall. The graph uses the dimensionless form of h_w^0 by multiplying it by the characteristic length and dividing by the thermal conductivity of the fluid. This can be applied to a fixed bed taking the characteristic length as the bed diameter instead of the particle diameter. The ratio of thermal conductivities of stainless steel and the gas mixtures is approximately 600. From this the graph presented by Ofuchi and Kunii (1965) gives a value for the dimensionless group of 22. Based on the bed diameter and fluid thermal conductivity, this predicts a value for h_w^0 of 22×10^{-2} $kJs^{-1}m^{-2}K^{-1}$. This value is comparable to literature values. Park et al. (2000) used a value of 4.2×10^{-2} $kJs^{-1}m^{-2}K^{-1}$ for a mixture of $H_2/CO_2/CH_4/CO$ using activated carbon, found by using h_w^0 as a fitting parameter. Choi at al. (2004) give a final value for the h_w as being 3.8×10^{-2} $kJs^{-1}m^{-2}K^{-1}$ in a methane and hydrogen separation over activated carbon. The work by Ruthven et al. (1975) suggests a value of 19.7×10^{-2} $kJs^{-1}m^{-2}K^{-1}$ for propylene, cis-2-butene and 1-butene using zeolite 5A.

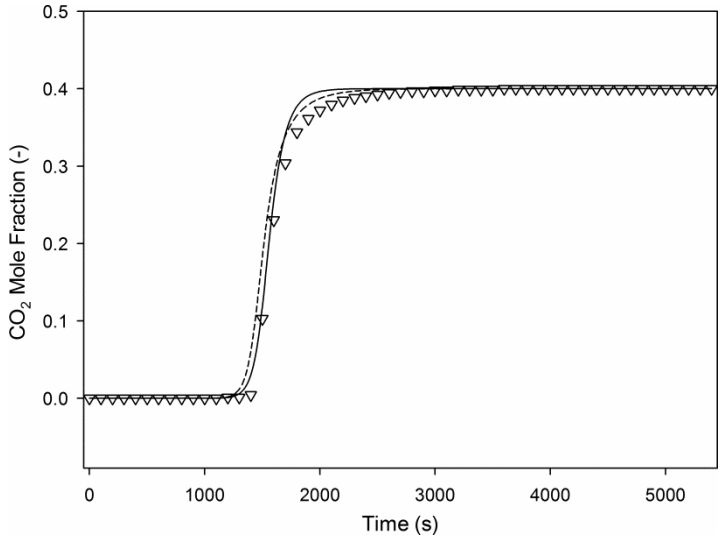

Figure 6.7: A comparison of simulations using values of 22×10^{-2} $kJs^{-1}m^{-2}K^{-1}$ (solid line) and 4.2×10^{2} $kJs^{-1}m^{-2}K^{-1}$ (dashed line) for the heat transfer coefficient of a stagnant gas with the experimental data for a CO_2 feed fraction of 0.4.

A comparison of the value for h_w^0 predicted by the graph from Ofuchi and Kunii (1965) and the value used by Park et al. (2000) is shown in Figure 6.7. The different values do not have a significant effect on the breakthrough time or the shape of the breakthrough curve simulated. Using a value of 4.2×10^{-2} $kJs^{-1}m^{-2}K^{-1}$ gives an SSD of 0.095 when combined for comparisons for all CO_2 feed fraction and a value of 22×10^{-2} $kJs^{-1}m^{-2}K^{-1}$ gives an SSD of 0.072. The lower value of h_w^0 appears to match the shape of the breakthrough curve more accurately but breaks through sooner giving the higher SSD. In this the system the accurate prediction of the breakthrough time is required and so a value for h_w^0 of 22×10^{-2} $kJs^{-1}m^{-2}K^{-1}$ is used.

6.4 Unmodified Activated Carbon PSA Cycle Modelling

Comparing simulations against the experimental data for breakthrough curves only allows the adsorption step of a PSA cycle to be validated. The simplicity of the experimental rig meant it was not possible to fully replicate a PSA cycle but it was possible to produce experimental data for a 3 step and a 4 step process, as shown in Section 5.6. Comparing the simulation output against the regenerative steps of a PSA cycle shows the suitability of the model for developing a PSA cycle. Both the 3 step and 4 step experimental results are compared to corresponding simulations.

6.4.1 3 Step Cycle

A full description of a 3 step cycle is given in Section 3.7.3 and the model that can replicate this is given in Section 4.11.3. The three step cycle includes an adsorption step at elevated pressure, a depressurisation and purge step, where the feed is pure nitrogen and in the first 60 seconds of the purge step the pressure is reduced to atmospheric pressure, and a pressurisation step.

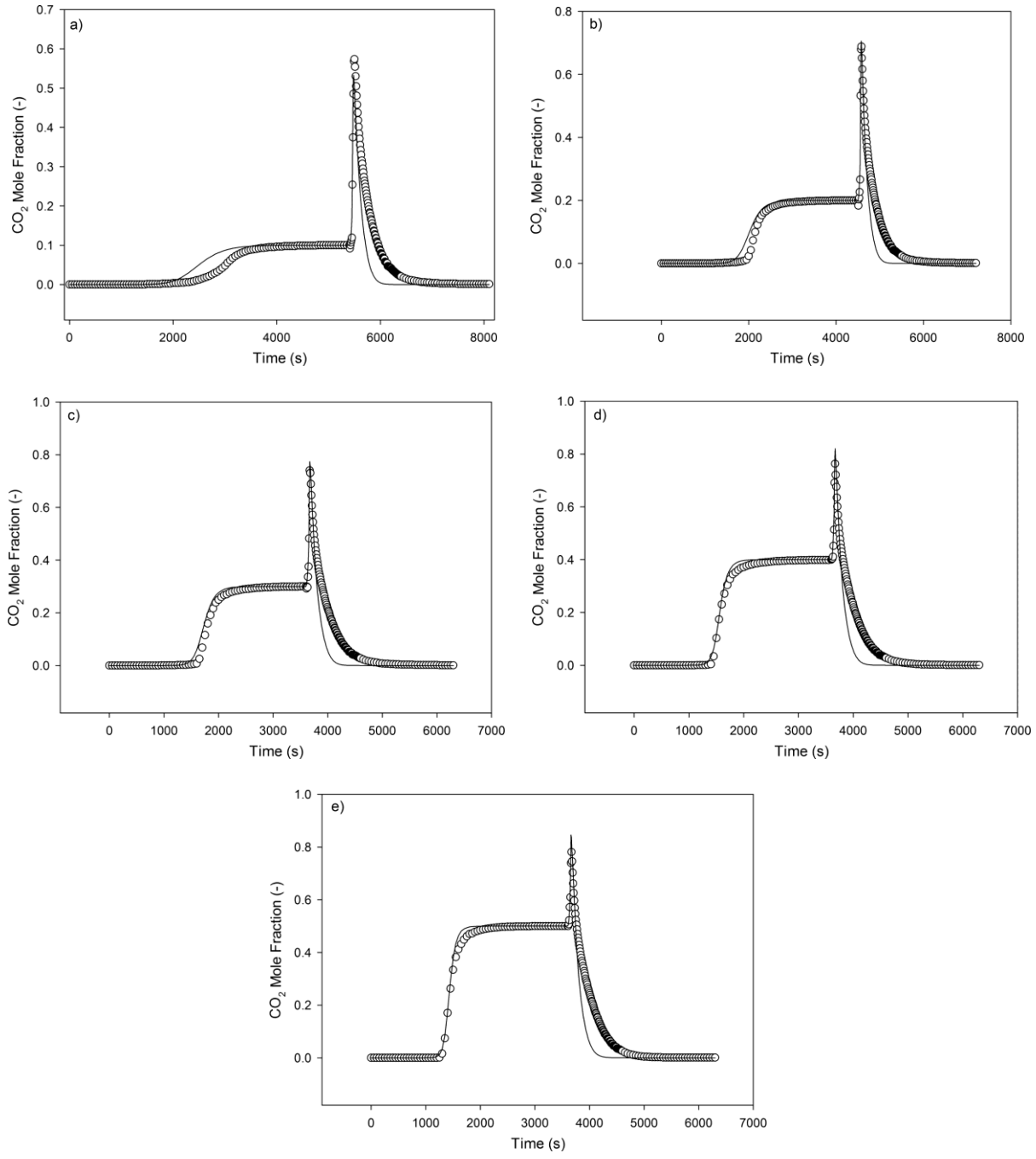

Figure 6.8: 3 step breakthrough curves with their corresponding simulation at CO_2 feed fractions of a) 0.1, b) 0.2, c) 0.3, d) 0.4 and e) 0.5

A comparison of the experimental carbon dioxide feed fraction at the bed exit for each carbon dioxide feed fraction against the corresponding simulation for the adsorption and purge step is given in Figure 6.8. The adsorption steps are the same

as for the breakthrough curves reported in Figure 6.2. The two key points of comparison for the purge step between the experimental and simulation data are the shape of the curve and the peak value. For all of the simulations, the peak in carbon dioxide in the outlet stream is accurately predicted during the depressurisation. This shows that the controlled depressurisation model used, described in Section 4.11.3, is able to replicate the depressurisation that is achieved by the back pressure regulator in the experiment. The purge that continues after the depressurisation is not simulated to the same degree of accuracy. The rate of decrease of carbon dioxide is much faster in the simulation giving a shorter time for the bed to return to a clean state. Table 6.4 shows the SSD for each carbon dioxide mole fraction and separates this between the adsorption step and the entire regeneration step. The regeneration step is more poorly matched than the adsorption step. The simulation of PSA cycles is limited in literature. Cavenati et al. (2006) and subsequent work in the same group by Lopes et al. (2011), did model a cyclic process. However, the sampling technique was insufficient to show the detail of the desorption peak and so these parts of the models are not validated. It is possible that the sudden changes in pressure result in changes in the mass transfer resistances of the system which have not previously been studied. However, a more likely cause is the empirical model for a system without a fixed bed, discussed in Section 6.2, is not capable of predicting the system response to the rapid change in pressure, flowrate and composition that occurs. The empirical model for the surrounding system is validated for the breakthrough of carbon dioxide at elevated pressure but has not been validated against experiments with rapid changes in conditions. It is not possible to study the rapid response of the surrounding system without the bed as the mass flow

controllers are not able to replicate the sharp increase in flowrate as the bed depressurises and desorption takes place. Schell et al. (2013) report a model used for a complete PSA cycle, although their system did not return the bed to a fully clean state. In their work, they are similarly not able to fully replicate the outlet carbon dioxide fraction during the regeneration steps, with the model consistently predicting a faster change in carbon dioxide fraction than is observed in their experiments. They implement an empirical model based on a stagnant tank with an improved fit to the experimental results.

Table 6.4: SSD between 3 step cycle experimental data and simulation data for the whole cycle and each of the steps for the unmodified activated carbon

	0.1	0.2	0.3	0.4	0.5
Whole Cycle	0.060	0.062	0.072	0.075	0.083
Adsorption Step	0.017	0.018	0.018	0.014	0.015
Regeneration Step	0.080	0.078	0.088	0.092	0.102

The other aspect for comparison is the peak value predicted in the simulation compared to the experimental result. The peak value of the 3 step desorption curve indicates the selectivity of the material for carbon dioxide over nitrogen. The peak values for the experimental data and the simulation data are presented in Table 6.5. Carbon dioxide feed fractions of 0.2 and 0.3 are predicted to a good degree of accuracy and the predictions at the other feed fractions are reasonable. For the lowest carbon dioxide feed fraction, the simulation under predicts the peak value. This is in agreement with Section 6.3.1, which suggests, based on the comparison of the experimental and simulation breakthrough curves in Figure 6.2, the carbon dioxide capacity is being under predicted for a feed fraction of 0.1. The simulations of the two highest carbon dioxide feed fractions over predict the peak values which

suggests at these feed fractions the selectivity is being over estimated. Considering the good agreement for the breakthrough curve in Figure 6.2 which is dependent on the carbon dioxide capacity, this would suggest the nitrogen capacity is being under predicted. The closeness of the values suggests that the model is able to replicate the changes occurring when the bed is depressurised. The same pattern between the exit peak values as the carbon dioxide feed fraction increases is seen in Table 6.5 for both the experimental and simulation data, with the gap between the peak values reducing each time.

Table 6.5: Comparison of the peak value of the desorption exit CO_2 fraction at each CO_2 feed fraction for the experimental and simulation data

CO_2 Feed Fraction (-)	Experimental Peak Desorption Exit CO_2 Fraction (-)	Simulation Peak Desorption Exit CO_2 Fraction (-)
0.1	0.57 ± 0.009	0.53
0.2	0.69 ± 0.003	0.71
0.3	0.75 ± 0.009	0.77
0.4	0.77 ± 0.006	0.82
0.5	0.78 ± 0.006	0.85

Despite the discrepancies between the experimental and simulation data, the agreement between the initial rise and the peak values suggests that the model is able to replicate the majority of the effects that occur during the regeneration of the bed in a PSA process.

6.4.2 4 Step Skarstrom Cycle

The 3 step cycle, although a useful indicator of the ability of the model to replicate regeneration steps, is not representative of a typical PSA process in industry. The most basic PSA cycle is a 4 step Skarstrom cycle which uses an adsorption step, a blowdown step, a purge step and a pressurisation step, as fully described in Section 3.7.4. This separates the depressurisation and purge steps that are grouped

together for a 3 step cycle. Therefore, during the blowdown step there is no flow passing through the bed. This allows the carbon dioxide outlet fraction to reach a maximum that is indicative of the selectivity of the material for the more adsorbed product over the less adsorbed product. The other key difference to the 3 step cycle is that the bed is not allowed to reach saturation, with the switch to the blowdown step occurring when the carbon dioxide exit fraction reaches 5% of the inlet fraction. As in the experiment, with the results presented in Section 5.6.2, the switch from the adsorption step to the purge step occurs at 1510 s, which was determined from the breakthrough curve.

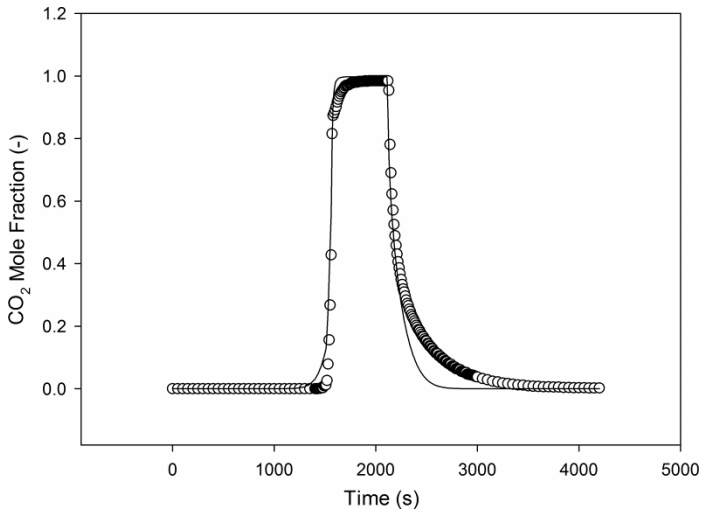

Figure 6.9: CO_2 exit mole fraction from experimental and simulation data for the adsorption, blowdown and purge steps of a 4 step Skarstrom cycle

The experimental and simulated CO_2 exit mole fractions for the first three steps of a 4 step Skarstrom cycle are reported in Figure 6.9. There is good agreement between the two, especially in the blowdown step. The overall cycle has an SSD of 0.050, with the blowdown and purge step having SSD values of 0.051 and 0.062 respectively. There is a slight discrepancy in the time for the system to reach the

maximum value, with the simulation reaching 99% of the maximum value 120 seconds sooner than the experimental data reaches 99% of its maximum value. The maximum values differ slightly, with the average experiment maximum at an exit fraction of 0.983 ± 0.06 and the simulation maximum at an exit value of 0.996. The maximum values for the 3 step cycle in Table 6.9 indicate that the simulation is over predicting the selectivity for carbon dioxide over nitrogen. This is further confirmed here with the simulation giving a higher maximum value than the experimental results.

As with the 3 step cycle, the carbon dioxide outlet fraction data presented in Figure 6.9 shows that the simulation predicts the bed being fully clean at an earlier time than is observed in the experimental data. The initial part of the purge step is replicated accurately but as the outlet carbon dioxide fraction approaches approximately 0.3, the simulation does not predict the same reduction in the rate the carbon dioxide outlet fraction is decreasing. The explanation for this is most likely to be measurement delays that occur in the experimental rig as suggested by Schell et al. (2013). However, this does not have the same rapid change in pressure as the three step cycle and so could indicate the simulation is not able to predict a mass transfer limitation for the purge step. It is not possible to be certain as very little work has investigated the validation of the regeneration steps for PSA systems.

Overall, the agreement between the experimental and simulation data gives confidence to further develop the model in order to represent effects of different PSA cycles. Being able to replicate the breakthrough time is key as this dictates the length of a step in the cycle. The first half of the purge step is also very important as a full cyclic PSA process would not return the bed to a clean state, as shown by

Schell et al. (2013). Therefore, the model accurately represents the aspects of the experimental data which are most important for a PSA system.

6.5 Modified Activated Carbon Modelling

In order to test the flexibility of the model, simulations were produced for the separation of CO_2/N_2 mixtures using the modified activated carbon. For this, the assumptions and correlations used for the unmodified material were used, i.e. multicomponent DSL, the Hsu and Haynes (1981) correlation for the dispersion coefficient, an energy balance without wall effects, the Yagi and Kunii (1960) correlation for the heat transfer coefficient and a stagnant heat transfer coefficient of $22x10^{-2}$ $kJs^{-1}m^{-2}K^{-1}$. The parameters that have been changed from Table 6.1 are given in Table 6.6. The extended DSL temperature independent parameters for the modified activated carbon are reported in Table 5.8.

Table 6.6: Parameters for the simulation of CO_2/N_2 breakthrough separations using modified activated carbon

Bed Length	m	0.065
Bed Density	kg m^3	191
Particle Diameter	m	1×10^{-3}
Pore Diameter	m	1.76×10^{-9}
Bed Voidage	-	0.4
Particle Voidage	-	0.85
CO_2 Heat of Adsorption	kJ mol^{-1}	26.6
N_2 Heat of Adsorption	kJ mol^{-1}	15.7

6.5.1 Breakthrough Modelling

A comparison between the experimental breakthrough data at each of the carbon dioxide feed fractions tested and their corresponding simulation is presented in Figure 6.10. The SSD and percentage difference in breakthrough time are reported in Table 6.7. Excellent agreement is seen between the simulation and experiment for

a carbon dioxide feed fraction of 0.2. There is a slight over prediction of the breakthrough time for a carbon dioxide feed fraction of 0.1 but the shape of the breakthrough curve is well matched, as evidenced by the low SSD. The breakthrough curves for carbon dioxide feed fractions of 0.3, 0.4 and 0.5 are all under predicted by the model, the extent of which increases at higher feed fractions. The cause of this stems from the isotherm model used. The carbon dioxide capacity predicted by the multicomponent DSL model, discussed in Section 5.5.1.1 and reported in Table 5.18, shows that the DSL model does not predict the change in capacity between 0.2 and 0.5 to be as large as the experimental results. The increase in capacity for a breakthrough with a carbon dioxide feed fraction of 0.4 to 0.5 is predicted to be 0.35 mol kg^{-1} for the DSL isotherm model but 0.64 mol kg^{-1} for the experimental data. This suggests that for the modified material, the isotherm model is not able to predict the breakthrough capacities at higher feed fractions.

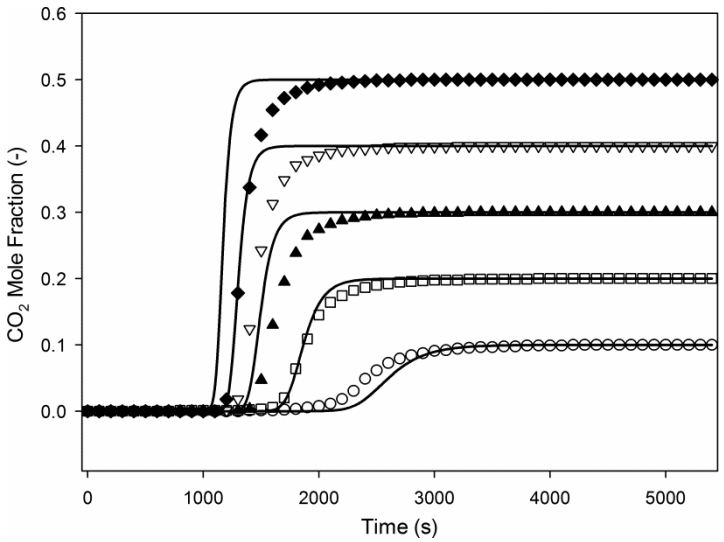

Figure 6.10: Simulation break through curves for the modified activated carbon material plotted against the corresponding experimental data with CO_2 feed fraction of 0.1 (white circles), 0.2 (white squares), 0.3 (black triangles), 0.4 (white triangles) and 0.5 (black diamonds).

Grande et al. (2013) reported similar under predictions of the breakthrough capacity at elevated pressures, however, this did not lead to under predictions of the breakthrough curve with their simulation results giving significantly longer breakthrough times than their experimental data for the highest pressures used. The results for the modified material differ from those for the unmodified material shown in Figure 6.2, where the lower feed fractions were not as well represented as the higher feed fractions. The results presented by Grande et al. (2013) and the results reported here show that the carbon dioxide capacity at elevated pressures is difficult to predict accurately.

Table 6.7: SSD values and the difference in breakthrough time for the comparison of the best fit simulation to the experimental breakthrough data for modified activated carbon.

CO_2 Feed Fraction	SSD	Breakthrough Time Difference
0.1	0.0083	-19.6%
0.2	0.0059	-1.8%
0.3	0.0275	5.5%
0.4	0.0460	7.6%
0.5	0.0655	9.1%
Total	0.1531	-

The shape of the simulation breakthrough curves in Figure 6.10 is similar to the experimental curves for carbon dioxide feed fractions of 0.1 and 0.2. However, for the higher carbon dioxide feed fractions, the simulations do not show the same degree of spreading as the experimental data. This is similar to the higher carbon dioxide feed fractions for the unmodified material in Figure 6.2, where the asymmetrical nature of the breakthrough curve was not represented. In both cases it is likely that the temperature change is not being fully accounted for, as a higher temperature rise and subsequent cooling would cause the breakthrough curve to

spread at the top. This is less important for the lower carbon dioxide feed fractions as the temperature rise is smaller and therefore the effect is less prominent. This suggests that the dispersion and mass transfer taking place is being accurately predicted by the correlations used. It is possible to use different correlations for the heat transfer coefficient to predict greater temperature changes. However, as discussed in Section 6.3.2.4, increased temperature changes result in the breakthrough time not being accurately represented, which is the focus of this work. As with the unmodified material, a significant temperature rise was not observed in the experimental temperature profile for the modified material and so it is also not possible to validate the temperature change taking place.

6.5.2 PSA Cycle Modelling

As with the unmodified material, simulations were carried out to replicate the PSA cycles for the modified activated carbon. A description of the simulation of 3 and 4 step cycles is given in Section 3.7.

6.5.2.1 Three Step Cycle

A comparison of the experimental data for a 3 step cycle and the simulation data for each CO_2 feed fraction for the adsorption and purge step in a 3 step cycle is presented in Figure 6.11. The adsorption step matches the results of the breakthrough curves reported in Figure 6.10. For the purge step, the initial increase in exit carbon dioxide mole fraction is accurately simulated but the peak value and the decrease in exit carbon dioxide mole fraction are not well matched. Table 6.8 reports the normalised SSD for each of the carbon dioxide mole fractions. The standard difference between the experimental and simulation data for the regeneration step is much larger than the adsorption step. The regeneration step

values are comparable to the SSD values for the unmodified activated carbon reported in Table 6.4. The initial increase shows that the general behaviour is being replicated. The discrepancy in the peak values between the simulation and experimental data is quantified in Table 6.9. The model is predicting a much higher selectivity for the carbon dioxide over nitrogen than is being observed in the experiment. The most likely explanation is that the isotherm is not accurately predicting the capacity for nitrogen. Garcia et al. (2013) showed that for CO_2/H_2 mixtures the DSL model tended to under predict the hydrogen uptake, especially at low CO_2 feed fractions. The extended DSL isotherm predicts low nitrogen capacities, given in Table 5.18, due to the interaction of the parameters on the two sites for the DSL isotherm, suggesting a high selectivity for carbon dioxide over nitrogen. In contrast to the poor agreement for the modified material, the peaks for the purge step using the unmodified activated carbon match with reasonable accuracy, as shown in Table 6.5. The predicted selectivities using the multicomponent DSL isotherm for the unmodified and modified activated carbons are given in Table 6.10. The predicted carbon dioxide selectivities for the unmodified material are considerably lower than the modified material and explain the much higher peak values predicted for the modified material in Table 6.9.

Table 6.8: SSD between 3 step cycle experimental data and simulation data for the whole cycle and each of the steps

	0.1	0.2	0.3	0.4	0.5
Whole Cycle	0.065	0.064	0.075	0.082	0.093
Adsorption Step	0.009	0.006	0.032	0.050	0.076
Regeneration Step	0.089	0.084	0.091	0.096	0.102

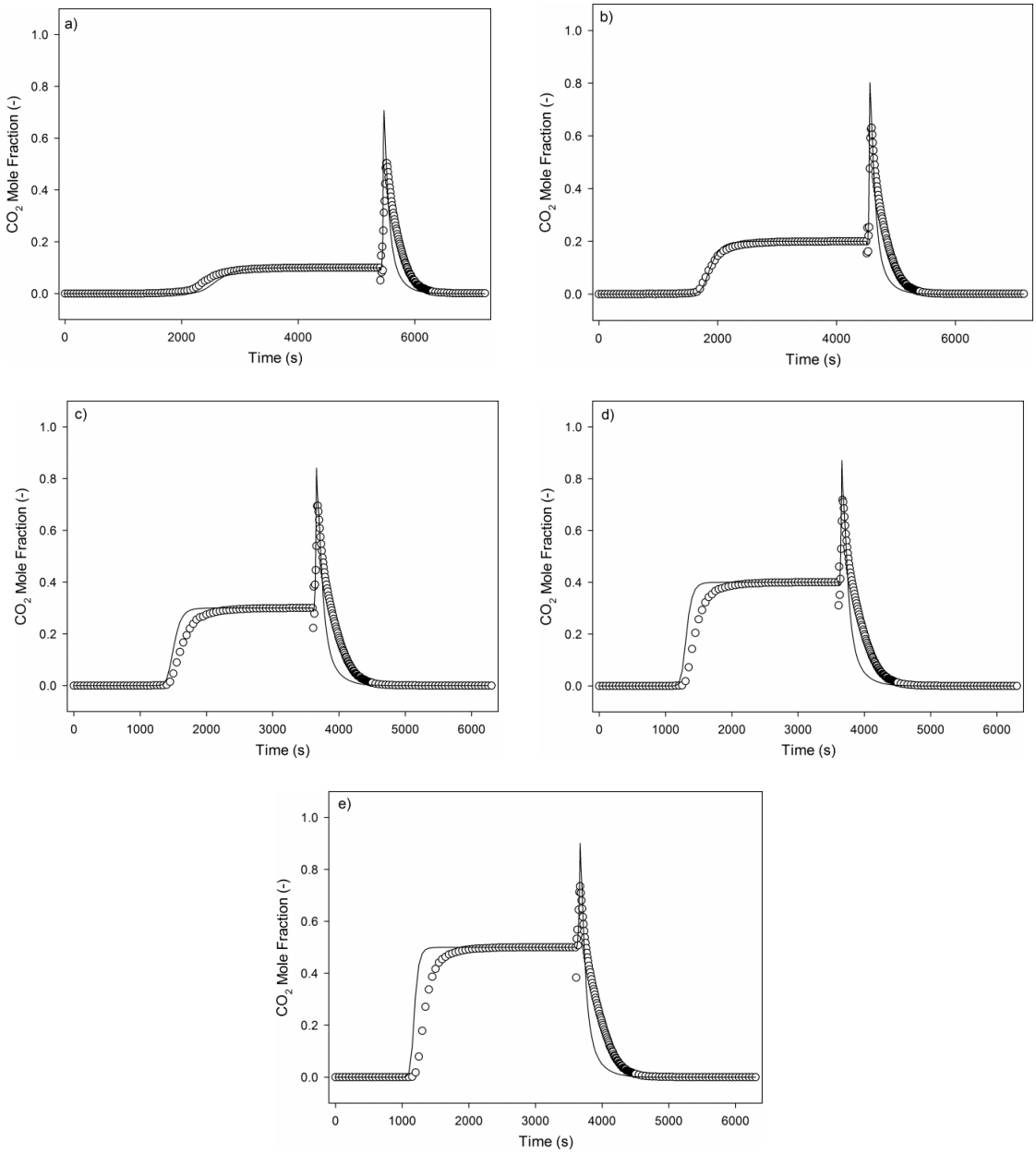

Figure 6.11: 3 step breakthrough curves for modified activated carbon with their corresponding simulation at CO_2 feed fractions of a) 0.1, b) 0.2, c) 0.3, d) 0.4 and e) 0.5

Table 6.9: Comparison of the peak value of the desorption exit CO_2 fraction at each CO_2 feed fraction for the experimental and simulation data for the modified activated carbon

CO_2 Feed Fraction (-)	Experimental Peak Desorption Exit CO_2 Fraction (-)	Simulation Peak Desorption Exit CO_2 Fraction (-)
0.1	0.51 ± 0.015	0.71
0.2	0.63 ± 0.006	0.80
0.3	0.70 ± 0.003	0.84
0.4	0.71 ± 0.029	0.87
0.5	0.74 ± 0.008	0.90

In a similar way to the unmodified material in Figure 6.8, Figure 6.11 shows the simulation is unable to match the purge of the bed after depressurisation for the modified material. The simulation predicts a more rapid decrease in the exit carbon dioxide mole fraction than is observed in the experiment. This is most likely due to the empirical model for the surrounding system being unable to predict the system response to the rapid changes in pressure and mole fraction. This is similar to the issues that Schell et al. (2013) reported in predicting the purge step.

Table 6.10: Comparison of the selectivity for carbon dioxide over nitrogen based on the multicomponent DSL isotherm calculated by dividing the carbon dioxide capacity by the nitrogen capacity.

Predicted Carbon Dioxide Selectivity over Nitrogen for the Unmodified Activated Carbon	Predicted Carbon Dioxide Selectivity over Nitrogen for the Modified Activated Carbon
1.5	9.0
3.3	22.3
5.7	40.3
8.7	61.4
12.9	96.5

6.5.2.2 4 Step Skarstrom Cycle

A comparison for a 4 step Skarstrom cycle was conducted between the experimental results and simulations. The four steps simulated were a pressurisation step (not shown), an adsorption step, a 600 second blowdown step with depressurisation occurring in the first 60 seconds and a 2100 second purge step. As with the experimental results, the system is switched from the adsorption step to the blowdown step after 1260 seconds. The experimental results for a 4 step Skarstrom cycle are compared to simulation results in Figure 6.12. Strong agreement is seen for the initial breakthrough in the adsorption step. This gives credence to the importance of the model predicting the breakthrough time over the shape of the

breakthrough curve that was discussed in Section 6.3.2. The SSD for the whole cycle is 0.049, which is skewed by the adsorption step as these points match perfectly. The blowdown step has a SSD of 0.077 and the purge step has a value of 0.053.

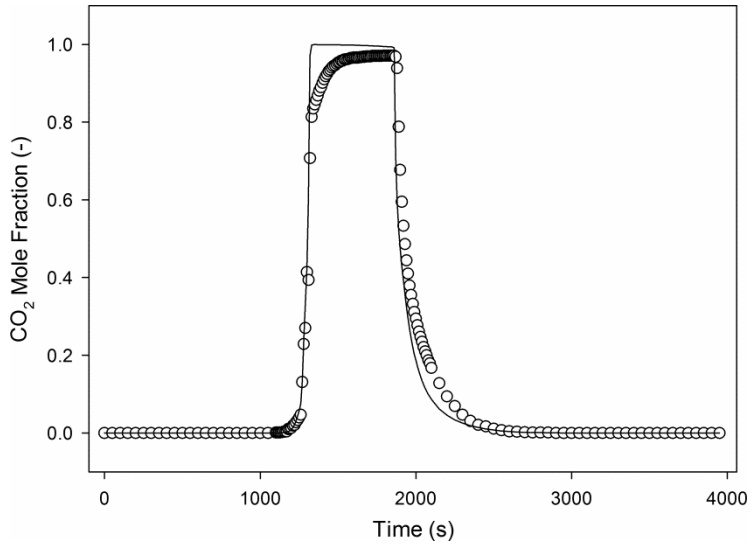

Figure 6.12: CO_2 exit mole fraction from experimental and simulation data for the adsorption, blowdown and purge steps of a 4 step Skarstrom cycle using modified activated carbon

The blowdown step occurs from 1260s to 1860s. The initial rise is well replicated but the broadening of the experimental curve as the system reaches equilibrium is not represented by the simulated results. As with the unmodified material, this is most likely due to the response of the surrounding system taking time to equilibrate. During the 60 second depressurisation the velocities through the CO_2 analyser are very high but after this there is no flow through the system so the equilibration needs to occur by diffusion. There might also be some lag in the system due to the 75 second response time of the analyser. The average maximum value for the experimental data was 0.985 ± 0.011 whereas the maximum value for the simulation was 0.9996. The maximum value for the simulation suggests a selectivity for carbon

dioxide over nitrogen of 2500, which is unlikely considering the capacity shown for the pure component isotherms. This is the same discrepancy that was observed for the 3 step model and emphasised by the high selectivities that the DSL isotherm predicts in Table 6.10. This further suggests that the nitrogen capacity is being under predicted by the multicomponent DSL isotherm.

The purge curve shown in Figure 6.12 is represented to a high degree of accuracy. Towards the lower exit carbon dioxide mole fractions, the simulation predicts a slightly higher rate of decrease than the experimental data. The SSD for the purge step of 0.053 is lower than any other cyclic simulation. It indicates a better fit than for the purge step of the unmodified material which has an SSD of 0.062. Compared to the 3 step, which had an SSD of 0.088 for the unmodified material and 0.092 for the modified material, the fit is considerably better. This indicates that the 3 step cycle model is not predicting the purge step as the system cannot respond to the sudden change in pressure and flowrate. However, for the four step cycle model it is possible to replicate the purge curve to a higher degree of accuracy.

6.6 Parameter Sensitivity Analysis

The main use for the model is to test adsorbents for their suitability for use in PSA systems. However, it can also be used to aid design of adsorbent materials by investigating which properties of the material have the biggest effect on the breakthrough curves, both in terms of the breakthrough time and the shape of the breakthrough curve. It is clear that for a given system it is desirable to have a long breakthrough time and a steep breakthrough curve as this maximises the use of the bed. Several parameters that can be controlled by the design of the adsorbent pellets were varied within the model and the breakthrough curves compared. For

each parameter a base case was established based on the parameters for the unmodified activated carbon as given in Table 6.1. The parameter was then varied, whilst keeping all other parameters constant, and the breakthrough curves compared. There were three parameters that had a significant effect on the breakthrough curve, the particle diameter, the bed voidage and the particle voidage. These results are reported in the subsequent sections.

6.6.1 Particle Diameter

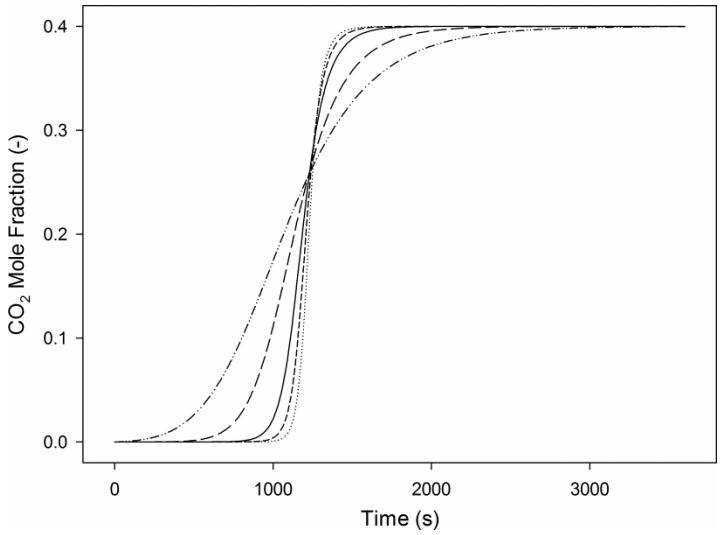

Figure 6.13: Sensitivity analysis for particle diameters of 1 x 10^{-4} m (dotted line), 5 x 10^{-4} m (short dashed line), 1 x 10^{-3} m (solid line), 2.5 x 10^{-3} m (long dashed line) and 5 x 10^{-3} m (dashed and dotted line).

The particle diameter affects the gas flow through the system and the pressure drop across a bed, resulting in a noticeable effect on the breakthrough curve. It was assumed that a change in particle diameter did not affect any other properties in the bed, i.e. the bed voidage remained constant. The correlations used for parameters such as the dispersion coefficient are built into the model and therefore varied appropriately. It was assumed that all correlations were valid for all particle diameters tested. The breakthrough curves for particle diameters of 0.1, 0.5, 1, 2.5

and 5 mm beads are given in Figure 6.13. As the particle diameter increases, the shape of the breakthrough curve is severely affected. The breakthrough capacity remains almost constant, as evidenced by the same fixed point at which all of the curves cross at. The capacity is expected to remain constant, as observed, since the particle diameter does not affect the adsorption capacity of the material or the amount of material in the system.

Table 6.11: Predicted values for the Reynolds number, dispersion coefficient, overall CO_2 mass transfer coefficient, CO_2 film mass transfer effect and CO_2 pore mass transfer effect at the particle diameters simulated

Particle Diameter (m)	Reynolds Number (-)	Dispersion Coefficient ($m^2\ s^{-1}$)	Overall CO_2 Mass Transfer Coefficient (s^{-1})	CO_2 Film Mass Transfer (s^{-1})	CO_2 Pore Mass Transfer (s^{-1})
1×10^{-4}	0.12	2.31×10^{-7}	0.158	49.2	42.7
5×10^{-4}	0.49	6.75×10^{-7}	0.137	2.36	1.71
1×10^{-3}	1.22	1.50×10^{-6}	0.099	0.67	0.43
2.5×10^{-3}	3.05	4.37×10^{-6}	0.035	0.14	0.068
5×10^{-3}	6.10	9.41×10^{-6}	0.011	0.043	0.017

As discussed in Section 5.4.1, the shape of the breakthrough curve is strongly dependent on the dispersion taking place and the mass transfer limitations. For each of the particle diameters tested, the values of the dispersion coefficient and the mass transfer coefficient that are predicted by their corresponding correlations are reported in Table 6.11. The dispersion coefficient is the degree of turbulent spreading that is occurring and therefore is greater at higher Reynolds numbers. An increase in particle diameter increases the turbulence in the system and therefore leads to a significant increase in the dispersion taking place. The mass transfer limitations also greatly increase as the particle diameter increases. The overall carbon dioxide mass transfer coefficient and the contribution of film and pore mass transfer limitations are

reported in Table 6.11. The third mass transfer effect, the micropore mass transfer, is assumed to have a constant contribution of 0.158 s^{-1} as this would be unaffected by the size of the particle used (Ruthven, 1984). It is clear that an increase in particle diameter significantly increases the mass transfer limitations. At very low particle diameters, only the micropore resistance is significant but above particle diameters of 1 mm, the film and pore mass transfer resistances become the controlling influences.

As discussed by Garg and Ruthven (1975), the mass transfer and dispersion effects are additive. Therefore, the greater dispersion and higher mass transfer effects lead to an increase in the degree of spreading that is occurring in the system. The effects are not as significant as the particle diameter decreases below 1 mm. Below this value the dispersion effects become negligible and the mass transfer is only limited by micropore diffusion. However, above 1 mm, small increases in particle diameter are seen to have very large effects. It can be inferred from this, therefore, that particle diameters should be minimised. Small particle sizes, however, have a detrimental effect on the pressure drop across the bed. The effects are not seen here as the bed is too small, but at industrial scale the pressure drop would increase rapidly as the particle size diminished (Mehta and Hawley, 1969). Therefore, a compromise would be needed between the two effects which could be quickly judged by use of the model presented here.

6.6.2 Bed and Particle Voidage

The voidage in the system indicates the amount of active adsorbent material in the bed. As discussed in Section 5.5.1.2, the carbon dioxide capacity on a volumetric basis rather than a mass basis is a much better indicator of the capacity of a PSA system for a fixed volume bed. Therefore, it is important to consider the bed density

that a given adsorbent would have. The degree to which modifying the bed density of the system affects the breakthrough curves has been tested by modifying the bed and particle voidages.

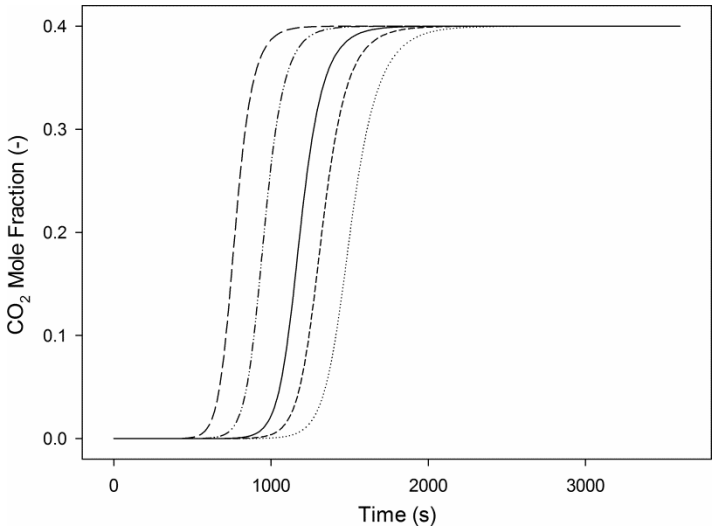

Figure 6.14: Sensitivity analysis for bed voidages of 0.3 (dotted line), 0.4 (short dashed line), 0.48 (solid line), 0.6 (dashed and dotted line) and 0.7 (long dashed line)

The bed voidage cannot be modified without affecting the bed density. Therefore, the bed density is modified accordingly to match a chosen bed voidage. This was achieved by assuming the material and particle densities remain constant, i.e. the particle was manipulated in such a way that the packing of the material changed without the material itself being modified. Simulations using voidages of 0.3, 0.4, 0.48, 0.6 and 0.7 were investigated as voidages can range from the densest regular packing for rhombohedral with a bed porosity of 0.26 up to the loosest forms with bed porosities of 0.88 (Dullen, 1979). Breakthrough curves for these simulations are plotted in Figure 6.14. It is apparent that the main effect is on the breakthrough time rather than the shape of the breakthrough curve. There is slightly more spreading observed for lower values of bed voidage as the interstitial velocity will be higher for a

smaller bed voidage. However, this effect is minimal compared to the change in capacity.

With a particle density of 500 kg m^{-3}, an increase in bed voidage of 0.1 results in a bed density decrease of 50 kg m^{-3}. Therefore a bed voidage of 0.3 has a bed density of 350 kg m^{-3} and a bed voidage of 0.7 has a bed density of 150 kg m^{-3}. This means at lower bed voidages there is more active adsorbent present, increasing the capacity of the overall system. Therefore, the design of any adsorbent should alter the shape of the material to increase the packing as this increases the carbon dioxide capacity.

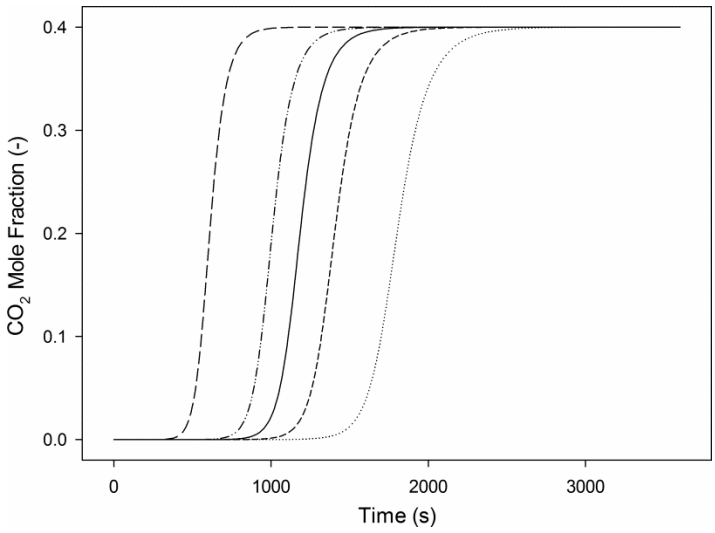

Figure 6.15: Sensitivity analysis for particle voidages of 0.6 (dotted line), 0.7 (short dashed line), 0.75 (solid line), 0.8 (dashed and dotted line) and 0.9 (long dashed line)

The particle voidage also has a significant role to play in the capacity of a given system. In order to vary this, it is assumed that the material density and the bed voidage remain constant. The particle and bed density can then be calculated for a chosen particle voidage. The simulation was run using particle voidages of 0.6, 0.7,

0.75, 0.8 and 0.9 and corresponding bed densities of 534, 428, 321, 262, 214 and 107 kg m^{-3}. This covers the full range of particle voidages possible for activated carbons (Dullen, 1979). The results of the simulations are presented in Figure 6.15. The shape of the breakthrough curve is unaffected as the flow regime is not impacted by the particle voidage and has a minimal effect on the mass transfer effects. The breakthrough capacity is strongly affected as there is more of the adsorbent in the same bed volume. In a similar way to the bed voidage, decreasing the particle voidage has a strong effect on the overall capacity and should be minimised to increase the capacity.

The degree to which changes to the bed and particle voidages affect the capacity of the system highlight the importance of maximising the amount of activated material. This is only an indication and might not possibly take in to account all of the effects that a change in bed voidage and particle voidage might have. Modifications to activated carbon tend to be based on opening up more of the pore structure which increases the pore volume (Chen et al., 2013). However, this increase in pore volume is more detrimental due to the decrease in bed density without giving sufficient increases in the adsorption capability of the material itself. This model shows that the focus needs to be on the structure of the material and maximising the bed density without reducing the capacity of the material.

6.7 Conclusion

A model has been established and validated against experimental data. This was first performed using the breakthrough curves for the separation of CO_2/N_2 mixtures using the unmodified activated carbon. By careful selection of suitable correlations, the model was able to simulate the breakthrough curves to a reasonable degree of

accuracy using independent values for the parameters rather than fitting the model to the experimental data. The model was then further validated against cyclic experimental data for the unmodified material. The 3 step and 4 step model was simulated to a good degree of accuracy, although the purge step in the simulation was faster than the experimental data.

The breakthrough curves for the modified material are not as accurately simulated. The breakthrough results suggest that the system requires an isotherm that predicts a higher capacity for carbon dioxide at higher carbon dioxide partial pressures. The PSA cycle simulations also suggest that the predicted nitrogen capacity needs to be higher as the selectivities found in the experiments are significantly lower than those predicted by the simulation. The purge step for the 4 step cycle is accurately represented, giving an overall good prediction of the 4 step cycle, with important variables such as the breakthrough time accurately predicted. This gives evidence for choosing parameters that can accurately predict the breakthrough time. The reasonable agreement suggests, to a first approximation, this model would be capable of indicating the most suitable way to operate a PSA system.

A parameter sensitivity study has shown that there are relatively few material parameters which strongly affect the breakthrough of a system. The particle diameter, bed void and particle void have a significant effect on the breakthrough curve. The particle diameter affects the shape of the breakthrough curve as the dispersion and mass transfer are sensitive to changes in it. Above 1 mm diameter particles, the spreading becomes significant. This suggests that in the design of a particle, the critical diameter, above which dispersion and mass transfer effects occur, needs to be found. Both the bed void and particle void affect the volume of

active material in a given fixed bed. In both cases lower voids result in longer breakthrough times without significant effects on the shape of the breakthrough curve. The extremes that were tested may not be achievable but it adds further evidence to the findings in Chapter 5 that the bed density needs to be maximised either through the design of the particle and packing of the bed or through the design of the material itself.

The model has been established in such a way that by knowing the dimensions of the bed, the physical characteristics of the adsorbent and the temperature dependent isotherm parameters, the system can be modelled straightforwardly. This can then be used to compare the dynamic response of the system to a first approximation without requiring experiments to be conducted which require a reasonable amount of the material to be produced. The validation of the model means it can be used to investigate the properties of a PSA system, which is done in Chapter 7.

Chapter 7 – Pressure Swing Adsorption Cycle Development

7.1 Introduction

The model presented and validated in Chapter 6 has been applied to develop pressure swing adsorption (PSA) systems that capture of carbon dioxide from syngas in integrated gasification combined cycle (IGCC) power plants. This is based on the possibility of them being less expensive and more efficient than the liquid absorption counterparts (Radosz et al., 2008). The removal of carbon dioxide from syngas by a PSA system presents a relatively unique situation in requiring the maximum purity and capture rate of both the heavy and light components. For post-combustion carbon dioxide capture only the carbon dioxide product is important as the nitrogen product is simply vented. Other more traditional systems also only captured one product, often the light product. The development of PSA processes was realised in the Skarstrom cycle aimed at producing oxygen and the process has been widely applied to hydrogen production, where the more strongly adsorbed components are not required (Ruthven, 1984).

The application of PSA systems for the recovery of both the light and heavy component at high pressures has not been widely studied. Casas et al. (2013b) have produced the most comprehensive study, studying a 10 step process and the conditions that affect the purity of the gases produced and the amount of each gas that is captured in the product. Schell et al. (2013) validated a 6 step model against experimental results without optimising the system. The work mainly aimed to validate the experimental set-up and therefore little consideration was given to producing the best process design. Agarwal et al. (2010) developed a superstructure-based simulation that was able to design a process for the separation of CO_2/H_2 mixtures for pre-combustion capture based on maximising the carbon

dioxide capture rate and purity whilst minimising the power consumption of the system. Xiao et al. (2009) investigated a vacuum pressure swing adsorption (VPSA) system for the separation of carbon dioxide from syngas at elevated temperatures and pressures.

The main aim of these studies was to produce a high quality carbon dioxide product, with Agarwal et al. (2010) being the only one to detail the quality of the light product but without carrying out an optimisation of any aspect of this. The main effect that a PSA system would have on the efficiency of an IGCC power plant is the loss of hydrogen. Therefore, it is very important to minimise this loss and it must be taken into consideration when evaluating PSA systems. The literature work also does not highlight the impact that each process step has on the overall system performance. The systems described have been studied to prove if the concept is capable of producing sufficient quality carbon dioxide product. However, in order to advance this technology the importance of each step in a PSA cycle needs to be understood to be able to evaluate which aspects are economically viable.

The work presented in this chapter addresses these issues to give a fuller understanding of the PSA processes which could be applied for industrial carbon capture processes. The simulations have been carried out to study the separations of CO_2/N_2 mixtures, as this was the separation validated in Chapter 6. Therefore, the quantitative values found for the quality of the gases produced will not be directly applicable to IGCC operations. However, the impact that each process step has on the quality of gases will be translatable to that process. The work is presented in such a way so as to build the PSA process from a basic 4 step Skarstrom cycle to a 10 step cycle implementing pressure equalisation, purge gas recovery and the use of

a heavy product rinse. Each of the new steps are evaluated to understand the effect they have on the quality of both the carbon dioxide product and the nitrogen product.

7.2 Model Set-Up

The aim of this chapter is to investigate different process configurations and to suggest improvements for the development of a PSA process for the capture of carbon dioxide from IGCC power plants. In order to do this a consistent model needs to be used. The axial dispersed plug flow model that is described in Section 4.6 is implemented. The only difference to the validated model is that the multicomponent Langmuir-Freundlich (LF) isotherm is used instead of the Dual-site Langmuir (DSL) isotherm. It was found that the LF isotherm gave a higher model stability which became important for PSA processes with a large number of beds and many discontinuities. The effect of using these two isotherms on the system is described in Section 6.3.2.1, where the DSL isotherm is shown to give a better fit to the experimental data. The LF model under predicts the breakthrough time by 6.9% compared the DSL model under prediction of 4.2%. However, as this chapter aims to study the aspects of a PSA cycle which will give significant process gains, the small under prediction for breakthrough time given by the LF isotherm will not affect the recommendations made.

Table 7.1: Gas stream feed conditions

Flowrate	(mol s^{-1})	7.2×10^{-5}
Pressure	(Pa)	2.5×10^{6}
Temperature	(K)	298
CO_2 Mole Fraction	(-)	0.4
N2 Mole Fraction	(-)	0.6

All other parameters are unaffected and remain the same as for the model used in Section 6.3.1. The feed stream is kept the same for all process configurations tested and these properties are given in Table 7.1. A full description of the solver set-up, the model configuration and the solution methods are given in Chapter 4.

7.3 Four Step Cycle

The Skarstrom cycle is the simplest PSA cycle, developed initially for separating oxygen and nitrogen. It has four basic steps: adsorption, blowdown, purge and pressurisation. The conditions of each of these steps can vary as well as the duration of each step so that it can be applied to a wide range of industrial separations (Ruthven, 1984). A 4 step Skarstrom cycle was validated against experimental data in Section 6.4.2. Here the conditions are altered for the cycle in order to maximise the carbon dioxide and nitrogen purities and capture rates.

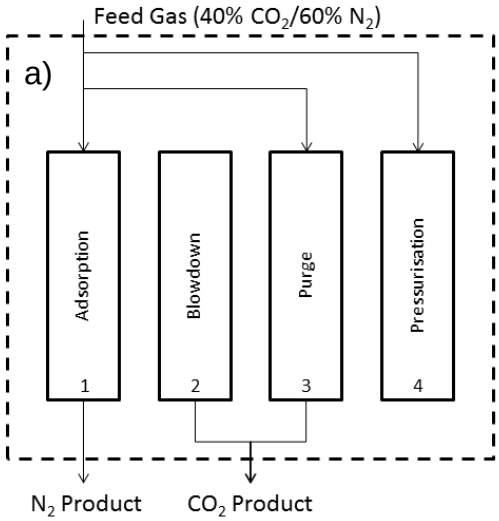

b)

1	Ad	BD	Pur	Press
2	BD	Pur	Press	Ad
3	Pur	Press	Ad	BD
4	Press	Ad	BD	Pur

Figure 7.1: 4 bed 4 step Skarstrom process configuration showing a) bed connections and b) bed sequencing. Ad – adsorption, BD – blowdown, Pur – purge with feed, Press – pressurisation.

A typical 4 step cycle is shown in Figure 7.1. The four process steps use high pressure adsorption, blowdown, purge step by a fraction of the feed gas and a

pressurisation step using a fraction of the feed gas. In order to realistically represent a PSA process unit some modifications were made to the model used in Section 6.4.2. These are mainly concerned with the adjustment of the feed conditions. First of all it was assumed that the pressurisation gas has the same properties of the adsorption feed gas stream rather than a pure nitrogen stream. In the industrial process the feed gas stream is at an elevated pressure and can therefore be used to pressurise the bed without the need for any additional equipment such as a compressor. The other key change is to purge the bed with a fraction of the feed gas stream. The main reason to use a pure nitrogen purge is to return the bed to a clean state, i.e. minimise the residual carbon dioxide in the bed. This results in a high nitrogen purity but reduces the nitrogen capture rate. For a gas turbine the purity of the light product would not need to be particularly high as a gas turbine can operate across a range of hydrogen concentrations (Miller, 2011). The use of a fraction of the feed gas for purging the system has been employed previously when the heavy product is also required (Casas et al., 2013b; Schell et al., 2013). This also limits the dilution of the heavy product by the light product.

It is possible to operate the bed in both a co-current and counter-current operation. In counter-current operation the gas flows in the opposing direction to the adsorption step during blowdown and purge step. This is used to minimise the amount of the more strongly adsorbed product in the light product (Ruthven, 1984). However, due to the desire to capture both the light and heavy product, the effect of using counter-current steps was evaluated. As there are no interactions between the 4 beds during the cycle, only one bed is simulated to reduce the computational time. The other beds are assumed to operate in the same way but one quarter of a cycle out of sync

with the previous cycle as shown in Figure 7.1. This was tested by running a simulation using 4 beds and there was no difference between the results for each bed. For the one bed operation the time was kept constant for each step by recording the adsorption time and then using this as the step length for the remaining steps in each cycle.

The co-current and counter-current operations were compared by running the two scenarios under the same conditions, given in Table 7.2. The feed stream is split between the adsorption, purge and pressurisation steps. The fractions were found iteratively in such a way that the length of the adsorption and pressurisation step would be the same. The fraction for the purge step was chosen to give the required cleaning of the bed whilst minimising loss of nitrogen. The purity of the carbon dioxide outlet set as the breakthrough point is chosen as a balance between the carbon dioxide and the nitrogen purity. The results reported are for the third cycle of a system and at this point the system has reached cyclic steady state, judged by the adsorption time for all beds matching the adsorption time of the previous step.

Table 7.2: Feed conditions and set adsorption switch point for a 4 step Skarstrom cycle

Feed Fraction for Adsorption	(-)	0.45
Feed Fraction for Purge	(-)	0.1
Feed Fraction for Pressurisation	(-)	0.45
CO_2 Mole Fraction Breakthrough Point	(-)	0.22

7.3.1 Cyclic Outputs

The pressure profile for both operations is reported in Figure 7.2 as the counter-current operation does not affect the pressure profile at the bed exit. The blowdown step shows the reduction in pressure. This is non-linear and is controlled by

maintaining a fixed exit flowrate at the bed exit in a similar way to a valve, as described in Section 4.11.3. It would be possible to adjust the exit flowrate so that the depressurisation time matched the length of the adsorption step, however, this does not affect the results of the system. In a similar way the pressurisation is not quite linear due to the system controlling the exit velocity at 0 ms^{-1}, as described in Section 4.12.1.

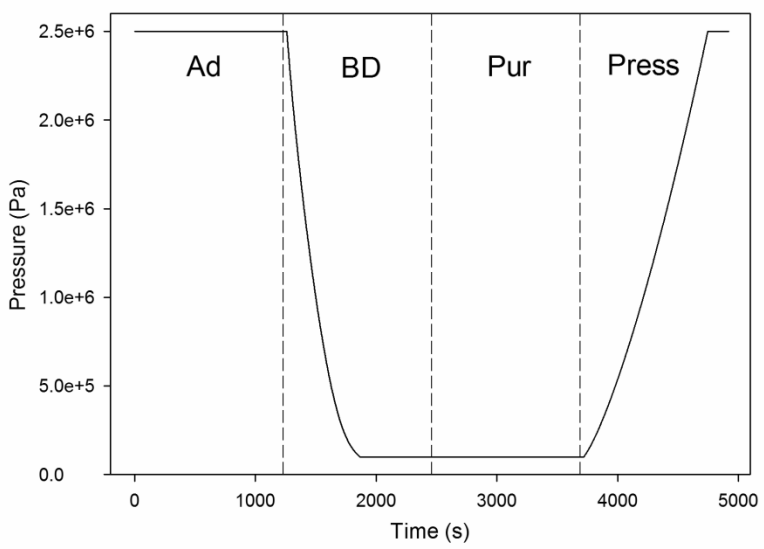

Figure 7.2: Pressure profile for a 4 step cycle

The exit carbon dioxide fraction for a 4 step Skarstrom cycle using co-current flows is shown in Figure 7.3a. The adsorption step has a low level of carbon dioxide in the exit stream. This is caused by the bed not being completely purged of carbon dioxide and then being pressurised with a fraction of the feed gas stream. The adsorption step continues until the exit fraction reaches 0.22, as set in the simulation. The system then switches to blowdown, where the fraction of carbon dioxide rises rapidly to a peak value of 0.986 and then levels off as the minimum pressure is reached. During the period between minimum pressure being reached and the start

of the purge step the carbon dioxide fraction remains constant as there is no flow in the system. The purge step then causes a reduction of the exit fraction of the bed to 0.476 as the residual high fraction of carbon dioxide is pushed out by the purge stream. The carbon dioxide in the outlet stream is reduced as the pressure is increased. This is due to the capacity of the adsorbent for carbon dioxide increasing with the pressure leading to residual carbon dioxide in the bed being adsorbed, along with fresh carbon dioxide in the feed stream.

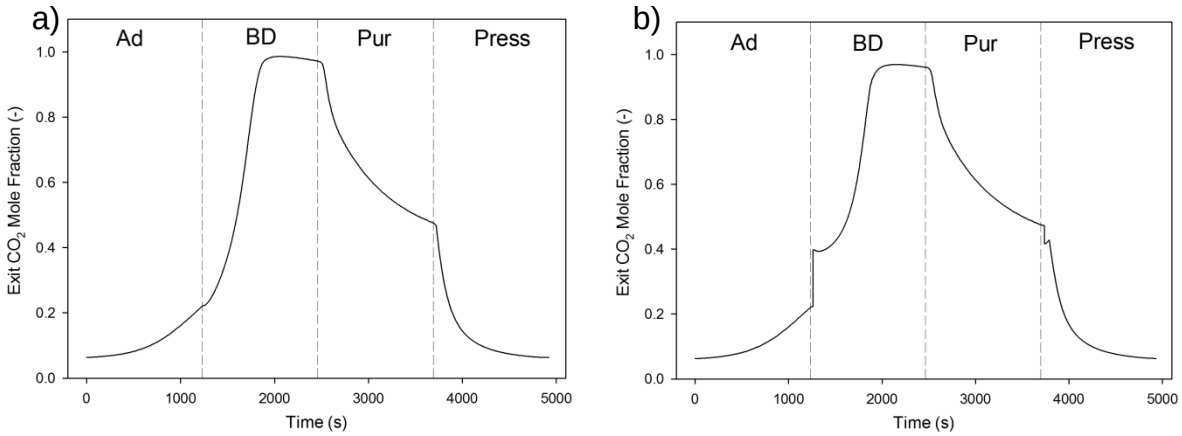

Figure 7.3: CO_2 exit fractions for a 4 step Skarstrom cycle for bed 1 as shown in Figure 7.1 using a) co-current operation and b) counter-current operation.

The outlet carbon dioxide mole fraction for a counter-current system is reported in Figure 7.3b. The main difference to the co-current cycle shown in Figure 7.3a is in the blowdown step. At the end of the adsorption step, the inlet of the bed becomes saturated with carbon dioxide and will therefore be at the same mole fraction as the feed, i.e. 0.4. Therefore, the outlet carbon dioxide mole fraction jumps to 0.4 when the bed is switched to counter-current operation for the blowdown step and the bed inlet becomes the bed exit. During the blowdown step the carbon dioxide mole fraction rises slowly and then at a rapid rate. The slow initial rate compared to the

co-current blowdown step in Figure 7.3a is due to the residual nitrogen at the back of the bed mixing with the carbon dioxide that is being desorbed, lowering the overall concentration of carbon dioxide. This is more prevalent whilst the bed is at higher pressures as the majority of carbon dioxide is released towards the end of the blowdown step at low pressures. As the residual nitrogen was not driven off during the depressurisation in the counter-current operation, it remains in the bed and lowers the peak value of carbon dioxide mole fraction in the outlet to 0.970. The bed being at equilibrium after the blowdown step causes the subsequent purge step to be very similar to that for the co-current operation, causing a reduction in mole fraction to 0.476 before the bed switches to co-current flow. The pressurisation step also gives a very similar carbon dioxide mole fraction profile as the bed is cleaned to a carbon dioxide mole fraction of approximately 0.4 during the purge step, meaning the switch in flow direction for the pressurisation step does not change the outlet concentration.

7.3.2 Capture Rates and Purities

From the results of the model it is possible to calculate the capture rate and the purity of both the nitrogen and carbon dioxide. The capture rate of the carbon dioxide is the amount of carbon dioxide in the outlet during the blowdown and purge steps divided by the total amount of carbon dioxide flowing in and the capture rate of the nitrogen is the amount of nitrogen in the outlet during the adsorption step divided by the total amount of nitrogen flowing in. The purities are the amount of each component output in the outlet stream during the steps in which that gas is collected, i.e. the adsorption step for nitrogen and the blowdown and purge step for the carbon dioxide, divided by the total amount of gas in those streams. The equations used to calculate these

values are given in Section 4.12.2. The important values from these figures are the nitrogen capture rate and the carbon dioxide purity. In an IGCC system where a CO_2/H_2 mixture needs to be separated, the capture rate of the hydrogen dictates the loss of efficiency in the system, as a high capture rate means a higher percentage of hydrogen in the feed stream is passed to the gas turbine. In the system simulated here, this is represented by the nitrogen capture rate. The required carbon dioxide purity will depend on the downstream application of the carbon dioxide, for sequestration this is typically 95% (Xiao et al., 2009). The nitrogen purity is not as important, as a gas turbine can operate over a large range of feedstock purities, with only the leading gas turbines able to operate with a hydrogen feed fraction above 0.9, and is more an indicator of the amount of carbon dioxide lost in the light product stream (Miller, 2011). The carbon dioxide capture rate will ideally be greater than 90% (Xiao et al., 2009), but it is less significant than the purity as the carbon dioxide product needs to be of sufficient quality for downstream processing.

Table 7.3: Capture rate and purities for carbon dioxide and nitrogen using a 4 step Skarstrom cycle with co-current and counter-current operation.

	Co-Current	Counter-current
CO_2 Capture Rate	84.6%	84.3%
CO_2 Purity	59.5%	58.9%
N_2 Capture Rate	56.5%	56.4%
N_2 Purity	88.7%	88.8%

The capture rates and purities of carbon dioxide and nitrogen for the co-current operation are reported in Table 7.3. The carbon dioxide purity is particularly low at 59.5%. As the entire blowdown and purge step products are collected, the residual nitrogen in the bed as well as the adsorbed nitrogen is collected. Figure 7.3a shows

that the fraction of carbon dioxide at the beginning of the blowdown step and the end of the purge step is low, which restricts the purity of carbon dioxide which can be achieved. The nitrogen capture rate is also low with a value of 56.5%. The low carbon dioxide concentrations in the blowdown and purge steps show that there is a large amount of nitrogen in the bed which is lost when it is captured in the carbon dioxide product. The carbon dioxide capture rate is relatively high and the nitrogen purity is comparable to a liquid absorption process. These are both controlled by the outlet carbon dioxide mole fraction at which the bed switches from adsorption to blowdown. Higher values for the switch carbon dioxide mole fraction would allow lower purge rates to occur which minimises the nitrogen loss and increases the carbon dioxide purity as there is less residual nitrogen in the bed. However, the nitrogen purity and carbon dioxide capture rate would also be decreased as more carbon dioxide would be collected in the nitrogen product during adsorption.

The capture rates and purities for the counter-current system are also reported in Table 7.3, with all of these values being comparable to the co-current operation. The similarity in the values is due to the entire contents of the blowdown and purge stream being captured for the carbon dioxide product. As long as the beds are returned to a similar state after the purge step, they will have the same amount of nitrogen and carbon dioxide in the system and therefore the pressurisation and adsorption step will not be different to the co-current set up. This suggests there is no advantage in using counter-current operation for a 4 step Skarstrom cycle. The main reason to use counter-current operation is to shift the carbon dioxide towards the front of the bed so as to not contaminate the nitrogen product (Ruthven, 1984).

However, in this work the operation is not set-up to maximise the purity of the nitrogen, negating the effects of counter-current operation.

A comparison with literature for either case is difficult as these exact conditions have not been reported in the literature. The work reported for high pressure separations use more than 4 steps in their cycle. Low pressure separations of CO_2/N_2 mixtures using 4 step cycles are more common for post-combustion capture but with slightly different process configurations as the focus is on the recovery of the carbon dioxide product only. Liu et al. (2011) considered a 4 step cycle similar to that shown in Figure 7.1a for a CO_2/N_2 separation using zeolite 13X (Z13X) but instead use the nitrogen product to purge the bed and vacuum conditions for the blowdown step. They achieved a carbon dioxide capture rate of 95.0% and a purity of 50.7%. Values for nitrogen were not given. Gomes and Yee (2002) employed a PSA cycle to a CO_2/N_2 separation using Z13X with the same configuration as Liu et al. (2011) and reported a nitrogen purity of 78% and capture rate of 50% without discussing the carbon dioxide capture rate or purity. Ko et al. (2002) also used the same configuration and reported nitrogen purities of 99% and nitrogen recoveries of 75.4% but to the detriment of the carbon dioxide purity of 24.4% and carbon dioxide capture rate of 9.4%. A different process configuration was used by Kikkinides et al. (1993) which is only achievable using VPSA. In that work the adsorption step was followed by a purge using the high purity carbon dioxide, after which the bed was depressurised to vacuum conditions. In doing this they achieved carbon dioxide purities of up to 96% and carbon dioxide recoveries of 77%, without discussing the quality of the nitrogen gas. This was only achieved through deep vacuum at 0.1 atm, with an increase to 0.3 atm resulting in carbon dioxide purity of 72% and a capture

rate of 39%. It is clear from literature values that the variation in results is large but the low carbon dioxide purity and nitrogen capture rate shown in Table 7.3 are comparable with literature. The simulated results also suggest that the typical 4 step Skarstrom cycle, even with process alterations, is not capable of producing the quality of gas required for an IGCC power plant with carbon dioxide capture.

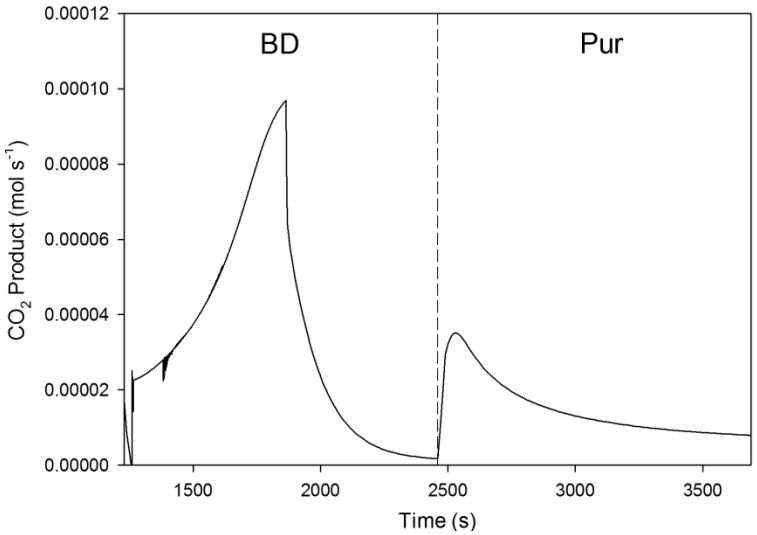

Figure 7.4: The amount of carbon dioxide produced during the blowdown and purge steps for a 4 step co-current Skarstrom cycle.

The 4 step Skarstrom cycle has been shown to not give sufficient carbon dioxide purity or nitrogen capture rate, but the simulation results from it indicate how best to improve the process. The carbon dioxide purity and nitrogen capture rate are strongly interrelated as a higher purity in the carbon dioxide product will mean less nitrogen is present and therefore this nitrogen will be in the nitrogen product, i.e. the nitrogen capture rate will be higher. From the profile of exit carbon dioxide mole fraction in Figure 7.3, it is clear that the overall carbon dioxide purity at the outlet is impacted by the low fraction in the initial parts of the blowdown step and at the end of the purge step. These parts of the steps are nitrogen rich and recycling them to the

process will reduce the nitrogen captured with the heavy product. Figure 7.4 shows the amount of carbon dioxide released during the blowdown and purge steps. The majority of the carbon dioxide is released during the blowdown step and therefore this step should be the focus of process modifications.

7.4 Pressure Equalisation

In order to produce higher purity carbon dioxide, the fraction of carbon dioxide in the blowdown stream needs to be higher. Co-current depressurisation, which partially depressurises the bed before switching to counter-current blowdown, has been employed to drive off residual nitrogen in the bed and to increase the initial carbon dioxide mole fraction during blowdown (Yang, 1987). This has been heavily investigated for hydrogen separation (Cen and Yang, 1986; Yang and Doong, 1985). Cen and Yang (1986) separated a CO/H_2 mixture over AC and achieved hydrogen recoveries of up to 97.9% and carbon monoxide recoveries of up to 82.9% and purities for both gases over 90%. However, it is not clear from systems that employ the co-current depressurisation how this stream is utilised and will lead to a loss of both products if the gas cannot be collected for either the heavy or light product. This can be circumvented by instead using this gas as a pressurisation stream through pressure equalisation steps. Pressure equalisation is implemented by connecting a depressurising bed with a pressurising bed and allowing the two to reach equilibrium. The primary purpose of this step is to conserve mechanical energy required for pressurisation but also results in higher recoveries of both gases (Yang, 1987).

7.4.1 Single Pressure Equalisation Step

7.4.1.1 Process Description

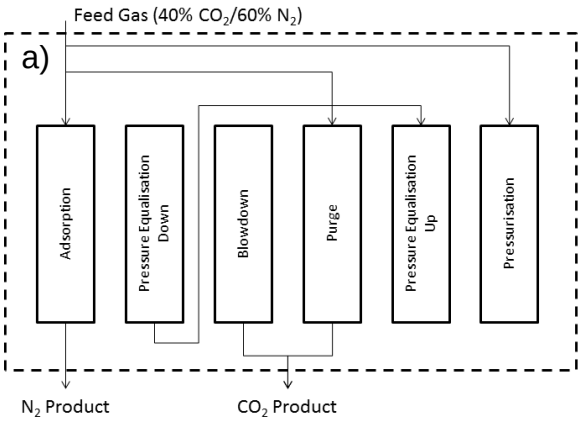

b)

1	Ad	ED1	BD	Pur	EU1	Press
2	ED1	BD	Pur	EU1	Press	Ad
3	BD	Pur	EU1	Press	Ad	ED1
4	Pur	EU1	Press	Ad	ED1	BD
5	EU1	Press	Ad	ED1	BD	Pur
6	Press	Ad	ED1	BD	Pur	EU1

Figure 7.5: Bed configuration for a 6 step process using one pressure equalisation step for 6 beds operating in parallel showing a) bed connections and b) bed sequencing. Ad – adsorption, ED – pressure equalisation down, BD – blowdown, Pur – purge with feed gas, EU – pressure equalisation up, Press - pressurisation

The bed configuration for a 6 step cycle employing one pressure equalisation step using 6 beds operating in parallel is shown in Figure 7.5. The bed operating in the pressure equalisation down step is connected to the feed of the bed operating in the pressure equalisation up step. The flow of gas is controlled to the pressure equalisation up bed until the pressure in this bed reaches the pressure of the pressure equalisation down bed. This set-up means that all steps take the same amount of time. If a bed finishes the operation it is undertaking, e.g. the bed becomes fully pressurised, before the adsorbing bed reaches breakthrough, the feed flowrate for that bed is reduced to zero. As with the 4 step process, this can be operated counter-currently. Counter-current operations are tested by running the ED1, BD and Pur steps counter-currently. The optimum split of the feed gas between

the different steps and the carbon dioxide breakthrough point at which the adsorption step switches is given in Table 7.4.

Table 7.4: Feed conditions and set adsorption switch point for a 6 step cycle

Feed Fraction for Adsorption	(-)	0.65
Feed Fraction for Purge	(-)	0.1
Feed Fraction for Pressurisation	(-)	0.25
CO_2 Mole Fraction Breakthrough Point	(-)	0.22

The pressure profile for a 6 step process is represented in Figure 7.6. The pressure profiles for the pressure equalisation step are seen in the second and fifth step. The depressurisation and pressurisation in these steps are controlled in the same way as for the blowdown and pressurisation steps, as discussed in Section 7.3. The pauses in the pressure change are during idle periods in which the bed is waiting for the adsorbing bed to reach the breakthrough point.

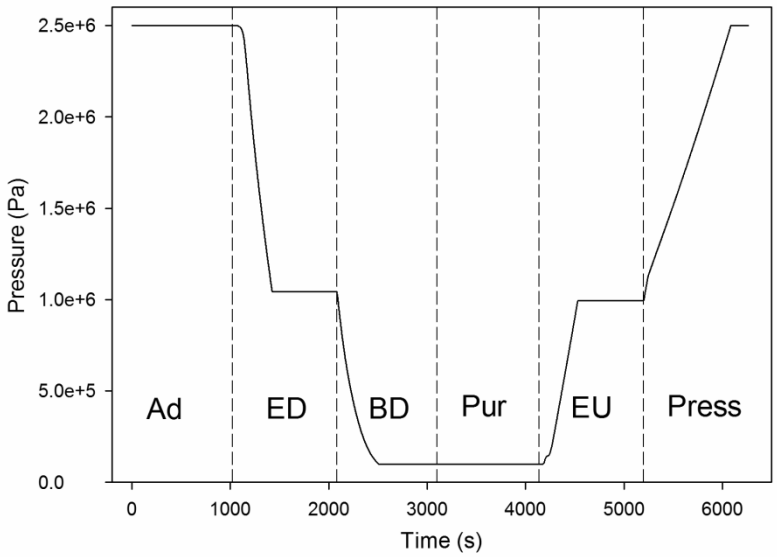

Figure 7.6: Pressure profile for a 6 bed 6 step PSA cycle

7.4.1.2 Simulation Outputs

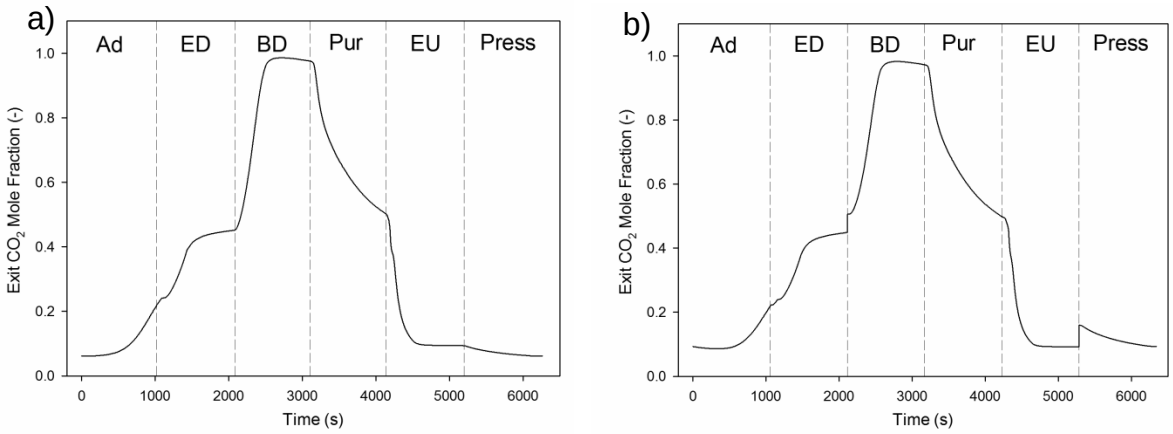

Figure 7.7: Results for a 6 step cycle using one pressure equalisation step for bed 1 as shown in Figure 7.5 using a) co-current operation and b) counter-current operation.

The exit CO_2 mole fraction for the simulation of bed 1 in Figure 7.5 for co-current operation is depicted in Figure 7.7a. The carbon dioxide fraction rises during the pressure equalisation down step to a mole fraction of 0.452, caused by the pressure differential drives the gas from a partially saturated bed to a clean bed, pushing much of the residual gas that is not adsorbed (primarily nitrogen) into the pressurising bed. The blowdown step then proceeds in the same manner as the co-current 4 step cycle but starting at a higher exit carbon dioxide mole fraction. The peak of the blowdown step is 0.986, which is identical to the 4 step co-current Skarstrom cycle. This is because the overall blowdown is the same and the difference is in the way in which the gases are collected. The purge step in the 6 step cycle records a decrease in the outlet carbon dioxide mole fraction to 0.502, similar to the purge step in the 4 step cycle. The reciprocating pressure equalisation step, where the bed is pressurised, leads to a sharp decrease in the carbon dioxide mole fraction, as the carbon dioxide is recaptured in the bed as the adsorbent capacity increases with the rise in

pressure. The pressurisation step then does not result in a significant change in the carbon dioxide mole fraction as the residual carbon dioxide has been adsorbed and the carbon dioxide in the feed stream is also being adsorbed.

The outlet carbon dioxide mole fraction for the counter-current operation is shown in Figure 7.7b. The change in flow direction for the blowdown step causes the carbon dioxide mole fraction to jump up from 0.449 to 0.50. The initial rate of increase is slightly diminished compared to the co-current operation and the peak value for the counter-current system is 0.979 compared to 0.986 for the co-current operation. This is caused by a small amount of residual nitrogen in the bed after the pressure equalisation down. The value of 0.979 for the counter-current operation is slightly higher than the 0.970 for the counter-current 4 step operation, showing that the residual nitrogen, which has been reduced here, is the cause for the reduction in peak values for counter-current operation. There is a slight rise in the carbon dioxide concentration at the start of the pressurisation step when the bed is switched back to co-current flow. This is caused by a higher carbon dioxide concentration at the exit of the bed resulting from the gas feeding at the inlet during the counter-current pressure equalisation up step. This then drops down as the adsorbent capacity continues to rise during the pressurisation step.

Table 7.5: Carbon dioxide and nitrogen capture rates and purities for 4 step co-current operation and for 6 step co-current and counter-current operation.

	4 Step Co-Current	6 Step Co-Current	6 Step Counter-current
CO_2 Capture Rate	84.6%	83.35%	82.20%
CO_2 Purity	59.5%	72.14%	71.86%
N_2 Capture Rate	56.5%	79.28%	80.39%
N_2 Purity	88.7%	89.85%	88.46%

The carbon dioxide and nitrogen capture rates and purities for the 6 step cycle operating co-currently and counter-currently are given in Table 7.5. Comparing this to the capture rates and purities for the 4 step cycle, the carbon dioxide capture rate and nitrogen purity are comparable and there are significant improvements for the carbon dioxide purity and nitrogen capture rate for the 6-step cycle. The increase of these two values is due to the recycle of the low quality depressurisation gas in the pressure equalisation down step. Having the residual nitrogen recycled allows it to be recaptured in the bed and then displaced during the adsorption step. This therefore increases the capture rate of the nitrogen and decreases the amount contaminating the carbon dioxide product. The co-current and counter-current values for both capture rates and purities are nearly identical. This confirms, along with the 4 step counter-current Skarstrom cycle discussed in Section 7.3.2, that counter-current operation offers no benefits for this system. This is most likely due to the conditions set to maximise the capture rate and purity of both products. It has rarely been discussed in the literature as counter-current operation was used in the initial 4 step Skarstrom cycle when looking to recover one product (Ruthven, 1984).

Schell et al. (2013) compared experimental data and simulations for the 6 step cycle using two beds to separate CO_2/H_2 mixtures using activated carbon at high pressures which was run using the counter-current operation. Their optimum separation gave a hydrogen purity of 88.5%, hydrogen capture rate of 93.0%, a carbon dioxide purity of 92.6% and a carbon dioxide capture rate of 88.0%. The hydrogen capture rate and carbon dioxide purity were considerably higher than those reported in this work. There are two key differences between the work: the length of the cycle time and the gases being separated. The rapid cycle time is employed in PSA operations in order

to limit the temperature changes from the heat of adsorption (Yang, 1987), however, in the experimental section of this thesis it was shown that the temperature change was minimal for this bed size and at the flowrates employed here, as discussed in Section 5.4.1. This, therefore, would not have an effect on the purity and recoveries observed. The use of a CO_2/H_2 mixture in the work by Schell et al. (2013) is the more likely cause of the difference. Their work is based on isotherms reported previously, where it can be seen that the selectivity of carbon dioxide over hydrogen is significantly greater than the selectivity for carbon dioxide over nitrogen (Schell et al., 2012b). This means that there is a lot less adsorbed hydrogen released during the depressurisation steps for a CO_2/H_2 mixture compared to nitrogen in a CO_2/N_2 mixture. This will allow for greater carbon dioxide purities as well as greater hydrogen capture rates.

Liu et al. (2011) employed a 6 step process for a CO_2/N_2 separation using Z13X at low pressure. In their system, the purge step used a fraction of the nitrogen product and was otherwise the same as the counter-current operation depicted in Figure 7.5. They achieved a carbon dioxide capture rate of 93.6% and a carbon dioxide purity of 58.2%, without a discussion of the quality of the nitrogen. The results presented in this study give a considerably higher carbon dioxide purity for only a slight loss in carbon dioxide capture rate when compared to the results presented by Liu et al. (2011). This is most likely caused by the higher pressures used in this study. At higher pressure the carbon dioxide capacity rises faster than the nitrogen capacity giving a better selectivity for carbon dioxide over nitrogen. Lopes et al. (2011) also use the 6 step process for the purification of hydrogen from a $H_2/CO_2/CO/CH_4/N_2$ mixture using activated carbon at 10 bar, where they achieved a hydrogen purity of

99.99% and a hydrogen capture rate of 71.0%, with no description of the quality of the heavy product. Compared to the system studied here, the light product purity is considerably higher and the light product capture rate slightly lower. This is caused by the system being optimised for hydrogen recovery, as the system must be set-up so that any lower purity hydrogen is captured as heavy product reducing the hydrogen capture rate.

As with the 4 step cycle, literature values can vary depending on the conditions used. However, this work clearly shows in Table 7.5 the significant improvement that the use of a pressure equalisation step causes compared to a 4 step cycle. The carbon dioxide purity is still below the 95% target and the nitrogen capture rate is also lower than the state of the art liquid absorption process.

7.4.2 Multiple Pressure Equalisation Steps

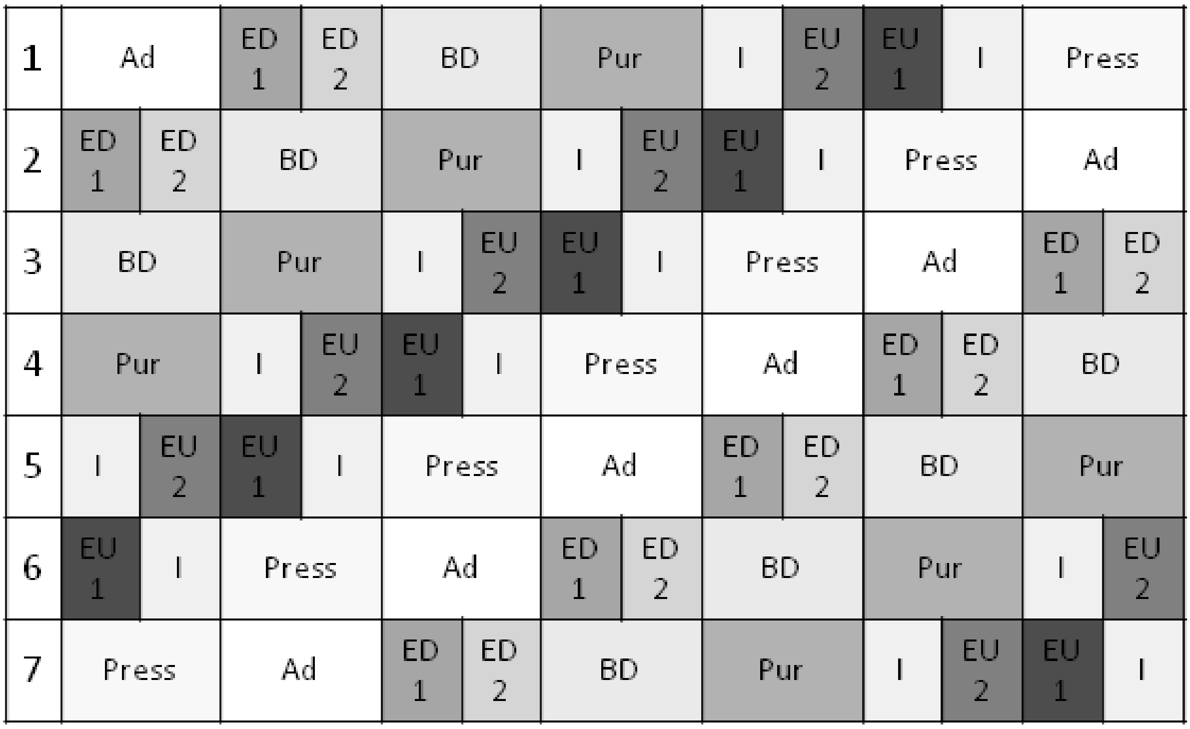

1	Ad		ED 1	ED 2	BD		Pur		I	EU 2	EU 1	I	Press	
2	ED 1	ED 2	BD		Pur		I	EU 2	EU 1	I	Press		Ad	
3	BD		Pur		I	EU 2	EU 1	I	Press		Ad		ED 1	ED 2
4	Pur		I	EU 2	EU 1	I	Press		Ad		ED 1	ED 2	BD	
5	I	EU 2	EU 1	I	Press		Ad		ED 1	ED 2	BD		Pur	
6	EU 1	I	Press		Ad		ED 1	ED 2	BD		Pur		I	EU 2
7	Press		Ad		ED 1	ED 2	BD		Pur		I	EU 2	EU 1	I

Figure 7.8: Bed arrangement for a 8 step - 7 bed system utilising 2 pressure equalisation steps. Ad – adsorption, ED – pressure equalisation down, BD – blowdown, Pur – purge with feed gas, I – idle, EU – pressure equalisation up, Press - pressurisation

Despite a significant improvement in the carbon dioxide purity for a 6 step cycle employing one pressure equalisation step, it is still low. A single pressure equalisation step leads to an increased purity as the low purity gas produced during the early part of depressurisation is recycled and recaptured. The limit to the recycle is due to the pressure between the two pressure equalisation beds converging and equilibrium being reached. More of the low purity depressurisation gas can be utilised by using multiple pressure equalisation steps. An 8 step process involving two pressure equalisation steps is shown in Figure 7.8. The additional equalisation step requires one extra bed. The pressure equalisation down can occur during one adsorption step, however, the pressure equalisation step up must be split over two beds and requires the use of idle steps. During the first equalisation down step, the depressurising bed is connected to a bed which has been held at a middle pressure. When these beds equalise, the pressurising bed then returns to an idle state before being pressurised to the final bed pressure in the next step of the cycle. The depressurising bed is then connected to a bed at low pressure which was has been idle. These two beds are then allowed to equilibrate in the second pressure equalisation step.

The feed conditions and the set adsorption switch time for a PSA cycle using two pressure equalisation steps are reported in Table 7.6. The second pressure equalisation step means there is a smaller pressure rise during the pressurisation step requiring a smaller pressurisation flowrate.

Table 7.6: Feed conditions and set adsorption switch point for an 8 step cycle utilising two pressure equalisation steps.

Feed Fraction for Adsorption	(-)	0.7
Feed Fraction for Purge	(-)	0.1
Feed Fraction for Pressurisation	(-)	0.2
CO_2 Mole Fraction Breakthrough Point	(-)	0.22

The outputs of a simulation of an 8 step cycle using 7 beds and two pressure equalisations steps are presented in Figure 7.9. The pressure profile in Figure 7.9b shows the operation of the pressure equalisation down in one cycle step and then the two pressure equalisation steps up with their corresponding idle periods. Figure 7.9a shows the effect on the outlet carbon dioxide mole fraction. The carbon dioxide mole fraction at the start of the blowdown step is 0.578. The maximum carbon dioxide mole fraction of 0.984 at outlet is comparable to the maximum observed for the 4 and 6 step cycles of 0.986 as the depressurisation process is very similar. The purge step closely resembles that of the 4 and 6 step cycles as well due to the similar nature of the conditions. The first pressure equalisation up step replicates the pattern observed in Figure 7.7a, with a sharp drop in the carbon dioxide mole fraction as the residual carbon dioxide is recaptured due to the rise in pressure. A further drop is seen for the second pressure equalisation up step for the same reason. The pressurisation step shows very little change as the residual carbon dioxide has all been readsorbed and the fresh carbon dioxide in the feed stream is adsorbed at the front end of the bed.

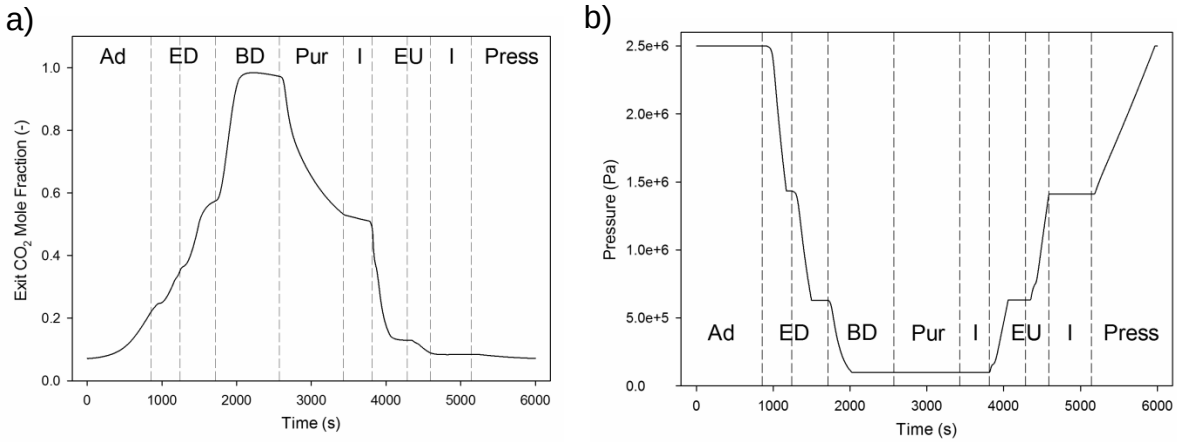

Figure 7.9: Results for an 8 step co-current cycle using two pressure equalisation step for bed 1 as shown in Figure 7.8, reporting the a) outlet CO_2 mole fraction and the b) inlet pressure profile.

The capture rates and purities for the 8 step system are reported in Table 7.7. Comparing this to the use of a single pressure equalisation step in a 6 step cycle, reported in Table 7.5, there is a 5.7% increase in the carbon dioxide purity and a 4.1% increase in the nitrogen capture rate. This is to be expected as more of the low purity depressurisation stream is being used to pressurise the bed rather than being collected as part of the carbon dioxide product.

Table 7.7: Carbon dioxide and nitrogen capture rates and purities for an 8 step 7 bed cycle

CO_2 Capture Rate	85.2%
CO_2 Purity	77.8%
N_2 Capture Rate	83.4%
N_2 Purity	88.4%

Casas et al. (2013b) reported a study mainly employing a system with 3 equalisation steps for the separation of a CO_2/H_2 mixture using activated carbon at 34 bar. As part of this study they considered the number of pressure equalisation steps, investigating the impact of using both 2 and 4 pressure equalisation steps. They ran simulations using a range of conditions to demonstrate the pay off between carbon

dioxide capture rate and carbon dioxide purity for a process with 2 pressure equalisation steps. The maximum capture rate achieved was 95% with a purity below 87% and the maximum purity achieved was 90% with a capture rate of 80%. There was not a detailed discussion of the hydrogen capture rate or purity and the effects the process parameters have on this. For a comparable capture rate of 85% to the work here, they achieved a carbon dioxide purity of just less than 90%. This is considerably higher than the 77.8% achieved here, however, as discussed in Section 7.4.1.2, the selectivity of carbon dioxide over hydrogen is much greater than the selectivity of carbon dioxide over nitrogen. This results in more adsorbed nitrogen in the system studied here and therefore reduced the achievable purity of carbon dioxide. Xiao et al. (2009) considered the separation of $CO_2/H_2O/H_2$ mixtures using Z13X at 27 bar and temperatures exceeding 250°C. The water content in these mixtures was 0.875, the carbon dioxide content was 0.036 and the remainder was hydrogen to simulate the wet gas that was produced after the water gas shift reactor in an IGCC power plant. The PSA process consisted of 2 pressure equalisation steps but also employed a compressor so that the equalisation can continue past the point where the pressures equilibrate and a vacuum desorption step. In their process they achieved a carbon dioxide purity of 93.9%, a carbon dioxide capture rate of 91.3% and a hydrogen purity of 97.4%, the hydrogen capture rate was not mentioned. These were considerably higher purities and capture rates than found in this study but this can be attributed to the use of hydrogen as well as the different process configuration which employs a vacuum desorption step.

An increased number of pressure equalisation steps would continue to improve the carbon dioxide purity attainable. Casas et al. (2013b) demonstrated in their

parametric study that an increase from 2 to 3 pressure equalisation steps caused a maximum purity increase from 90% to 94% and a further increase to 4 pressure equalisation steps caused the maximum purity to reach 96%. Lopes et al. (2011) also showed an improvement in gas quality when increasing from one pressure equalisation step to three, with the hydrogen capture rate from a CO_2/H_2 mixture increasing from 71.0% to 82.4%. This study was not able to simulate a 3 equalisation step process as the simulation became too cumbersome to complete. However, this work has shown the importance of the pressure equalisation steps and the gains achieved by increasing the number of these steps. Previous work has only focused on the capture rate the heavy component but here it has been shown that the pressure equalisation steps increase the capture rate of the light component.

7.5 Purge Gas Recycle

Maximising the carbon dioxide concentration during the blowdown of the bed by implementing pressure equalisation gives large improvements in the carbon dioxide purity and the nitrogen capture rate. However, the purge step also has an impact on these values as the exit stream from the purge bed is captured for the carbon dioxide product. Previous work for processes recovering the heavy product has used systems where the purge is not done by the feed gas or the light product but instead with the heavy product (Chou and Chen, 2004; Kikkinides et al., 1993). The processes that use this are VPSA processes and therefore can recycle the low pressure heavy product into the atmospheric pressure bed without the use of a compressor. However, this does suggest process gains can be made by effectively recycling the purge stream.

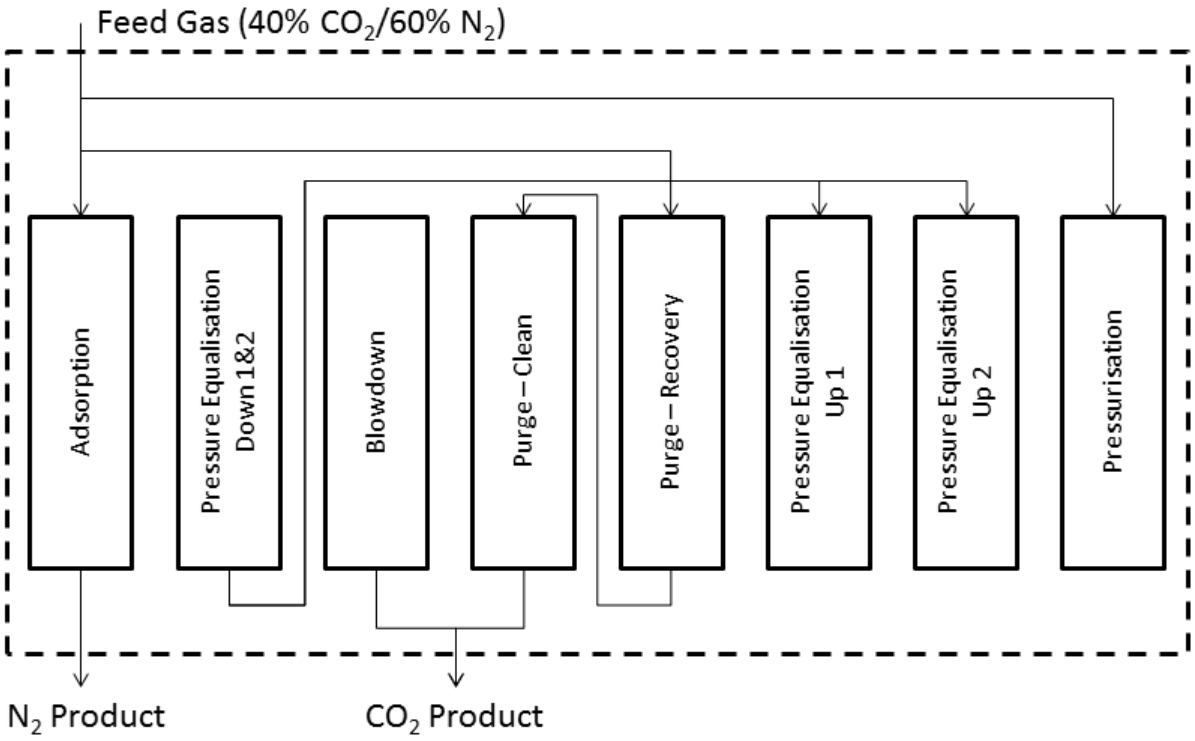

Figure 7.10: Process configuration for a 9 step cycle using 2 pressure equalisation steps and a recycled purge stream.

This work suggests applying a staged purge using two steps. As with the pressure equalisation step, it is preferable to use low quality gas elsewhere in the process rather than allowing it to be captured in the heavy product. Figure 7.10 shows a process configuration where the low purity purge gas is recycled to another column which is also purging. This has two affects, the first is to decrease the overall purge flowrate as by having two beds purging, the purge time has doubled. The second is that only purge gas with relatively high carbon dioxide purity is captured. The feed conditions and set adsorption switch point for this process are given in Table 7.8.

Table 7.8: Feed conditions and set adsorption switch point for a 9 step cycle utilising 2 pressure equalisation step, a CO_2 rinse step and a purge recovery step

Feed Fraction for Adsorption	(-)	0.71
Feed Fraction for Purge	(-)	0.04
Feed Fraction for Pressurisation	(-)	0.25
CO_2 Mole Fraction Breakthrough Point	(-)	0.22

The exit carbon dioxide mole fraction for a PSA process utilising a purge recovery step is reported in Figure 7.11. The influence of the additional purge step on this profile is only observed during the two purge steps. This can be compared to the purge step in Figure 7.9a and it is apparent that the gradient is less steep during the two purge steps, caused by the lower flowrate. The carbon dioxide mole fraction at the end of the purge step for the 9 step cycle is 0.606, compared to 0.533 for the 8 step cycle. This higher value does not have a significant effect on the adsorption times, which are 857 seconds and 846 seconds for the 9 step and 8 step cycles respectively. At the end of the first purge step, where the bed was fed by the gas from the second purge step, the carbon dioxide mole fraction is 0.744. This improves the overall purity of the carbon dioxide product as the average fraction of carbon dioxide in this stream was higher compared to the 8 step process. The other steps in the 9 step cycle show the same trends as the 8 step cycle, with any deviation caused by the slight increase in carbon dioxide concentration at the end of the second purge step. The maximum value in the blowdown step is 0.984, which is the same as for the 8 step cycle.

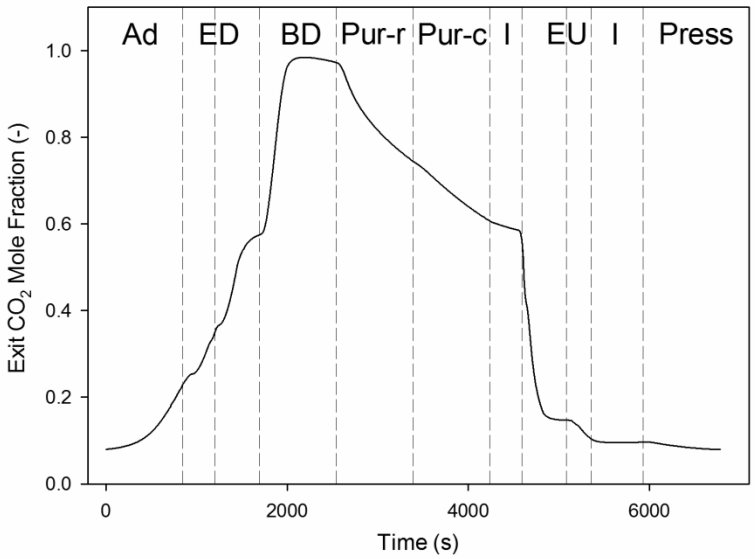

Figure 7.11: Results for a 9 step co-current cycle using two pressure equalisation steps, a CO_2 rinse step and a purge recovery step for bed 1, reporting the a) outlet CO_2 mole fraction and the b) inlet pressure profile.

The effect of using a second purge step on the capture rates and purities is reported in Table 7.9. There is an improvement in the carbon dioxide purity, when compared to the 8 step cycle value in Table 7.7, due to higher quality gas being collected during the first purge step. However, this comes at the expense of a lower capture rate for the 9 step cycle. More of the carbon dioxide remains in the bed after the purge step, as indicated by the higher carbon dioxide mole fraction at the end of the second purge step. It is therefore carbon dioxide that is not captured in the heavy product and this also explains the slight reduction in the nitrogen purity. An equally significant effect as the increase in carbon dioxide purity is the increase in the nitrogen capture rate. The biggest area of loss of nitrogen is in the fraction of the feed that is used for the purge gas, as this is not recovered elsewhere. The use of two purge steps allowed the purge flowrate to decrease significantly. This means a higher feed fraction of the gas stream is used in the adsorption and pressurisation

steps, where the gas will then be collected during the adsorption step. The carbon dioxide product also has a higher proportion of carbon dioxide with approximately the same flowrates, which indicates that there is less nitrogen in the heavy product stream leading to an increase in the nitrogen capture rate.

Table 7.9: Carbon dioxide and nitrogen capture rates and purities for a 9 step 8 bed cycle

CO_2 Capture Rate	80.89%
CO_2 Purity	82.78%
N_2 Capture Rate	89.13%
N_2 Purity	87.33%

7.6 Heavy Product Rinse

The 8 step cycle utilises all of process steps which can be implemented without requiring additional equipment. There are other process steps which use equipment such as compressors to further improve the quality of the captured gases. Traditional PSA systems where the heavy product is the desired product employ a heavy product rinse before depressurisation, i.e. after adsorption and before pressure equalisation or blowdown, where it has been shown to give significant improvement to the purity of the heavy product (Yang, 1987). This has been widely applied to post-combustion capture system using VPSA where the bed is adsorbing at atmospheric pressure so that the heavy product used for the rinse step does not require pressurisation (Choi et al., 2003; Chou and Chen, 2004; Chue et al., 1995; Kikkinides et al., 1993; Liu et al., 2011; Takamura et al., 2001). However, to apply that to a PSA system where the adsorption step occurs at elevated pressures would mean that the heavy product captured at low pressure would need to be repressurised to be used for the rinse. Chue et al. (1995) used VPSA but their adsorption step was at 1.2 MPa and therefore required a compressor to pressurise

the rinse feed stream but they did not discuss the impact this added energy requirement would have. The system used here has an even higher adsorption pressure of 2.5 MPa and it would therefore be expensive to pressurise the rinse gas. There are also issues relating to the use of the gas which is produced from the rinse step. In post-combustion systems, only the carbon dioxide is desired and therefore this gas can be discarded, although this does cause a significant reduction in the capture rate for the carbon dioxide. Kikkinides et al. (1993) recycled the product of this step back to the flue gas stream, although were still only able to achieve a carbon dioxide capture rate of 77%.

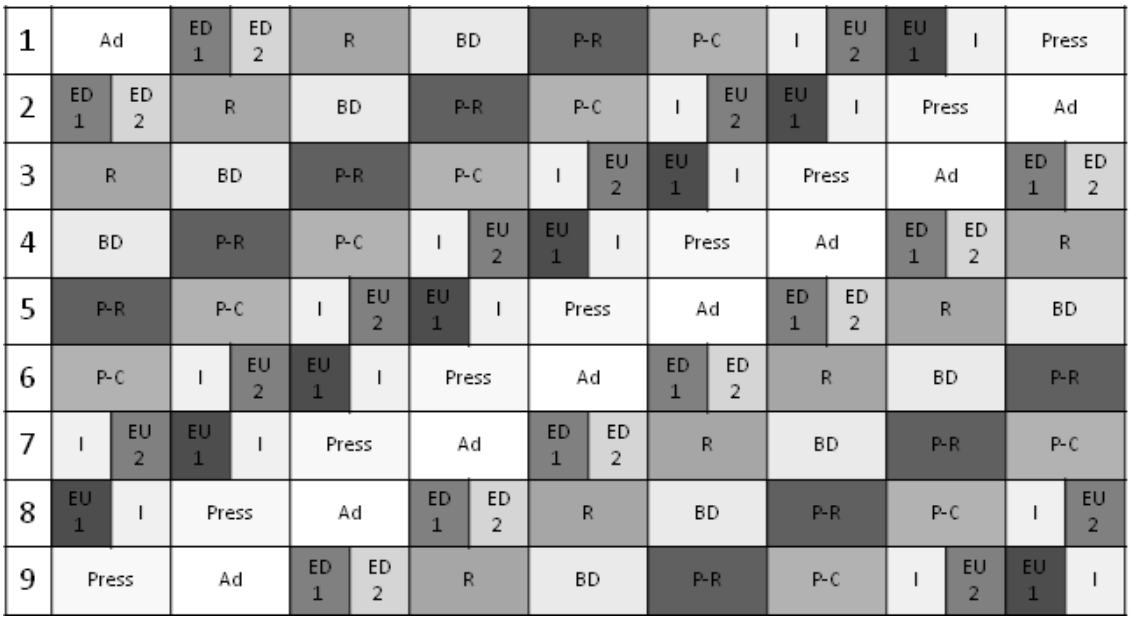

Figure 7.12: Bed arrangement for a 9 step - 8 bed system utilising 2 pressure equalisation steps and a heavy product rinse between pressure equalisation and blowdown. Ad – adsorption, ED – pressure equalisation down, R- rinse, BD – blowdown, P-R – purge with recycle, P-C – purge with feed gas, I – idle, EU – pressure equalisation up, Press - pressurisation

This work instead suggests moving the rinse step to after the pressure equalisation steps. Yang (1987) theorised that it should be possible to combine the rinse with the heavy product and co-current depressurisation, although at that point it had not been

tested. As discussed in Section 7.4, pressure equalisation is an extension of co-current depressurisation where the product is recycled back into the process. If a heavy product rinse was implemented after the two pressure equalisation steps and before the blowdown step, the heavy product used for the rinse step would not need to be pressurised to 2.5 MPa but instead to an intermediary pressure. The configuration of the beds and the process arrangement are depicted in Figure 7.12 and Figure 7.13 respectively. A compressor is required in order to reach the pressure of the bed after the second pressure equalisation step. The use of the rinse product also needs to be evaluated. Recapturing the rinse product as part of the carbon dioxide product is not feasible as this would negate the use of the heavy rinse stream. Therefore, the two remaining options are to leave it as a rinse product or to combine it with the light product. Combining it with the adsorption stream does have the disadvantage of requiring further compression of the stream up to 2.5 MPa to match the pressure in the adsorption product stream. However, not using the rinse product will mean those gases are not collected in either product stream.

The feed conditions and the adsorption breakthrough point are provided in Table 7.10. The adsorption, purge and pressurisation conditions are the same as those used in the 9 step PSA cycle as the rinse step does not heavily impact these steps. The carbon dioxide rinse stream is simulated as a separate stream rather than as a recycle as depicted in Figure 7.13 so as to simplify the computation. The conditions of this stream are assumed as such to give sufficient flow to fully saturate the column and the composition is chosen to be close to the final product purity produced. When the exit carbon dioxide mole fraction reaches a value of 94.5% the flow of the rinse stream is stopped.

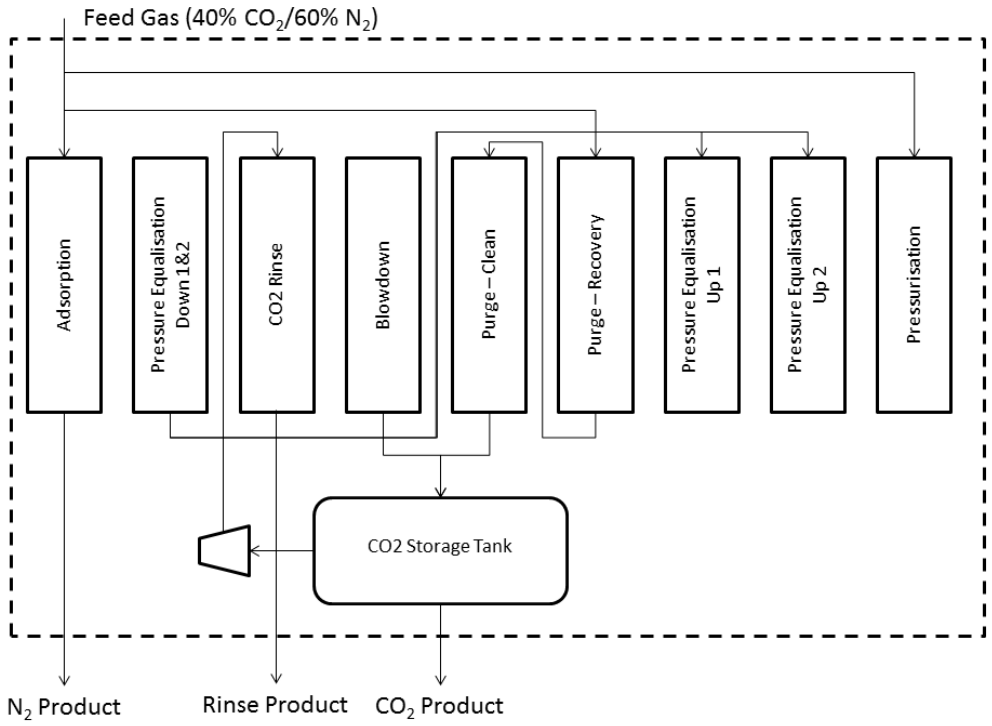

Figure 7.13: Process configuration for the first step of a 9 step 8 bed process utilising two pressure equalisation steps and a carbon dioxide rinse.

Table 7.10: Feed conditions and set adsorption switch point for a 9 step cycle utilising 2 pressure equalisation step and a CO_2 rinse step

Feed Fraction for Adsorption	(-)	0.71
Feed Fraction for Purge	(-)	0.04
Feed Fraction for Pressurisation	(-)	0.25
CO_2 Mole Fraction Breakthrough Point	(-)	0.22
Rinse Step Purity	(-)	0.95

The resulting exit carbon dioxide mole fraction for the 10 step process is illustrated in Figure 7.14. The difference for the exit carbon dioxide mole fraction of the 10 step system compared to the 9 step system in Figure 7.11 is for the additional carbon dioxide rinse step and in the blowdown step. For the 10 step process, the rinse step causes a sharp increase in exit carbon dioxide mole fraction before plateauing at the

fraction of the carbon dioxide rinse feed and the rinse feed is stopped. During the blowdown step the bed is then saturated with relatively high purity carbon dioxide which is then driven out by the resulting pressure drop in the system. The maximum for this value is 0.992, which is higher than for all the previous PSA cycles which had maximum values of 0.986. The purge steps and pressurisation steps remain the same as the 9 step process.

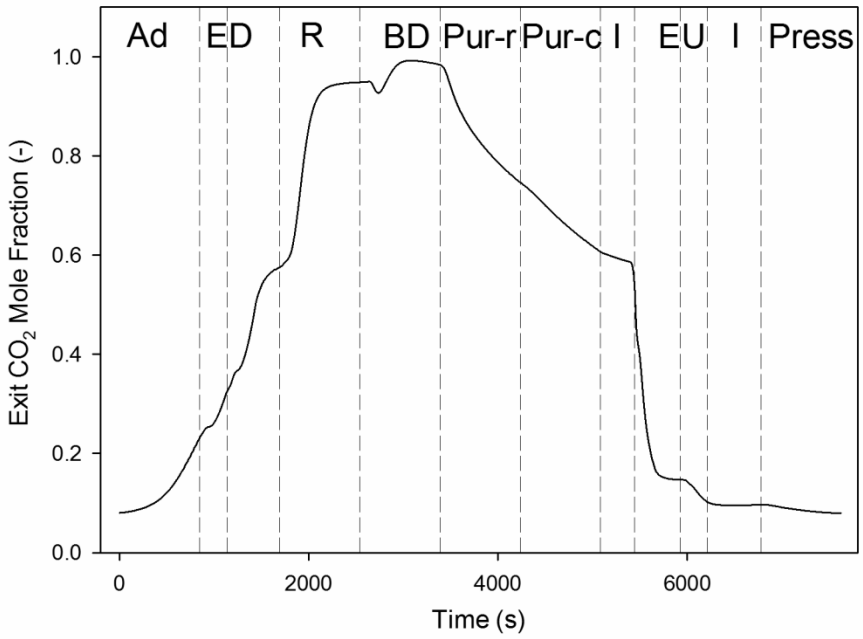

Figure 7.14: Results for a 10 step co-current cycle using two pressure equalisation step and a CO_2 rinse for bed 1 as shown in Figure 7.12, reporting the a) outlet CO_2 mole fraction and the b) inlet pressure profile.

The analysis of the capture rates and purities depend on whether the rinse stream is collected as part of the light product or is discarded as waste. The capture rates and purities for each of these options are given in Table 7.11. The carbon dioxide capture rate and purity are identical for both streams. This is because the use of the rinse product does not affect the carbon dioxide product. The use of a carbon dioxide rinse stream gives a significant rise in the carbon dioxide purity, increasing

from 82.8% for the 9 step process to 93.8% for the 10 step process. This is caused by the blowdown step having a considerably higher concentration of carbon dioxide in it from the rinse step. The carbon dioxide capture rate on the other hand shows a significant reduction to 66.0% from 80.9%. The use of the heavy product stream causes a fraction of the carbon dioxide product to be reintroduced into the process and therefore lost as carbon dioxide product. The effect on the nitrogen product depends on whether it is combined with the rinse product. For a system where the rinse product is left as waste, the capture rate and purity are comparable to the 9 step cycle. Integration of the rinse product into the nitrogen product leads to a significant increase in the capture rate. A large fraction of the nitrogen that is lost during the blowdown step is instead captured by the rinse step. The only remaining loss for the nitrogen product is the nitrogen in the purge feed stream. Combining the rinse product with the nitrogen product significantly lowers the nitrogen purity as the rinse product stream has a high concentration of carbon dioxide.

Table 7.11: Carbon dioxide and nitrogen capture rates and purities for a 9 step 8 bed cycle, considering the rinse product combined with the Adsorption product and the rinse product as a waste stream

	Rinse as Waste	Rinse combined with Adsorption Product
CO_2 Capture Rate	66.00%	66.00%
CO_2 Purity	93.77%	93.77%
N_2 Capture Rate	86.34%	96.01%
N_2 Purity	87.35%	70.41%

The process change proposed here causes the need for a compromise between the carbon dioxide purity and capture rate. The reduction in carbon dioxide capture rate is significant, however, it may be necessary to meet purity requirements needed for carbon dioxide sequestration. The increased purity also comes with an increased

capture cost due to the required compressor. The other operating costs will remain constant and therefore a reduction in the capture rate and the rise in operating costs will give a significantly higher cost per tonne of carbon dioxide captured.

A recommendation on the effectiveness of combining the rinse product with the nitrogen product will depend on the economics of the IGCC power plant. The nitrogen purity is the performance indicator which is the most manageable. In an IGCC process, the gas turbine can be configured to run with different qualities of gas and could therefore be adjusted to accommodate the lower light product purity. More significant is the increase in nitrogen capture rate. The inclusion of the rinse step already adds the need of a compressor and further compression would be required to combine the rinse product with the nitrogen product. The main efficiency loss from introducing a PSA system to an IGCC power plant is the loss of light product reducing the overall efficiency of the plant as the PSA process has few other energy costs. Therefore, an increase of light product capture rate from 89.1% for a 9 step process to 96.0% for a 10 step process could make the system more viable. At the very least the increase in capture rate would need to increase the energy output of the plant to match the energy requirement of the two compressors that would be needed. Further work combining a PSA process with an IGCC power plant would be required to test this.

7.7 Conclusion

The work in this chapter systematically studied the development of a PSA process for separating carbon dioxide and nitrogen at elevated pressure with the aim of producing high quality carbon dioxide and nitrogen product. Previous work which has produced two products from high pressure streams have not investigated the

effect of each step on the 4 key performance indicators, the carbon dioxide purity, the carbon dioxide capture rate, the light product purity and the light product capture rate, often not reporting the light product capture rate which is vital for minimising the efficiency loss of an IGCC power station.

The 4 step Skarstrom cycle was proven to not give sufficient carbon dioxide purity and nitrogen capture rate for such a system. It highlighted that the low quality carbon dioxide product at the start of the blowdown step and at the end of the purge step need to be recycled effectively. Pressure equalisation was found to be an efficient use of the low quality gas from the start of the blowdown step as it allows the residual nitrogen to be driven off and adsorbed in another bed. A second pressure equalisation step was found to increase the performance of the process further. The carbon dioxide purity rose from 59.5% for a 4 step process to 77.8% for an 8 step process, with the nitrogen capture rate rising from 56.5% to 83.4%. The carbon dioxide purity was lower than those reported in literature (Casas et al., 2013b). This was attributed to those studies looking at CO_2/H_2 separations and the selectivity of activated carbon for carbon dioxide over hydrogen is significantly greater than the selectivity for carbon dioxide over nitrogen. This work also found for both systems with a pressure equalisation step and the 4 step cycle that counter-current operation had no significant effect on the quality of the gases is produced. Counter-current operation was first implemented in processes recovering only the light component and is only required when producing high purity light product.

Two further process developments are suggested here. The first is to use a two stage purge, where the lower quality purge gas is recycled and used to purge a bed immediately after blowdown. This increases the carbon dioxide purity up to 82.8%

but does cause a reduction in the carbon dioxide capture rate as it is instead collected in the nitrogen product. There is a significant increase in the nitrogen capture rate to 89.1% caused by a much lower purge flowrate. The use of a heavy product rinse step after pressure equalisation down but before blowdown was also investigated. This showed that there can be a large payoff between purity and capture rate as the carbon dioxide purity increased to 93.8% but the carbon dioxide capture rate dropped to 66.0%, as a large proportion of the carbon dioxide product was used in the rinse step. The rinse step also requires pressurisation of the recycled feed stream which will increase operational costs. The nitrogen product is dependent on the way in which the exit stream from the rinse step is used. Combining the rinse product with the nitrogen stream increases the nitrogen capture rate to 96.0% but decreases the nitrogen purity to 70.4% and also requires pressurisation of this stream up to the adsorption pressure. However, not combining this stream means that these gases are lost from the system. The decision on the most efficient use of this stream will depend on the increased capture rate producing more energy than the compressors for this step require.

The work presented here provides a more thorough understanding of the effect each step in a PSA cycle has on the quality of the gases produced as well as suggesting two novel approaches for doing this. It shows the importance of recycling gas streams in order to maximise the capture rate of each gases. Compared to previous work, an added emphasis has been placed on the light component capture rate which is vital for this process to be viable for integration with an IGCC power plant.

Chapter 8 – Conclusions and Future Work

8.1 Conclusions

This study aimed to investigate activated carbons for the removal of carbon dioxide from gas mixtures at high pressure. The full development from the analysis of the material through to the implementation of a cyclic model was evaluated. The material was studied under equilibrium conditions and dynamic conditions experimentally in order to understand any disparities between the two techniques. A model was then validated against the experimental data for both breakthrough and cyclic experiments. Finally, the full development of a cyclic model, including the effect of each of the different process steps, was explored.

8.1.1 Experimental Investigation

The material was investigated experimentally by characterising the physical properties of the material, producing equilibrium isotherm data and conducting dynamic experiments for breakthrough and cyclic systems. This led to several key conclusions:

- The Langmuir-Freundlich and Dual-site Langmuir isotherms were able to represent the entire isotherm. The Langmuir isotherm over predicted the low pressure regions and under predicted the high pressure regions. This was caused by the heterogeneous nature of the surface of the activated carbon materials.
- Breakthrough experiments allowed the materials to be compared under dynamic conditions. From these experiments, it was found that the modified activated had a higher capacity for carbon dioxide than the unmodified material on a mass basis, with a carbon dioxide feed mole fraction of 0.5

resulting in carbon dioxide capacities of 7.48 ± 0.09 mol kg^{-1} and 6.09 ± 0.06 mol kg^{-1} respectively. However, on a volumetric basis the unmodified material had a capacity of 1594 ± 16 mol m^{-3} than the modified material of 1429 ± 16 mol m^{-3} for a carbon dioxide feed fraction of 0.5. It is more important to compare materials on a volumetric basis as the size of the bed is a key design requirement in adsorption systems. The modified material has an increased adsorption capacity on a mass basis due to an increase in pore surface area. However, this is a result of further opening of the pore structure which has decreased the particle density. Therefore, future material development needs to consider increasing adsorption capacity without lowering the particle density.

- The multicomponent dual-site Langmuir isotherm was proven to be most suitable for predicting the breakthrough capacity for both the unmodified and modified activated carbons. The IAST model based on the Langmuir-Freundlich isotherm was also suitable for the unmodified materials. All other models studied under-predicted the carbon dioxide capacity. This is because these models all over predict the reduction in carbon dioxide capacity caused by the adsorption of nitrogen.
- The cyclic experiments showed that both materials had a high selectivity for carbon dioxide over nitrogen, 59.9 mol_{CO2}/mol_{N2} and 65.9 mol_{CO2}/mol_{N2} for the unmodified and modified materials respectively. This further emphasised the minimal effect that adsorption of nitrogen had on the capacity of the material for carbon dioxide.

8.1.2 Model Validation

An axial dispersed plug flow model was validated against experimental data for the unmodified activated carbon and the implementation for several correlations discussed. The model was then further compared to cyclic systems and to systems using the modified activated carbon. Finally, a parameter sensitivity study was conducted. This work led to the following conclusions:

- The model was able to successfully predict the breakthrough curve of the unmodified material. The breakthrough time was accurately simulated, with the model able to predict the breakthrough time with 2.3% for a carbon dioxide feed fraction of 0.5, which is a key system indicator for cyclic models. The Hsu and Haynes (1981) correlation was the most suitable or predicting the dispersion coefficient and shows at high pressure the effect of a porous material on the dispersion of the system is minimal.
- The modified material was simulated with less success, with the simulation predicting a steeper breakthrough curve than found in the experiment. However, the breakthrough time was well simulated.
- The cyclic curves were difficult to simulate. This is an area that is under studied and is highly complex because of the effects of the surrounding pipe and instruments on the breakthrough curve. However, a four step cycle was predicted to a high degree of accuracy. The breakthrough was well simulated and the initial rise in bed concentration well matched. The purge step also showed reasonable agreement between the experimental data and the model. The accuracy of the simulation shows that the model is suitable for predicting PSA systems to a first approximation.

- The parameter sensitivity study, which has not previously been conducted for the high pressure separation of carbon dioxide, showed that the particle diameter and system voidages had the most significant effect on the breakthrough. The particle diameter caused a change in the shape of the breakthrough curve, with particles larger than 1 mm having a significant degree of spreading. The shape of the breakthrough curve was unaffected by changes to the bed or particle voidage but the breakthrough time was impacted. Systems with a higher voidage had lower breakthrough times, and therefore breakthrough capacities, due to the reduction of active adsorbent material in the same volume of bed.

8.1.3 PSA Cycle Development

The validated model was further developed into a cyclic model and different process configurations were simulated and compared based on the purity and capture rate of both the heavy product and light product to give the following conclusions:

- A 4 step Skarstrom cycle is not capable of producing a high purity carbon dioxide stream or a high nitrogen capture rate due to the low quality gas is incorporated into the carbon dioxide product stream. The use of counter-current operation for the blowdown and purge steps had no significant effect on the performance indicators.
- Pressure equalisation steps significantly improved the quality of both gases. The use of two pressure equalisation step produced a heavy product stream with a carbon dioxide purity of 77.8% and a nitrogen capture rate of 83.4%. This showed the importance of recycling the low quality gas from the

blowdown step. The 6 step system also showed that there was no advantage to counter-current operation.

- A novel second purge step was suggested in order to recycle the low quality gas from the purge step. The carbon dioxide purity increased to 82.8% and there was a significant increase in the nitrogen capture rate to 89.1%. This was caused by the recycling of the stream but also a result of the low purge flow rate required.
- Finally, a novel rinse step was suggested. Instead of a rinse step after the adsorption step, a rinse step was simulated after the second pressure equalisation down step. The carbon dioxide purity was 93.8%, which was close to the target of 95%. However, this came at a significant loss in carbon dioxide capture rate which was 66.0%. It is also important to note that this step requires a compressor to produce the rinse stream which would decrease the efficiency of the process. The effect on the nitrogen product was dependent on if the product from the rinse step was collected in the nitrogen product or discarded as waste. If the gas is collected as nitrogen product, the nitrogen capture rate increased to 96.0%, but with a reduction in nitrogen purity to 70.4%. However, the nitrogen purity is less important due to the range of conditions a gas turbine could be operated under. The recycling of the rinse product would need a further compressor so that it was at the same pressure as the outlet of the adsorption step which would decrease the efficiency of the process.

8.2 Future Work

This study has provided a clearer understanding of the methods needed to study adsorption systems for carbon dioxide capture and in the development of PSA cycles. As the application of adsorption to high pressure capture is still in its infancy, there are several avenues for development of this work in the future.

8.2.1 Analysis of Adsorbent Materials

The requirement to study materials under dynamic conditions was highlighted in this work. An extension of this would be to evaluate other materials for both pre and post combustion capture on this basis. A combination of material development and simulation would allow for the rapid screening of materials. The use of the model would remove the requirement to use the experimental breakthrough rig for a large number of adsorbents, which would require larger quantities of any material to be produced. The inputs to the model are based on material properties and are simply the particle diameter, the material and bulk densities, the heat of adsorption, specific heat capacity of adsorbent and the isotherm properties. The breakthrough curves for different materials can then be simulated to show which has the greatest adsorption capacity and breakthrough profile. This would provide a more suitable comparison than simply comparing the equilibrium adsorption capacity of each material.

8.2.2 Experiments Using Multicomponent Gas Mixtures

The experiments performed in this study were done using idealised gas mixtures with only two components. The two components studied constitute the majority of the syngas that exits the water gas shift reactor. However, the syngas produced from an IGCC power plant with coal as a feedstock also contains many impurities, the key ones being water and sulphur compounds. Both of these can reduced the adsorption

capacity of activated carbon as they are often more strongly adsorbed. Performing experiments using gas mixtures with the same components as a typical syngas would be beneficial. This will allow any reduction in capacity or degradation caused by the impurities to the adsorbent to be observed. The results could then be used in conjunction with the model studied in this work in order to produce more realistic simulations, taking into account the complete gas mixture.

8.2.3 Industrial Scale Simulations

The simulation of this bed has been on an experimental scale. However, it is important to simulate the optimal PSA unit at an industrial scale to identify possible scale-up issues. For example a larger bed is most likely to be close to adiabatic conditions resulting in a more significant temperature change. With the development of an industrial scale model, it would then be possible to connect such a model to an IGCC power plant model. This would show the impact the carbon dioxide removal would have on the efficiency of the power plant. Connection to a dynamic model of an IGCC power plant would allow the light product stream from the PSA unit to be fed to a gas turbine model and the impact of carbon dioxide capture on the net plant efficiency to be found. This would allow comparisons to be made to other capture technologies to evaluate which is the most suitable. A further extension of the connection of the system with the IGCC power plant model would be the incorporation of such a power plant model into the gCCS system developed by Process System Enterprise. This program has the capability to incorporate the transportation and storage aspects into the simulation and therefore the entire CCS chain could be simulated. This would allow the complete energy impact for the separation of carbon dioxide to be found.

8.2.4 Economic Evaluation

Finally, there is a need for a study on the economics of a PSA system for pre-combustion capture. The separations for pre-combustion capture require complex bed sequences and arrangements and so far there has been no indication on the economics of these systems. There will be a capital cost penalty associated with more beds in a cycle and this will need to be compared with the operating costs and efficiency gains a more complex system may have. Such an analysis would allow further design constraints to be implemented which will inform the design of a final PSA system. This would also provide the final comparison between different capture technologies so that the most suitable pre-combustion capture system can be found.

Appendix A Extended DSL Isotherm Site Interaction

A.1 DSL Site Pairing

The extended DSL isotherm is given in Section 4.2. For the binary mixtures this can be expanded to give Equation A.1.1 for one component and Equation A.1.2 for the second component. For the pure component isotherm energetic site 1 and 2 are assigned so that the higher capacity, and therefore energetic site, is site 1 by convention. When the DSL isotherm is extended to binary mixtures, the interaction of each component to each site needs to be defined. In Equation A.1.1 and A.1.2 it has been assumed that site 1 for both components is the most energetic site. However, it is possible that the site which is found to be the most energetic for component 1 is the least energetic for component two. If this is the case the extension of the DSL isotherm would give Equations A.1.3 and A.1.4. This is explained in detail by Ritter et al. (2011), where it is suggested that it is not possible from the pure component isotherm to establish which relationship best represents the system as the numbering of the sites is arbitrary. For the work presented here, it was found that Equations A.1.1 and A.1.2 best represented the system as the capacities predicted by Equations A.1.3 and A.1.4 were too low.

Table A.1: The 4 possible extensions of the DSL isotherm.

$q_1^* = \frac{q_{1,s,1}B_{1,1}Py_1}{\left(1+B_{1,1}Py_1+B_{1,2}Py_2\right)} + \frac{q_{2,s,1}B_{2,1}Py_1}{\left(1+B_{2,1}Py_1+B_{2,2}Py_2\right)}$	A.1.1
$q_2^* = \frac{q_{1,s,2}B_{1,2}Py_2}{\left(1+B_{1,1}Py_1+B_{1,2}Py_2\right)} + \frac{q_{2,s,2}B_{2,2}Py_2}{\left(1+B_{2,1}Py_1+B_{2,2}Py_2\right)}$	A.1.2
$q_1^* = \frac{q_{1,s,1}B_{1,1}Py_1}{\left(1+B_{1,1}Py_1+B_{2,2}Py_2\right)} + \frac{q_{2,s,1}B_{2,1}Py_1}{\left(1+B_{2,1}Py_1+B_{1,2}Py_2\right)}$	A.1.3
$q_2^* = \frac{q_{1,s,2}B_{1,2}Py_2}{\left(1+B_{1,1}Py_1+B_{2,2}Py_2\right)} + \frac{q_{2,s,2}B_{2,2}Py_2}{\left(1+B_{2,1}Py_1+B_{1,2}Py_2\right)}$	A.1.4

Appendix B IAST Derivation for LF and DSL Isotherms

B.1 Summary of IAST

The ideal adsorbed solution theory (IAST) as developed by Myers and Prausnitz (1965) is a method used for predicting binary mixture capacities from pure component isotherm data. It uses the concept of equilibrium between a liquid solution and a vapour phase and applies it to the equilibrium between the adsorbed phase and the bulk phase. It can be applied to a system where the adsorbed phase is thermodynamically ideal and the analogy to Raoult's law is given by Equation B.1.1 (Rouquerol et al., 1999). A relationship between the spreading pressure and the equilibrium pressure is found by the integration of the pure-component isotherm to give Equation B.1.2.

$$p_i = x_i p_i^0(\pi) \qquad \text{B.1.1}$$

$$\frac{\pi_i^0 A}{RT} = \int_0^{p_i^o} \frac{q_i^{pure}}{p_i} dp_i \qquad \text{B.1.2}$$

The next assumption is that the spreading pressure of each component is equal and equal to that of the mixture, thus allowing an equation without the spreading pressure to be found that is purely dependent on the pure component isotherm. The solution of this situation allows x_i and p_i^0 to be found. A further relationship is then needed to the adsorbed amount. As the solution is ideal then it can be said that there is no change in the area/molecule on mixing (Ruthven, 1984), leading to Equation B.1.3. The component concentration for each phase is then related to the total by the component mass fraction in the adsorbed phase in Equation B.1.4. In a binary system this would give sufficient equations to solve for q_i.

$$\frac{1}{q_t} = \sum \frac{X_i}{q_i^{pure}} \qquad \text{B.1.3}$$

$$q_i = x_i q_t \qquad \text{B.1.4}$$

B.2 Solution for the Langmuir-Freundlich Isotherm

Equation B.1.2 uses the pure component isotherm to solve for the mass fraction in the adsorbed phase. The Langmuir-Freundlich isotherm is given by Equation B.2.1. The integral of this divided by the partial pressure is needed to solve Equation B.1.2, given by Equation B.2.2 and solved to give Equation B.2.3.

$$q_i^{pure} = \frac{q_{si} B_i p_i^{n_i}}{1 + B_i p_i^{n_i}} \qquad \text{B.2.1}$$

$$\int_0^{p_i^o} \frac{q_i^{pure}}{p_i} dp_i = \int_0^{p_i^o} \frac{q_{si} B_i p_i^{n_i - 1}}{1 + B_i p_i^{n_i}} dp_i \qquad \text{B.2.2}$$

$$\int_0^{p_i^o} \frac{q_i^{pure}}{p_i} dp_i = \frac{q_{si}}{n_i} ln\left(1 + B_i {p_i^0}^{n_i}\right) \qquad \text{B.2.3}$$

If this is then equated for a binary system such that $\pi_1 = \pi_2$, then Equation B.2.4 can be derived. The relationship from Equation B.1.1 puts this in terms of mass fraction of each component in the adsorbed phase and that the component fractions sum to 1 to give Equation B.2.5.

$$q_{s1} ln\left(1 + B_1 {p_1^0}^{n_1}\right) = q_{s2} ln\left(1 + B_2 {p_2^0}^{n_2}\right) \qquad \text{B.2.4}$$

$$q_{s1} ln\left(1 + B_1 \left(\frac{p_1}{x_1}\right)^{n_1}\right) = q_{s2} ln\left(1 + B_2 \left(\frac{p_2}{1 - x_1}\right)^{n_2}\right) \qquad \text{B.2.5}$$

Equation B.2.5 can be solved numerically to find x_1 and therefore x_2. These values can be used in conjunction with Equations B.1.3 and B.1.4 to find the capacity in the component phase at the specified temperature, pressure and concentration.

B.3 Solution for the Dual-Site Langmuir Isotherm

The same can be done with a Dual-site Langmuir isotherm given by Equation B.3.1. The integral of the DSL divided by the partial pressure is given by Equation B.3.2 which can be solved to give Equation B.3.3.

$$q_i^{pure} = \frac{q_{1,si} B_{1,i} p_i}{1 + B_{1,i} p_i} + \frac{q_{2,si} B_{2,i} p_i}{1 + B_{2,i} p_i} \qquad \text{B.3.1}$$

$$\int_0^{p_i^o} \frac{q_i^{pure}}{p_i} dp_i = \int_0^{p_i^o} \frac{q_{1,si} B_{1,i}}{1 + B_{1,i} p_i} + \frac{q_{2,si} B_{2,i}}{1 + B_{2,i} p_i} \quad dp_i \qquad \text{B.3.2}$$

$$\int_0^{p_i^o} \frac{q_i^{pure}}{p_i} dp_i = q_{1,si} ln\left(1 + B_{1,i} p_i^0\right) + q_{2,si} ln\left(1 + B_{2,i} p_i^0\right) \qquad \text{B.3.3}$$

If this is then equated for a binary system such that $\pi_1 = \pi_2$, then Equation B.3.4 is produced. The relationship from Equation B.1.1 puts this in terms of mass fraction of each component in the adsorbed phase and that the component fractions sum to 1 to give Equation B.3.5.

$$q_{1,s1} ln\left(1 + B_{1,1} p_1^0\right) + q_{2,s1} ln\left(1 + B_{2,1} p_1^0\right) = q_{1,s2} ln\left(1 + B_{1,2} p_2^0\right) + q_{2,s2} ln\left(1 + B_{2,2} p_2^0\right) \qquad \text{B.3.4}$$

$$q_{1,s1} ln\left(1 + \frac{B_{1,1} p_1}{x_1}\right) + q_{2,s1} ln\left(1 + \frac{B_{2,1} p_1}{x_1}\right) = q_{1,s2} ln\left(1 + \frac{B_{1,2} p_2}{1 - x_1}\right) + q_{2,s2} ln\left(1 + \frac{B_{2,2} p_2}{1 - x_1}\right) \qquad \text{B.3.5}$$

Equation B.3.5 can be solved numerically to find x_1 and therefore x_2. These values can be used in conjunction with Equations B.1.3 and B.1.4 to find the capacity in the component phase at the specified temperature, pressure and concentration.

Appendix C BET Isotherm Analysis

C.1 BET Isotherm Analysis

The analysis of the BET isotherm for the unmodified activated carbon is shown here. Figure C.1.1shows the isotherm results for nitrogen at 77K. The maximum quantity adsorbed was 318.9 $cm^3\ g^{-1}$ STP, giving a single point adsorption total pore volume of 0.493 $cm^3\ g^{-1}$.

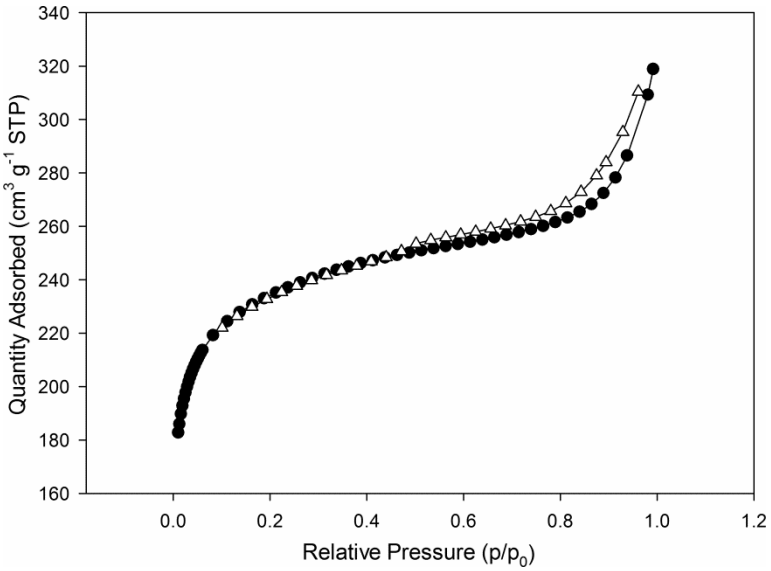

Figure C.1.1: BET results for N2 at 77K showing the adsorption (black circles) and desorption (white triangles) curves

The BET equation is given by Equation C.1.1.

$$\frac{p/p_0}{v(1-p/p_0)} = \frac{1}{v_m c} + \frac{c-1}{v_m c}(p/p_0) \qquad \text{C.1.1}$$

(Gregg and Sing, 1991)

This means a plot of

$$\frac{p/p_0}{v(1-p/p_0)} \quad vs \quad (p/p_0)$$

Gives a slope and intercept respectively of

$$\frac{1}{v_m c} \; and \; \frac{c-1}{v_m c}$$

Where v_m is the number of moles of adsorbate per gram of adsorbent. This is connected to the pore surface area of the material by Equation C.1.2.

$$S_{BET} = \frac{v_m}{22400} L a_m \qquad \text{C.1.2}$$

(Gregg and Sing, 1991)

Where L is avagadro's constant and a_m is the average area of a molecule of nitrogen which have values of 6.02 x 10^{23} molecules mol^{-1} and 16.2 x 10^{-20} m^2 $molecule^{-1}$.

The plot for the linearised version of the BET equation is given in Figure C.1.2 with a trend line included. The slope of the trend line is 0.004825 ± 0.000002 g cm^{-3} STP and the y-intercept is 9.1478 x10^{-6} ± 1.0392 x10^{-6} g cm^{-3} STP. This gives a monolayer capacity of 206.8 cm^3 g^{-1} STP. Substituting this into Equation C.1.2, the BET pore surface area is calculated to be 900.4 ± 0.41 m^2 g^{-1}.

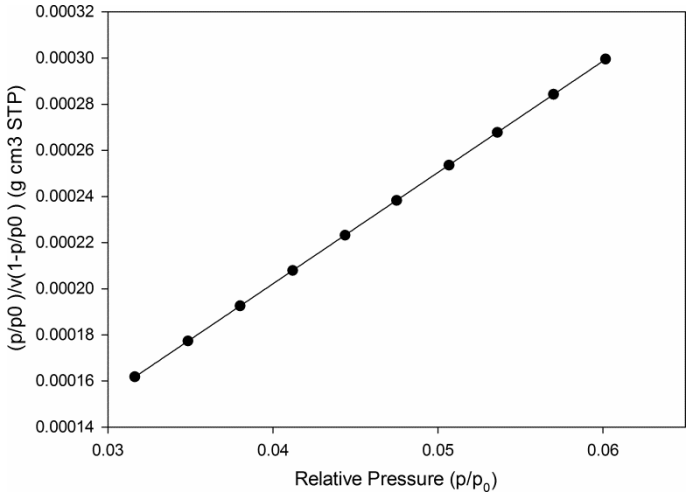

Figure C.1.2: Plot for finding the monolayer volume based in the BET equation

The average pore diameter can be found from the BET measurements by using the 4V/A method, where V is the total pore volume and A is the BET pore surface area. This gives an average pore width of 2.19 nm.

A t-plot was produced to find the deviation from the standard isotherm (Gregg and Sing, 1991). The linear range of the isotherm was found to be between relative pressures of 0.614 and 0.714 which gave predictions for the statistical thickness to be 0.753 and 0.881 nm based on the Harkins and Jura approximation. The t-plot for this is given in Figure C.1.3. The trend line for this had a slope of 28.6 ± 0.16 $cm^3\ g^{-1}\ nm^{-1}$ STP and an intercept of 232.7 ± 0.13 $cm^3\ g^{-1}$ STP. The micropore volume is found by multiplying the intercept by a constant to convert from standard conditions to actual conditions, which gives a micropore volume of 0.360 $cm^3\ g^{-1}$. The external surface area, S_a is calculated by multiplying the slope by the thickness of a nitrogen molecule, 0.354 nm, and a constant to give an external surface area of 44.1 $m^2\ g^{-1}$. The external surface area is then taken away from the BET surface area to give the micropore area, S_{micro}, which is calculated to be 856.1 $m^2\ g^{-1}$.

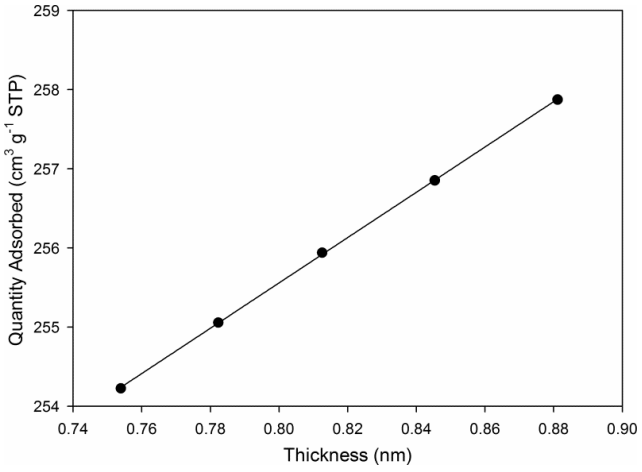

Figure C.1.3: t-plot based on a thickness range of 0.74 – 0.9 nm

Appendix D Carbon Dioxide Flow Controller Correction

D.1 Carbon Dioxide Flow Controller Correction

The carbon dioxide flow controller required a correction factor depending on the pressure to the inlet. The correction factor values at each pressure as supplied by the manufacturer are reported in Table D.1. Linear interpolation was used for intermediate pressures.

Table D.1: Carbon dioxide mass flow controller correction values.

Inlet pressure	Correction factor
35	1.000
33	1.022
31	1.045
29	1.071
27	1.086
25	1.102
23	1.117
21	1.135
19	1.152
17	1.17
15	1.181
13	1.199
11	1.214
9	1.231
7	1.247
5.2	1.261

Appendix E Risk Assessment

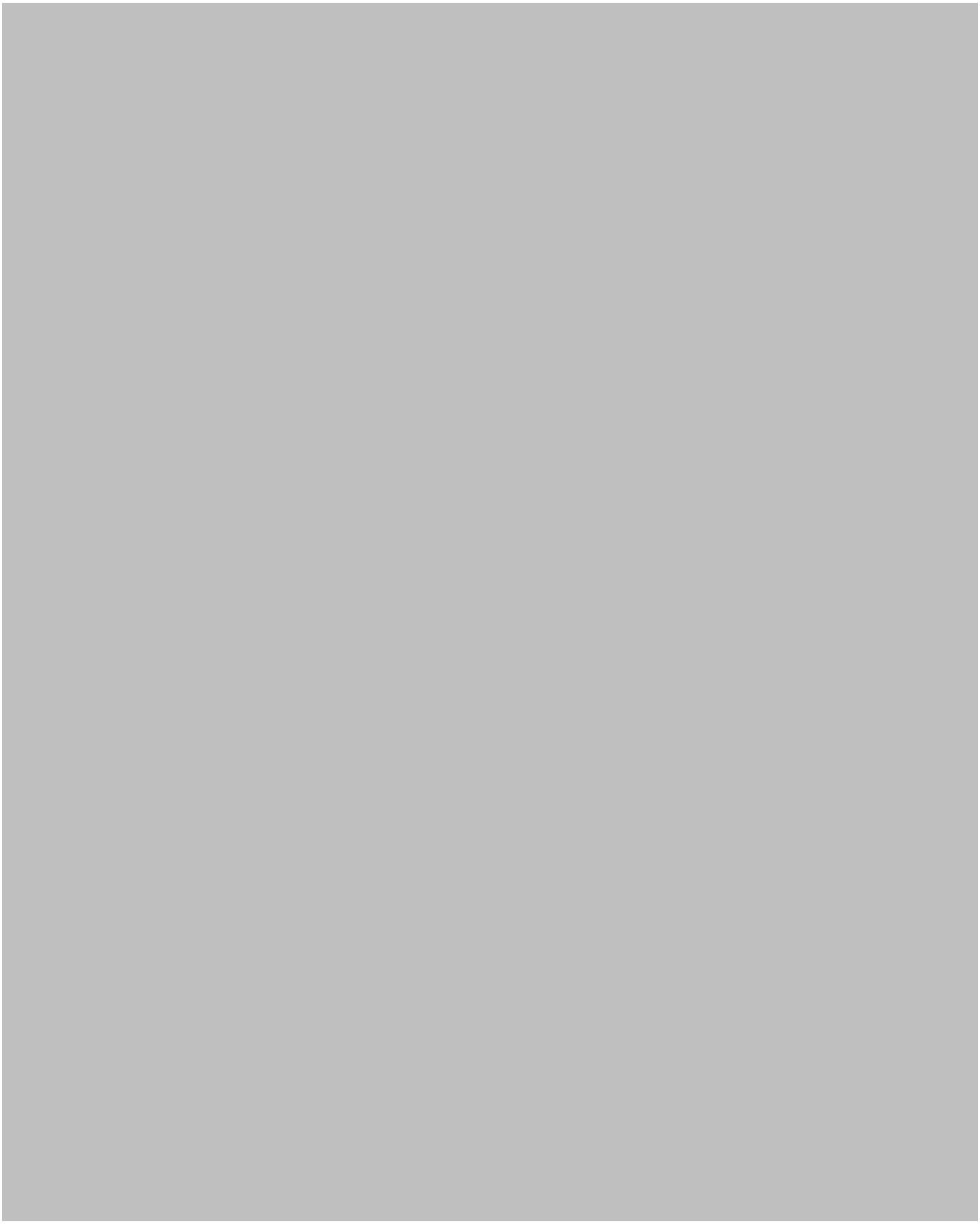

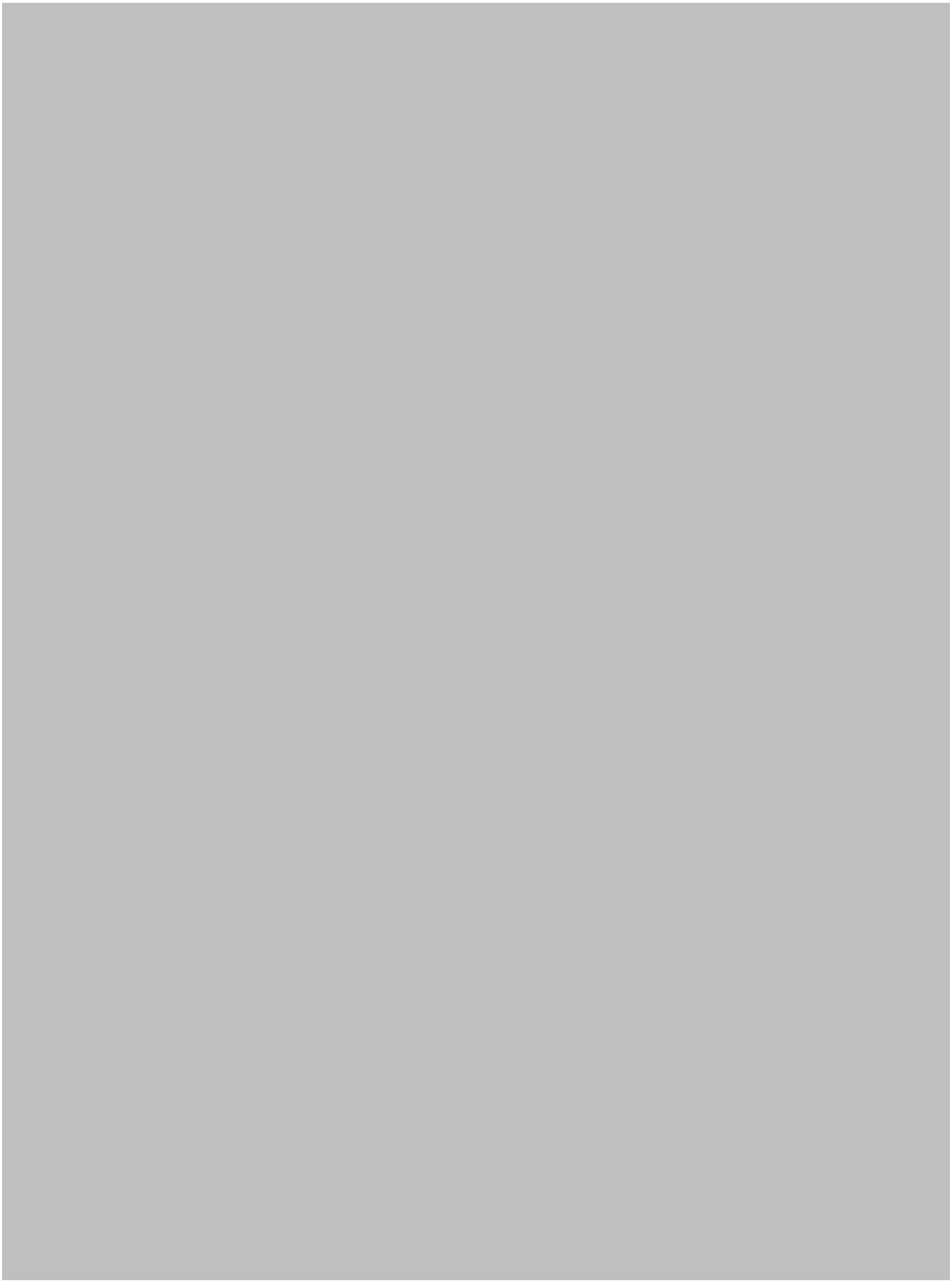

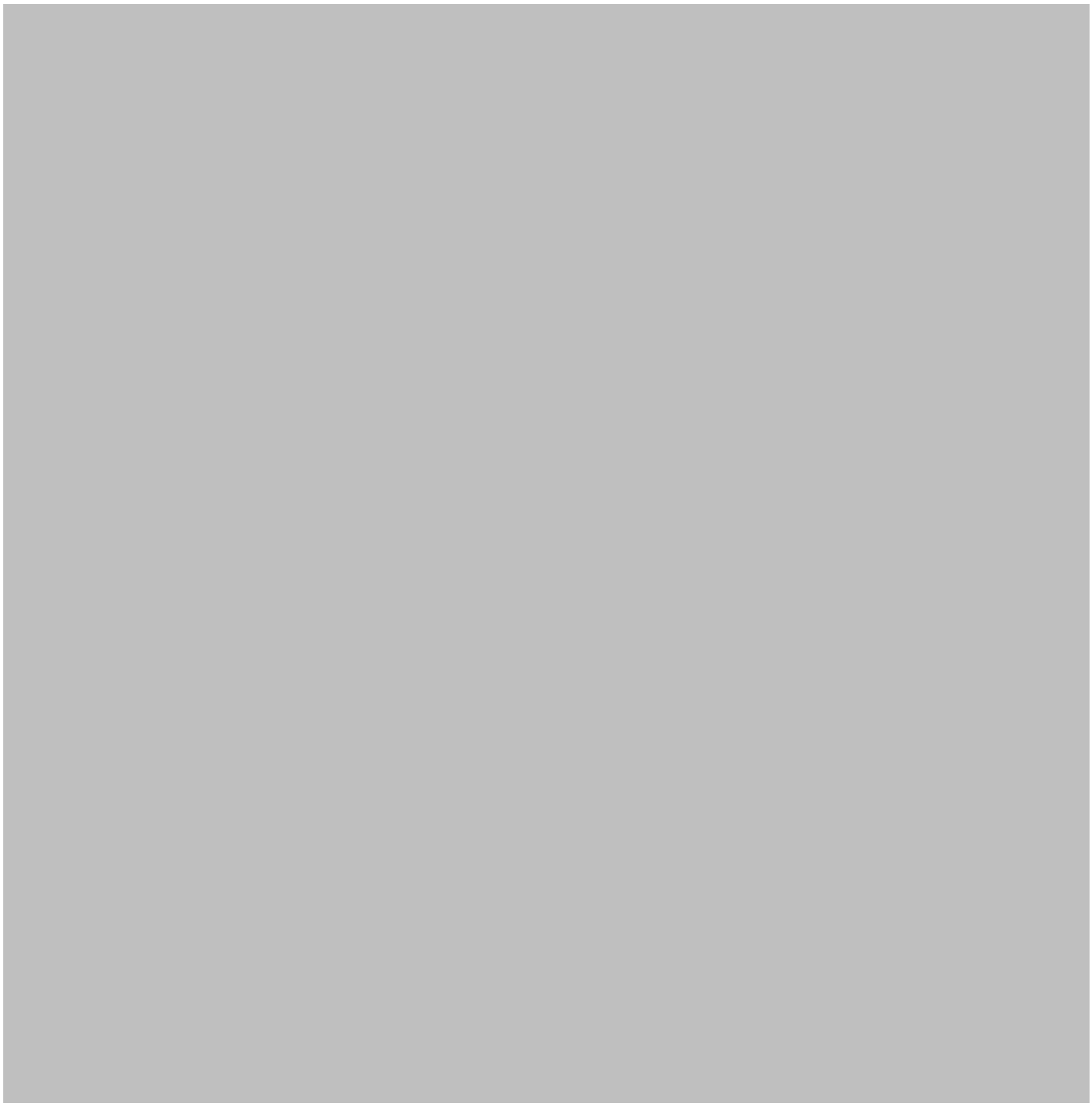

Appendix F gProms Code

The gProms code is split between the 4 main elements, VARAIBLE TYPES, MODELS, TASKS and PROCESSES. The MODEL defines the equations being solved and the TASKS define the sequence of the system. This Appendix shows the code for implementing the equations shown in Chapter 4 in the models. The implementation of the TASK for the 4 step model described in Section 4.12.1 is also shown.

F.1 Models

F.1.1 Dispersion Model

```
PARAMETER
   # Number of components
   NoComp        AS                INTEGER

   # Bed length, density and cross-sectional area
   BedLength     AS                REAL

   # Ideal gas constant
   R             AS                REAL

   # Bed Void
   BedVoid       AS                REAL


DISTRIBUTION_DOMAIN
   Axial AS [ 0 : BedLength ]


VARIABLE

   # Mole Fractions
   y       AS DISTRIBUTION(NoComp,Axial)    OF     MoleFraction
   yprod   AS DISTRIBUTION(NoComp)          OF     NoType

   # Superficial gas velocity
   u       AS DISTRIBUTION(Axial)           OF      Velocity

   # Volumetric Flow
   Q       AS DISTRIBUTION(Axial)           OF      VolumetricFlowrate
```

```
  # Pressure
  P             AS DISTRIBUTION(Axial)      OF      Pressure

  # Temperature
  T             AS DISTRIBUTION(Axial)      OF      Temperature

  # Feed conditions
  Pfeed         AS                                  Pressure
  Tfeed         AS                                  Temperature
  yfeed         AS ARRAY(NoComp)            OF      NoType
  Qfeed         AS                                  Velocity

  # Dispersion Coefficient
  Dispersion    AS                                  Diffusivity

  # Bed Properties
  BedDiameter   AS                                  Length
  BedArea       AS                                  Area

BOUNDARY

  # At the feed end
  FOR i := 1 TO NoComp DO
    y(i,0) = yfeed(i) ;
  END # For
  P(0) = Pfeed ;
  T(0) = Tfeed ;
  u(0) = Qfeed / BedArea / BedVoid ;

  # At Bed Exit
  PARTIAL(y(,BedLength),Axial) = 0 ;
  PARTIAL(u(BedLength),Axial) = 0 ;


EQUATION

  # Component mass balance
  FOR i := 1 TO NoComp DO
    FOR z := 0|+ TO BedLength|- DO
      $y(i,z) = -u(z) * PARTIAL(y(i,z) , Axial)
            + Dispersion * PARTIAL(y(i,z) , Axial , Axial);
    END # For
  END # For

  # Overall mass balance
  FOR z := 0|+ TO BedLength|- DO
    PARTIAL(u(z) , Axial) = 0 ;
  END

  # Mole Fraction at Bed End
  FOR i := 1 to NoComp DO
    y(i,BedLength) = yprod(i) ;
  END # For


  # Isothermal and Isobaric operation
  FOR z := 0|+ TO BedLength DO
    T(z) = Tfeed ;
```

```
    P(z) = Pfeed ;
  END # For

  # Volumetric Flow
  FOR z := 0 TO BedLength DO
    Q(z) = u(z) * BedArea * BedVoid ;
  END # For

  # Bed Area
  BedArea = BedDiameter^2 / 4 * 3.141 ;
```

F.1.2 Adsorption Model

```
PARAMETER

  # Number of components
  NoComp        AS              INTEGER

  # Bed Properties
  BedLength     AS              REAL
  BedDiameter   AS              REAL
  BedArea       AS              REAL
  BedDensity    AS              REAL

  # Adsorbent Properties
  Dp            AS              REAL

  # Ideal gas constant
  R             AS              REAL

  # Isotherm Parameters
  k11           AS ARRAY(NoComp)    OF REAL
  k12           AS ARRAY(NoComp)    OF REAL
  k13           AS ARRAY(NoComp)    OF REAL
  k14           AS ARRAY(NoComp)    OF REAL
  k21           AS ARRAY(NoComp)    OF REAL
  k22           AS ARRAY(NoComp)    OF REAL
  k23           AS ARRAY(NoComp)    OF REAL
  k24           AS ARRAY(NoComp)    OF REAL

  phys_prop   AS FOREIGN_OBJECT

  # For Dispersion
  RMM           AS ARRAY(NoComp)    OF  REAL
  visccomp      AS ARRAY(NoComp)    OF REAL
  phi           AS ARRAY(NoComp)    OF REAL

  # For MT
  rpore         AS                      REAL
  tortuosity    AS                      REAL
  Dc_rc2        AS ARRAY(NoComp)    OF REAL

DISTRIBUTION_DOMAIN
  Axial AS [ 0 : BedLength ]
```

```
UNIT
   Diffus AS Diffusivity
   EB AS EB_Non_Isothermal_w_wall


VARIABLE

# Assigned Variables
   # Feed conditions
   Pfeed      AS                    Pressure
   Tfeed      AS                    Temperature
   Yfeed          AS ARRAY(NoComp)              OF      MoleFraction
   Qin            AS                            VolumetricFlowrate
   Qfeednorm      AS                            VolumetricFlowrate
   Tair           AS                            Temperature
   ypress         AS ARRAY(NoComp)              OF      MoleFraction

#Dependent Variables
   # Mole fraction
   y              AS DISTRIBUTION(NoComp,Axial)  OF      MoleFraction
   yfinal         AS                            MoleFraction
   # Solid phase concentrations
   q              AS DISTRIBUTION(NoComp,Axial)          OF      SolidConcentration
   # Equilibrium solid phase concentrations
   qeq            AS DISTRIBUTION(NoComp,Axial)          OF      SolidConcentration
   # Superficial gas velocity
   u              AS DISTRIBUTION(Axial)                 OF      Velocity
   # Pressure
   P              AS DISTRIBUTION(Axial)                 OF      Pressure
   # Temperature
   T              AS DISTRIBUTION(Axial)                 OF      Temperature
   # Concentration
   C              AS DISTRIBUTION(Axial)                 OF      NoType
   ci             AS DISTRIBUTION(NoComp,Axial)          OF      NoType
   density        AS DISTRIBUTION(Axial)                 OF      NoType
   viscosity      AS DISTRIBUTION(Axial)                 OF      NoType
   heatcap        AS DISTRIBUTION(Axial)                 OF      NoType
   thermalcond    AS DISTRIBUTION(Axial)                 OF      NoType
   Qvol           AS DISTRIBUTION(Axial)                 OF      VolumetricFlowrate

# For Parameter Estimation
   BedVoid        AS                                             NoType
   PartVoid       AS                                             NoType
   TotVoid        AS                                             NoType
   Dispersion     AS                                             Diffusivity

# For Dispersion
   Diff           AS DISTRIBUTION(Axial)                 OF      Diffusivity
   Re             AS                                             NoType
   Sc             AS                                             NoType
   Peclet         AS                                             NoType
```

```
# For MT
   Dk          AS ARRAY(NoComp)                          OF    Diffusivity
   Dpore       AS ARRAY(NoComp)                          OF    Diffusivity
   k           AS ARRAY(NoComp)                          OF    MassCoefficient
   kf          AS                                              MassCoefficient

# For Isotherm
   qs1         AS DISTRIBUTION(NoComp,Axial)             OF    NoType
   B1          AS DISTRIBUTION(NoComp,Axial)             OF    NoType
   qs2         AS DISTRIBUTION(NoComp,Axial)             OF    NoType
   B2          AS DISTRIBUTION(NoComp,Axial)             OF    NoType

# For Ergun
   A_erg       AS                                              NoType
   B_erg       AS                                              NoType


SET
   RMM         := [44 , 28] ;
   visccomp    := [1.82e-5 , 1.53e-5] ;
   phi(1)      := (1 + (visccomp(1)/visccomp(2))^0.5 *
               (RMM(2)/RMM(1))^0.25)^0.5/(8*(1+RMM(1)/RMM(2)))^0.5 ;
   phi(2)       := (1 + (visccomp(2)/visccomp(1))^0.5 *
               (RMM(1)/RMM(2))^0.25)^0.5/(8*(1+RMM(2)/RMM(1)))^0.5 ;
   Dc_rc2      := [7.19e-2 , 1.06e-2] ;
   rpore       := 6.13e-9 ;
   tortuosity  := 1.414 ;


BOUNDARY

   # At the feed end
   For i := 1 to NoComp DO
      -Dispersion*PARTIAL(y(i,0),Axial) = u(0) * (Yfeed(i) - y(i,0)) ;
   END # For

   P(0) = Pfeed ;
   u(0) = Qin / BedArea / BedVoid ;
   - EB.HeatDisp(0) * PARTIAL(T(0),Axial) = phys_prop.VapourDensity(Tfeed,Pfeed,yfeed) *
                        phys_prop.VapourHeatCapacity(Tfeed,Pfeed,yfeed)/1000 * u(0) * (Tfeed - T(0)) ;

   # At the end of the bed
   PARTIAL(T(BedLength), Axial) = 0 ;
   PARTIAL(P(BedLength), Axial) = 0 ;
   PARTIAL(y(,BedLength),Axial) = 0 ;
   PARTIAL(u(BedLength),Axial) = 0 ;


EQUATION

   # Normalised Flowrate
   Qin = Qfeednorm*(1e5*Tfeed/(Pfeed*273))/1e6/60 ;

   # Total Voidage
   TotVoid = BedVoid + PartVoid - BedVoid*PartVoid ;
```

```
# Component mass balance
FOR i := 1 TO NoComp DO
   FOR z := 0|+ TO BedLength|- DO
      TotVoid*$y(i,z) = -BedVoid*u(z)*PARTIAL(y(i,z), Axial)
            + BedVoid*Dispersion  * (PARTIAL(y(i,z), Axial , Axial) + 2/C(z) * PARTIAL(y(i,z),Axial) *
            PARTIAL(C(z), Axial))
            - (1-TotVoid) / (C(z)) * ($q(i,z) - y(i,z) * SIGMA($q(,z)));
   END # For
END # For

# Overall mass balance
FOR z := 0|+ TO BedLength|- DO
   TotVoid*$C(z) = BedVoid*Dispersion*PARTIAL(C(z),Axial,Axial) -
            BedVoid*PARTIAL(u(z)*C(z),Axial) - (1-TotVoid) * SIGMA($q(,z)) ;
END # For

FOR z := 0 TO BedLength DO
   C(z) = (P(z)/(R*T(z))) ;
END

FOR i := 1 TO NoComp DO
   FOR z := 0 TO BedLength DO
      ci(i,z)=C(z)*y(i,z) ;
   END # For
END # For

# Adsorption rate equation
FOR i := 1 TO NoComp DO
   FOR z := 0 TO BedLength DO
      $q(i,z) = k(i) * ( (qeq(i,z)) - q(i,z) ) ;
   END # For
END # For

# Dual Site Langmuir Isotherm
FOR z := 0 TO BedLength DO
   FOR i := 1 TO NoComp DO
      qs1(i,z) = k11(i)*exp(k12(i)/(R*T(z))) ;
      B1(i,z) = k13(i)*exp(k14(i)/(R*T(z))) ;
      qs2(i,z) = k21(i)*exp(k22(i)/(R*T(z))) ;
      B2(i,z) = k23(i)*exp(k24(i)/(R*T(z))) ;
      qeq(i,z) =  BedDensity / (1-TotVoid) * (qs1(i,z)*B1(i,z)*P(z)*y(i,z) / (1 + SIGMA(B1(,z)*P(z)*y(,z)))
            + qs2(i,z)*B2(i,z)*P(z)*y(i,z) / (1 + SIGMA(B2(,z)*P(z)*y(,z)))) ;
   END # For
END # For

# Ergun Equation
A_erg = 150 * (1+2*Dp/(3*BedDiameter*(1-BedVoid)))^2 ;
B_erg = 1.75 * (1+2*Dp/(3*BedDiameter*(1-BedVoid))) ;
For z:= 0|+ TO BedLength|- DO
   -PARTIAL(P(z), Axial) = A_erg * phys_prop.VapourViscosity(T(z),P(z),y(,z)) * (1 - BedVoid)^2 * u(z) /
            (BedVoid^3 * Dp^2)
                              + B_erg * (1-BedVoid) / (Dp * BedVoid^3) * u(z) * ABS(u(z)) *
            phys_prop.VapourDensity(T(z),P(z),y(,z)) ;
END # For
```

```
# End Mole Fraction
yfinal = y(2,BedLength) ;
FOR z := 0 TO BedLength DO
   density(z) = phys_prop.VapourDensity(T(z),P(z),y(,z)) ;
   viscosity(z) = phys_prop.VapourViscosity(T(z),P(z),y(,z)) ;
   heatcap(z) = phys_prop.VapourHeatCapacity(T(z),P(z),y(,z)) ;
   thermalcond(z) = phys_prop.VapourConductivity(T(z),P(z),y(,z)) ;
   Qvol(z) = BedArea * u(z) ;
END # For

# Connection to Diff
P()       = Diffus.P() ;
T()       = Diffus.T() ;
Diff()    = Diffus.Diff() ;

# Dispersion
Re = density(BedLength) * u(0) * Dp / viscosity(BedLength) ;
Sc = viscosity(BedLength) / (Diff(0) * density(BedLength)) ;
Peclet = 1/(0.328/(Re*Sc) + 3.33/(1+0.59/(Re*Sc))) ;
Dispersion = u(0) * Dp / Peclet ;

# MT Coeff
kf = Diff(0)/(Dp/2) * (2 + 1.1 * Re^0.6 * Sc^0.33) ;
FOR i := 1 TO NoComp DO
   Dk(i) = 9700 * rpore * (Tfeed/RMM(i))^0.5 ;
   Dpore(i) = PartVoid * Dk(i) * Diff(0) / (tortuosity * (Dk(i)+Diff(0))) ;
   k(i) = 1 / (Dp/2 * qeq(i,0) / (3*kf*ci(i,0)) + (Dp/2)^2*qeq(i,0) / (15*PartVoid*Dpore(i)*ci(i,0)) + 1 /
          15/Dc_rc2(i)) ;
END # For

# Connection to EB
T = EB.T ;
Tfeed = EB.Tfeed ;
Tair = EB.Tair ;
u = EB.u ;
q = EB.q ;
y = EB.y ;
P = EB.P ;
Re = EB.Re ;
BedVoid = EB.BedVoid ;
TotVoid = EB.TotVoid ;
```

F.1.3 Diffusivity Model

```
PARAMETER
      NoComp          AS                          INTEGER
      BedLength       AS                          REAL
      RMM             AS ARRAY(NoComp)    OF      REAL
      sig             AS ARRAY(NoComp)    OF      REAL
      sigmix          AS                          REAL
      EpsoKap         AS ARRAY(NoComp)    OF      REAL
      EpsoKapmix      AS                          REAL
      Omega           AS                          REAL


DISTRIBUTION_DOMAIN
   Axial AS [ 0 : BedLength ]
```

```
VARIABLE
P       AS DISTRIBUTION(Axial)      OF      Pressure
T       AS DISTRIBUTION(Axial)      OF      Temperature
Tdim    AS DISTRIBUTION(Axial)      OF      Temperature
Diff    AS DISTRIBUTION(Axial)      OF      Diffusivity


SET
RMM             := [44 , 28] ;
sig             := [3.996 , 3.617] ;
sigmix          := 0.5 * SIGMA(sig()) ;
EpsoKap         := [190 , 97] ;
EpsoKapmix      := PRODUCT(EpsoKap())^0.5 ;
Omega           := 1.042 ;



EQUATION
   FOR z := 0 TO BedLength DO
      Tdim(z) = T(z)/ EpsoKapmix ;
      Diff(z) = (0.0018583*(T(z)^3*(1/RMM(1)+1/RMM(2)))^0.5 / (P(z)/1e5*sigmix^2*Omega))/1e4 ;
   END # For
```

F.1.4 Energy Balance Model

```
PARAMETER
   # Number of Components
   NoComp               AS                          INTEGER

   # Bed Properties
   BedLength            AS                          REAL
   BedDiameter          AS                          REAL
   BedArea              AS                          REAL
   BedDensity           AS                          REAL

   # Adsorbent Properties
   Dp                   AS                          REAL

   # Heat transfer coefficients
   HeatCapacityPart     AS                          REAL
   HeatAdsorp           AS ARRAY(NoComp) OF         REAL
   HeatTranStag         AS                          REAL
   alphaw               AS                          REAL

   # Ideal gas constant
   R                    AS                          REAL

   # Physical Properties
   phys_prop             AS                         FOREIGN_OBJECT


DISTRIBUTION_DOMAIN
   Axial AS [ 0 : BedLength ]


VARIABLE
   # Temperature
```

```
T          AS DISTRIBUTION(Axial)              OF      Temperature
Tfeed      AS                                          Temperature
Tair       AS                                          Temperature

# Superficial Velocity
u          AS DISTRIBUTION(Axial)              OF      Velocity

# Solid Phase Concentration
q          AS DISTRIBUTION(NoComp,Axial)       OF      SolidConcentration

# Pressure
P          AS DISTRIBUTION(Axial)              OF      Pressure

# Mole Fraction
y          AS DISTRIBUTION(NoComp,Axial)       OF      MoleFraction

# BedVoid
BedVoid    AS                                          NoType
TotVoid    AS                                          NoType

# Calcing HTCoeffWall
HTCoeffWall  AS DISTRIBUTION(Axial)            OF      NoType
Pr           AS DISTRIBUTION(Axial)            OF      NoType
Re           AS DISTRIBUTION(Axial)            OF      NoType
PrRe         AS DISTRIBUTION(Axial)            OF      Dimensionless

HeatDisp     AS DISTRIBUTION(Axial)            OF      NoType
yagi         AS DISTRIBUTION(Axial)            OF      NoType
```

EQUATION

```
# HT Coeff Wall
FOR z := 0 TO BedLength DO
   Pr(z) = phys_prop.VapourHeatCapacity(T(z),P(z),y(,z))*phys_prop.VapourViscosity(T(z),P(z),y(,z))/
         phys_prop.VapourConductivity(T(z),P(z),y(,z)) ;
   PrRe(z) = 2.19*(Pr(z) * Re(z))^(1/3) ;
   HTCoeffWall(z) = yagi(z) ;
   yagi(z) = HeatTranStag + alphaw * phys_prop.VapourHeatCapacity(T(z),P(z),y(,z))/1000 *
         phys_prop.VapourDensity(T(z),P(z),y(,z)) * u(z) ;

   HeatDisp(z) = phys_prop.VapourConductivity(T(z),P(z),y(,z))*(7+0.5*Pr(z)*Re(z))/1000;

END # For
# Non-Isothermal
FOR z := 0|+ TO BedLength|- DO
   (TotVoid * phys_prop.VapourDensity(T(z),P(z),y(,z)) *
         phys_prop.VapourHeatCapacity(T(z),P(z),y(,z))/1000 + BedDensity * HeatCapacityPart) * $T(z) =
        - phys_prop.VapourDensity(T(z),P(z),y(,z)) * phys_prop.VapourHeatCapacity(T(z),P(z),y(,z))/1000 *
         BedVoid * PARTIAL(T(z) *u(z)/BedVoid ,Axial)
        + HeatDisp(z) * PARTIAL(T(z),Axial,Axial)
        + (1 - TotVoid) * SIGMA(HeatAdsorp()*$q(,z))
                - 4 * HTCoeffWall(z) / BedDiameter * (T(z) - Tair) ;
END # For
```

F.2 Tasks

F.2.1 4 Step Skarstrom Cycle

```
PARAMETER
  Column      AS MODEL Whole_System_Full

SCHEDULE

  SEQUENCE

     CONTINUE FOR Column.ad_time
     REASSIGN
        WITHIN Column DO
           yfeedsys := ypurge ;
        END
     END
     SWITCH
        Column.Press_set := Column.deflow ;
     END
     CONTINUE UNTIL Column.Qfeednormsys <= Column.Qblow_1

     SWITCH
        Column.Press_set := Column.Depress ;
     END

     REASSIGN
        Column.deflowrate := Column.deflowRate_2 ;
     END # Reassign

     CONTINUE UNTIL Column.Qoutmole >= Column.Depress_outmole

     WHILE Column.Pfeedsys >= Column.Plow DO
           SEQUENCE
              REASSIGN
                 Column.error_de := -OLD(Column.Qoutmole)+Column.Depress_outmole ;
                 Column.DepressRate := OLD(Column.DepressRate)*
                                          (OLD(Column.error_de)*Column.Depress_prop+1) ;
              END # Reassign
              CONTINUE FOR 0.1
           END # Sequence
     END # While

     REASSIGN
        Column.DepressRate := Column.DepressRateInt ;
        Column.error_de    := Column.Error_de_int ;
     END # Reassign

     SWITCH
        Column.Press_set := Column.deflow ;
     END
     CONTINUE UNTIL Column.Qfeednormsys <= Column.Qblow_2

     SWITCH
        Column.Press_set := Column.Con ;
     END
```

```
    CONTINUE FOR Column.blow_time

    SWITCH
      Column.Press_set := Column.reflow ;
    END
    CONTINUE UNTIL Column.Qfeednormsys >= Column.Qpurge
    SWITCH
      Column.Press_set := Column.Con ;
    END

    CONTINUE FOR Column.purge_time

  END # Sequence
```

Appendix G Compressibility Factor Calculation

G.1 Compressibility Factor Calculation

The cubic equation of state is often used to account for the deviation from the ideal gas law, with a two parameter cubic equation shown by Equation G.1.1.

$$\mathrm{P} = \frac{RT}{V-b} - \frac{a}{V^2 + ubV + wb^2} \qquad \text{G.1.1}$$

Another form of Equation G.1.1 is shown by Equation G.1.2 based on compressibility. (Reid et al., 1987)

$$Z^3 - (1 + B^* - uB^*)Z^2 + (A^* + wB^* - uB^* - uB^{*2})Z - A^*B^* - wB^{*2} - wB^{*3} = 0 \qquad \text{G.1.2}$$

$$A^* = \frac{aP}{R^2T^2} \qquad \text{G.1.3}$$

$$B^* = \frac{bP}{RT} \qquad \text{G.1.4}$$

There are several equation of states used for predicting the values of u, w, a and b The Peng-Robinson equation has previously been applied to high pressure adsorption systems by Casas et al. (2012). For the Peng-Robinson equation of state the value for u is 2 and the value for w is -1. The pure component values for a and b are given by Equations G.1.5 and G.1.6 respectively.

$$\mathrm{a} = \frac{0.45724R^2T_c^2}{P_c}\left[1 + \mathrm{f}\omega\left(1 - T_r^{1/2}\right)\right]^2 \qquad \text{G.1.5}$$

$$\mathrm{b} = \frac{0.07780RT_c}{P_c} \qquad \text{G.1.6}$$

$$\mathrm{f}\omega = 0.37464 + 1.54266\omega - 0.26992\omega^2 \qquad \text{G.1.7}$$

For gas mixtures the proportion of the constants a and b need to be found using Equations G.1.8 and G.1.9 respectively. The value of $\overline{k_{ij}}$ for a CO_2/N_2 mixture using the Peng-Robinson equation is -0.017.

$$a_m = \sum_i \sum_j y_i y_j (a_i a_j)^{1/2} (1 - \overline{k_{ij}}) \qquad \text{G.1.8}$$

$$b_m = \sum_i y_i b_i \qquad \text{G.1.9}$$

The properties used in the calculation of the compressibility for CO_2/N_2 mixtures are given in Table G.1. The range of compressibility factors calculated for the gas mixtures simulated in this study are reported in Table G.2.

Table G.1: Carbon dioxide and nitrogen properties for the calculation of compressibility. (Reid et al., 1987)

		Carbon Dioxide	Nitrogen
T_c	(K)	304.1	126.2
P_c	(bar)	73.8	33.9
ω	(-)	0.239	0.039
T	(K)	298	298
P	(bar)	25	25

Table G.2: CO_2/N_2 mixture compressibility factors for the range of carbon dioxide feed fractions studied.

CO_2 Mole Fraction	Z (-)
0	0.958
0.1	0.951
0.2	0.943
0.3	0.934
0.4	0.925
0.5	0.915

Table G.3: Nomenclature used in Appendix G.

A^*	Condition constant used in cubic equation of state
a	Condition constant used in cubic equation of state
a_m	Condition constant used in cubic equation of state for gas mixtures
B^*	Condition constant used in cubic equation of state
b	Condition constant used in cubic equation of state
b_m	Condition constant used in cubic equation of state for gas mixtures
fω	Condition constant used in cubic equation of state
$\overline{k_{ij}}$	Condition constant used in cubic equation of state for gas mixtures
P	Pressure
P_c	Critical pressure
R	Gas constant
T	Temperature
T_c	Critical Temperature
T_r	Relative Temperature
u	Condition constant used in cubic equation of state
V	Gas volume
w	Condition constant used in cubic equation of state
y	Component mole fraction
Z	Compressibility factor
ω	Pitzer's acentric factor

Appendix H Component Mass Balance Derivation

H.1 Component Mass Balance Derivation

The general component mass balance is given by Equation H.1.1.

$$\varepsilon_t \frac{\partial c_i}{\partial t} = -\varepsilon_b \frac{\partial (c_i v)}{\partial z} + \varepsilon_b D_{ax} \frac{\partial^2 c_i}{\partial z^2} - \rho_b \frac{\partial q_i}{\partial t} \qquad \text{H.1.1}$$

It is possible to represent the component concentration as a product of the total concentration and the component mole fraction in Equation H.1.2 and then expanded to give Equation H.1.4.

$$\varepsilon_t \frac{\partial (C y_i)}{\partial t} = -\varepsilon_b \frac{\partial (C y_i v)}{\partial z} + \varepsilon_b D_{ax} \frac{\partial^2 (C y_i)}{\partial z^2} - \rho_b \frac{\partial q_i}{\partial t} \qquad \text{H.1.2}$$

$$\varepsilon_t \left(C \frac{\partial y_i}{\partial t} + y_i \frac{\partial C}{\partial t} \right) = -\varepsilon_b \left(C v \frac{\partial y_i}{\partial z} + y_i \frac{\partial (C v)}{\partial z} \right) + \varepsilon_b D_{ax} \left(\frac{\partial}{\partial z} \left(C \frac{\partial y_i}{\partial z} + y_i \frac{\partial C}{\partial z} \right) \right) - \rho_b \frac{\partial q_i}{\partial t} \qquad \text{H.1.3}$$

$$\varepsilon_t \left(C \frac{\partial y_i}{\partial t} + y_i \frac{\partial C}{\partial t} \right) = -\varepsilon_b \left(C v \frac{\partial y_i}{\partial z} + y_i \frac{\partial (C v)}{\partial z} \right) + \varepsilon_b D_{ax} \left(C \frac{\partial^2 y_i}{\partial z^2} + 2 \frac{\partial y_i}{\partial z} \frac{\partial C}{\partial z} + y_i \frac{\partial^2 C}{\partial z^2} \right) - \rho_b \frac{\partial q_i}{\partial t} \qquad \text{H.1.4}$$

The overall mass balance is given by Equation H.1.5 and multiplied by the component mole fraction to given Equation H.1.6.

$$\varepsilon_t \frac{\partial C}{\partial t} = -\varepsilon_b \frac{\partial (Cv)}{\partial z} + \varepsilon_b D_{ax} \frac{\partial^2 C}{\partial z^2} - \rho_b \sum_{i=1}^{n} \frac{\partial q_i}{\partial t} \qquad \text{H.1.5}$$

$$\varepsilon_t y_i \frac{\partial C}{\partial t} = -\varepsilon_b y_i \frac{\partial (Cv)}{\partial z} + \varepsilon_b D_{ax} y_i \frac{\partial^2 C}{\partial z^2} - \rho_b y_i \sum_{i=1}^{n} \frac{\partial q_i}{\partial t} \qquad \text{H.1.6}$$

Equation H.1.6 can be subtracted from Equation H.1.4 to give Equation H.1.7. This can then be divided by the total concentration to give Equation H.1.8.

$$\varepsilon_t C \frac{\partial y_i}{\partial t} = -\varepsilon_b C v \frac{\partial y_i}{\partial z} + \varepsilon_b D_{ax} \left(C \frac{\partial^2 y_i}{\partial z^2} + 2 \frac{\partial y_i}{\partial z} \frac{\partial C}{\partial z} \right) - \rho_b \frac{\partial q_i}{\partial t} + \rho_b y_i \sum_{i=1}^{n} \frac{\partial q_i}{\partial t} \qquad \text{H.1.7}$$

$$\varepsilon_t \frac{\partial y_i}{\partial t} = -\varepsilon_b v \frac{\partial y_i}{\partial z} + \varepsilon_b D_{ax} \left(\frac{\partial^2 y_i}{\partial z^2} + \frac{2}{C} \frac{\partial y_i}{\partial z} \frac{\partial C}{\partial z} \right) - \frac{\rho_b}{C} \left(\frac{\partial q_i}{\partial t} - y_i \sum_{i=1}^{n} \frac{\partial q_i}{\partial t} \right) \qquad \text{H.1.8}$$

Appendix I Carbon Dioxide Hold-up of Experimental Pipe System

I.1 Carbon Dioxide Hold-up of Experimental Pipe System

The surrounding pipe system of the experimental set-up has a certain residence time due to the volume of the system. As discussed in Section 5.3.2.1, the amount of carbon dioxide accumulated in the system would expect to be linear when plotted against the CO_2 feed fraction which passes through the origin.

The plot for CO_2/N_2 systems is shown in Figure I.1.1 A trend line has been fitted which has a gradient of 5.15 ± 0.14 x 10^{-2} mol and a y-intercept of 4.66 ± 0.46 x 10^{-3} mol.

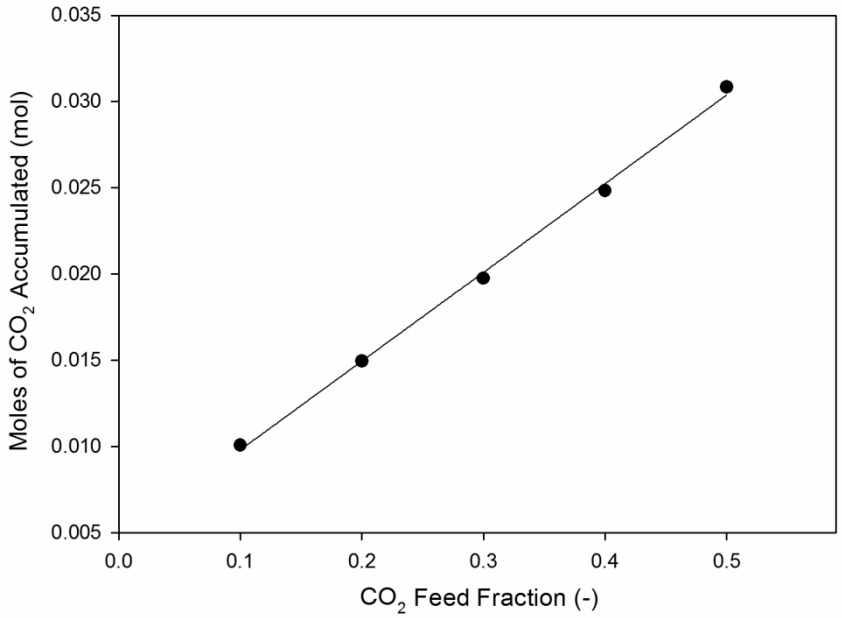

Figure I.1.1: The accumulated carbon dioxide for CO_2/N_2 systems at CO_2 feed fractions of 0.1, 0.2, 0.3, 0.4 and 0.5.

The plot for CO_2/H_2 separations is shown in Figure I.1.2. A trend line has been fitted which has a gradient of 4.42 ± 0.10 x 10^{-2} mol and a y-intercept of 5.59 ± 0.34 x 10^{-3} mol.

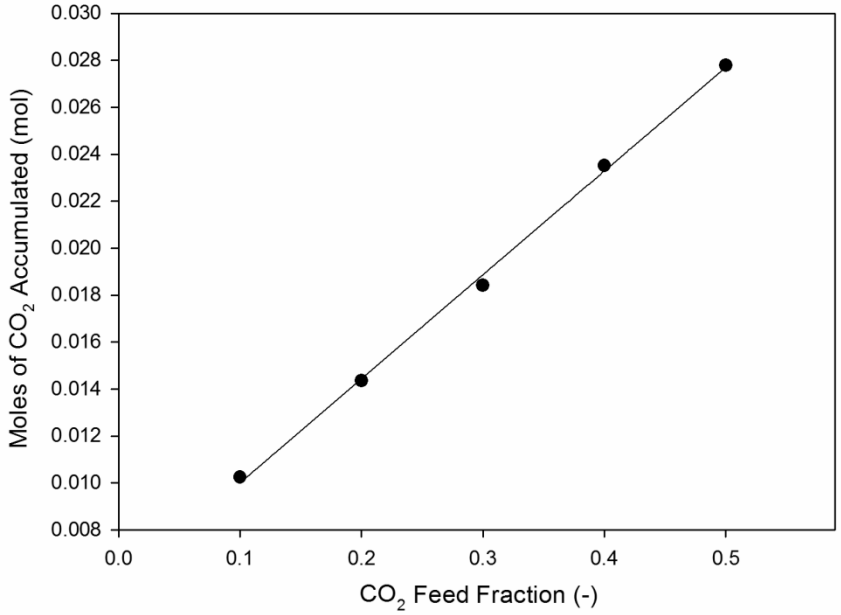

Figure I.1.2: The accumulated carbon dioxide for CO_2/H_2 systems at CO2 feed fractions of 0.1, 0.2, 0.3, 0.4 and 0.5.

Appendix J Dispersion and Mass Transfer Coefficient Calculation

J.1 Dispersion Coefficient

The dispersion coefficient can be predicted from a range correlations which calculate the Peclet number, the dimensionless group used in the evaluation of the dispersion coefficient. The Reynolds number is the ratio of inertial and viscous forces and the Schmidt number is the ratio of viscous and diffusive properties (Bird et al., 2001). The sum of the Reynolds' and Schmidt number is used for finding the Peclet number. The two dimensionless groups are:

$$Re = \frac{\rho u d_p}{\mu} \; and \; Sc = \frac{\mu}{\rho D_{AB}}$$

These are both affected by the viscosity of the gas and the gas density, however, when the number are multiplied together the two properties cancel out making the system only dependent on the particle diameter, the gas velocity and the gas diffusivity. The particle diameter is 1 mm and the gas velocity is 7.41 X 10^{-4} m s^{-1} for all CO_2 feed fractions. The gas diffusivity for a CO_2/N_2 mixture is 6.12 x 10^{-7} m^2 s^{-1} and 2.22 x 10^{-6} m^2 s^{-1} for a CO_2/H_2 mixture. The dispersion coefficient can be calculated by the Wakao and Funazkri (1978) correlation, the general correlation given in Ruthven (1984) and the Hsu and Haynes (1981) correlation, all shown in Section 4.7.1. The calculated dispersion coefficients from these three correlations for each of the system studied are presented in Table J.1.

Table J.1: Dispersion coefficient calculated from three correlations for all system studied here.

		Diffusivity	Wakao		General		Hsu and Haynes	
		(m^2 s^{-1})	Pe	D_{ax} (m^2 s^{-1})	Pe	D_{ax} (m^2 s^{-1})	Pe	D_{ax} (m^2 s^{-1})
CO_2/N_2	AC	6.12×10^{-7}	0.103	6.03×10^{-6}	0.906	6.82×10^{-7}	0.412	1.50×10^{-6}
CO_2/N_2	MAC	2.22×10^{-6}	0.059	1.26×10^{-5}	0.975	7.61×10^{-7}	0.398	1.86×10^{-6}
CO_2/H_2	MAC	6.12×10^{-7}	0.017	4.48×10^{-5}	0.415	1.79×10^{-6}	0.457	1.62×10^{-6}

J.2 Mass Transfer Coefficient

The mass transfer coefficient which incorporates the surface, macropore and micropore mass transfer resistances can be calculated by a correlation presented by Farooq and Ruthven (1990). These correlations for the parameters describing the mass transfer resistance are reported in Section 4.7.2. Each individual resistance can be calculated from the respective part of the correlation as each resistance is assumed to be additive, as shown by Equations J.2.1 to J.2.3.

$$\frac{1}{k_{surface,i}} = \frac{d_p q_{0,i}}{6 k_f c_{0,i}} \qquad \text{J.2.1}$$

$$\frac{1}{k_{macropore,i}} = \frac{d_{pore}^2 q_{0,i}}{60 \varepsilon_p D_{pore} c_{0,i}} \qquad \text{J.2.2}$$

$$\frac{1}{k_{micropore,i}} = \frac{r_c^2}{15 D_c} \qquad \text{J.2.3}$$

These can be calculated for all three systems studied here as shown in Table J.2. The values for hydrogen using the modified activated carbon are not presented as hydrogen is assumed to not adsorb on the system. Calculating values for hydrogen being adsorbed would require the hydrogen isotherm. The carbon dioxide isotherm data for this separation is based on pure component data.

Table J.2: Mass transfer resistances for all systems studied.

		AC – CO_2/N_2		MAC – CO_2/N_2		MAC – CO_2/H_2*	
		CO_2	N_2	CO_2	N_2	CO_2	H_2
$k_{surface,i}$	(s^{-1})	0.67	8.60	0.41	37.5	1.27	-
$k_{macropore,i}$	(s^{-1})	0.43	5.47	0.31	28.2	1.07	-
$k_{micropore,i}$	(s^{-1})	0.16	1.08	0.16	1.08	0.16	-
k_i	(s^{-1})	0.099	0.81	0.083	1.01	0.12	1.08

*All values found assume that no hydrogen is adsorbed and the carbon dioxide adsorbed amount is based on a pure component isotherm.

Appendix K System Model Parameters

K.1 System Model Parameters

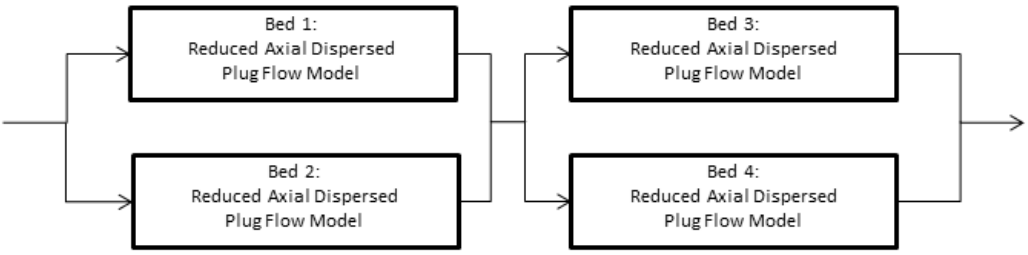

Figure K.1.1: Model configuration for the simulation of the system without a bed

The system without the bed, described in Section 3.6.2, was fitted to experimental data using a configuration of beds, as shown in Figure K.1.1, with each bed based on the reduced axial dispersed plug flow model. Beds 1 and 2 were matched to the analyser response and the same parameters were used for all carbon dioxide mole fraction. The bed lengths were found through iteration to match the breakthrough time. The bed area and dispersion coefficient were found using the gProms parameter estimation tool. Beds 3 and 4 were matched to the response of the analyser to the experiments for the system without the bed. The bed lengths were found through iteration to match the breakthrough time and were kept constant for all carbon dioxide mole fractions. The bed area and dispersion coefficient were found using the gProms parameter estimation tool individually for each carbon dioxide feed fraction. The parameters for all four beds are shown in Table K.1.

Table K.1: Parameters used for the simulation of the system without a bed

			0.1	0.2	0.3	0.4	0.5
Bed 1	Bed Length	(m)	0.002	0.002	0.002	0.002	0.002
	Bed Area	(m^2)	1.25×10^{-3}	1.25×10^{-3}	1.25×10^{-3}	1.25×10^{-3}	1.25×10^{-3}
	Dispersion	($m^2\ s^{-1}$)	4.14×10^{-9}	4.14×10^{-9}	4.14×10^{-9}	4.14×10^{-9}	4.14×10^{-9}
Bed 2	Bed Length	(m)	1	1	1	1	1
	Bed Area	(m^2)	1.05×10^{-4}	1.05×10^{-4}	1.05×10^{-4}	1.05×10^{-4}	1.05×10^{-4}
	Dispersion	($m^2\ s^{-1}$)	1.21×10^{-2}	1.21×10^{-2}	1.21×10^{-2}	1.21×10^{-2}	1.21×10^{-2}
Bed 3	Bed Length	(m)	5.5	5.5	5.5	5.5	5.5
	Bed Area	(m^2)	9.39×10^{-6}	6.50×10^{-6}	3.98×10^{-6}	3.15×10^{-6}	3.00×10^{-6}
	Dispersion	($m^2\ s^{-1}$)	9.14×10^{-3}	4.61×10^{-3}	1.32×10^{-3}	1.20×10^{-3}	1.41×10^{-3}
Bed 4	Bed Length	(m)	4.5	4.5	4.5	4.5	4.5
	Bed Area	(m^2)	9.47×10^{-6}	7.27×10^{-6}	7.56×10^{-6}	7.89×10^{-6}	7.44×10^{-6}
	Dispersion	($m^2\ s^{-1}$)	1.82×10^{-4}	6.06×10^{-5}	9.61×10^{-5}	3.98×10^{-5}	1.84×10^{-5}

List of References

Agarwal, A., Biegler, L.T., Zitney, S.E., 2010. Superstructure-Based Optimal Synthesis of Pressure Swing Adsorption Cycles for Precombustion CO2 Capture. Industrial & Engineering Chemistry Research 49, 5066-5079.

Ahn, H., Lee, C.-H., Seo, B., Yang, J., Baek, K., 1999. Backfill Cycle of a Layered Bed H2 PSA Process. Adsorption 5, 419-433.

Bell, D.A., Towler, B.F., 2010. Coal gasification and its applications. Elsevier Science, Oxford.

Bird, R.B., Stewart, W.E., Lightfoot, E.N., 2001. Transport Phenomena, 2nd ed. John Wiley & Sons, Inc., Chichester.

Bottani, E.J., Tascon, J.M.D., 2008. Adsorption by carbons. Elsevier, London.

BP, 2014. BP Statistical Review of World Energy 2014, London.

Casas, N., Schell, J., Blom, R., Mazzotti, M., 2013a. MOF and UiO-67/MCM-41 adsorbents for pre-combustion CO2 capture by PSA: Breakthrough experiments and process design. Separation and Purification Technology 112, 34-48.

Casas, N., Schell, J., Joss, L., Mazzotti, M., 2013b. A parametric study of a PSA process for pre-combustion CO2 capture. Separation and Purification Technology 104, 183-192.

Casas, N., Schell, J., Pini, R., Mazzotti, M., 2012. Fixed bed adsorption of CO2/H-2 mixtures on activated carbon: experiments and modeling. Adsorption-Journal of the International Adsorption Society 18, 143-161.

Cavenati, S., Grande, C.A., Rodrigues, A.E., 2006. Separation of mixtures by layered pressure swing adsorption for upgrade of natural gas. Chemical Engineering Science 61, 3893-3906.

Cen, P.-L., Chen, W.-N., Yang, R.T., 1985. Ternary Gas Mixture Separation by Prssure Swing Adsorption: A Combined Hydrogen-Methane Seaparation and Acid Gas Removal Process. Industrial Engineering Chemical Process Design and Development 24, 1201-1208.

Cen, P.-L., Yang, R.T., 1986. Bulk Gas Separation by Pressure Swing Adsorption. Industrial Engineering Chemical Fundamentals 25, 758-767.

Chen, C., Rubin, E.S., 2009. CO2 control technology effects on IGCC plant performance and cost. Energy Policy 37, 915-924.

Chen, Z., Deng, S., Wei, H., Wang, B., Huang, J., Yu, G., 2013. Activated carbons and amine-modified materials for carbon dioxide capture — a review. Frontiers of Environmental Science & Engineering 7, 326-340.

Chiesa, P., Consonni, S., Kreutz, T., Williams, R., 2005. Co-production of hydrogen, electricity and CO2 from coal with commercially ready technology.

Part A: Performance and emissions. International Journal of Hydrogen Energy 30, 747-767.

Choi, B.-U., Nam, G.-M., Choi, D.-K., Lee, B.-K., Kim, S.-H., Lee, C.-H., 2004. Adsorption and regeneration dynamic characteristics of methane and hydrogen binary system. Korean Journal of Chemical Engineering 21, 821-828.

Choi, C.-T., Wen-Chung, H., 1994. Incorporation of a valve equation into the simulation of a pressure swing adsorption process. Chemical Engineering Science 49, 75-84.

Choi, W.-K., Kwon, T.-I., Yeo, Y.-K., Lee, H., Song, H., Na, B.-K., 2003. Optimal operation of the pressure swing adsorption (PSA) process for CO_2 recovery. Korean Journal of Chemical Engineering 20, 617-623.

Chou, C.-T., Chen, C.-Y., 2004. Carbon dioxide recovery by vacuum swing adsorption. Separation and Purification Technology 39, 51-65.

Chue, K.T., Kim, J.N., Yoo, Y.J., Cho, S.H., Yang, R.T., 1995. Comparison of Activated Carbon and Zeolite 13X for CO2 Recovery from Flue Gas by Pressure Swing Adsorption. Industrial & Engineering Chemistry Research 34, 591-598.

Committee on Climate Change, 2010a. The Fourth Carbon Budget: Reducing Emissions Through the 2020s, London.

Committee on Climate Change, 2010b. Meeting Carbon Budgets - Ensuring a low-carbon recovery: 2nd report to Parliament, London.

Danckwerts, P.V., 1953. Continuous flow systems: Distribution of residence times. Chemical Engineering Science 2, 1-13.

Dantas, T.L.P., Luna, F.M.T., Silva Jr, I.J., de Azevedo, D.C.S., Grande, C.A., Rodrigues, A.E., Moreira, R.F.P.M., 2011. Carbon dioxide–nitrogen separation through adsorption on activated carbon in a fixed bed. Chemical Engineering Journal 169, 11-19.

Delgado, J.A., Rodrigues, A.E., 2008. Analysis of the boundary conditions for the simulation of the pressure equalization step in PSA cycles. Chemical Engineering Science 63, 4452-4463.

Delgado, J.A., Uguina, M.A., Sotelo, J.L., Águeda, V.I., Sanz, A., Gómez, P., 2011. Numerical analysis of CO2 concentration and recovery from flue gas by a novel vacuum swing adsorption cycle. Computers & Chemical Engineering 35, 1010-1019.

Delgado, J.A., Uguina, M.A., Sotelo, J.L., Ruíz, B., 2006. Fixed-bed adsorption of carbon dioxide-helium, nitrogen-helium and carbon dioxide-nitrogen mixtures onto silicalite pellets. Separation and Purification Technology 49, 91-100.

Descamps, C., Bouallou, C., Kanniche, M., 2008. Efficiency of an Integrated Gasification Combined Cycle (IGCC) power plant including CO2 removal. Energy 33, 874-881.

Do, D.D., 1998. Adsorption Analysis: Equilibria and Kinetics. Imperial College Press, London.

Doong, S.J., Yang, R.T., 1986. Bulk Separation of Multicomponent Gas Mixtrues by Pressure Swing Adsorption: Pore/Surface Diffusion and Equilibrium Models. AIChE Journal 32, 397-410.

Doong, S.J., Yang, R.T., 1987a. Bidisperse Pore Diffusion Model for Zeolite Pressure Swing Adsorption. AIChE Journal 33, 1045-1049.

Doong, S.J., Yang, R.T., 1987b. Hydrogen Purification by the Multibed Pressure Swing Adsorption Process. Reactive Polymers 6, 7-13.

Drage, T.C., Blackman, J.M., Pevida, C., Snape, C.E., 2009a. Evaluation of Activated Carbon Adsorbents for CO2 Capture in Gasification. Energy & Fuels 23, 2790-2796.

Drage, T.C., Kozynchenko, O., Pevida, C., Plaza, M.G., Rubiera, F., Pis, J.J., Snape, C.E., Tennison, S., 2009b. Developing activated carbon adsorbents for pre-combustion CO2 capture. Energy Procedia 1, 599-605.

Dreisbach, F., Staudt, R., Keller, J.U., 1999. High Pressure Adsorption Data of Methane, Nitrogen, Carbon Dioxide and their Binary and Ternary Mixtures on Activated Carbon. Adsorption 5, 215-227.

Dullen, F.A.L., 1979. Porous Media: Fluid Transport and Pore Structure. Academic Press, London.

European Commission - Joint Research Centre (JRC)/PBL Netherlands Environmental Assessment Agency, 2011. Emission Database for Global Atmospheric Research (EDGAR), release version 4.2 ed.

Farooq, S., Ruthven, D.M., 1990. Heat effects in adsorption column dynamics. 2. Experimental validation of the one-dimensional model. Industrial & Engineering Chemistry Research 29, 1084-1090.

Figueroa, J., Fout, T., Plasynski, S., McIlvried, H., Srivastava, R.D., 2008. Advances in CO2 capture technology-The U.S. Department of Energy's Carbon Sequestration Program. International Journal of Greenhouse Gas Control 2, 9-20.

Gao, F., Zhou, J., Bian, Z., Jing, C., Hu, J., Liu, H., 2013. Dynamic properties in CO2 adsorption on amine-modified MCM-41. Proceedings of the Institution of Mechanical Engineers, Part E: Journal of Process Mechanical Engineering 227, 106-116.

Gao, W., Butler, D., Tomasko, D.L., 2004. High-Pressure Adsorption of CO2 on NaY Zeolite and Model Prediction of Adsorption Isotherms. Langmuir 20, 8083-8089.

García, S., Gil, M.V., Martín, C.F., Pis, J.J., Rubiera, F., Pevida, C., 2011. Breakthrough adsorption study of a commercial activated carbon for pre-combustion CO2 capture. Chemical Engineering Journal 171, 549-556.

García, S., Pis, J.J., Rubiera, F., Pevida, C., 2013. Predicting Mixed-Gas Adsorption Equilibria on Activated Carbon for Precombustion CO2 Capture. Langmuir 29, 6042-6052.

Garg, D.R., Ruthven, D.M., 1975. Performance of molecular sieve adsorption columns: combined effects of mass transfer and longitudinal diffusion. Chemical Engineering Science 30, 1192-1194.

Global CCS Institute, 2013. The Global Status of CCS: 2013, Canberra, Australia.

Glueckauf, E., Coates, J.I., 1947. 241. Theory of chromatography. Part IV. The influence of incomplete equilibrium on the front boundary of chromatograms and on the effectiveness of separation. Journal of the Chemical Society (Resumed), 1315-1321.

Gomes, V.G., Yee, K.W.K., 2002. Pressure swing adsorption for carbon dioxide sequestration from exhaust gases. Separation and Purification Technology 28, 161-171.

Grande, C.A., 2012. Advances in Pressure Swing Adsorption for Gas Separation. ISRN Chemical Engineering 2012, 13.

Grande, C.A., Blom, R., Möller, A., Möllmer, J., 2013. High-pressure separation of CH4/CO2 using activated carbon. Chemical Engineering Science 89, 10-20.

Gregg, S.J., Sing, K.S.W., 1991. Adsorption, surface area, and porosity. Academic Press.

Himeno, S., Komatsu, T., Fujita, S., 2005. High-Pressure Adsorption Eqeuilbria of Methane and Carbon Dioxide on Several Activated Carbons. Journal of Chemical Engineering Data 50, 369-376.

Hsu, L.K.P., Haynes, H.W., 1981. Effective diffusivity by the gas chromatography technique: Analysis and application to measurements of diffusion of various hydrocarbons in zeolite NaY. AIChE Journal 27, 81-91.

IEA, 2012. Energy technology perspectives: Pathways to a clean energy system, France.

Kikkinides, E.S., Yang, R.T., Cho, S.H., 1993. Concentration and recovery of carbon dioxide from flue gas by pressure swing adsorption. Industrial & Engineering Chemistry Research 32, 2714-2720.

Ko, D., Siriwardane, R., Biegler, L.T., 2002. Optimization of a Pressure-Swing Adsorption Process Using Zeolite 13X for CO2 Sequestration. Industrial & Engineering Chemistry Research 42, 339-348.

Ko, D., Siriwardane, R., Biegler, L.T., 2005. Optimization of Pressure Swing Adsorption and Fractionated Vacuum Pressure Swing Adsorption Processes for CO2 Capture. Industrial & Engineering Chemistry Research 44, 8084-8094.

Krishnan, G., Steele, D., O'Brien, K., Callahan, R., Berchtold, K., Figueroa, J., 2009. Simulation of a Process to Capture CO2 From IGCC Syngas Using a High Temperature PBI Membrane. Energy Procedia 1, 4079-4088.

Kunze, C., Spliethoff, H., 2010. Modelling of an IGCC plant with carbon capture for 2020. Fuel Processing Technology 91, 934-941.

Langmuir, I., 1918. THE ADSORPTION OF GASES ON PLANE SURFACES OF GLASS, MICA AND PLATINUM. Journal of the American Chemical Society 40, 1361-1403.

Leva, M., 1947. Heat Transfer to Gases through Packed Tubes. Industrial & Engineering Chemistry 39, 857-862.

LeVaque, R.J., 2007. Finite Difference Methods for Ordinary and Partial Differential Equations. Society for Industrial and Applied Mathematics, Philadelphia.

Levenspiel, O., 1999. Chemical Reaction Engineering (3rd Edition). John Wiley & Sons, pp. 293-320.

Liang, X., Reiner, D., Li, J., 2011. Perceptions of opinion leaders towards CCS demonstration projects in China. Applied Energy 88, 1873-1885.

Liaw, C.H., Wang, J.S.P., Greenkorn, R.A., Chao, K.C., 1979. Kinetics of fixed-bed adsorption: A new solution. AIChE Journal 25, 376-381.

Liu, W., King, D., Liu, J., Johnson, B., Wang, Y., Yang, Z., 2009. Critical Material and Process Issues for CO2 Separation from Coal-Powered Plants. Journal of Materials 61, 36-44.

Liu, Z., Grande, C.A., Li, P., Yu, J., Rodrigues, A.E., 2011. Multi-bed Vacuum Pressure Swing Adsorption for carbon dioxide capture from flue gas. Separation and Purification Technology 81, 307-317.

Lopes, F.V.S., Grande, C.A., Ribeiro, A.M., Oliveira, E.L.G., Loureiro, J.M., Rodrigues, A.r.E., 2009. Enhancing Capacity of Activated Carbons for Hydrogen Purification. Industrial & Engineering Chemistry Research 48, 3978-3990.

Lopes, F.V.S., Grande, C.A., Rodrigues, A.E., 2011. Activated carbon for hydrogen purification by pressure swing adsorption: Multicomponent breakthrough curves and PSA performance. Chemical Engineering Science 66, 303-317.

Marsh, H., Rodriguez-Reinoso, F., 2006. Activated Carbon. Elesevier Limited, Oxford.

Martin-Martinez, J.M., Torregrosa-Macia, R., Mittelmeijer-Hazelelger, M.C., 1994. Mechanisms of Adsorption of CO2 in the micropores of activated anthracite. Fuel 74, 111-114.

Martín, C.F., García, S., Beneroso, D., Pis, J.J., Rubiera, F., Pevida, C., 2012. Precombustion CO2 capture by means of phenol–formaldehyde resin-derived carbons: From equilibrium to dynamic conditions. Separation and Purification Technology 98, 531-538.

Martin, C.F., Plaza, M.G., Pis, J.J., Rubiera, F., Pevida, C., Centeno, T.A., 2010. On the limits of CO2 capture capacity of carbons. Separation and Purification Technology 74, 225-229.

Martin, C.F., Stockel, E., Clowes, R., Adams, D.J., Cooper, A.I., Pis, J.J., Rubiera, F., Pevida, C., 2011. Hypercrosslinked organic polymer networks as potential adsorbents for pre-combustion CO2 capture. Journal of Materials Chemistry 21, 5475-5483.

Mehta, D., Hawley, M.C., 1969. Wall Effect in Packed Columns. Industrial & Engineering Chemistry Process Design and Development 8, 280-282.

Miller, B.G., 2011. Clean coal engineering technology. Butterworth-Heinemann, Burlington, MA.

Myers, A.L., Prausnitz, J.M., 1965. Thermodynamics of mixed-gas adsorption. AIChE Journal 11, 121-127.

Nikolic, D., Giovanoglou, A., Georgiadis, M.C., Kikkinides, E.S., 2008. Generic Modeling Framework for Gas Separations Using Multibed Pressure Swing Adsoprtion Processes. Industrial Engineering Chemical Research 47, 3156-3169.

Nord, L.O., Anantharaman, R., Bolland, O., 2009. Design and off-design analyses of a pre-combustion CO2 capture process in a natural gas combined cycle power plant. International Journal of Greenhouse Gas Control 3, 385-392.

Ofuchi, K., Kunii, D., 1965. Heat-transfer characteristics of packed beds with stagnant fluids. International Journal of Heat and Mass Transfer 8, 749-757.

Ordorica-Garcia, G., Douglas, P., Croiset, E., Zheng, L., 2006. Technoeconomic evaluation of IGCC power plants for CO2 avoidance. Energy Conversion Management 47, 2250-2259.

Pan, H., Ritter, J.A., Balbuena, P.B., 1998. Examination of the Approximations Used in Determining the Isosteric Heat of Adsorption from the Clausius−Clapeyron Equation. Langmuir 14, 6323-6327.

Park, J.-H., Kim, J.-N., Cho, S.-H., 2000. Performance Analysis of Four-Bed H2 PSA Process Using Layered Beds. AIChE Journal 46, 790-802.

Park, J.-H., Kim, J.-N., Cho, S.-H., Kim, J.-D., Yang, R.T., 1998. Adsorber dynamics and optimal design of layered beds for multicomponent gas adsorption. Chemical Engineering Science 53, 3951-3963.

Perry, R.H., Green, D.W., Maloney, J.O., 1997. Perry's chemical engineers' handbook, 7th ed. McGraw-Hill, London.

Radosz, M., Hu, X., Krutkramelis, K., Shen, Y., 2008. Flue-Gas Carbon Capture on Carbonaceous Sorbents: Toward a Low-Cost Multifunctional Carbon Filter for “Green” Energy Producers†. Industrial & Engineering Chemistry Research 47, 3783-3794.

Reid, R.C., Prausnitz, J.M., Poling, B.E., 1987. The Properties of Gases and Liquids 4th ed. McGraw-Hill, Inc., U.S.A.

Ribeiro, A.M., Grande, C.A., Lopes, F.V.S., Loureiro, J.M., Rodrigues, A.E., 2008. A parametric study of layered bed PSA for hydrogen purification. Chemical Engineering Science 63, 5258-5273.

Ritter, J.A., Bhadra, S.J., Ebner, A.D., 2011. On the Use of the Dual-Process Langmuir Model for Correlating Unary Equilibria and Predicting Mixed-Gas Adsorption Equilibria. Langmuir 27, 4700-4712.

Romano, M.C., Chiesa, P., Lozza, G., 2010. Pre-combustion CO2 capture from natural gas power plants, with ATR and MDEA processes. International Journal of Greenhouse Gas Control 4, 785-797.

Rother, J., Fieback, T., 2013. Multicomponent adsorption measurements on activated carbon, zeolite molecular sieve and metal–organic framework. Adsorption 19, 1065-1074.

Rouquerol, F., Roquerol, J., King, K.S.W., 1999. Adsorption by powders and porous solids: principles, methodology, and applications. Academic Press, San Diego.

Ruthven, D.M., 1984. Principles of Adsorption and Adsorption Processes. John Wiley & Sons, Inc., New York.

Ruthven, D.M., Garg, D.R., Crawford, R.M., 1975. The performance of molecular sieve adsorption columns: non-isothermal systems. Chemical Engineering Science 30, 803-810.

Salem, M.M.K., Braeuer, P., Szombathely, M.v., Heuchel, M., Harting, P., Quitzsch, K., Jaroniec, M., 1998. Thermodynamics of High-Pressure Adsorption of Argon, Nitrogen, and Methane on Microporous Adsorbents. Langmuir 14, 3376-3389.

Samanta, A., Zhao, A., Shimizu, G.K.H., Sarkar, P., Gupta, R., 2011. Post-Combustion CO2 Capture Using Solid Sorbents: A Review. Industrial & Engineering Chemistry Research 51, 1438-1463.

Santos, M.P.S., Grande, C.A., Rodrigues, A.E., 2011. Pressure Swing Adsorption for Biogas Upgrading. Effect of Recycling Streams in Pressure

Swing Adsorption Design. Industrial & Engineering Chemistry Research 50, 974-985.

Schell, J., Casas, N., Blom, R., Spjelkavik, A.I., Andersen, A., Cavka, J.H., Mazzotti, M., 2012a. MCM-41, MOF and UiO-67/MCM-41 adsorbents for pre-combustion CO2 capture by PSA: adsorption equilibria. Adsorption-Journal of the International Adsorption Society 18, 213-227.

Schell, J., Casas, N., Marx, D., Mazzotti, M., 2013. Precombustion CO2 Capture by Pressure Swing Adsorption (PSA): Comparison of Laboratory PSA Experiments and Simulations. Industrial & Engineering Chemistry Research 52, 8311-8322.

Schell, J., Casas, N., Mazzotti, M., 2009. Pre-combustion CO2 capture for IGCC plants by an adsorption process. Energy Procedia 1, 655-660.

Schell, J., Casas, N., Pini, R., Mazzotti, M., 2012b. Pure and binary adsorption of CO, H2, and N2 on activated carbon. Adsorption 18, 49-65.

Seader, J.D., Henley, E.J., Roper, D.K., 2010. Separation Process Principles. John Wiley & Sons.

Shafeeyan, M.S., Wan Daud, W.M.A., Shamiri, A., 2014. A review of mathematical modeling of fixed-bed columns for carbon dioxide adsorption. Chemical Engineering Research and Design 92, 961-988.

Shekhawat, D., Luebke, D.R., Pennline, A., 2003. A Review of Carbon Dioxide Selective Membranes, U.S. DOE Topical Report, West Virginia.

Shen, C., Grande, C.A., Li, P., Yu, J., Rodrigues, A.E., 2010. Adsorption equilibria and kinetics of CO2 and N2 on activated carbon beads. Chemical Engineering Journal 160, 398-407.

Sioshansi, F.P., 2009. Generating Electricity in a Carbon-Constrained World. Elsevier Academic Press.

Sips, R., 1948. On the Structure of a Catalyst Surface. The Journal of Chemical Physics 16, 490-495.

Sircar, S., Golden, T.C., Rao, M.B., 1996. Activated carbon for gas separation and storage. Carbon 34, 1-12.

Siriwardane, R.V., Shen, M.-S., Fisher, E.P., Poston, J.A., 2001. Adsorption of CO2 on Molecular Sieves and Activated Carbon. Energy & Fuels 15, 279-284.

Sjostrom, S., Krutka, H., 2010. Evaluation of solid sorbents as a retrofit technology for CO2 capture. Fuel 89, 1298-1306.

Sun, N., Sun, C., Liu, H., Liu, J., Stevens, L., Drage, T., Snape, C.E., Li, K., Wei, W., Sun, Y., 2013. Synthesis, characterization and evaluation of activated spherical carbon materials for CO2 capture. Fuel 113, 854-862.

Takamura, Y., Narita, S., Aoki, J., Hironaka, S., Uchida, S., 2001. Evaluation of dual-bed pressure swing adsorption for CO2 recovery from boiler exhaust gas. Separation and Purification Technology 24, 519-528.

Thomas, D.C., Benson, S., 2005. Carbon dioxide capture for storage in deep geologic formations. Elsevier, Oxford.

van Selow, E.R., Cobden, P.D., van den Brink, R.W., Hufton, J.R., Wright, A., 2008. Performance of sorption-enhanced water-gas shift as a pre-comustion CO2 capture technology. Energy Procedia 00, 000-000.

Wakao, N., Funazkri, T., 1978. Effect of fluid dispersion coefficients on particle-to-fluid mass transfer coefficients in packed beds : Correlation of sherwood numbers. Chemical Engineering Science 33, 1375-1384.

Wakao, N., Kaguei, S., Funazkri, T., 1979. Effect of fluid dispersion coefficients on particle-to-fluid heat transfer coefficients in packed beds: Correlation of nusselt numbers. Chemical Engineering Science 34, 325-336.

Wang, Q., Luo, J., Zhong, Z., Borgna, A., 2011. CO2 capture by solid adsorbents and their applications: current status and new trends. Energy & Environmental Science 4, 42-55.

Warmuzinski, K., Tanczyk, M., 1997. Multicomponent pressure swing adsorption Part I. Modelling of large-scale PSA installations. Chemical Engineering and Processing 36, 89-99.

Won, W., Lee, K.S., 2011. Adaptive predictive collocation with a cubic spline interpolation function for convection-dominant fixed-bed processes: Application to a fixed-bed adsorption process. Chemical Engineering Journal 166, 240-248.

Won, W., Lee, S., Lee, K.S., 2012. Modeling and parameter estimation for a fixed-bed adsorption process for CO2 capture using zeolite 13X. Separation and Purification Technology 85, 120-129.

Xiao, P., Wilson, S., Xiao, G., Singh, R., Webley, P., 2009. Novel adsorption processes for carbon dioxide capture within an IGCC process. Energy Procedia 1, 631-638.

Yagi, S., Kunii, D., 1960. Studies on heat transfer near wall surface in packed beds. AIChE Journal 6, 97-104.

Yang, J., Lee, C.-H., 1998. Adsorption Dynamics of a Layered Bed PSA for H2 Recovery from Coke Oven Gas. AIChE Journal 44, 1325-1334.

Yang, R.T., 1987. Gas Separation by Adsorption Processes. Butterworths, London.

Yang, R.T., Doong, S.J., 1985. Gas Separation by Pressure Swing Adsorption: A Pore-Diffusion Model for Bulk Separation. AIChE Journal 31, 1829-1832.

List of Publications

Oral Presentations:

S. Caldwell, J. Wood and B. Al-Duri, 2013. Development of a High-Pressure Solid Adsorption Model for Use in Pre-Combustion Carbon Dioxide Capture. Oral presentation at the 9th World Congress of Chemical Engineering, Seoul, Korea, 18 – 23 August 2013. Presentation FrO-T221-4.

J. Wang, J. Wood, S. Caldwell and Y Wang, 2011. Modelling of Pre-Combustion Carbon Dioxide Capture and Power Plant Cycle at IGCC Power Stations. Oral Presentation at the Mathematical Modelling and Simulation of Power Plants and CO2 Capture Workshop, Warwick, UK, 20-21 March 2012.

Poster Presentations:

S. Caldwell, J. Wood and B. Al-Duri, 2014. Modelling of Pressure Swing Adsorption Systems at High Pressure Using Fixed Beds for Pre-Combustion Carbon Dioxide Capture. Poster Presentation at the Advanced Process Modelling Forum 2014, London, UK, 1-3 April 2014.

S. Caldwell, J. Wood and B. Al-Duri, 2013. Modelling of High Pressure Solid Adsorption Systems Using Fixed Beds for Pre-Combustion Carbon Dioxide Capture. Poster Presentation at the Advanced Process Modelling Forum 2013, London, UK, 17-18 April 2013.

List of Publications

S. Caldwell, J. Wood and B. Al-Duri, 2012. Modelling of High Pressure Solid Adsorption Systems Using Fixed Beds for Pre-Combustion Carbon Dioxide Capture. Poster Presentation at the MEGS III Annual Conference, Birmingham, UK, 18-19 September 2012.

S. Caldwell, J. Wood and B. Al-Duri, 2012. Modelling Integrated Gasification Combined Cycle (IGCC) Power Station with Carbon Capture. Poster Presentation at the CO2Chem-CO2ChemEng Conference, Sheffield, UK, 3-4 April 2012.

S. Caldwell, J. Wood and B. Al-Duri, 2011. Modelling Integrated Gasification Combined Cycle (IGCC) Power Station with Carbon Capture. Poster Presentation at the Midland Energy Graduate School II Christmas Event and MEGS Inaugural Lecture, Loughborough, UK, 13 December 2011.